15 JULY 1969

MULTISPECTRAL IMAGING OF MARS

FROM A LANDER
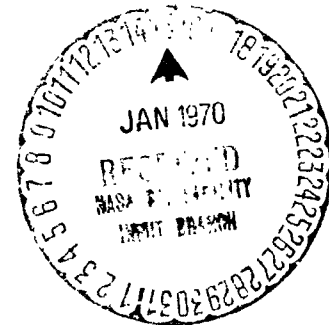
PREPARED FOR

LANGLEY RESEARCH CENTER
NATIONAL AERONAUTICS AND SPACE ADMINISTRATION

GENERAL ⓖ ELECTRIC

Re-entry & Environmental
Systems Division

3198 Chestnut St., Philadelphia, Pa. 19101
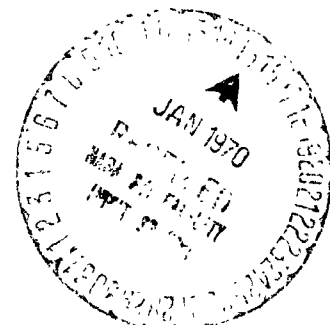
MULTISPECTRAL IMAGING OF MARS

FROM A LANDER

(FINAL DRAFT)

By Dr. V. Klemas
Dr. E. L. G. Odell

15 July 1969

Re-entry and Environmental Systems Division
General Electric Company
Philadelphia, Pa.

for

Langley Research Center

NATIONAL AERONAUTICS AND SPACE ADMINISTRATION

i

ACKNOWLEDGEMENT

TABLE OF CONTENTS

TABLE OF CONTENTS (Cont)

TABLE OF CONTENTS (Cont)

TABLE OF CONTENTS (Cont)

LIST OF TABLES

LIST OF ILLUSTRATIONS

LIST OF ILLUSTRATIONS (Cont)

LIST OF ILLUSTRATIONS (Cont)

x

LIST OF ILLUSTRATIONS (Cont)

LIST OF ILLUSTRATIONS (Cont)

SECTION 1

INTRODUCTION AND SUMMARY

On some earth-related reconnaissance missions, the interpretation of pictures can be considerably enhanced by taking advantage of scene spectral contrast in addition to intensity contrast. Although this approach may have little value on a colorless surface such as the Moon's, there are some indications of color differences on Mars. For instance, astronomers have observed orange-yellow bright areas, gray-brown dark areas, white polar caps, and yellow and white clouds on Mars. Figure 1-1 illustrates the marked albedo difference between the dark and bright areas of Mars. In Figure 3-12 are shown the spectral reflectivity signatures of some materials that have reasonable probability of existing on Mars, such as limonite, basalt, and primitive lichen vegetation. The increased reflectivity and larger differences in reflectivity in the near infrared suggest that color bands added in this region may enhance contrast in the image and help identify the type of constituents present.

The primary purpose of this study was to develop a technique for selecting color bands for an imaging system; secondly to investigate the advantages to be gained from using certain solid state detectors; and thirdly to determine if it is feasible by means of data compression, adaptive control, and optimizing the number of grey levels in each color band, to keep the total number of data bits down to a fraction above that required for a black and white panorama from the lander, which has a very limited telemetry rate.

As shown in the flow diagram of Figure 1-2, the study consists of both analytical and experimental tasks. In Section 2 the existing observational data on Mars are summarized, twelve likely surface constituents are selected (Tables 1-1 and 2-5) and the reflection spectra are presented between 0.3 micron and 5 microns. (Figure 2-11 to 2-23.)

In Section 3 a description and results are presented of the analytical approach which was used to multiply the spectral reflectivity of the selected constituents by the illumination, atmospheric transmission, filter transmission and detector spectral response so as to

obtain response and modulation functions (Figure 3-14 to 3-35) for all constituents and each detector considered. (Figure 1-2.) By locating optical band-pass filters at the points where the modulation function is largest, optimum discrimination between the constituents can be obtained. In Section 5 the number of equivalent grey levels in each band to accomplish the discrimination is derived. On-board signature determination, simple data compression schemes and a limited degree of adaptive control are considered in Section 6.

The experimental work is described in Sections 4 and 7. In Section 4 analytical results are compared with outputs of densitometer scans across negatives of photographs taken of a test scene. The photographs were taken with filters and solar illumination. The test scene was composed of the materials shown in Figures 1-3 and 4-1. Section 7 describes the results of discrimination experiments performed with GE's Multispectral Test Facility (Figure 1-4) on a test scene similar to that in Figure 1-3. The false color discrimination pictures resulting from this experiment are shown in Figures 7-6 to 7-12.

The final conclusions are summarized in Section 8.

Suggestions for expanding the work in follow-on studies beyond the present limited scope are presented in Section 9. During the entire report the reader must not lose sight of these limitations. For instance, sun angles and camera angles were held fixed close to zenith. As discussed in Section 9, the effect of variations in reflectivity due to varying sun and camera angles should be considered in follow-on work. References and computer logic diagrams are presented in Sections 10 and 11 respectively.

Table 1-1. List of Constituents

1.	Felisitic Rhyolite	7.	Goethite
2.	Granite	8.	Pulverized Limonite
3.	Basalt	9.	Silica Sand
4.	Dunite	10.	Gypsum Sand
5.	Olivine	11.	Calcium Carbonate
6.	Serpentine	12.	Lichen

Table 1-2. List of Sensors

0.3 to 0.8 Micron	0.6 to 2.0 Microns
Type 2 Cadmium Sulfide	Silcon PIN Type 654
Type 5 Cadmium Sulfide	Germanium Type 653
Type 5 H Cadmium Sulfide	Germanium PIN Type 655
S-11	**1.0 to 5.0 Microns**
S-20	Indium Arsenide
S-10 (Multispectral Test)	Lead Sulfide
0.3 to 1.1 Microns	Lead Selenide
	Thermistor Flakes
S-1	**Film (Densitometer Test)**
Silicon	
Type 3 Cadmium Selenide	Ektachrome
Type 4 Cadmium Selenide	Kodachrome
Type 7 Cadmium Sulfide	Plus-X
	I-Z infrared
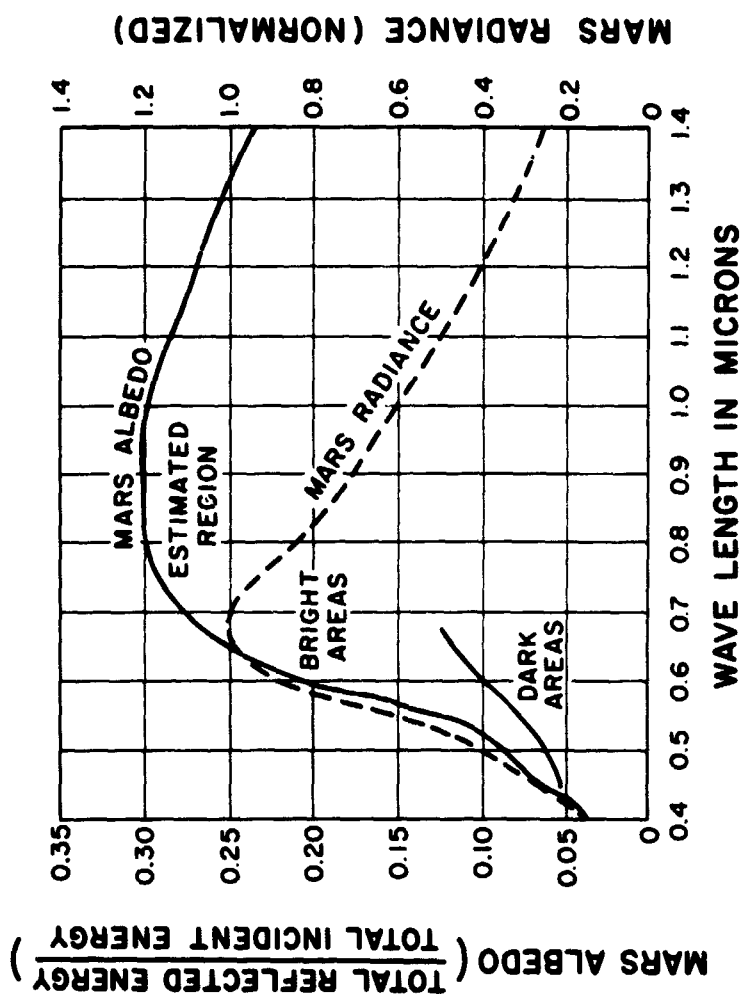
Figure 1-1. Mars Albedo and Radiance

FIGURE 1-2. STUDY APPROACH
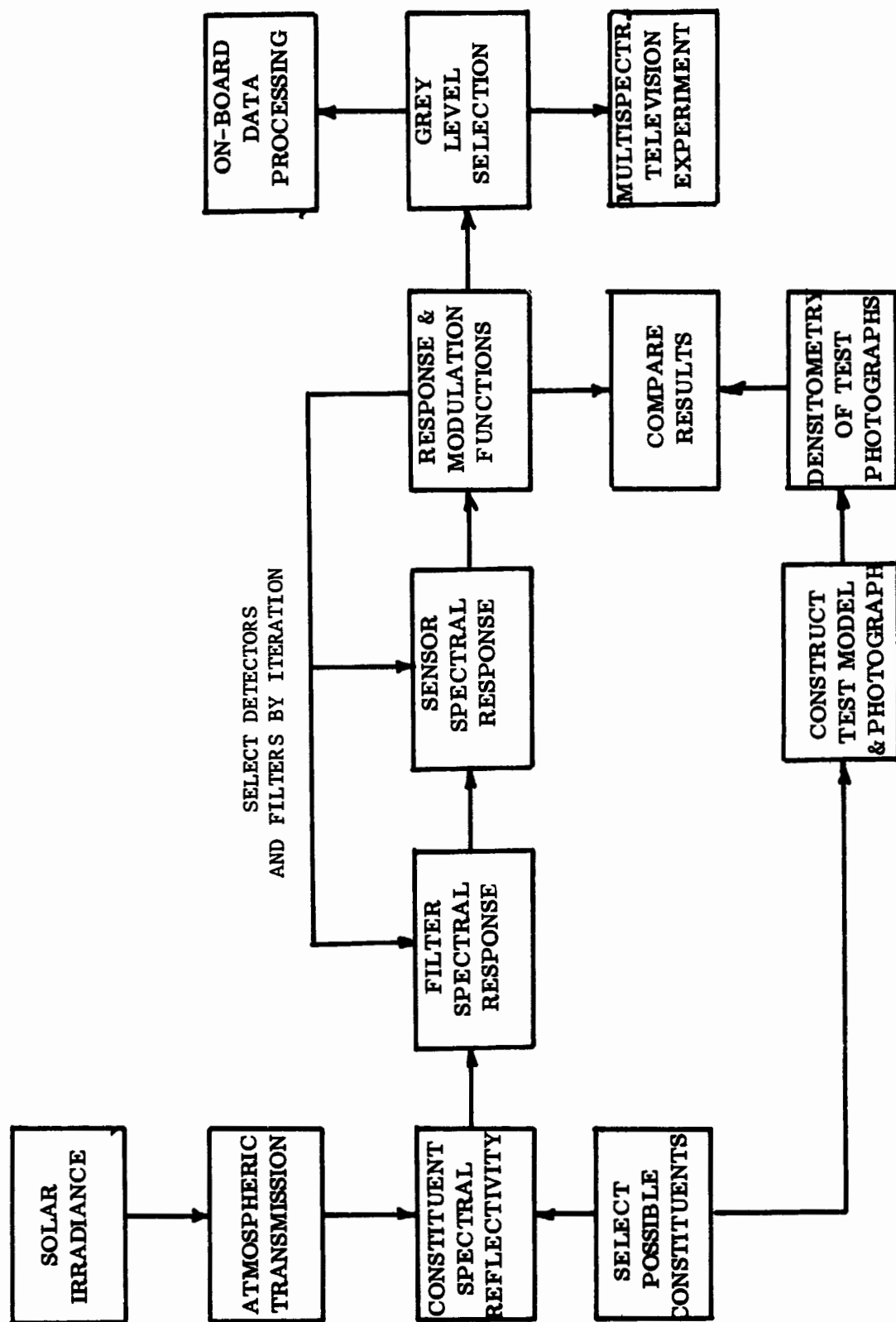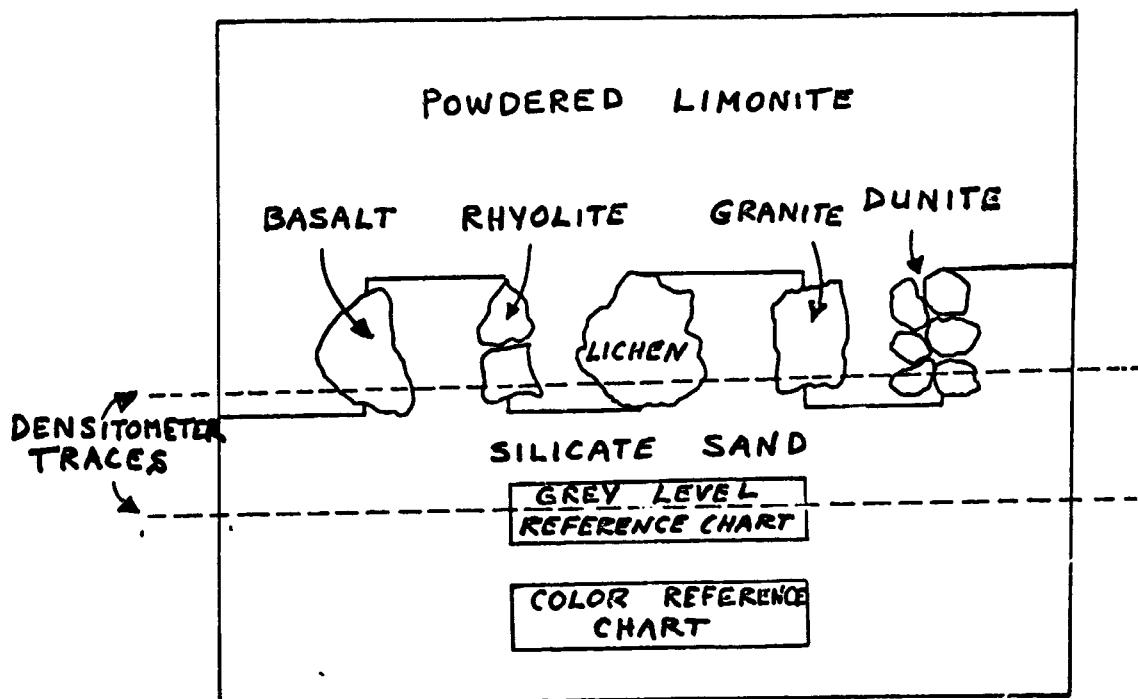
Figure 1-3. Scene Arrangement and Geometry
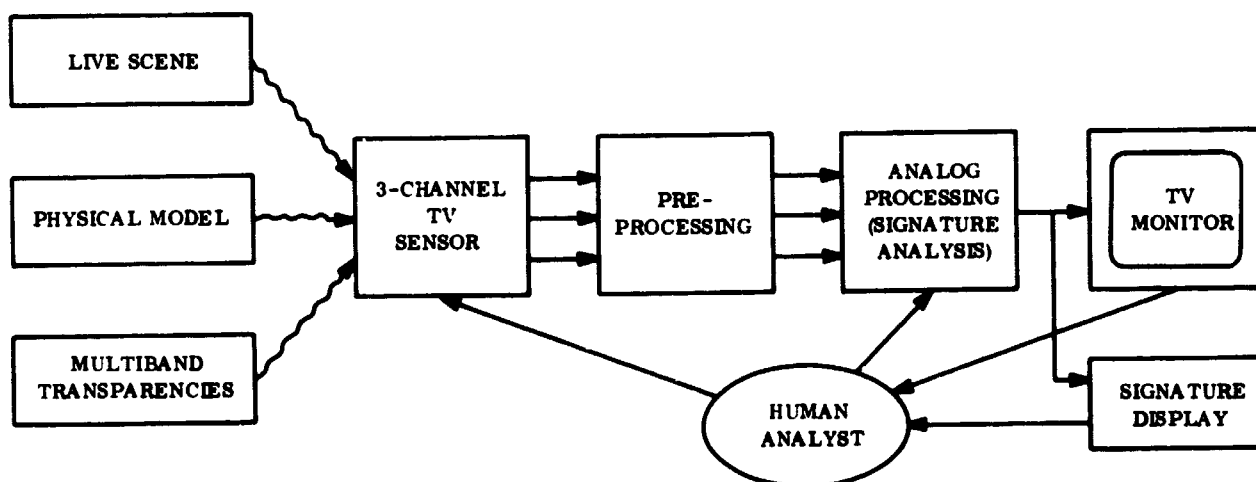
Figure 1-4. Multispectral Test System Block Diagram

SECTION 2

OPTICAL CHARACTERISTICS OF MARS

2.1 OBSERVED PHOTOMETRIC CHARACTERISTICS OF MARS

2.1.1 SPECTRAL REFLECTIVITY

Although superficial visual examination of Mars indicates that the planet is red in color, a closer examination reveals the presence of bright ochre areas; dark areas; and, at the poles, white areas. Broadband measurements of the spectral reflectivity of the bright and dark areas expressed in terms of geometrical albedo (e. g., see References 1 and 2) typically yield the results shown in Figure 2-1. A complete summary of observations prior to 1969 involving whole disk photometry appears in Figure 2-2. (Conditions under which this curve was produced are described in Reference 3.) The figure illustrations show that the geometrical albedo in the visual part of the spectrum rises rapidly with increasing wavelength. The albedo of the dark areas exhibits similar behavior, but its rate of increase with wavelength is considerably slower than that for the bright areas.
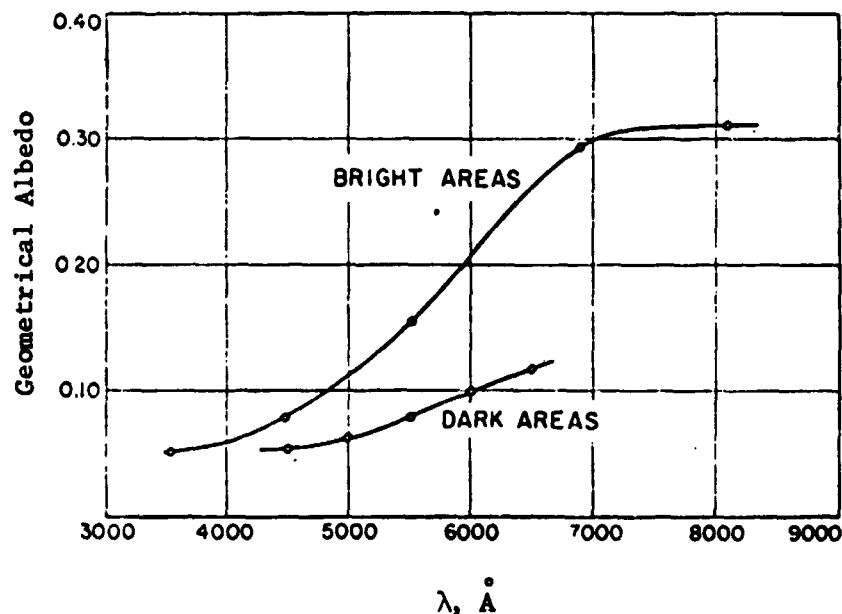
Figure 2-1. Variation in Geometrical Albedo with Wavelength [Geometrical albedo is the ratio of the average brightness of the planet viewed at 0 degrees phase to the brightness of a perfectly diffusing disk of the same diameter normal to the incident illumination (Loomis, A.A., "Some Geological Problems of Mars," Bulletin of the Geological Society of America, Vol. 76)]
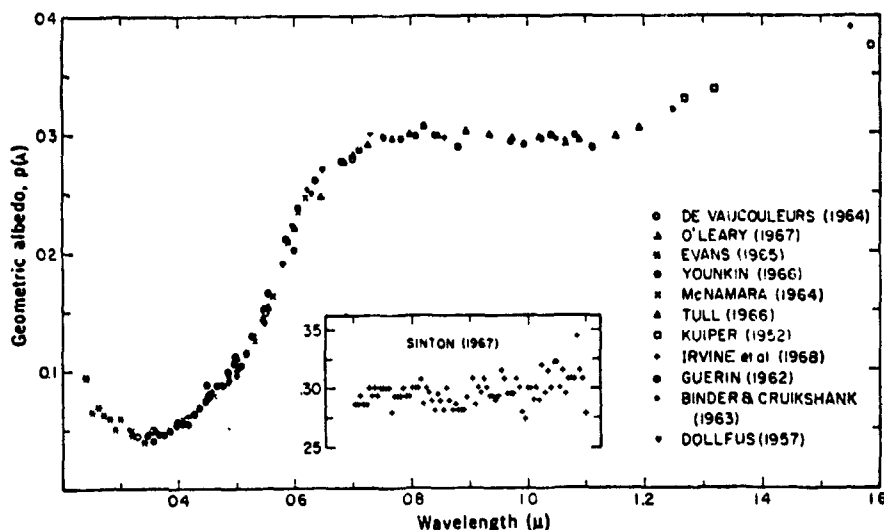
Figure 2-2. Spectral Geometric Albedo of Mars [All measurements have been adjusted in the vertical scale to match the albedo values calculated by de Vaucouleurs (Reference 2)]

The nature of the spectral reflectivity indicates that the reddish color of both the bright and dark areas is real and is the consequence of generally low albedo, decreasing toward the shorter wavelengths, from 0.33 in the extreme red (6900 Å) to 0.18 in the visual green-yellow (5550 Å) to 0.046 in the ultraviolet (3600 Å). Hence, the reflected light contains relatively more radiation in the red portion of the spectrum than the incident light. In the blue and violet portions, the reflectivity is remarkably low, approaching that of soot. There exist numerous reports of blue-green coloration of dark areas. Such appearance is attributable to a psychophysiological effect first described by Purkyně. According to this effect, a neutral colored region adjacent to a brightly colored area takes on colors complementary to those of the bright area. Orange-red and blue-green are complementary colors.

Another characteristic feature of the spectral reflectivity is the broad shallow dip centered around 1 micron. This feature is commonly referred to as the "limonite band." Its very existence is disputed by various observers. A detailed discussion of problems involved in its detection is given in Reference 1.

The albedo of Mars varies with the location on the surface of the planet. For instance, in the yellow portion of the spectrum there are certain bright areas on the surface of Mars with an albedo of 0.15 and other dark areas where the albedo is 0.05. The average value for the whole planet in visible light is generally quoted as 0.15. This value is larger than the albedo of the Moon and Mercury but considerably less than that of Venus or Earth.

2.1.2 SURFACE CONTRAST

In the green, yellow, and red regions of the spectrum, the surface markings are visible, with the contrast between the bright and dark areas increasing with wavelength. At a wavelength of approximately 4500 Å, the dark areas become indistinct; below this wavelength the contrast is completely washed out. An indication of this effect is present in Figure 2-1. A better illustration of the disappearance of contrast with decreasing wavelength is shown in Figure 2-3. A striking observational fact is that there are brief periods when the con-
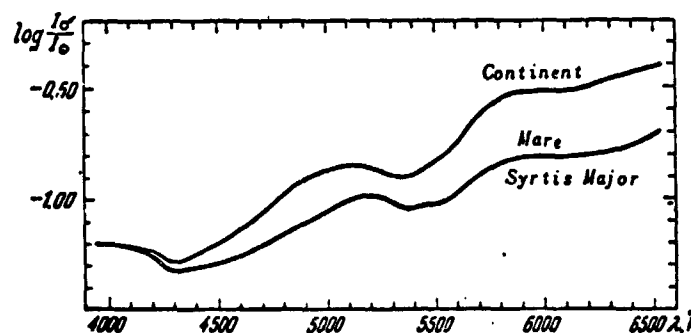
Figure 2-3. Apparent Reflectivity of the Continents and Seas as a Function of Wavelength (Reference 4) [Ordinate: logarithm of the intensity ratios in an arbitrary continuous spectrum of Mars and Sun; zero point was arbitrarily selected]

trast is clearly present in the blue region of the spectrum. The loss of contrast below 4500 $\overset{o}{A}$ and its sudden appearance have come to be known respectively as "blue haze" and "blue clearing." Attempts to account for these effects lead to numerous controversial hypotheses, none of which are very successful. Historical accounts of these difficulties are given in many places (e.g., Reference 4). One of the latest hypotheses is advanced in Reference 1, in which the assumed model of the surface leads naturally to the loss of contrast at short wavelengths. Blue clearings are attributed to a combination of seeing the presence of Martian clouds, and the size of dark areas being observed.

2.1.3 POLARIMETRY

Although no use is made of polarimetry in the present study, a brief discussion of such observations is appropriate since this source of information is likely to be of crucial importance in choosing between alternate hypotheses on the structure and composition of the Martian surface. Typical polarization curves are shown in Figure 2-4. Curves denoted by b refer to bright regions and curve d to dark areas. Superscript α indicates that the curve is based on observations during the 1952 and 1954 oppositions; superscript β refers to oppositions of 1948 and 1950.

The most characteristic feature of Martian polarization curves is the region of negative polarization for phase angles smaller than about 30 degrees. The negative branch is present in the radiation of both the bright and dark areas.

2.1.4 INTERPRETATION

Detailed discussions of various attempts to interpret photometric and polarimetric observations of Mars are given in references 1, 4, 5 and 6. Various scientific arguments eventually led to the following hypotheses.

According to one school of thought, originated by Dollfus (Reference 7), Martian reflectivity and the degree of polarization can be matched accurately by the pulverized ferric oxide polyhydrates, such as limonite. Dollfus found that among many terrestrial materials examined by him, powdered limonite was the only one whose polarization characteristics

2-4
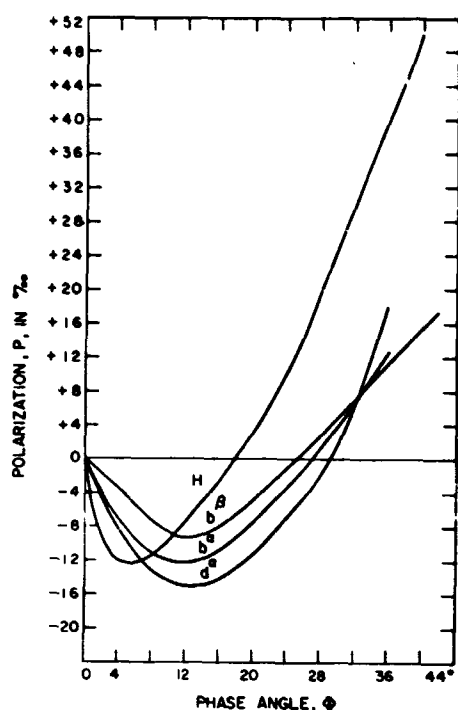
Figure 2-4. Comparison of Polarization Curves for Bright and Dark Areas of Mars with the Corresponding Curve for Pulverized Hematite (Curve 4) [After Dollfus, Reference 1]

matched those of Mars in detail. Ideas of Dollfus have attained their highest state of development in the work of Sagan and Pollack (Reference 1). These authors constructed a consistent theory in which goethite, a form of hydrated ferric oxide, plays a major role. They present evidence that both the dark and bright areas of the planet are covered by this material and that the photometric appearance is primarily the result of a difference in particle sizes. The bright areas are covered by particles whose mean radius is 25 microns, whereas the dark areas are characterized by particles whose average size is 100 microns. At their darkest, the dark areas are thought to be covered by particles as large as 200 microns. Within this theory, the seasonal changes in dark areas are a consequence of seasonal wind transport of dust which results in a change in the mean particle diameter covering the area. The indicated particle size is not inconsistent with the rate of dissipation of yellow clouds and the measured values of so-called thermal inertia. Within this scheme of things, there is no "blue haze." The loss of contrast toward the shorter wavelengths is due to the transition from multiple to single scattering for the particle size distributions involved. Finally, according to Sagan's and Pollack's results, the latest polarization measurements are consistent with the latest independent surface pressure estimates. Sagan and Pollack come to an additional interesting conclusion that the polarization observations not only do not require a significant contribution from aerosols, but are, in fact, inconsistent with such a contribution.

Minerals other than hydrated ferric oxides were suggested for the red-orange material covering the surface of Mars. From an examination of the spectrum of Mars in the wave-

length range of 0.4 to 2.5 microns, Kuiper (Reference 8) concluded that the deserts may consist of an igneous material similar to felsitic rhyolite, a rock composed mainly of aluminum and potassium silicate minerals with small amounts of dark colored minerals, several of which contain iron. Adams (Reference 3) succeeded in matching the whole disk reflectivity curve by oxidized basalt. Not much else can be said about the suggestions of Kuiper and Adams. They have not investigated consequences which may follow from their hypotheses in terms of polarization behavior of their materials, effect of the state of aggregation, thermal properties, etc.

Finally, it must be mentioned that unlike the emission and absorption spectra of gases, polarization properties and reflection spectra do not provide specific means of mineral identification. The difficulties are particularly acute in the near infrared region of the spectrum due to the presence of the Earth's atmospheric interference, the general similarity of reflection spectra of many minerals, and the fact that Martian observations in this region are not too numerous.

2.1.5 ATMOSPHERIC EFFECTS

For the purposes of the present study, the following assumptions were made concerning the atmosphere:

1. No aerosols are present.

2. The atmosphere is plane-parallel.

3. In the spectral region from 0.35 to 0.80 micron, Rayleigh scattering dominates radiation transport.

4. In the near infrared, radiation transport is affected by CO_2 bands and, to a much lesser degree, by H_2O bands.

In addition, it was assumed that it is sufficient to estimate atmospheric effects for the mean Sun-Mars distance.

The problem then is to estimate the solar illumination of the surface of Mars. In the wavelength range from 0.35 to 0.80 micron, the flux of radiation G_λ at the bottom of the assumed atmosphere was computed in terms of Chandrasekhar's functions γ_1, γ_r, and $\bar{s}$. Both the direct and scattered radiation were accounted for. In the case of scattered radiation, all significant Rayleigh scattering orders were included. The relationhip between the optical depth τ and the wavelenght λ for this model atmosphere is given in Table 2-1. The computation includes the effect of albedo A of the surface underlying the atmosphere.

Table 2-1. Optical Depth as a Function of Wavelength

λ	0.345	0.380	0.450	0.563	0.668	0.7175	0.7925
τ	0.15	0.10	0.05	0.02	0.01	0.0075	0.005
A	0.35	0.30	0.25	0.20	0.15	0.10	0.05

For $\tau = 0.15$, six scattering orders were accounted for; for $0.1 \le \tau \le 0.15$, two orders; and for $\tau < 0.1$, only primary scattering was included. Computations were carried out for ten values of sun zenith angle θ_0. These values are given in Table 2-2. The last value listed closely corresponds to the instant of sunset or sunrise. Typical results are shown in Figures 2-5 and 2-6. Figure 2-7 gives the correction factor enabling one to compute the flux at values of albedo other than 0.25.
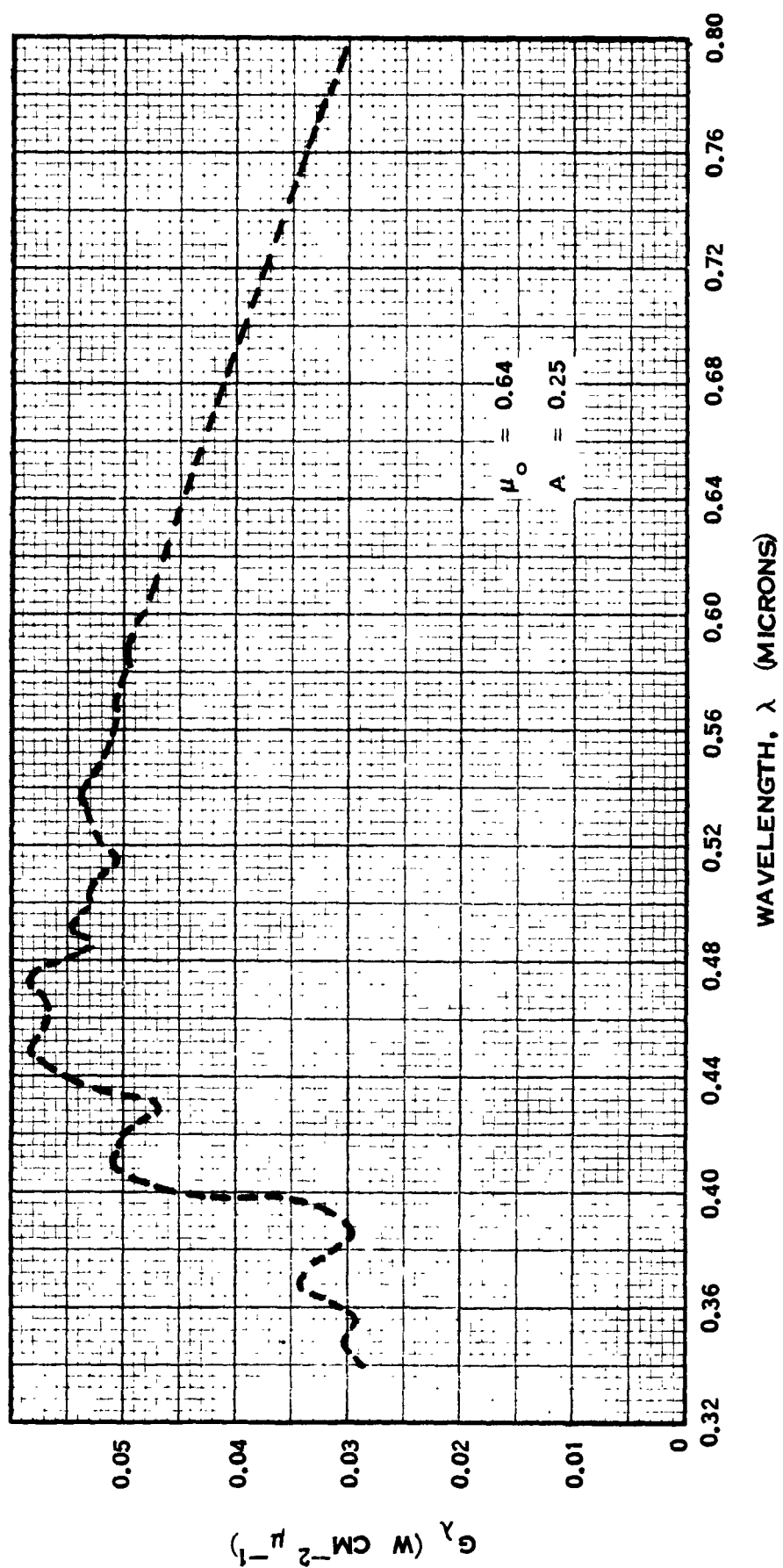
Figure 2-5. G_λ for Sun Zenith Angle of $50^\circ 12'$
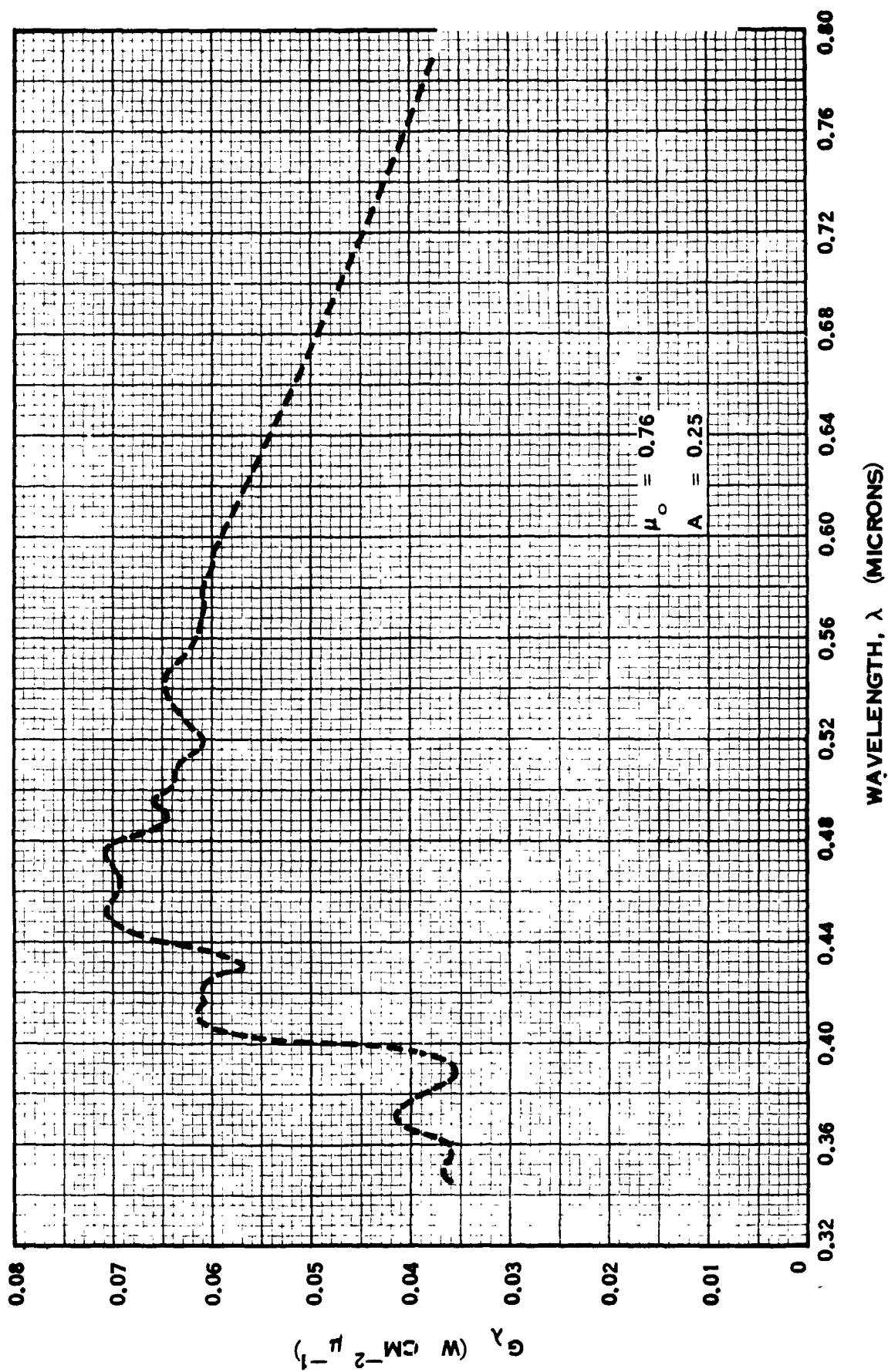
Figure 2-6. G_λ for Sun Zenith Angle of $40°32'$
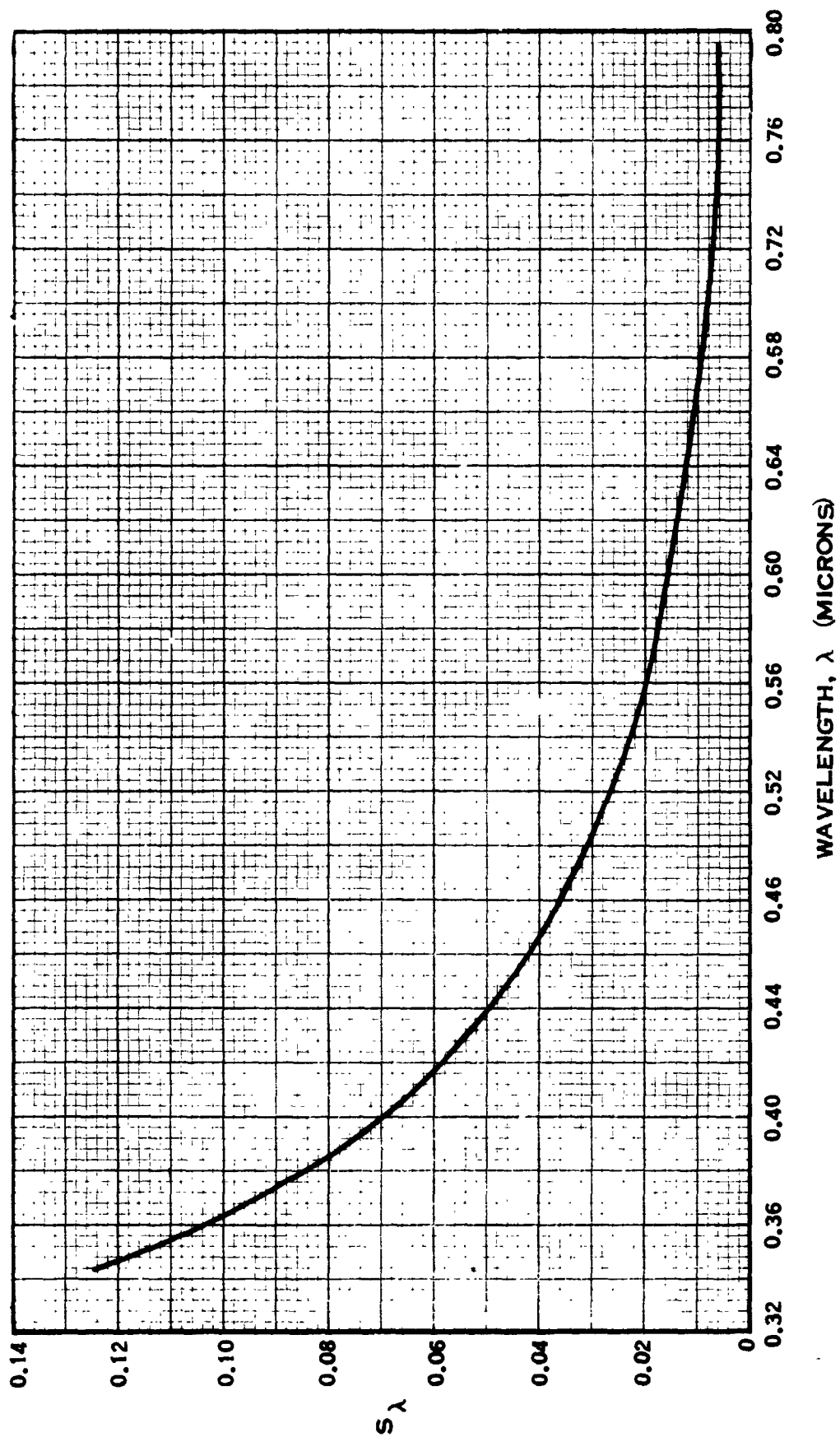
Figure 2-7. $S_\lambda = \bar{s}/(1 - 0.25\,\bar{s})$ as a Function of Wavelength

Table 2-2. Sun Zenith Angles used in Computations

θ_0	$u_0 = \cos \theta_0$
0°	1.000
$11^\circ 30'$	0.98
20°	0.94
$30^\circ 40'$	0.86
$40^\circ 32'$	0.76
$50^\circ 12'$	0.64
$58^\circ 40'$	0.52
$70^\circ 06'$	0.34
$79^\circ 37'$	0.18
$88^\circ 48'$	0.02

Practical usage of these curves is illustrated in the following numerical examples.
Let the following quantities be given:

Albedo, A = 0.18

Sun Zenith Angle, θ = 45 degrees

Wavelength, λ = 0.420 micron

The quantity G_λ is to be found as follows:

Step 1. Determine G_λ without correction for albedo:

$\cos \theta = \cos 45^\circ = 0.707$

$\therefore \mu_o = 0.707$

This value of μ falls between two values of μ_o ($\mu_{01} = 0.64$; $\mu_{02} = 0.76$) for which curves are available. Use a linear interpolation on μ_o (using A = 0.25 for the present):

$$G_\lambda(\mu_o) = G_\lambda(\mu_{01}) + \left(\frac{\mu_o - \mu_{01}}{\mu_{02} - \mu_{01}} \right) \left[G_\lambda(\mu_{02}) - G_\lambda(\mu_{01}) \right]$$

where

$$\mu_{01} < \mu_o < \mu_{02}$$

$$G_{0.42}(0.707) = G_{0.42}(0.64) + \left(\frac{0.707 - 0.640}{0.760 - 0.640} \right) \left[G_{0.42}(0.76) \right.$$

$$\left. - G_{0.42}(0.64) \right]$$

From Figure 2-6,

$$G_{0.42}(0.64) = 0.051 \text{ w cm}^{-2} \mu^{-1}$$

From Figure 2-7,

$$G_{0.42}(0.76) = 0.061 \text{ w cm}^{-2} \mu^{-1}$$

Then

$$G_{0.42}(0.707) = 0.051 + \frac{0.067}{0.12} (0.061 - 0.051)$$

$$= 0.051 + 0.006$$

2-12

$$G_{0.42} = 0.057 \text{ watts cm}^{-2} \text{ micron}^{-1}$$

Step 2. Correction for albedo, A = 0.18, is next:

$$G (A = 0.18) = G (A = 0.25) + \left[G (A = 0.25) \right] \cdot \left[S_\lambda \right] \left[\Delta A \right]$$

Now

$$G (A = 0.25) = 0.057$$

From Figure 2-7,

$$S_{(\lambda = 0.42)} = 0.057$$

$$\Delta A = -0.07, \text{ i.e., } (0.18 - 0.25)$$

$$G_{0.42} = 0.057 + (0.057)(0.057)(-0.07)$$

$$= 0.057 - 0.000227$$

$$G = 0.057 \text{ watts cm}^{-2} \text{ micron}^{-1} \text{ for A} = 0.18, \lambda = 0.42, \text{ and } \theta = 45 \text{ degrees}$$

For he assumed atmosphere, Rayleigh scattering becomes insignificant at wavelengths beyond 0.8 micron. Other atmospheric models lead to even smaller scattering effects.

Beyond 1 micron, illumination is primarily determined by transmission losses due to band absorption of atmospheric constituents. The atmosphere is assumed to consist

mostly of CO_2, N_2, and trace quantities of A and H_2O. For this composition, the atmospheric transmission will be determined by the absorption spectrum of CO_2 and H_2O vapor. Argon and nitrogen have no absorption bands in the region between 1.0 and 5.0 microns.

Since the filter bandwidths used in this study are quite wide, the transmission of the atmosphere can be treated in a manner suggested by Elder and Strong (Reference 10). According to these researchers, the region between 0.7 and 6.0 microns is divided into seven regions of relatively high transmission located between the centers of strong CO_2 and H_2O absorption bands.

Elder and Strong and later Howard, Burch, et al.(Reference 11) showed that the transmission within the so-called atmospheric windows can be represented by relatively simple empirical relations.

Examples of these relations, given in graphical form and extrapolated to concentrations which may reasonably be expected to exist on Mars, are shown in Figures 2-8, 2-9 and 2-10. It is estimated that the concentration of H_2O in one Martian air mass is less than 15 to 20 microns of precipitable water; the concentration of CO_2 is such as to yield a partial pressure of 7 millibars maximum (85 to 100 meter-atmospheres). Atmospheric windows are defined in Table 2-3.

Table 2-3. Atmospheric Windows

Window No.	Wavelength Limits (microns)	Window No.	Wavelength Limits (microns)
I	0.72 - 0.94	V	1.90 - 2.70
II	0.94 - 1.13	VI	2.70 - 4.30
III	1.13 - 1.38	VII	4.30 - 6.00
IV	1.38 - 1.90		
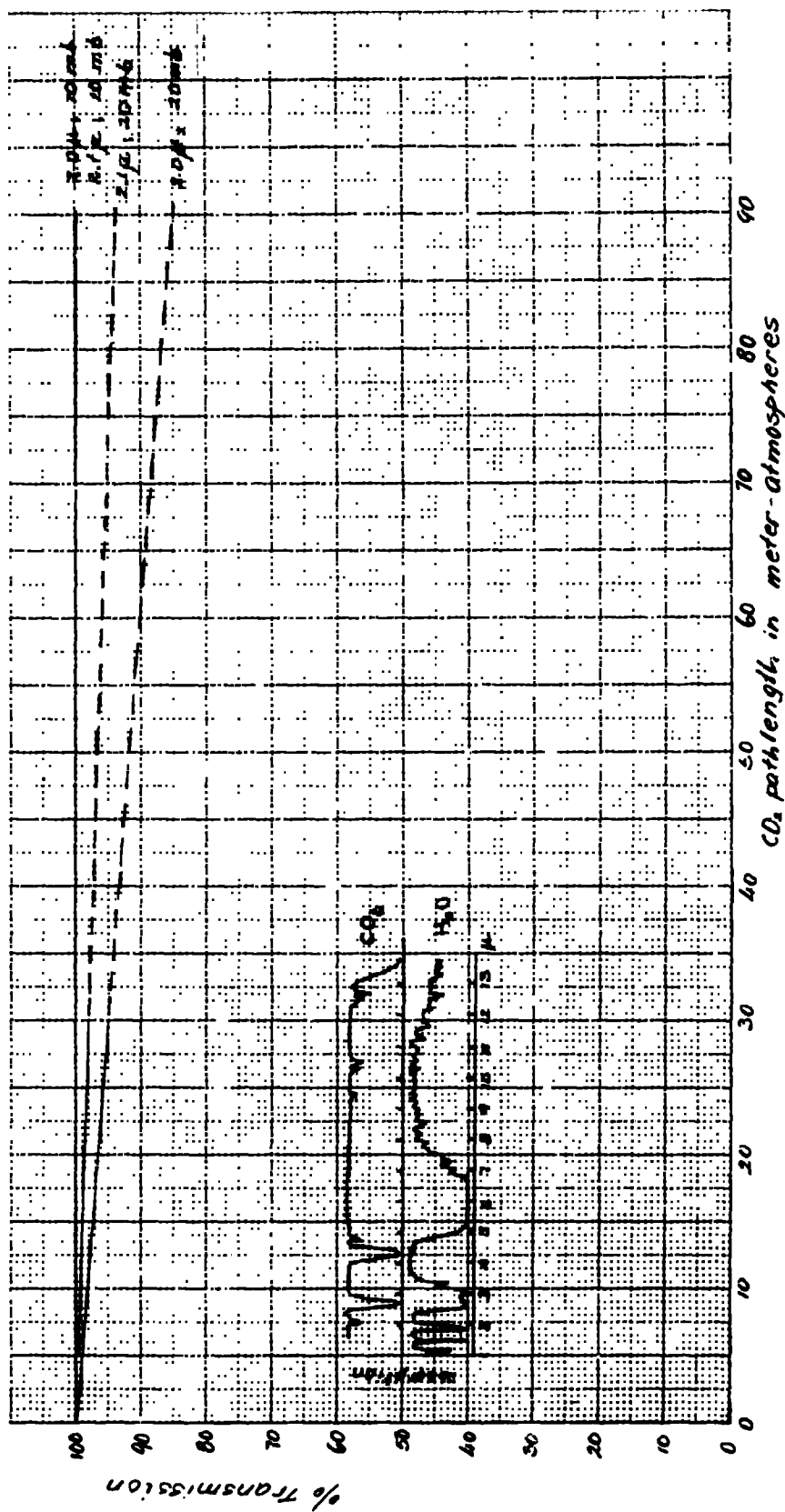
Figure 2-8. Transmission in the Vicinity of 2.0 Micron Band of CO_2 at Two Atmospheric Pressures ($\Delta\lambda = 0.1$ Micron)

2-15
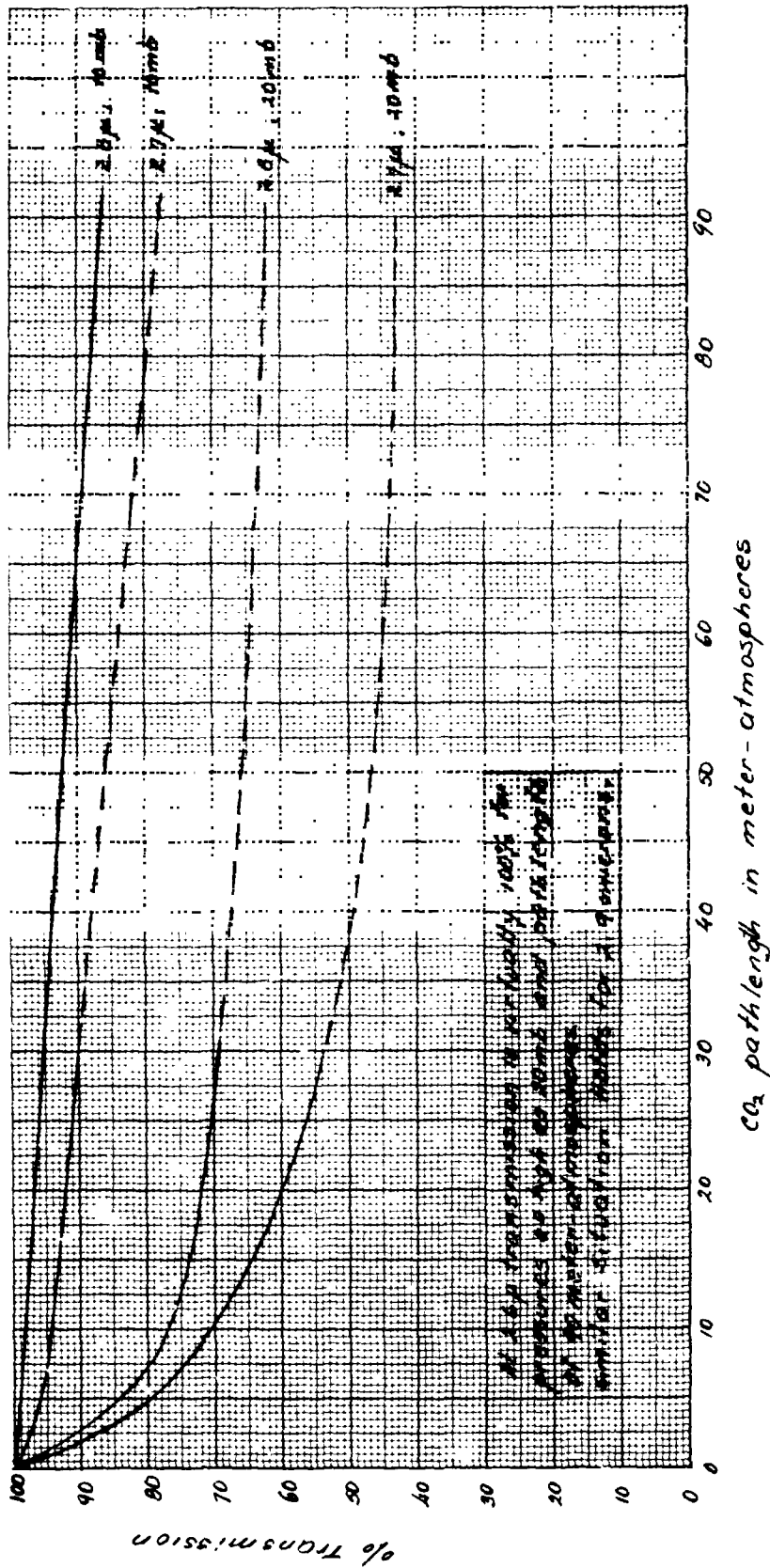
Figure 2-9. Transmission Through 2.7 Micron Band of CO_2 at Two Atmospheric Pressures
$(\Delta\lambda = 0.1 \text{ Micron})^2$
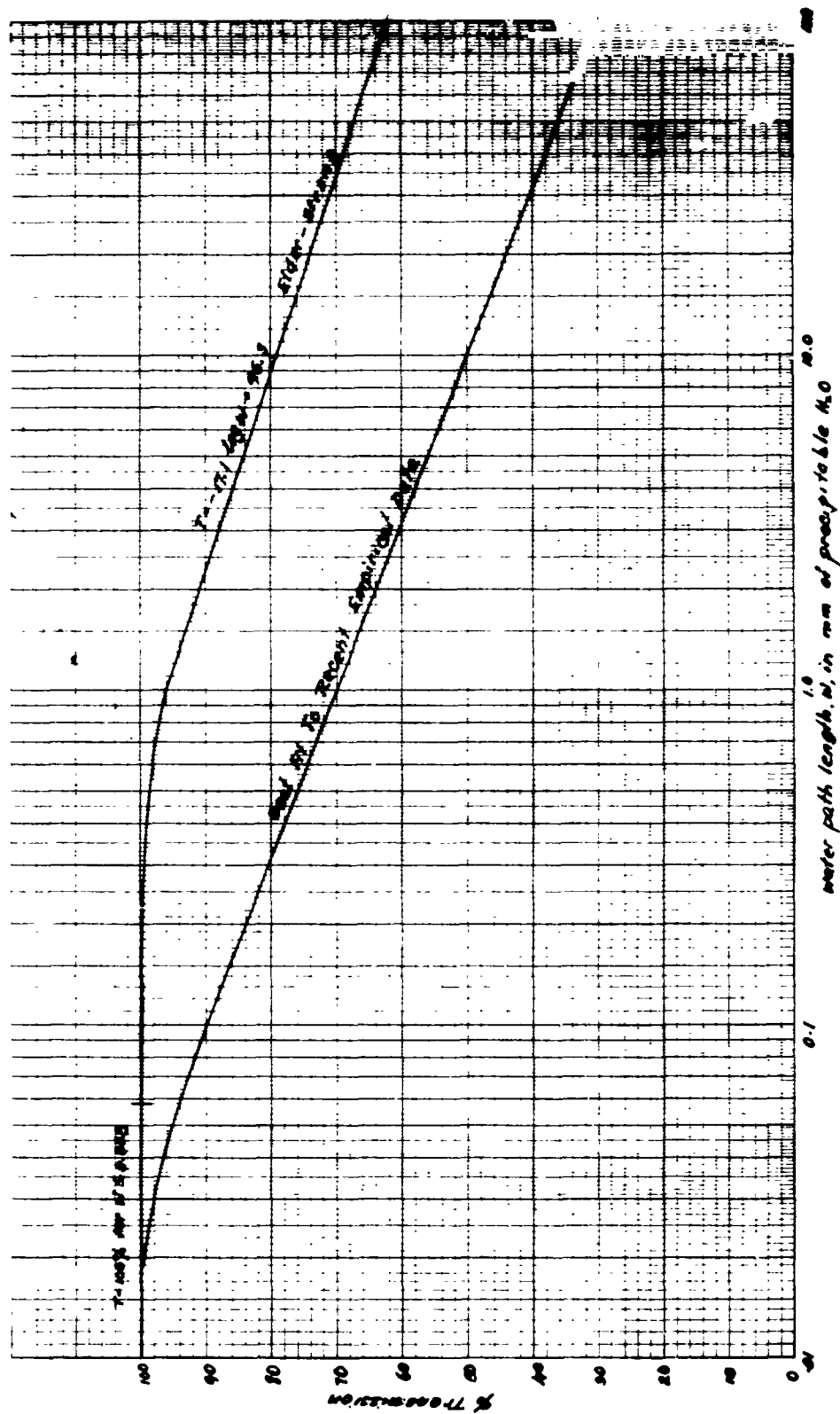
Figure 2-10. Transmission of Window III (1.13 to 1.38 Microns)

For a very small water path, resulting from the small partial pressure of water vapor, the dependence of transmission on total pressure can be approximated by:

$$T_1 = T_2 \left(\frac{P_2}{P_1} \right)^{1/8}$$

where T_2, the transmission at 760 mm Hg, is taken from the transmission curves appropriate for windows II to VII.

The integrated absorption for various CO_2 bands can be approximated by the following expressions:

$$\int A_\nu \, d\nu = C W^{1/2} (P + p)^k \tag{2-1}$$

$$\int A_\nu \, d\nu = C + D \log W + K \log (P + p) \tag{2-2}$$

where the total absorption is given in cm^{-1}; W, the CO_2 concentration in centimeter-atmospheres; p, the partial pressure of CO_2 in mm of Hg, and P, total pressure, in mm of Hg. The constants are given in Table 2-4.

Equation 2-1 is to be used below the limiting value of $\int A_\nu \, d\nu$ and Equation 2-2 above this value. The second equation is to be used for the 4.3μ band for all values.

The qualitative nature of low resolution absorption spectra of H_2O and CO_2 is shown in the inset of Figure 2-8.

2.2 SELECTION OF PROBABLE MATERIALS

The materials selected for study can be assumed, with varying degrees of confidence, to occur on the surface of Mars. The list is in no way comprehensive, and some of the items may prove to be absent. Knowledge of the composition and geological structure of Mars is extremely sketchy, but close-range surveys and actual sampling of the Moon has strengthened the credibility of the techniques employed in determining the geology of remote planets. Any group of reasonably common mineral materials spanning a large range of spectral reflectances would serve to demonstrate the image analysis technique presented here. The choice of materi.·· which may be present on Mars focuses this technique on early Mars lander programs.

Table 2-4. Atmospheric Constants

CO_2 Band	Band Limits	C	k	Limiting $\int A_\nu \, d\nu$
5.2	5.35 – 5.05	0.024	0.40	30
4.8	5.05 – 4.63	0.12	0.37	60
2.7	2.87 – 2.63	3.15	0.43	50
2.0	2.11 – 1.92	0.492	0.39	80
1.6	1.67 – 1.53	0.063	0.38	80
1.4	1.50 – 1.38	0.058	0.41	80
CO_2 Band	Band Limits	C	D	K
4.3	4.63 – 4.00	27.5	34	31.5
2.7		-137	77	68
2.0		-536	138	114

Currently accepted hypotheses for the origin of the solar system indicate that all of the terrestrial planets, and most of the planetary satellites, are principally silicates, with varying amounts of free metal. The alpha-scattering experiment on Surveyor V corroborated this belief with respect to the Moon by showing a chemical composition close to that of basalt. Since rocks of basaltic composition make up the oceanic crust of the Earth and may also underlie the continental crust, basalt seems to be primordial, and may be characteristic surface material on the other terrestrial planets. New basalt is continually brought to the crustal surface along the mid-oceanic ridges on Earth, but the mantle from which it seems to come is believed to differ somewhat in composition from basalt. There is evidence that some surface exposures of peridotite and dunite may represent hernial protrusions of mantle rock throughout the crust. One interpretation of the outflow of fresh rock along the mid-oceanic ridges implies a genetic relationship between this phenomenon and the very existence of major depressions in the crust, such as ocean basins.

The hard facts available for Mars are insufficient to permit formulation of any but the most generalized model of Mars. Different investigators, using the same information, have drawn opposite conclusions regarding the relative heights of the light and dark areas of Mars. The occurrence or nonoccurrence of marine sediments on Mars cannot be known until it is established whether there are, or have been, extensive structural depressions and sufficient free liquid water to permit a sedimentation process. Even the Mariner IV pictures do not reveal this kind of information (Reference 12). Therefore, it cannot yet be assumed that Mars has, in its geological history, experienced the kind of interaction between land and sea that seems to be genetically important to petrogenesis on Earth.

The granitic rocks, including their lava or near-surface equivalents such as rhyolite, may be present if Mars has had geosynclinal accumulations of sediment, with attendant crustal deformation and the invasion of overlying rocks by acidic magma (Reference 13). If the rate of erosion has been low, due to progressive loss or absorption of water, it might be expected that rocks of deep-seated origin, such as granite, have not been exposed at the surface. If this is true, rhyolitic rocks, if they were formed, would be more likely to be observed. Conversely, if erosion by any agency, especially that by windborne particles, has been prolonged and severe, it might be expected that the extrusive rocks such as

rhyolite, trachyte, or basalt would have been cut away, exposing large areas of deep-seated granite, gabbro, or peridotite.

The present evidence indicates that Mars has an extremely arid surface environment marked by high winds which occasionally can be seen to carry dust or sand (References 14 and 15). Such a condition will inevitably lead to typical eolian erosion of exposed rock surfaces and deposition of rock waste as thick accumulations in major depressions on prevailing-wind lee slopes, as transient sheets on other surfaces, and probably as extensive dune deserts such as those in the Sahara. The Mariner photographs do not show the Martian surface as a featureless waste of sand blanketing all rock, but rather as one with mountainous crater walls (Reference 12). We can expect to find accumulations of coarse rock waste as talus, mingled with windborne sand and silt.

Much of the eolian sand may have been converted to sandstone by cementation with iron oxide, gypsum, calcium carbonate, or other salts leached out of the rocks. This process presupposes sufficient water in the past or present to provide the necessary chemical mobility. Deposits of loess, composed of windborne silt grains, may occur in areas segregated from dunes of sand-sized particles. The mineralogy of these sands and silts should be similar to that of Earth's eolian sediments. In the absence of abundant free water, it is likely that the total content of feldspar will be greater, with a corresponding lower amount of clay minerals derived from chemical weathering of the feldspars. Free silica, as quartz or chalcedony, may well be the dominant mineral in the sand deposits, due to its chemical stability and resistance to abrasion. Sorting of minerals during transport by the wind will take place as a function of particle size, density, and shape (Reference 16). Concentrations of heavy minerals, such as magnetite, zircon, titanite, and the ferromagnesians, may well be found as pockets and streaks at the base of various sand beds.

The red coloration of Mars, in various hues as a function of time and space, has probably dominated efforts to interpret the geology of the planet. Several investigators, led by A.

Dollfus (Reference 7), have identified the mineral limonite, hydrated iron oxide, as the most probable source of this color. The arguments for this conclusion are reasonable and as a consequence the literature devotes considerable attention to the material. Limonite or the nonhydrated iron oxide, goethite, occur extensively on Earth, but usually in minute quantities. The mineral very often forms as a thin film on the surfaces of rocks or sand grains, entirely masking the characteristics of the mineral it coats. The deposition occurs as precipitation from ground water or surface water where evaporation of the water results in a locally saturated solution. A review of the Gemini and Apollo color photography of the Earth reveals that only the oceans make this the "Blue Planet", for the land surfaces are predominantly reddish. Very few soils are blue or green; most of them are shades of red, yellow, or brown. The presence of minor amounts of iron oxide accounts for most of this coloration. We should not expect to find on Mars any extensive deposits of loose limonite, although it is possible that layers of hardpan, soil, and gravel cemented into a solid rock by limonite, may be found below the surface.

The presence or absence of life forms on Mars consitutes the heart of Man's interest in the planet. This report is not the place to argue the point, but it should be noted that the presence of some form of vegetation would have profound implication for the surface , characteristics of the planet. Presumably, plants using photosynthesis there would need osmotic devices, such as roots, to penetrate the substrate to gain access to ground water and dissolved minerals (nutrients). Such devices would contribute to decomposing and disintegrating rocks and soils. Also, the very essence of life, as Man knows it, is that the individual must eventually die in order to assure survival of the species. The implication of this is that the cellular material composing the body of the plant is ultimately returned to the soil to contribute to the slow accumulation of decaying organic matter which can serve as nutrient for other plants. Many investigators have proposed that the symbiotic organism of fungus and algae, known as lichen, which survives even the severest conditions of cold and aridity on Earth, may qualify as a Martian plant.

In order to provide experimental materials which would simulate some of the assumed Martian conditions discussed here, and for which spectral reflectance data have been published, the list in Table 2-5 was prepared. The criteria for selection of these materials were commercial availability and their probability of occurrence on Mars.

Table 2-5. List of Selected Materials

	Rock	Mineral	Sediment	Life Form
Rhyolite*	X			
Granite*	X			
Basalt*	X			
Dunite*	X			
Olivine		X		
Serpentine	X	X		
Goethite		X		
Limonite*		X		
Silica Sand*			X	
Gypsum Sand			X	
Calcium Carbonate		X		
Lichen*				X

* Materials actually used in photo experiments

2.3 REFLECTION SPECTRA OF PROBABLE MATERIALS

Spectral reflectance signatures used in the analytical part of the study are shown in Figures 2-11 to 2-23. These spectra were obtained from the literature, mainly from References 17 and 18.

All thirteen spectra are given in terms of the total hemispherical reflectance. Measurements of directional reflectances were not used in this work. Spectra of Reference 17 were obtained with a modified Beckman DK-2 ratio-recording spectrophotometer and an integrating sphere attachment. A similar instrument, Beckman DK-2A with a total reflectance attachment, was used to obtain the reflectance spectra in the wavelength range from 0.5 to 2.5 microns given in Reference 18. Beyond 2.5 microns a Cary Model 90 double-beam spectrophotometer with an infrared total reflectance attachment was used.

The references indicated for the figures give geographical locations from which samples of the measured materials were obtained.
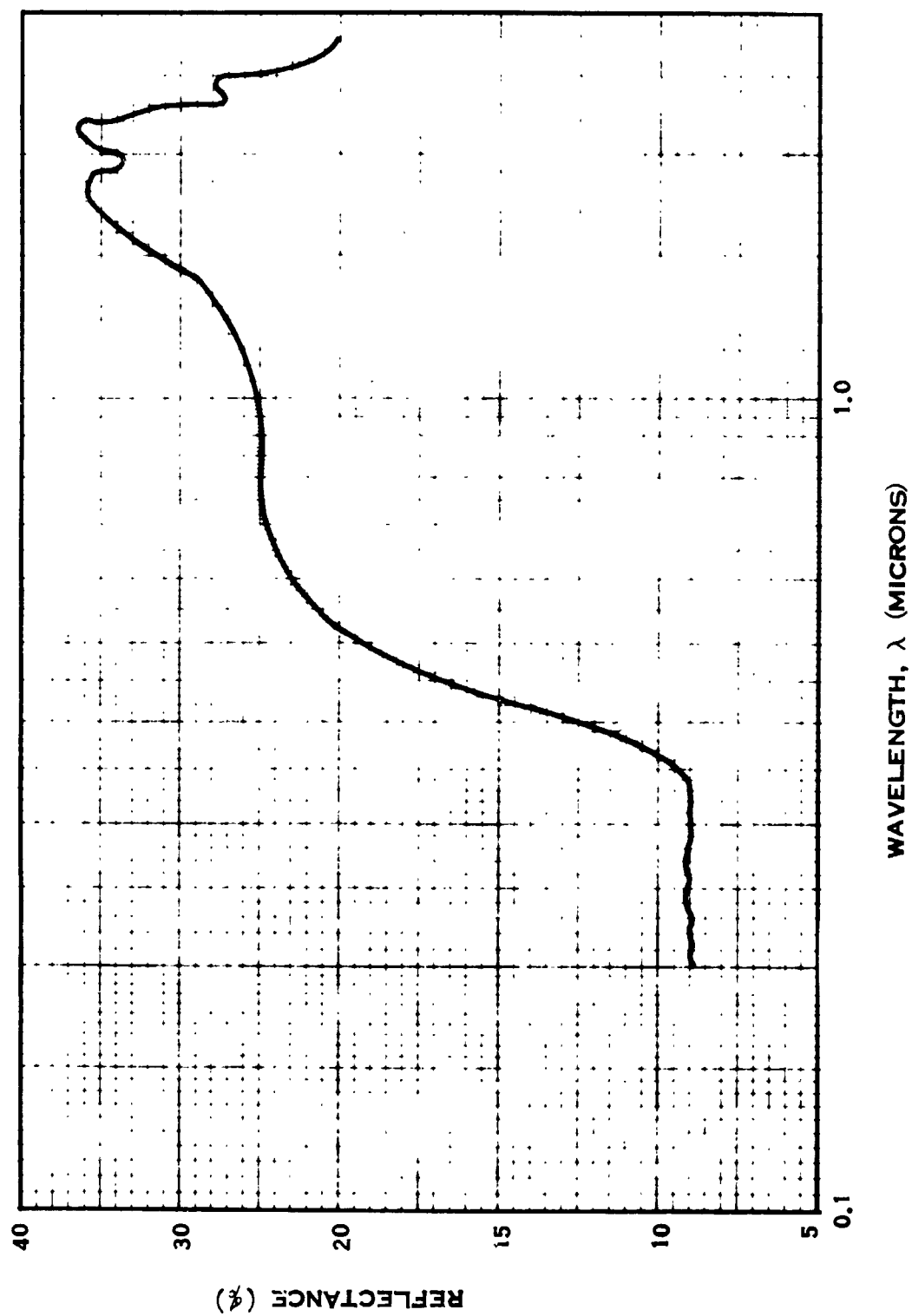
Figure 2-11. Spectral Reflectance of Felsitic Rhyolite (Ferric Oxide Impurities) [Reference 17]
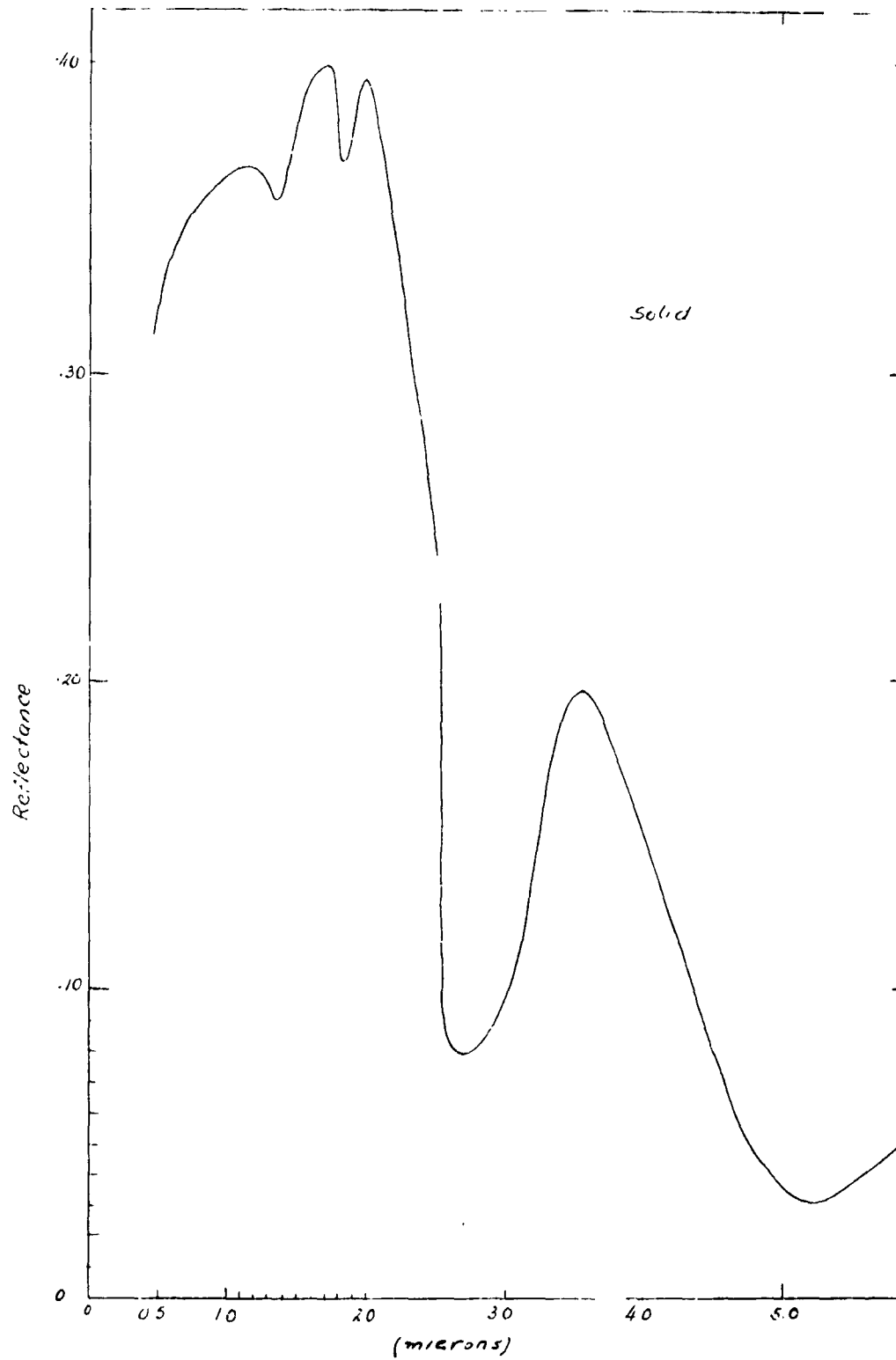
Figure 2-12. Spectral Reflectance of NAA Standard Granite [Reference 18]
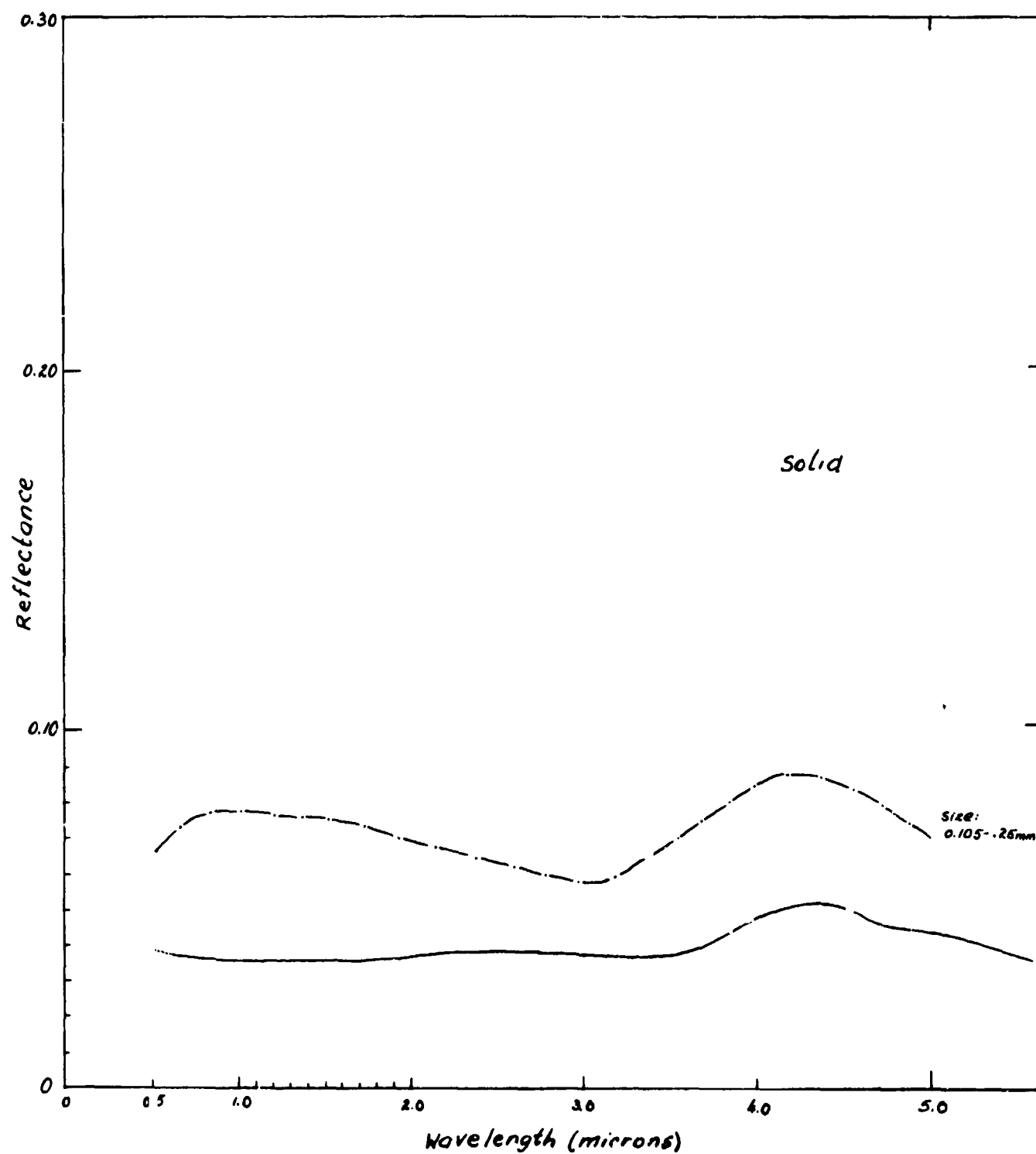
Figure 2-13. Spectral Reflectance of NAA Standard Oregon Basalt [Reference 18]
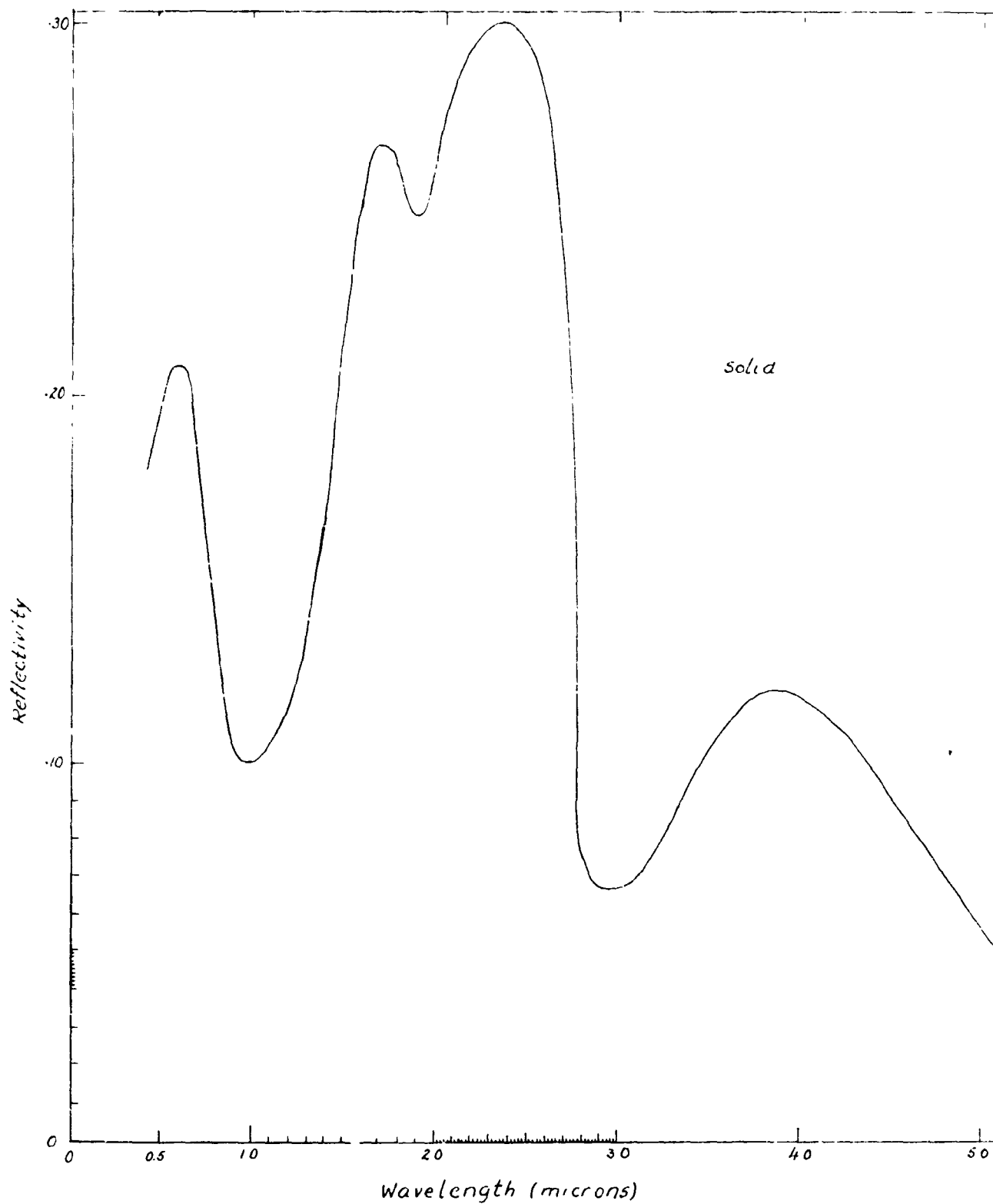
Figure 2-14. Spectral Reflectance of Dunite - Marenfelder Moar (Germany) Reference 18]
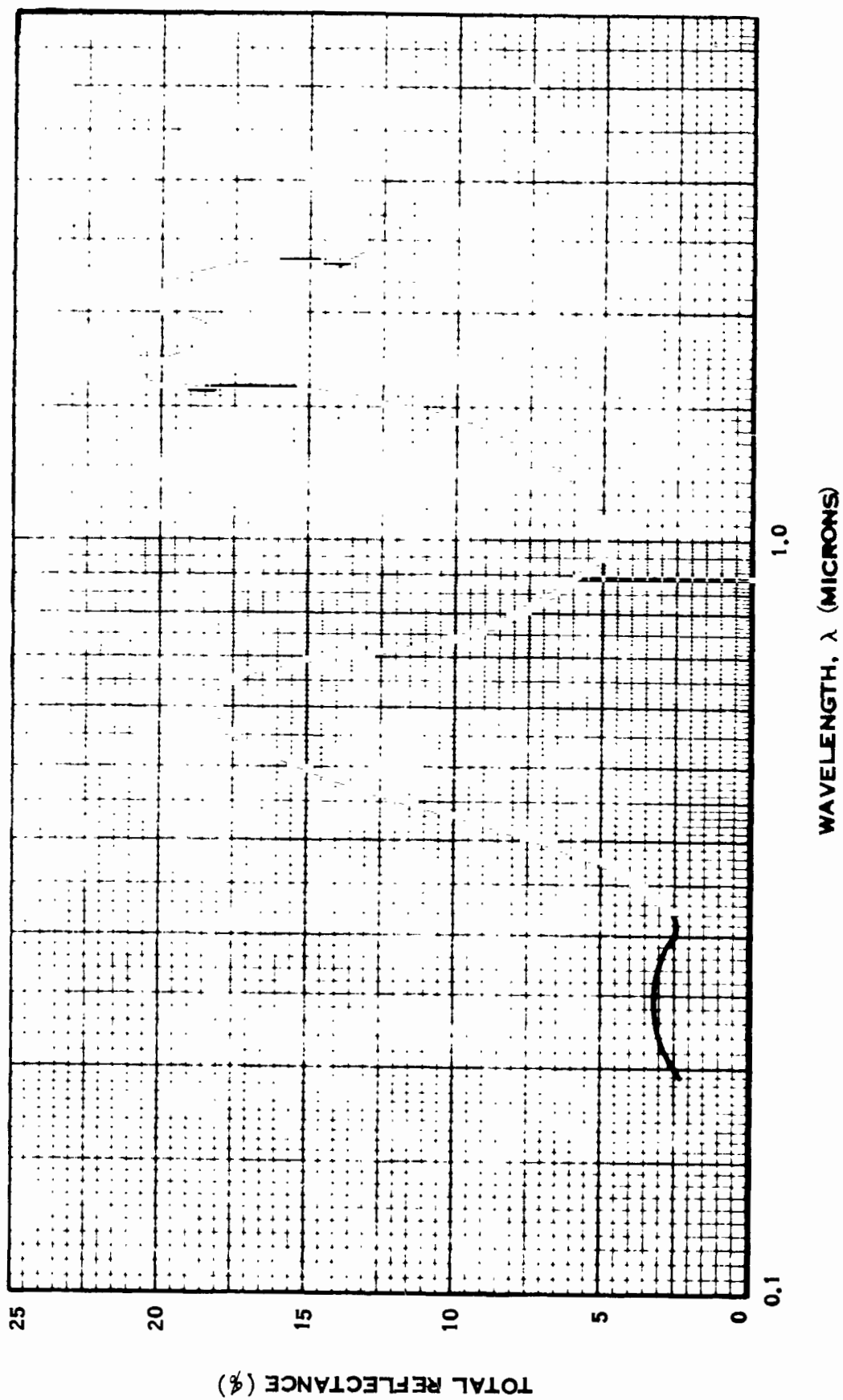
Figure 2-15. Spectral Reflectance of Olivine [Reference 17]

WAVELENGTH, λ (MICRONS)
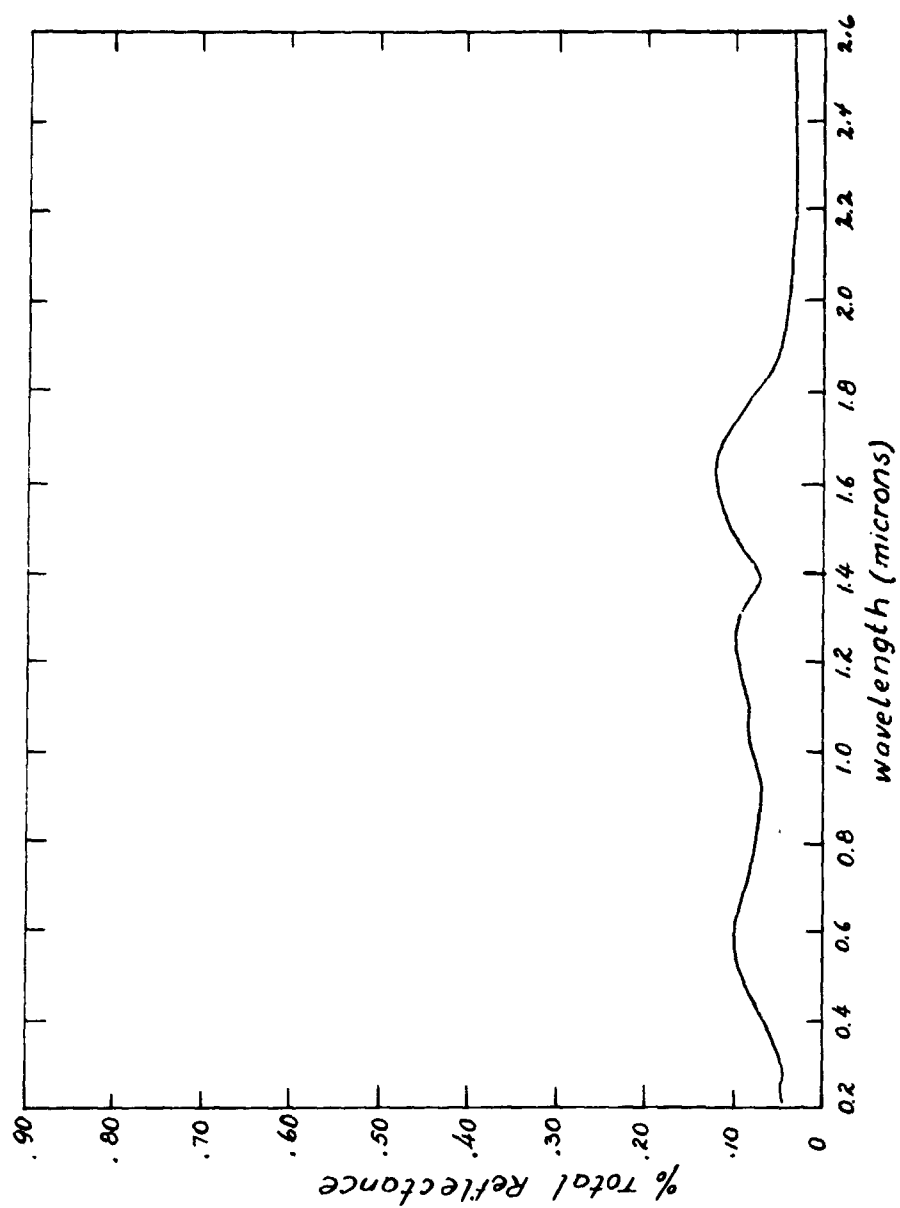
TOTAL REFLECTANCE (%)

Figure 2-16. Spectral Reflectance of Serpentine [Reference 17]

WAVELENGTHS, λ (MICRONS)
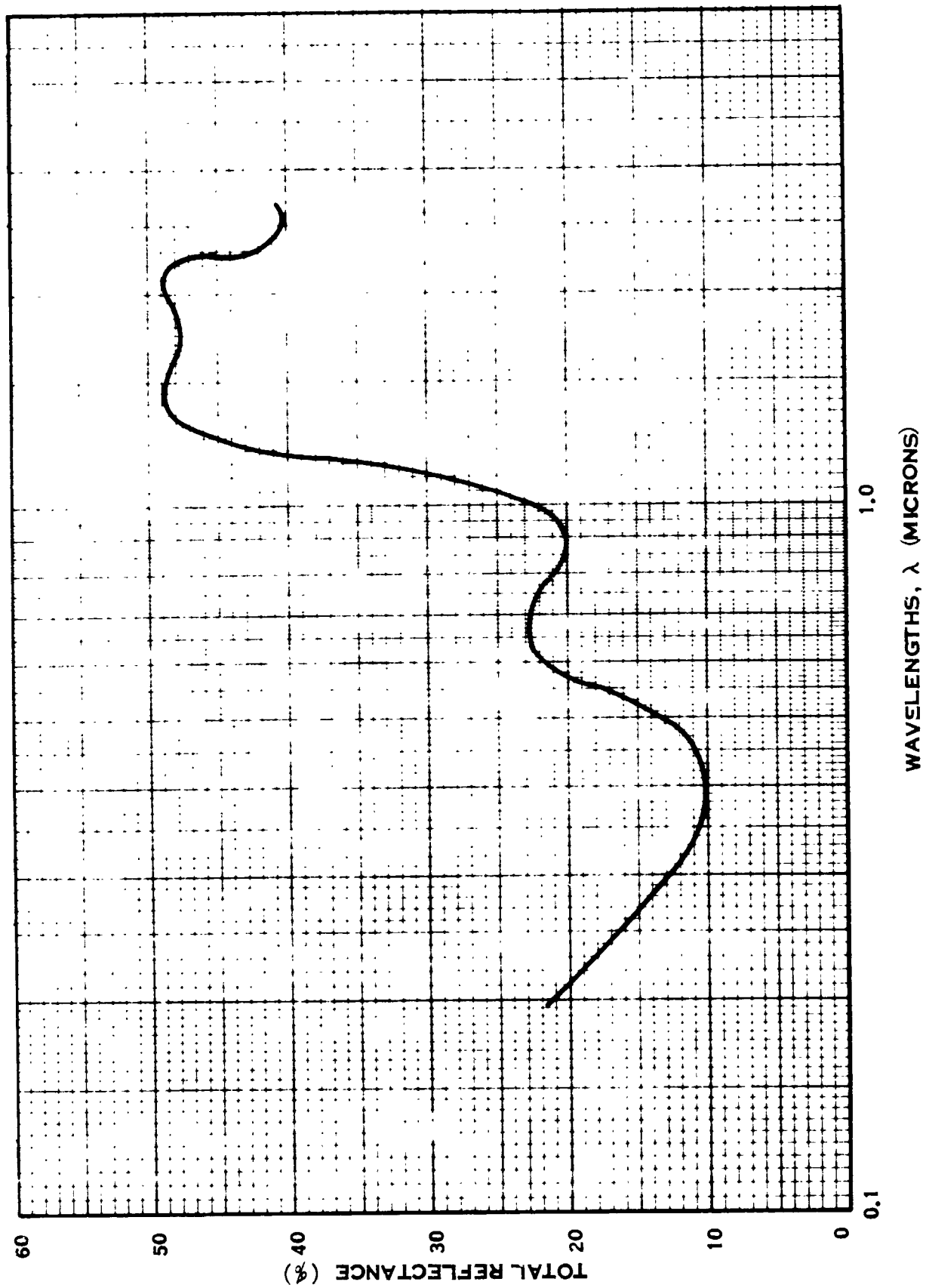
Figure 2-17. Spectral Reflectance of Goethite (Powdered) [Reference 17]

2-31
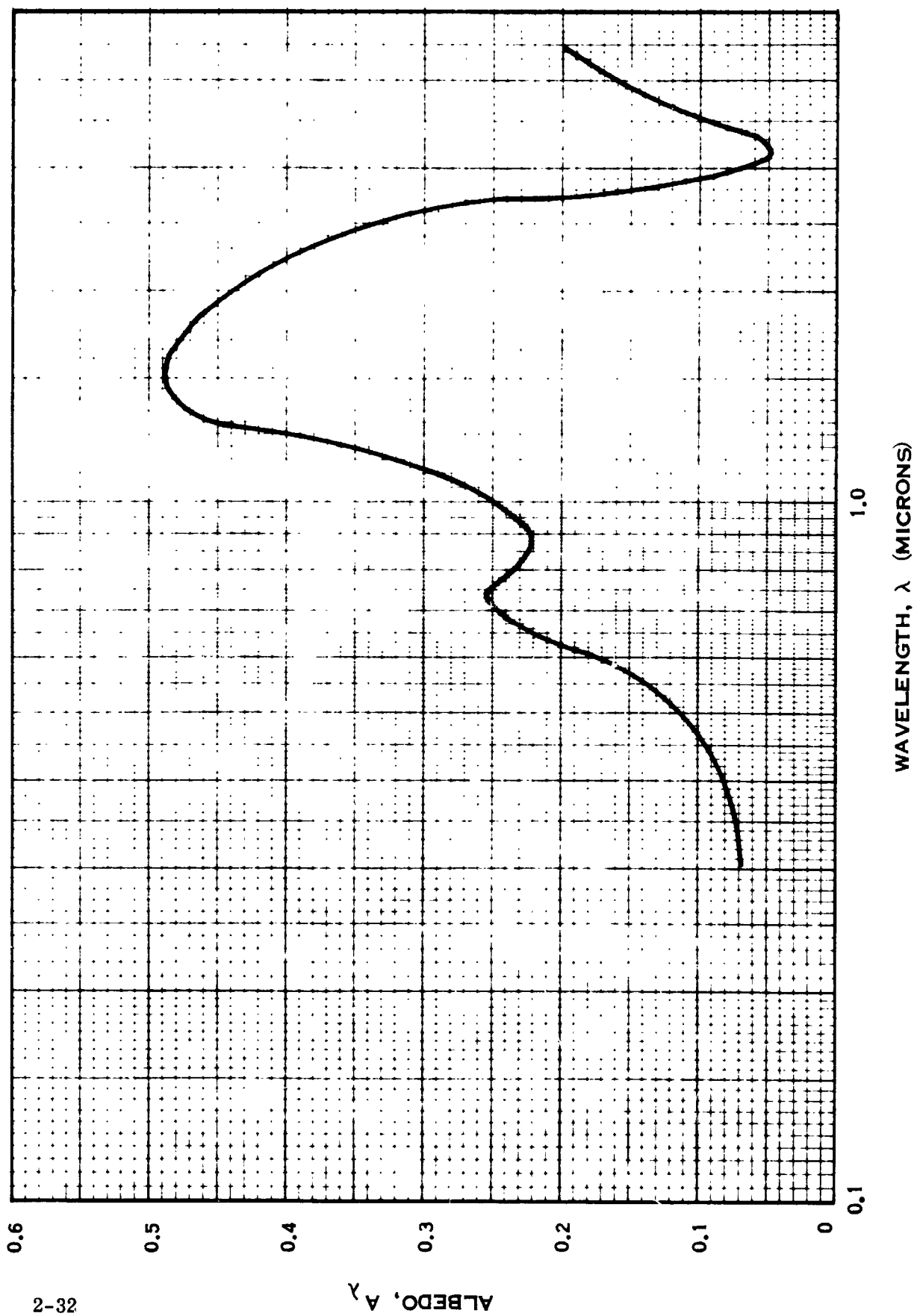
Figure 2-18. Spectral Reflectance of Powdered Limonite (One Form) [Reference 17]

WAVELENGTH, λ (MICRONS)

ALBEDO, A$_\lambda$

2-32
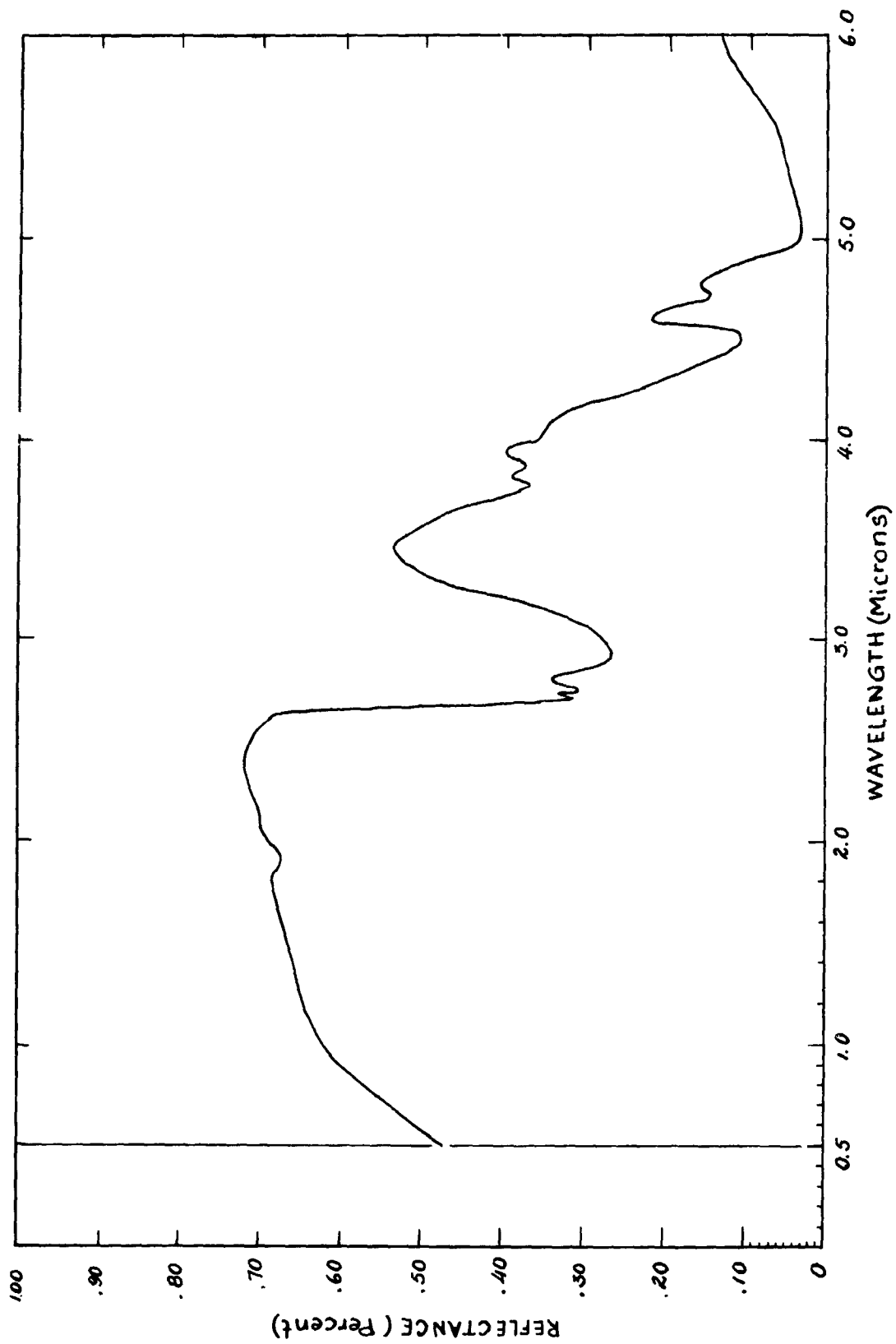
Figure 2-19. Spectral Reflectance of Silica Sand (Sized and Washed) [Reference 17]

2-33
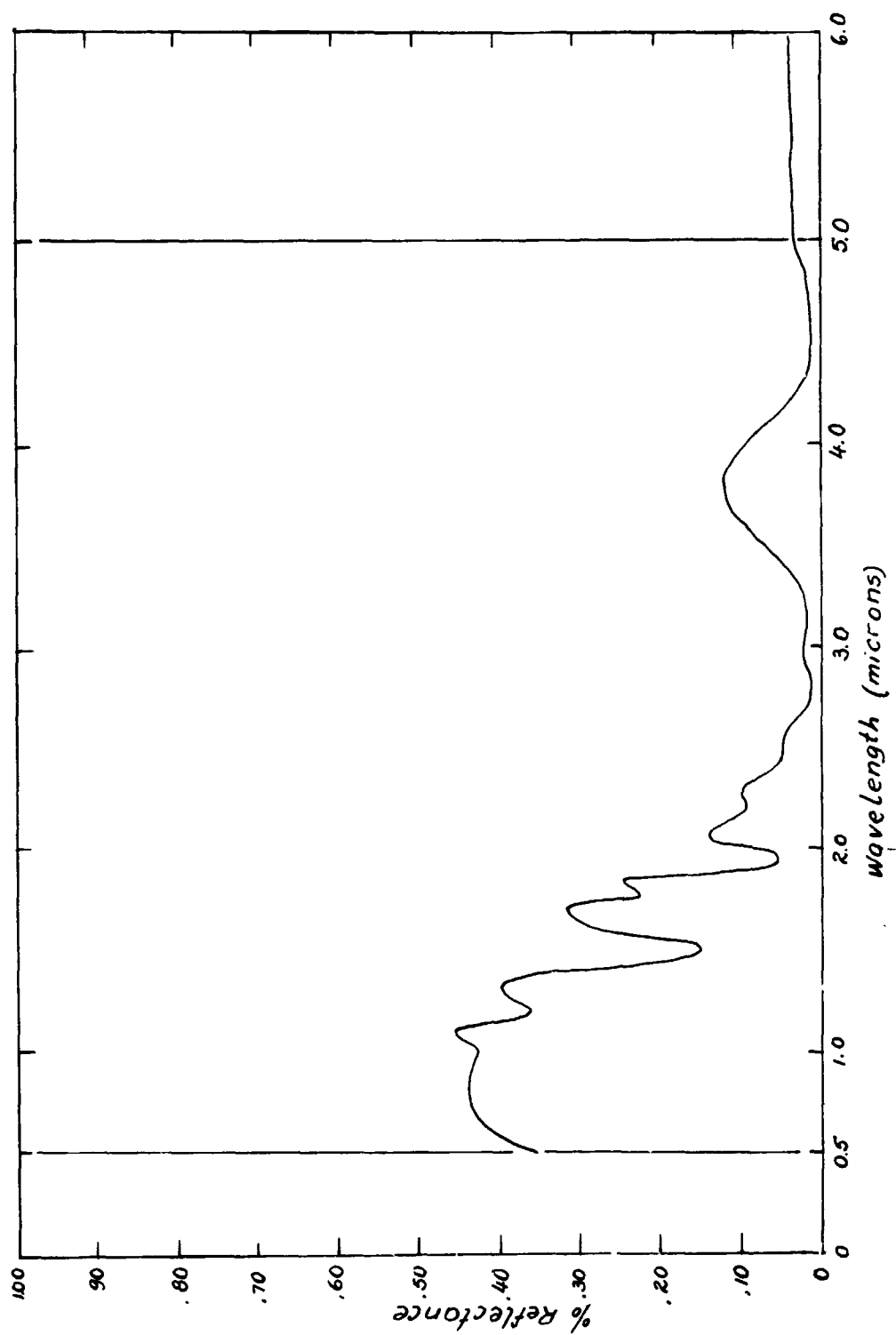
Figure 2-20. Spectral Reflectance of Natural Gypsum Sand [Reference 17]
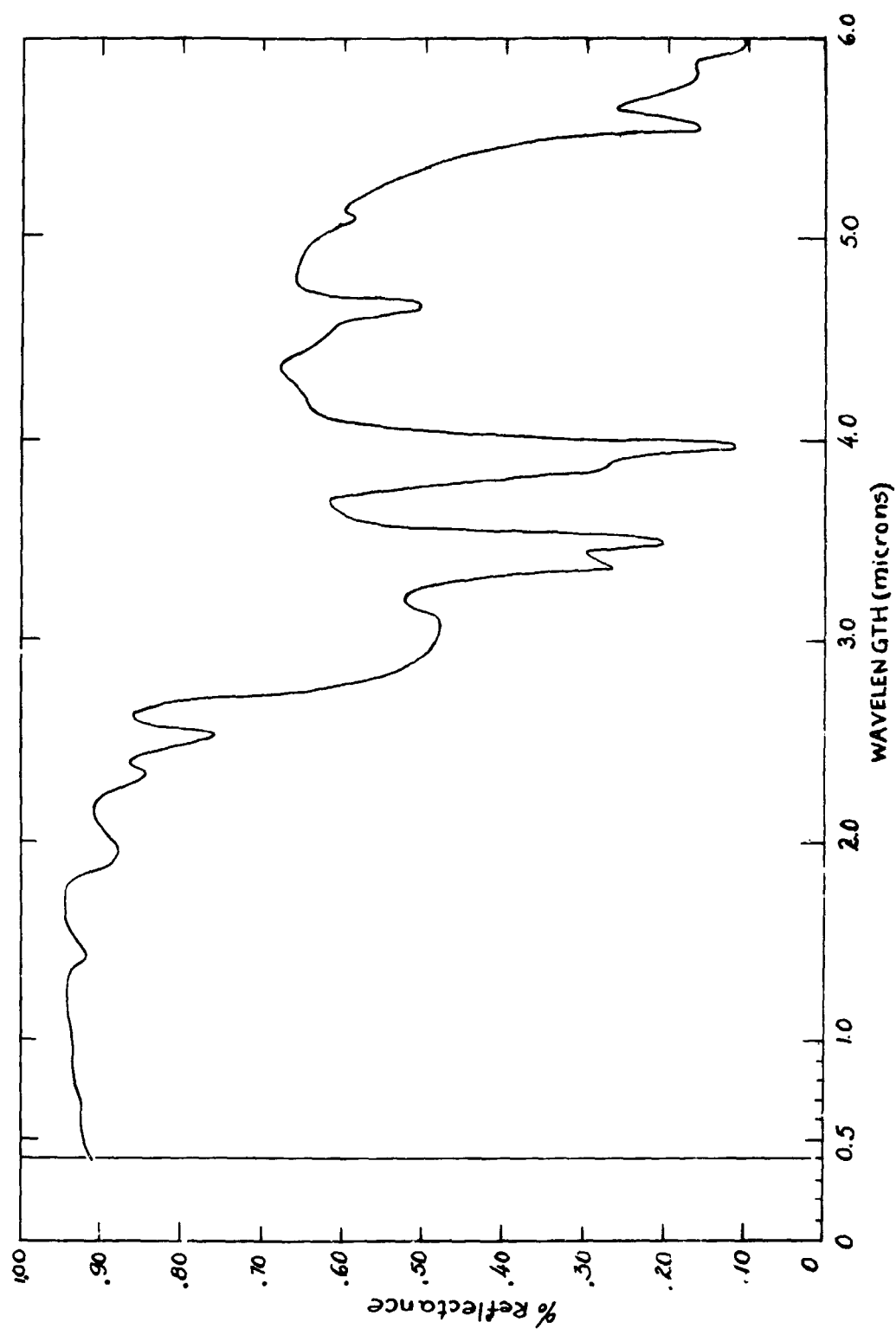
Figure 2-21. Spectral Reflectance of Granular Calcium Carbonate [Reference 17]

2-35
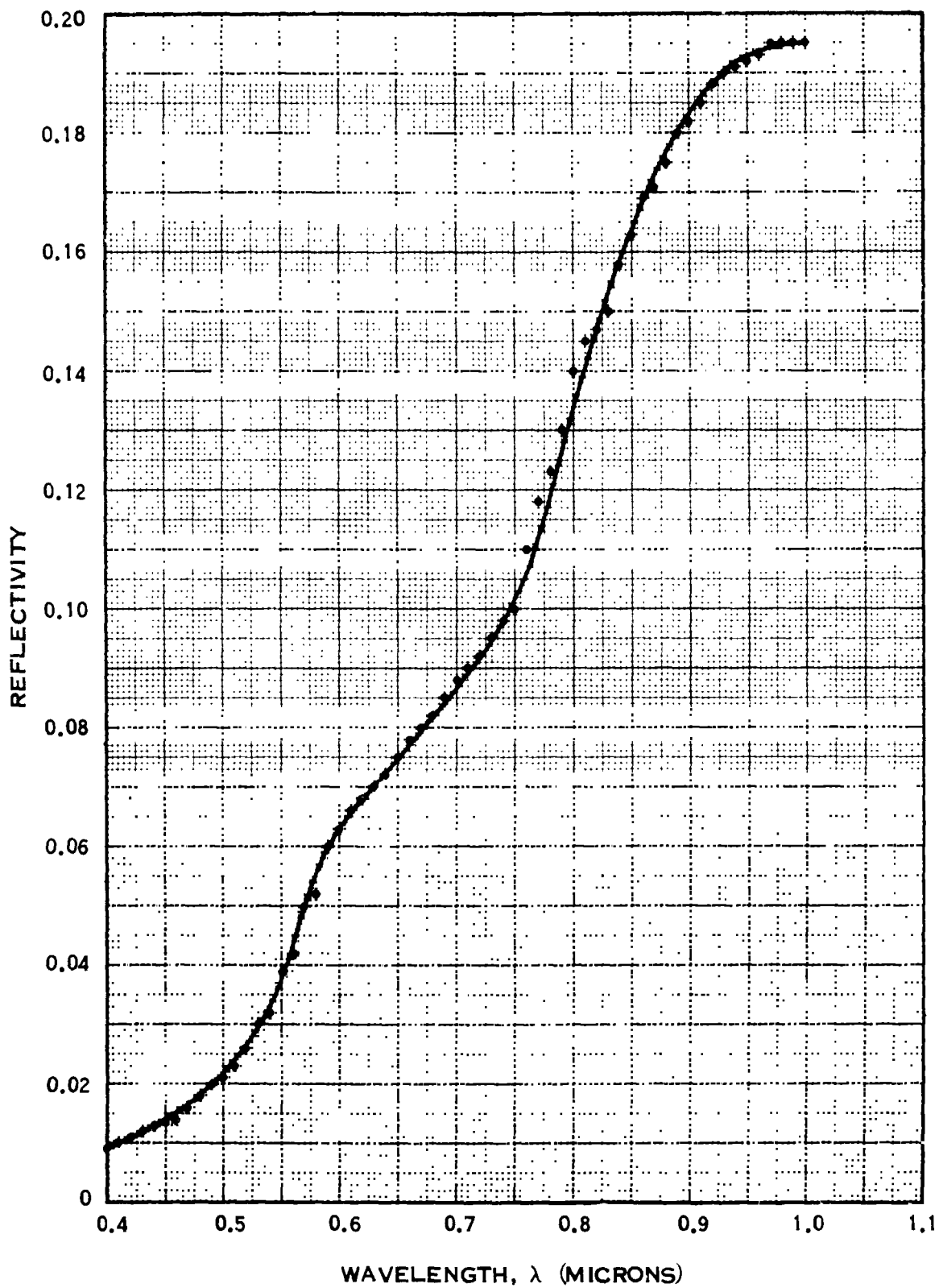
Figure 2-22. Spectral Reflectance of Lichen [After Levitin Reference 32]
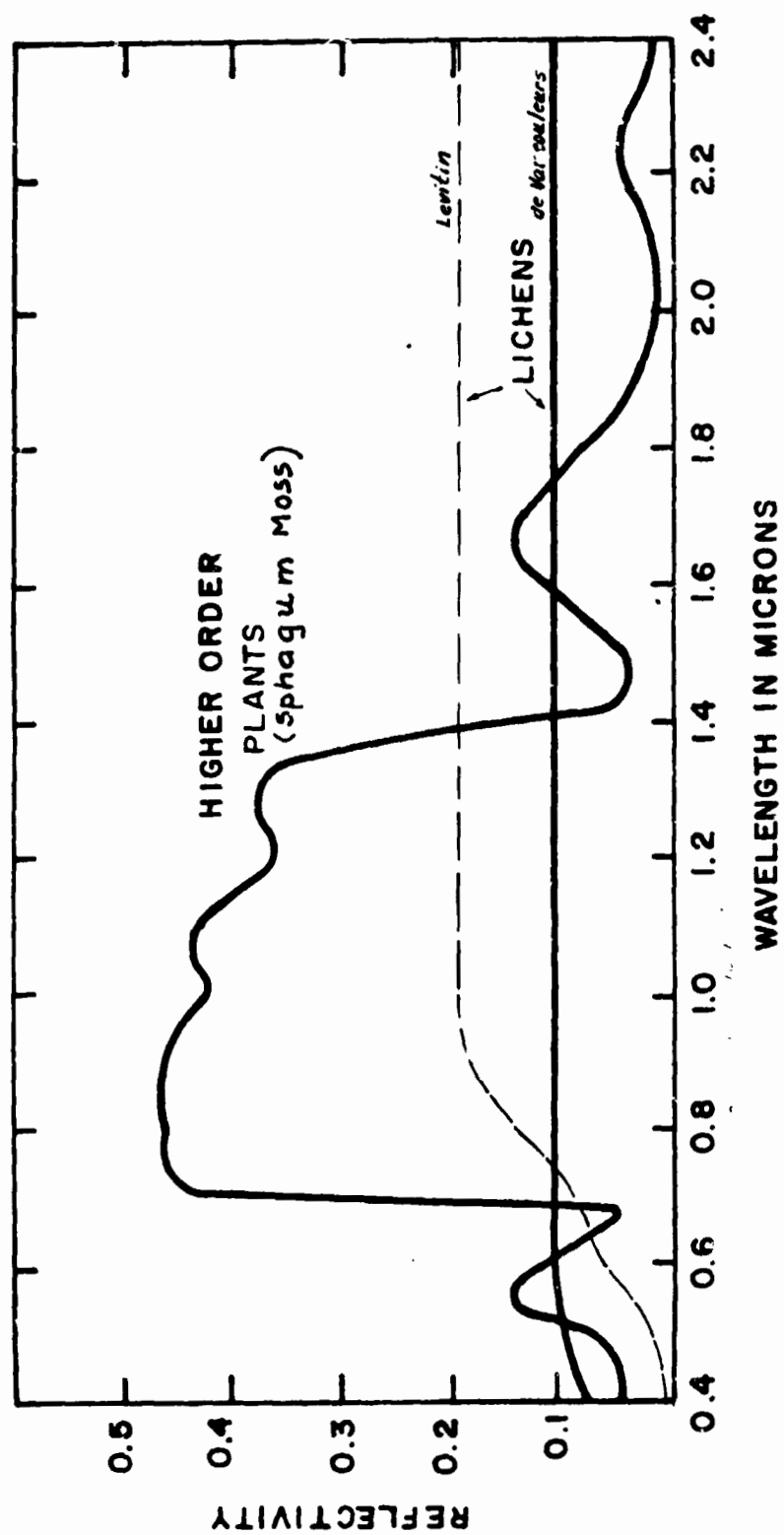
Figure 23. Typical Reflectivity of Plants [References 8 and 32]

SECTION 3

SELECTION OF DETECTORS AND SPECTRAL BANDS

3.1 <u>INTRODUCTION</u>

Before discussing in detail the logic used in selecting the optimum detectors and associated spectral bands, it is pertinent to briefly review the prime objective of this part of the study. It is to select the best combination of detector and filter bands for optimum contrast on a scanning type of imaging system. The scanning system is assumed to be capable of accepting any solid state detectors within the spectral band 0.3 to 5.0 microns. The description of the detector, as given, is meant to include photo-emissive, photo-conductive, photo-voltaic and bolometric transducers. A considerable amount of study and experimentation has been applied to attaining maximum scene contrast on film or plates; this study in no way attempts to repeat this work and for this reason the film medium has been excluded from the study. Accordingly the emphasis of the study is an effective means of comparing the performances of different detector and filter combinations. The number of detectors chosen and the technique that was developed to choose appropriate filter-detector combinations will be discussed below.

At this point it is also pertinent to mention some of the limitations of the study. Owing to its restricted scope it has not been possible at this stage to discuss the affect of these important parameters on band and detector selection.

1. Signal to noise ratio

2. Detector frequency response

3. Spatial resolution of the sensor

4. Varying sun angles

5. Varying constituent reflectivities

During the discussion of the results and occasionally elsewhere, the possible affects of these factors will be briefly mentioned.

Because of the above limitations for this particular study we have assumed:

1. Constituent reflectivities are invariant

2. The sensor output is noiseless

3. The detector response time does not affect the sensor output

3.1.1 OUTLINE OF THE APPROACH

The basic concept utilized has been that of a computer simulation of the imaging process. The flow of monochromatic radiant power from the solar source is followed through the Martian atmosphere, onto the surface constituent, through the atmosphere again, through the sensor optics and finally onto the detector element. A final integration is performed on the wavelength limits of the detector or filter and the output of the program, assuming a linear electronic amplifier, is proportional to the sensor output. This flow is shown below together with the appropriate symbols that will be used throughout this chapter.

TABLE 3-1. RADIANT FLUX FLOW DIAGRAM

Parameter	Symbol
Solar Irradiance	H_λ
X	
Martian Atmospheric Transmission	$(T_A)_\lambda$
↓	
Martian Irradiance	$(H_m)_\lambda$
X	
Constituent Reflecting Power	R_λ
↓	
Constituent Radiance	
X	
Surface Atmospheric Transmission	$(T_A)_\lambda^1$
X	

TABLE 3-1. RADIANT FLUX FLOW DIAGRAM (Cont)

Parameter	Symbol
Optical Relative Transmission	$\overline{(T_o)}_\lambda$
X	
Detector Relative Response	$\overline{(S_\lambda)}$
↓	
Sensor Monochromatic Output	$[S.O.]_\lambda$

Using the above parameters, the sensor output [SO] is obtained from the simple expression:

$$\left[SO\right]^{\lambda_2}_{\lambda_1} = \int^{\lambda_2}_{\lambda_1} H_\lambda \cdot (T_A)_\lambda \cdot R_\lambda \cdot (T_A)^1_\lambda \cdot \overline{(T_o)}_\lambda \cdot \overline{(S_\lambda)} \, d\lambda \qquad 3\text{-}1$$

or if, as is likely on Mars, the surface transmission $(T_A)^1_\lambda = 1$, and also if surface radiance data is used the alternate expression is:

$$\left[SO\right]^{\lambda_2}_{\lambda_1} = \int^{\lambda_2}_{\lambda_1} (H_m)_\lambda \cdot R_\lambda \cdot \overline{(T_o)}_\lambda \cdot \overline{(S_\lambda)} \cdot d\lambda \qquad 3\text{-}2$$

The inclusion of a constant of proportionality will convert $[SO]^{\lambda_2}_{\lambda_1}$ to the correct sensor output units. This basic calculation is repeated for each type of detector and each waveband selected. In order to compare the detector performance; however, a different criterion is required and will be discussed in the appropriate section.

In addition to the theoretical analysis, some experimental work has been performed in an attempt to verify the validity of the theoretical approach (Sections 4.0 and 6.0). Although these experiments could not cover the full spectral range of the investigation, verification of the technique in a restricted spectral range serves to demonstrate the feasibility of the method.

3.2 BASIC DATA

In order to carry out the study, certain data was required and used throughout. These will be discussed in the next few sections.

3.2.1 THE SELECTION OF THE CANDIDATE DETECTORS

In order to acquire a wide cross-section of the detectors currently available, all detector manufacturers listed in the Optical Manufacturers Directory were solicited for details of their products. A return of about 50% was obtained. Not all replies were pertinent to the original request for data. The final selection consisted of 15 suitable detectors. The range of wavelengths over which they were responsive varied from detector to detector, but it was possible to group them into four distinct bands. The spectral range of these bands and the detectors within each band are enumerated below:

TABLE 3-2. DETECTOR BANDS

Band I

$(0.3\,\mu - 0.8\,\mu)$

S11

S20

Type 2 – Cadmium Sulphide

Type 5 – Cadmium Sulphide

Type 5H – Cadmium Sulphide –

Band II

$(0.3\,\mu - 1.1\,\mu)$

S1

Silicon

CdSe (4) – Cadmium Selenide

CdSe (3) – Cadmium Selenide

CdS (7) – Cadmium Sulphide

3-4

Band III

(0.6 μ - 2.0 μ)

Silicon PIN Type 654

Germanium Type 653

Germanium PIN Type 655

Band IV

(1.0 μ - 5.0 μ)

Indium Arsenide

Lead Sulphide

Lead Selenide

Thermistor Flake

The normalized relative responses of these sensors plotted against wavelength are shown in Figures 3-1 to 3-4.

Added to these were the responses of the sensitive materials used for the two supporting experiments. These were Plus X, I-Z Infrared, and the S10 photocathode. The responses of these are displayed in a similar manner to those above in Figure 3-5 to 3-6.

3.2.2   THE MARTIAN IRRADIANCE

The Martian Irradiance was obtained in two parts, that covering the 0.3-0.8 microns (Figure 3-7A) and that from 1 -5 microns. The long wavelength region was modified for the CO_2 and H_2O absorption and the composite curve obtained as shown in Figure 3-7B.

3.2.3 OPTICAL TRANSMISSION

The transmitting (and reflecting) components of the imaging system can be taken into consideration in the programs. However in most cases they do no have spectral variations of transmission or reflectivity; this situation applies to the visible and the infrared. Therefore throughout the study it has been assumed that these are equal to one. When filter bands are used they are considered as separate transmitting media to that of the optics.

3.2.4 THE CONSTITUENT REFLECTIVITIES

The list of available reflectivities were shown in Section two. Early runs indicated a less confusing situation would exist if fewer than the twelve available constituents were used in the analysis. Accordingly a representative sample of six were chosen on the criteria that they would be a fair cross section of the various forms given in table 2.5 and also that they would be well represented in the film and discrimination experiments. The six chosen wer : Rhyolite, Basalt, Dunite (Rocks), Limonite (Mineral), Silica Sand (Sediment), and Lichen (Life form.)

3.3 BROADBAND OUTPUTS

3.3.1 THE DERIVATION OF THE BROAD BAND OUTPUTS

"Broadband" used here refers to the full spectral range of the detector under examination. This in some cases e.g. CdSe can be of the order of only 0.1 micron at the half-peak response levels, but more generally is of the order 0.2 microns and greater.

As a result of the statement made in Section 3.2.3 with respect to the optical transmission, the revised form of Equation 3-2 becomes

$$[S.O.]_{\lambda_1}^{\lambda_2} = \int_{\lambda_1}^{\lambda_2} (H_m)_\lambda \cdot R_\lambda \cdot (\overline{S}_\lambda) \cdot d\lambda \qquad 3\text{-}3$$

The computer program written for this part of the study (MULTSPEC) evaluates this integral, and as is seen from the simplified flow diagram, (Appendix 11-1) the omitted transmission factors exist as options in the program. Common to all wavebands is the "scene", the selection of which is described in Section 2.2. The reflectivities of the constituents were divided into the four bands corresponding to those in which the detectors were grouped. The Martian irradiance was treated in a similar manner. The appropriate sensor response was normalized to the value of its peak response, which became 1 in all cases. The constituent reflectivities and the Martian irradiance remained unnormalized. The digital outputs of the computer program are presented as histograms of the outputs for the various constituents versus detector material.

3-6

3.3.2 DISCUSSION OF THE BROAD BAND RESULTS

Broadband results obtained for the four wavelength bands are shown in Figures 3-8, 3-9, 3-10 and 3-11.

The results that will be described in this section refer specifically to the scene consisting of Rhyolite, Limonite, Dunite, Basalt, Silica Sand and Lichen. Different conclusions as to the merit of using a detector or combination of detectors will in mose cases apply when the scene constituents are changed. A few examples demonstrating this point have been included. The reason for including the broad band findings in this study are twofold; firstly they are required for a later task, that of comparing intensity resolution to spectral resolution; secondly, it is of interest to know which of the selected detectors has the best overall capability without the aid of spectral filters.

The visible and near infrared bands have constituent outputs that are very similar in terms of order of magnitude. This is not too surprising in view of the data shown in Figure 3-12 which is a plot of the reflectivities of the constituents as a function of wavelength.

The irradiance in this part of the spectrum is a relatively smooth function, and consequently the sensor output in general follows the magnitude of the reflectivities when the detector spectral range is relatively narrow. For detectors like Si and SI where the spectral reflectivity contributes to the signal over a wide spectral band, the relative detector outputs are not easily predicted.

It is not suprising therefore that the relative order of output throughout the 0.4 - 0.8 micron band and 0.4 - 1.1 micron band is very similar (see Figures 3-8 and 3-9). However closer inspection of the two figures reveal that there are significant differences in the outputs that can result in greater or lesser contrast. For example, the S11 detector output for Rhyolite and Limonite differs by nearly a factor of two whereas the same materials for CdSe3 and CdSe4 differ by less than one percent.

3-7

Owing to the rise in reflectivity of Limonite in the 1-2.5 micron region the relative outputs follow a slightly different regime in the 0.6-2.0 micron band. The high spectral selectivity of the three detectors in this band also affect the integrated detector output significantly. The overall effect can be seen in Figure 3-10. The final band extending from 1 micron to 5 microns contains four detectors, three of which are spectrally selective with the fourth having an essentially flat response throughout the whole of the band. Surprisingly the outputs of the Lead Sulphide, Lead Sulphide and the Thermistor flake are essentially similar. However owing to the very low irradiance from about 3 microns together with the fairly broad CO_2 absorption band at 3.5 microns, the contribution outputs of wavelengths greater that 3 microns is relatively insignificant, and may account for the similar spectrally selective and thermistor flake results. This part of the study although incidental to the main problem has shown the value of considering in detail the performance of intermediate band and broad band detectors as components of an imaging sensor.

A greater selectivity can be obtained by using narrow bands of the order 100-300 $\overset{o}{A}$ together with the appropriate detector; the results obtained by using this combination is discussed in the next section.

3.4   NARROW BAND OUTPUTS

3.4.1   DERIVATION OF THE NARROW BAND OUTPUTS
The narrow band has typically a half peak transmission width of about 100 $\overset{o}{A}$, although the analysis technique capable of handling infinitely small bandwidths, practical considerations indicate that signal-to-noise considerations preclude the use of very narrow bands. It is important to choose the correct narrow bands and also their spectral location, for they may have a total width of as little as 2% of the spectral band of the detector. If a practical limitation of say 5 or 6 filters is imposed, this implies that the sensor system may only be using as little as 10% to 15% of the total band available. The correct positioning of these filters is therefore imperative. A simple calculation shows that the possible combinations of constit-

tuent, detectors and filters in the narrow band case can soon become astronomically large, and is a situation ideally suited to a solution employing reiterative computer techniques.

The computer technique chosen was based on the principles used in MULTSPEC. In the new program, called FILTSPEC, the parameters $(Hm)_\lambda \cdot R_\lambda \cdot \bar{S}_\lambda$ are again multiplied together as before. In this program, however, the wavelength increment as is a function of the width of the narrow band filter which is an additional multiplying term. This filter has the characteristic shape of a manufactured interference filter; the filter transmission is normalized to the peak transmission which as before is made equal to 1. The filter is adjusted to a position at the cut-in wavelength of the detector and the first integral under the filter band is performed viz:

$$\left[S.O\right]_\lambda^{\lambda Fo} = \int_{\lambda_1}^{\lambda Fo} (H_m)_\lambda \cdot R_\lambda \cdot (\bar{T_F})_\lambda \cdot (\bar{S})_\lambda \cdot d\lambda \qquad 3\text{-}4$$

where $\lambda F_o = \lambda_1 +$ the width of the narrow band filter at the 1% Peak Transmission width. (Approximately 2X half-peak transmission width.)

Let $\lambda F_o - \lambda_1 = \Delta\lambda$, then 3.4 becomes:

$$\left[S.O\right]_{\lambda_1}^{\lambda_1+\Delta\lambda} = \int_{\lambda_1}^{\lambda_1+\Delta\lambda} (H_m)_\lambda \cdot R_\lambda \cdot (\bar{T_F})_\lambda \cdot (\bar{S}_\lambda) \cdot d\lambda \qquad 3\text{-}5$$

The value of the integral is stored and is subsequently plotted against the wavelength of the peak transmission of the filter i.e. λ (peak) $= \lambda_1 + \Delta\frac{\lambda}{2}$. The filter is then moved along the wavelength scale to a position where its peak transmission is at $\lambda_1 + \Delta\lambda$ and the integral performed again. This process is repeated along the full spectral range of the detector and may involve from 30 to 80 steps for one constituent and one sensor combination. This "sliding filter" technique is shown diagrammetrically in Figure 3-13.

3.4.2 DISCUSSION OF NARROW BAND RESULTS

The results are given in Figures 3-14 to 3-30 in the form of plots of sensor output vs. wavelength (microns) for each constituent and each of the four wavelength bands. For each detector there are plots of a family of six curves, each curve representing the output of the

detector for that constituent. The method of identifying each constituent is accomplished by using numbers from 1 to 6 according to the following code:

1	Rhyolite	(abbreviation RHY)
2	Limonite	(abbreviation LIM)
3	Dunite	(abbreviation DUN)
4	Basalt	(abbreviation BAS)
5	Silica	(abbreviation SIL)
6	Lichen	(abbreviation LIC)

This code is retained throughout the study for these constituents.

These curves will be used and discussed more extensively in connection with the modulation outputs. However it is appropriate to briefly discuss here their significance. Each of point of each curve represents the output that the sensor would give for a narrow band filter of the shape shown in Figure 3-13. In the visible and near infrared parts of the spectrum, the half peak width of the filter is 150 $\overset{o}{A}$ and in the infrared 450 $\overset{o}{A}$: along the abcissa is plotted the wavelength at which the filter has its peak transmission. The overall shape of the curve follows that of the spectral response of the detector, however, a close comparison of the relative outputs indicates that as is to be expected they are in the same order of magnitude as the reflectivity curves in Figure 3-12. Silica therefore is the dominant output at all wavelength up to 3 microns. Dunite, Rhyolite and Lichens have persistently low outputs and therefore,in a scene in which they are adjacent to Silica,would render considerable contrast; but adjacent to each other they would give rise to a very low contrast scene. A study of the bands shows that the best spectral regions to use are 0.4-0.45 μ, 0.68-0.78 μ, 1μ-1.1μ. 1.25μ -1.5μ . What these curves do not show clearly is the relative merit of placing a given narrow band at a particular spectral location. It is, for example, extremely difficult to judge the contrast resulting from placing the narrow band close to the cut in, or cut off, regions of the detector response; the region around its peak response is easier to assess , (but even then it is difficult to compare the relative merits of the bands). It was for this reason that the modulation concept was introduced and further discussion of these curves will take place in connection with the modulation technique.

3.5   MODULATION ANALYSIS

The technique outlined above is ideally suited to investigations using one type of detector only; it has been used frequently and successfully for aerial reconnaissance using film as the detector medium. To compare the merits of more than one detector a different kind of criterion is needed, one that is not dependent on the type, magnitude or spectral location of the detector response. It is clear that this criterion must be a function of the detector output. This type of requirement implies a normalization technique may be suitable, as for example, in contrast evaluation in film photography. In the latter case a contrast function is formed from the density from adjacent exposed areas: this can be in one of three forms:

    (a)   The Contrast Ratio (CR)

    (b)   The Contrast Difference (CD)

    (c)   The Contrast Modulation (CM)

If we represent the exposure of these adjacent areas by V_1 and V_2 respectively $(V_1 \neq V_2)$, we have for

$$\text{(a)} \quad CR = \frac{V_1}{V_2} \quad\quad \text{where } 0 < CR < \infty$$

$$\text{(b)} \quad CD = \frac{V_1 - V_2}{V_2}$$

$$\text{or} \quad = \frac{V_1 - V_2}{V_1} \quad\quad \text{where } 1 < CD < \infty$$

$$\text{(c)} \quad CM = \frac{V_1 - V_2}{V_1 + V_2} \quad\quad \text{where } 0 < CM < 1$$

The first two have the disadvantage that one of their bounds is infinity; this yields a criterion that is no better than the calculated outputs of the detectors. The third criterion

is the most applicable, primarily because its numerical range lies within 0 and 1, and for this reason was the criterion chosen.

In applying the technique a scene is chosen (Section 2.0), and the detectors are evaluated on the assumption that any of the scene constituents can be adjacent to any of the others in the hypothetical scene arrancement. Thus if there are n constituents, the number of possible arrangements of adjacent (different) constituents is $^{n}C_{2}$. The method described can be used for both the broad band and narrow band analyses.

3.5.1 MODULATION ANALYSIS FOR BROAD BANDS
A value of

$$[SO]_{\lambda\,1}^{\lambda\,2} = \int_{\lambda\,1}^{\lambda\,2} (H_m)_\lambda \cdot R_\lambda \cdot (S_\lambda^-) \, d\lambda \qquad 3\text{-}6$$

was determined for each detector for each of the constituents of the scene, so that if we denote each of the constituents for simplicity as A, B, C, D, E, F, (n = 6), the corresponding output for each constituent is

$$[SO]_A, \quad [SO]_B, \quad [SO]_C, \quad [SO]_D, \quad [SC]_E, \quad [SO]_F$$

the integral being performed over the same wavelength range $\lambda_1 - \lambda_2$. A modulation value for, say, constituents A and B $(M)_{AB}$ is given by

$$(M)_{AB} = \frac{\left| [SO]_A - [SO]_B \right|}{(SO)_A + (SO)_B} \qquad 3\text{-}7$$

In a similar way $(M)_{AC}$, $(M)_{AD}$, $(M)_{AE}$, $(M)_{AF}$ can be obtained. Thus in this way the scene is treated in a statistical manner in which it is supposed that an equal probability exists for any two constituents of the scene being adjacent to one another. In this circumstance the output modulation of the signal is expressed by the modulation term above. It was mentioned above that owing to the restricted scope of the study, variations in the illumination a d

reflectivities of the constituents cannot be taken into account, consequently the situation being studied is not truly representative in nature in which significant variations in a constituent reflectivity occurs.

There are several modulation functions that can be derived: the"Discrimination Modulation" (DM) of a constituent which for constituent A is given by:

$$(DM)_A = \left[(M)_{AG} + (M)_{AC} + (M)_{AD} + (M)_{AE} + (M)_{AF} \right] /n-1 \qquad 3-8$$

and the "Scene Modulation" (SM) which is given by

$$\left(SM \right) = \left[(DM)_A + (DM)_B + (DM)_C + (DM)_D + (DM)_E + (DM)_F \right] /n: \qquad 3-9$$

Each of the modulation terms given above were determined for each sensor in each of the given wavebands; the values obtained are given in the histogram Figure 3-31 – in addition the values of DM for the constituents as a function of detectors are shown in Table 3-3.

TABLE 3-3. CONSTITUENT MODULATIONS FOR THE TEST SCENE

	DM RHY	DM LIM	DM UN	DM BAS	DM SIL	DM LIC
S11	0.40	0.51	0.40	0.47	0.52	0.73
S20	0.37	0.38	0.39	0.45	0.51	0.72
CdS2	0.31	0.36	0.30	0.39	0.47	0.69
CdS5	0.28	0.31	0.28	0.37	0.46	0.64
CdS5H	0.31	0.39	0.31	0.40	0.47	0.69
Si	0.24	0.24	0.29	0.32	0.45	0.44
S1	0.25	0.25	0.27	0.35	0.46	0.49
CdSe3	0.24	0.24	0.30	0.33	0.45	0.46
CdSe4	0.24	0.24	0.29	0.33	0.44	0.49
CdS7	0.26	0.27	0.26	0.36	0.46	0.59
653	0.28	0.30	0.46	0.29	0.42	0.34
654	0.23	0.23	0.29	0.25	0.43	0.34
655	0.24	0.24	0.34	0.25	0.44	0.27
PbS	0.25	0.27	0.31	0.25	0.43	0.33
PbSe	0.23	0.25	0.30	0.23	0.41	0.26
In As	0.23	0.24	0.28	0.24	0.42	0.25
Flake	0.23	0.24	0.31	0.24	0.42	0.26

3.5.2 BROADBAND MODULATION RESULTS

Somewhat unexpectedly the greatest scene modulation occurs in the blue part of the spectrum. Examination of Figure 3-12, in which is plotted all the constituent reflectivities, indicates that the prime causes of this high modulation is very low reflectivity of Lichen and the high reflectivity of Silica Sand. It is noticeable that at longer wavelengths the Lichen reflectivity increases and the average modulation decreases accordingly.

In the infrared the reflectivities vary considerably and Limonite, Dunite and Rhyolite follow each other closely so that the integrated outputs for these constituents are similar, which is a condition that gives rise to low scene contrast. This is clearly illustrated in the modulation values given in Figure 3-11. For broadband scene contrast therefore, the best sensors to use between 0.4 and 1.1μ are the S11 and S20 detectors. In the infrared the best results are obtained with the Silicon PIN 654 diode.

3.5.3 MODULATION ANALYSIS FOR NARROW BANDS

The method used is identical to that used for the broad bands, the only difference being the width of the band: equation 3-4 is used in determining the values of SM and constituent DM's for each of the narrow band positions. Utilizing this technique and exhibiting the results in a plot of DM's and SM vs. peak wavelength of each position of the narrow band filter, a visual representation of the analysis is obtained. With this data, it is possible to position the required broad bands or narrow bands for optimum discrimination. The results are presented for all the bands in the following section.

3.5.4 NARROW BAND MODULATION RESULTS

For each detector a family of curves for the DM's and SM of the constituents was drawn; these curves were derived from the narrow band output results. Four samples of these curves are shown in Figures 3-32 to 3-35 representing the 0.4-0.8 micron, 0.4-1.1 micron, 0.6-2.0 micron and 1-5 micron spectral bands respectively. The variation of the constituent modulations (numbered) and the scene modulation (dashed) are plotted against wavelength in the same way as the narrow band ou'uts. Their variation with wavelength was found to be identical for each detector in each band. The shapes of the curves were found to correlate

in shape, but not in absolute magnitude with a modulation plot (Figure 3-36) derived from the reflectivity curve of Figure 3-12. A simple analysis for an extremely narrow band (less than 150 $\overset{\text{o}}{\text{A}}$ wide) shows that this result can be expected. Using the symbols described in Section 3.1.1 and the modulation terms evaluated in 3. .1

$$(M)_{AB} = \frac{\left| [S.O]_A - [S.O]_B \right|}{[S.O]_A + [S.O]_B} \tag{3-10}$$

$$(M)_{AB} = \frac{\left| \int_{\lambda_1}^{\lambda_2} (H_m)_\lambda (R_A)_\lambda (\bar{S}_\lambda)(T_F)_\lambda d\lambda - \int_{\lambda_1}^{\lambda_2} (H_m)_\lambda (R_B)_\lambda (\bar{S}_\lambda)(T_F)_\lambda d\lambda \right|}{\int_{\lambda_1}^{\lambda_2} (H_m)_\lambda (R_A)_\lambda (\bar{S}_\lambda)(T_F)_F d\lambda + \int_{\lambda_1}^{\lambda_2} (H_m)_\lambda (R_B)_\lambda (\bar{S}_\lambda)(T_F)_\lambda d\lambda} \tag{3-11}$$

now since the band is very narrow $\lambda_1 - \lambda_2 = \Delta\lambda$ and over this small wavelength interval $(H_m\lambda$ $(\bar{S}_\lambda)$ $(TF)_\lambda$ can be assumed constant over the interval and so the equation becomes

$$(M)_{AB} = \frac{(H_m)_\lambda (\bar{S}_\lambda)(T_F)_\lambda \Delta\lambda . (R_A - R_B)}{(H_m)_\lambda (\bar{S}_\lambda)(T_F)_\lambda \Delta\lambda \quad R_B + R_B}$$

$$(M)_{AB} \approx \frac{R_A - R_B}{R_A + R_B}. \tag{3-12}$$

Thus for extremely narrow bands (circa 10 $\overset{\text{o}}{\text{A}}$) the output modulation or the sensor may be expected to follow that of the reflectivities unless very sharp gradients in the irradiance or the detector response occur. For bands of the width for which the narrow bands results above were calculated (150 $\overset{\text{o}}{\text{A}}$ wide) indicates that the influence of the narrow band filter is insignificant; the changes arising out of increasing the band width and differing filter shape require further investigation.

3.5.4.1   Selection of Spectral Bands for Scene Contrast

Narrow bands can be selected from the modulation plots and the narrow band sensor outputs. The objective of the selection is to acquire maximum modulation of the sensor output, assuming a random arrangement of scene constituents. Clearly then to satisfy this requirement the region of greatest average modulation must be located. Although detector noise has not been included in this study, it is obvious that in regions where the detector outputs are less than about 30% of their peak an undesirable signal to noise ratio may exist. According to these criteria it is seen from inspection of the 0.4 to 0.8 micron and 0.4 - 1.1 micron bands (Figures 3-32 and 3-33) that the greatest modulation occurs at 0.4 micron and falls off momentarily to about .65 microns. Throughout the whole of this region however the modulation is high, being between 0.4 and 0.5. Since the modulation curves for all the detectors are identical, it follows that any of them could be used. However as a consequence of the noise considerations mentioned above, the sensors recommended for the 0.4 - 0.8 and 0.4 - 1.1 micron band are S11, S20 and Si. For purpose of contrast maximization any other bands may be selected throughout the spectral sensitivity range of the detectors but the contrast obtained will always be less than that around 0.4 microns.

In the infrared the scene modulation is consistently less than that in the visible up to 3 microns; beyond 3 microns it rises rapidly up to 0.46, drops to 0.32 at 0.37 microns, and then rises to nearly 0.5 at 4.8 microns. These findings indicate the IR imaging should be confined to wavelengths greater than 3 microns. However a difficulty arises. At wavelengths greater than 3 microns the spectral selective detectors yield very little output. This situation is further made worse by the substantial CO_2 absorption band at 3.5_μ. A full signal-noise analysis may negate the use of $3.2_\mu - 3.7_\mu$ band 1, which is considered the best in the IR. The alternatives are the $2.8_\mu - 3.0_\mu$ band and the band between 1.0_μ and 1.25_μ. Any of the detectors listed in either the 0.6 - 2.0 micron or the 1-5 micron band can be used. Obviously the one with the best noise figure and appropriate frequency response would be chosen.

3.5.4.2 Narrow Band Selections for Constituent Discrimination

It will be assumed throughout this section that the objective is to discriminate between as many of the scene constituents as is possible.

The degree of difficulty of discriminating the constituents against one another depends primarily on the variation of their reflectivity as a function of wavelength. With reference to Figure 3-12 it can be seen that Silica, Basalt and Limonite present the least d. :ulty; Rhyolite, Dunite and Lichen the greatest difficulty. The spectral location of the best bands to choose for discrimination can be found by careful examination of the sensor output and modulation curves. It is essential to use both sets of curves because in certain spectral bands the amplitude of the scene modulation does not indicate uniquely the degree of difference in the constituent outputs.

In the visible and near infrared bands (0.4-1.1 micron) the following bands are excluded on the grounds that they contain two or more outputs that are within 5% of each other. These bands are:

$$0.45\,\mu - 0.56\,\mu \; ; \; 0.62\,\mu - 0.66\,\mu \; ; \; 0.78\,\mu - 0.96\,\mu \; .$$

The useable bands are therefore:

$$\text{Up To } .45\,\mu \; ; \; 0.56 - 0.63\,\mu \; ; \; 0.66 - 0.78\,\mu \; ; \; 0.96 - 1.1\,\mu \; .$$

The best band for discrimination is the band up to 0.45 microns, the next two being 0.66 - 0.78 microns and 0.96 - 1.1 microns and the last 0.56 - 0.63 microns. The selection of the 0.56 - 0.63 as the least desirable band appears to be paradoxical in relation to its higher average modulation (0.47); however this high figure is primarily due to the low value of the Lichen reflectivity, and it can be seen that the separation of the Dunite, Limonite and Rhyolite outputs in this band will present difficulties.

Employing the same technique to the IR part of the spectrum the following bands may not be used:

1.5 - 1.25 microns; 1.6 - 3.2 microns; 3.7 - 3.9 microns; 4.2 - 4.7 microns

The same uncertainty with the signal to noise ratio exists at wavelength greater than 3 microns. However, the suggested bands for discrimination are:

1 - 1.1μ . 1.3 - 1.5 microns; 3.2 - 3.7 microns; 4.7 microns +

3.6 CONCLUSIONS

A simple examination of the results shows that in order to acquire maximum scene contrast with an imaging system a considerable knowledge of the spectral characteri tics must be available. The exclusion of a constituent in the test scene could alter the scene modulations completely and could also alter the spectral locations of the optimum bands. Several factors which could not be considered for this small study, are known to significantly affect the contrast of any real scene. These factors are the variation in constituent reflectivity (for example as a function of particle size) and the noise intorduced by the optical transducer. The latter can be included theoretically without difficulty; the former must be acquired through experimentation.

With the very simple scene considered the modulation technique proved to be a valuable concept in evaluation of the relative merit of broad band detectors. More will be said on this point in the section dealing with the film experiment.

The modulation concept was found to be a less powerful technique in the narrow band. Although the analysis of the narrow band outputs was aided by the availability of the modulation plots, the latter as a result of the averaging process, led to ambiguous results in some cases. (An interesting feature of the narrow band modulations, however, may be their dependance on the shape and width of the narrow band filter. This property may prove to be a valuable criteria for choosing the optimum filter.) In this study 'perfect' filters were considered. However

in view of the apparant importance of the filter shape ,a foreseeable development of the technique is in the evaluation of the manufactured filter and its inherent defects,such as broadband breakthrough and sideband breakthrough. Defects in manufactured filters are usually present in varying degrees and the transmission of unwanted radiant-energy can obviously degrade the system performance, and the modulation technique may prove to be a rapid means of evaluating the magnitude of the degradation.

The computer simulation of the detector output has proved to be a rapid and less expensive alternative to an experiment to find the optimum band for high contrast rendition. It would have proved time consuming and expensive to experimentally investigate the filter and detector constituents as accomplished by the computer on the same scale of thoroughness. Ultimately recourse to an experiment is always needed and the early phases of that stage are described in a later section.

The final conclusion is that the technique and the results obtained in this study are well worth developing to a further stage of sophistication in the areas to be outlined presently, so that in future years,when more accurate estimates of the surface constituents of Mars are available, the optimum imaging system can be designed to suit the spectral characteristics of these constituents.

FIGURE 3-1(o.4 μ -0.8 μ)   BAND DETECTOR RESPONSES

FIGURE 3.2 (0.3μ -1.1μ) BAND DETECTOR RESPONSES

TYPE 4 CADMIUM SELENIDE

TYPE 2 CADMIUM SELENIDE

S-1

TYPE 7 CADMIUM SULFIDE

SILICON

WAVELENGTH (MICRONS)
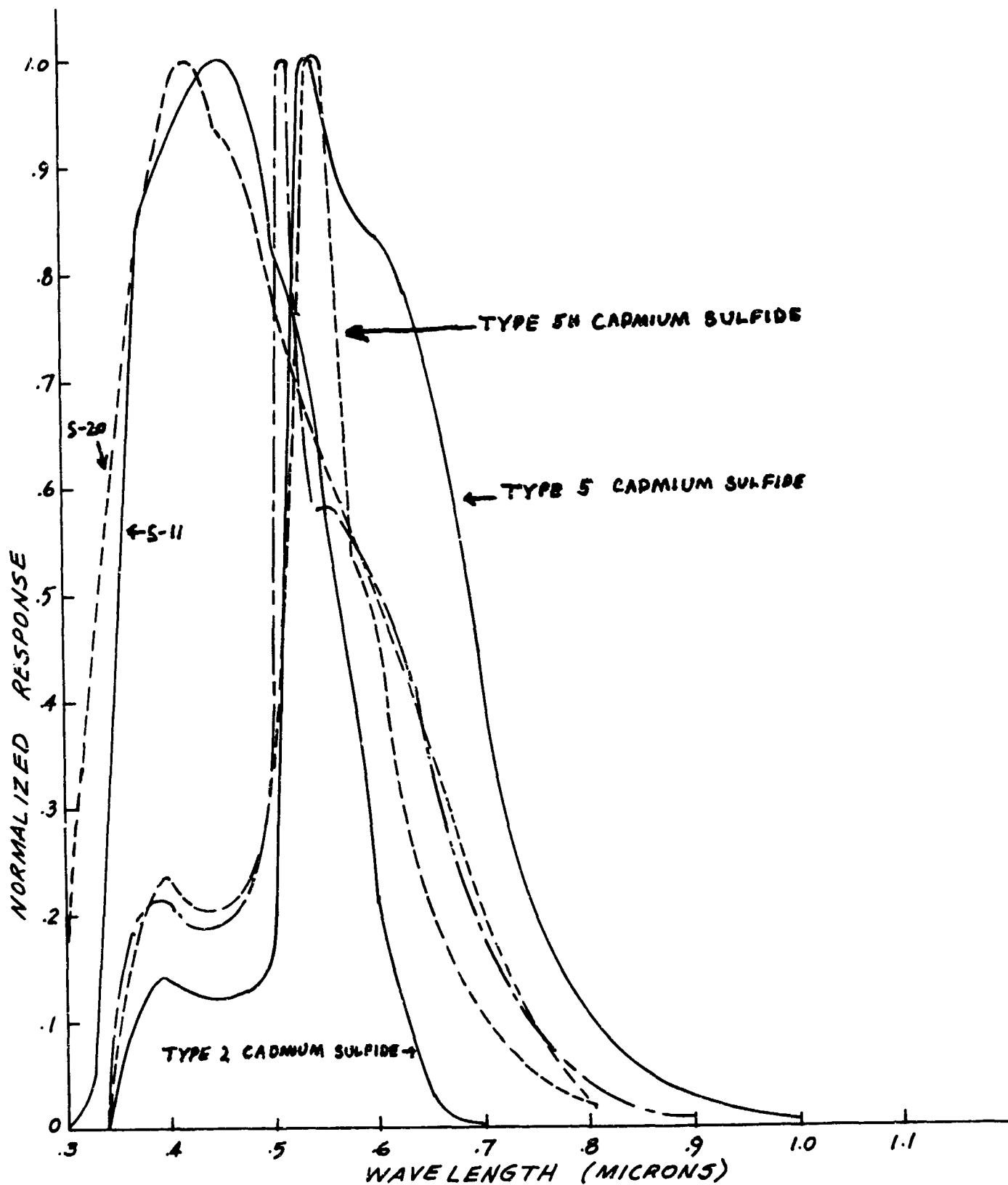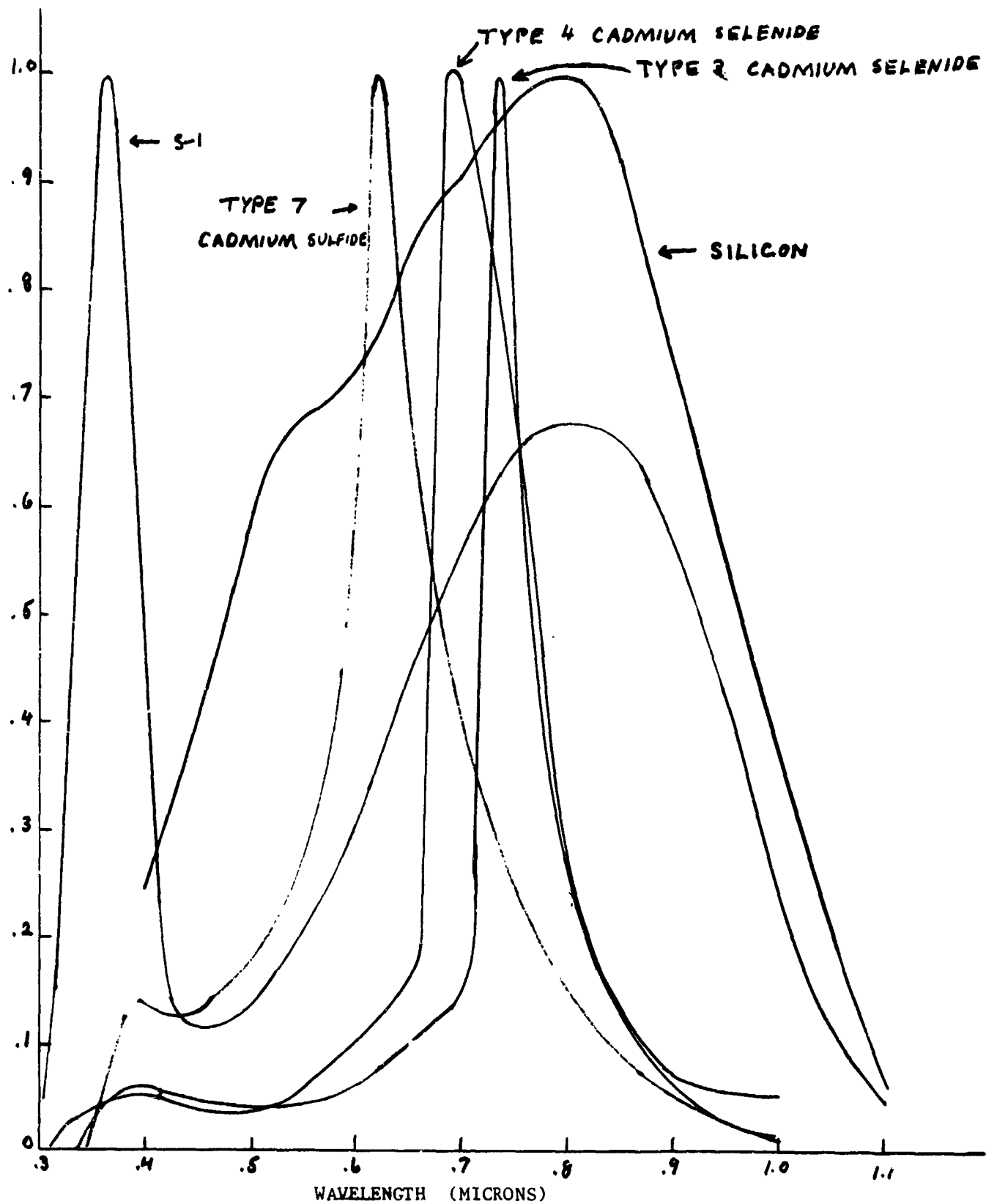
FIGURE3-3 (0.6 μ -2.0 μ)   BAND DETECTOR RESPONSES
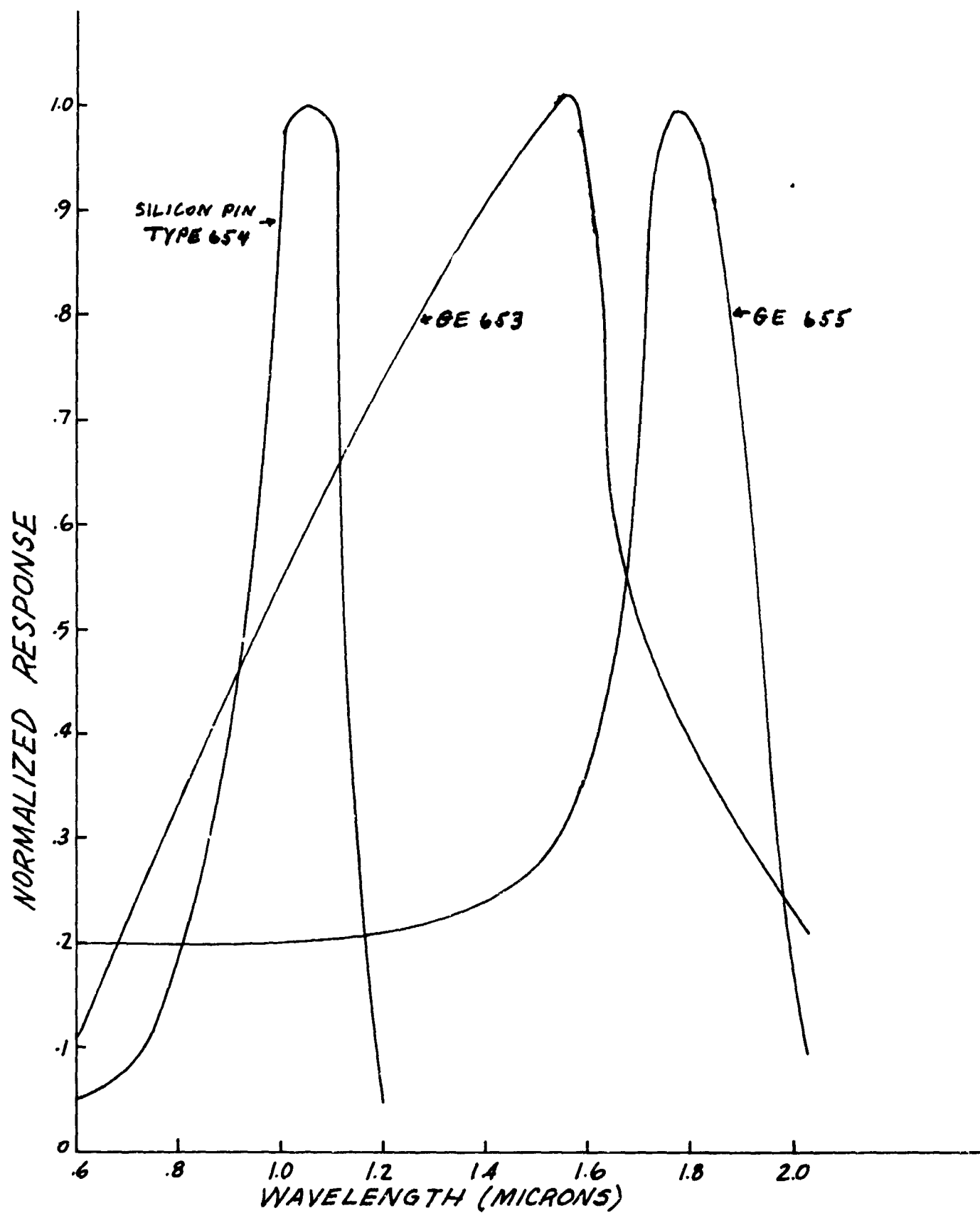
FIGURE3-4(1μ -5μ)   BAND DETECTOR RESPONSES
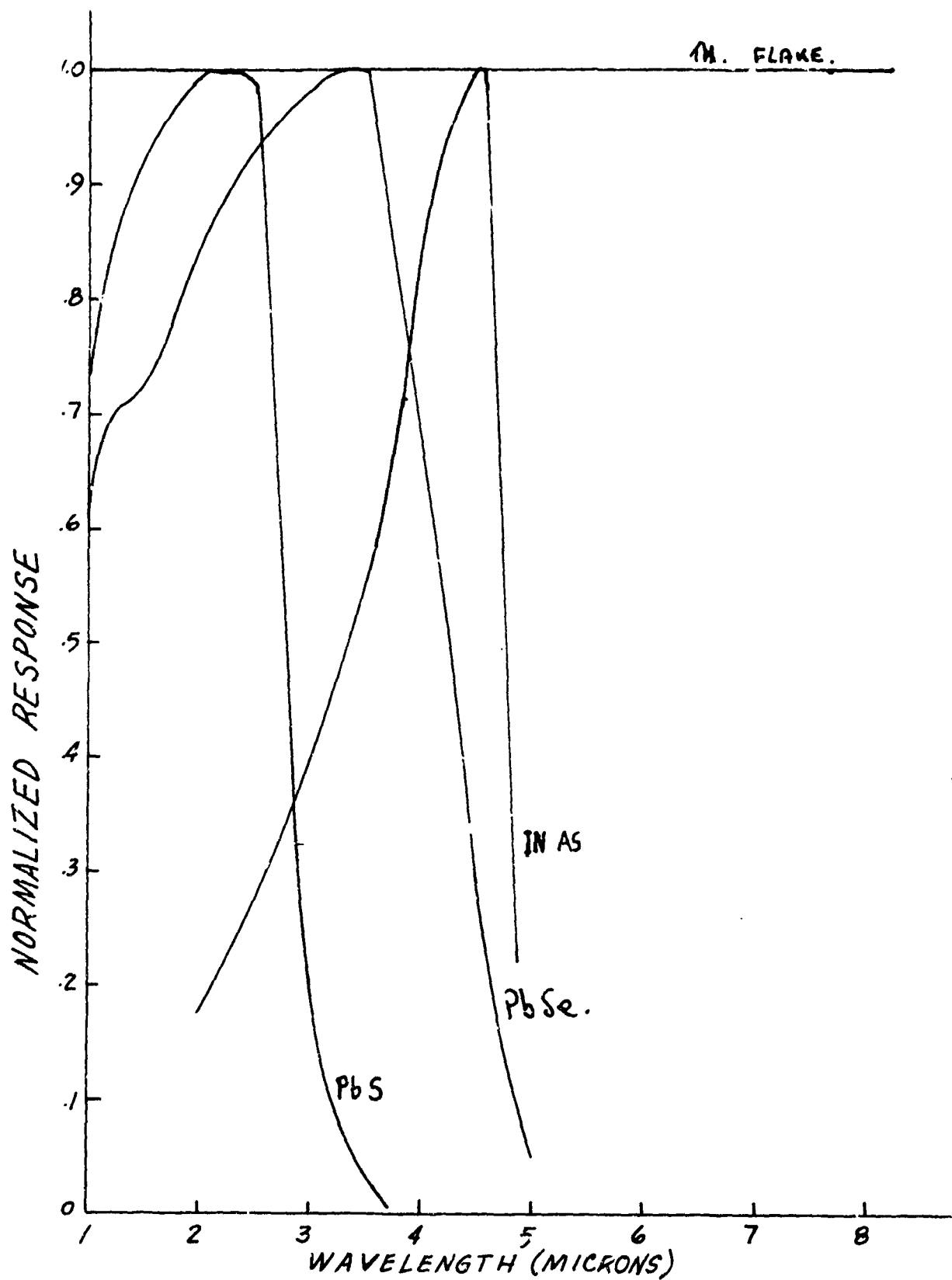
FIGURE 3-5
SPECTRAL SENSITIVITY

KODAK PLUS X

WAVELENGTH (MICRONS)

RELATIVE SENSITIVITY
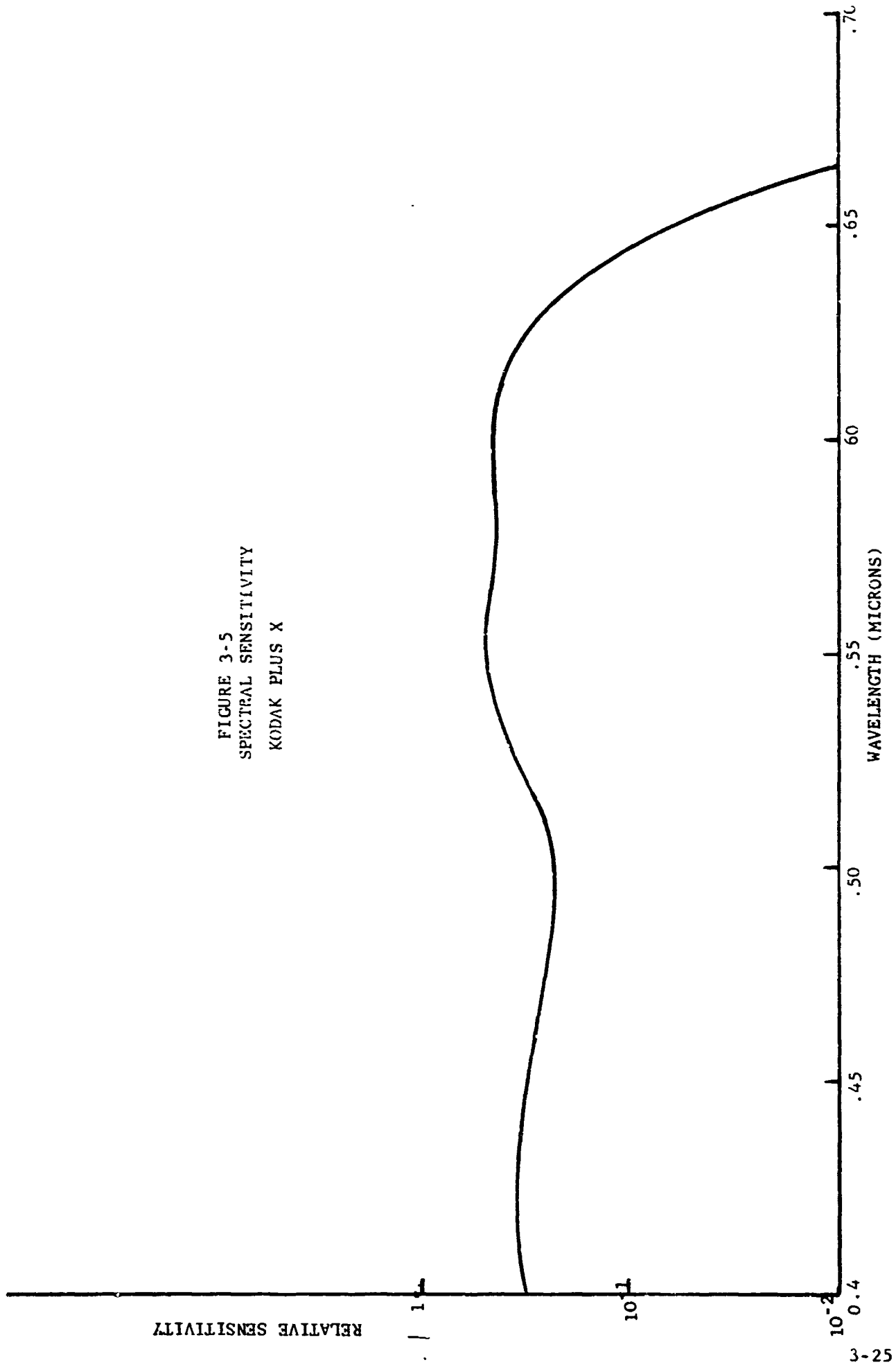
SPECTRAL SENSITIVITY

KODAK SPECTROSCOPIC PLATE, TYPE I-Z

WAVELENGTH (MICRONS)

FIGURE 3-6

RELATIVE RESPONSE

D=0.1 Above Gross FOG

D=0.6 Above Gross Fog
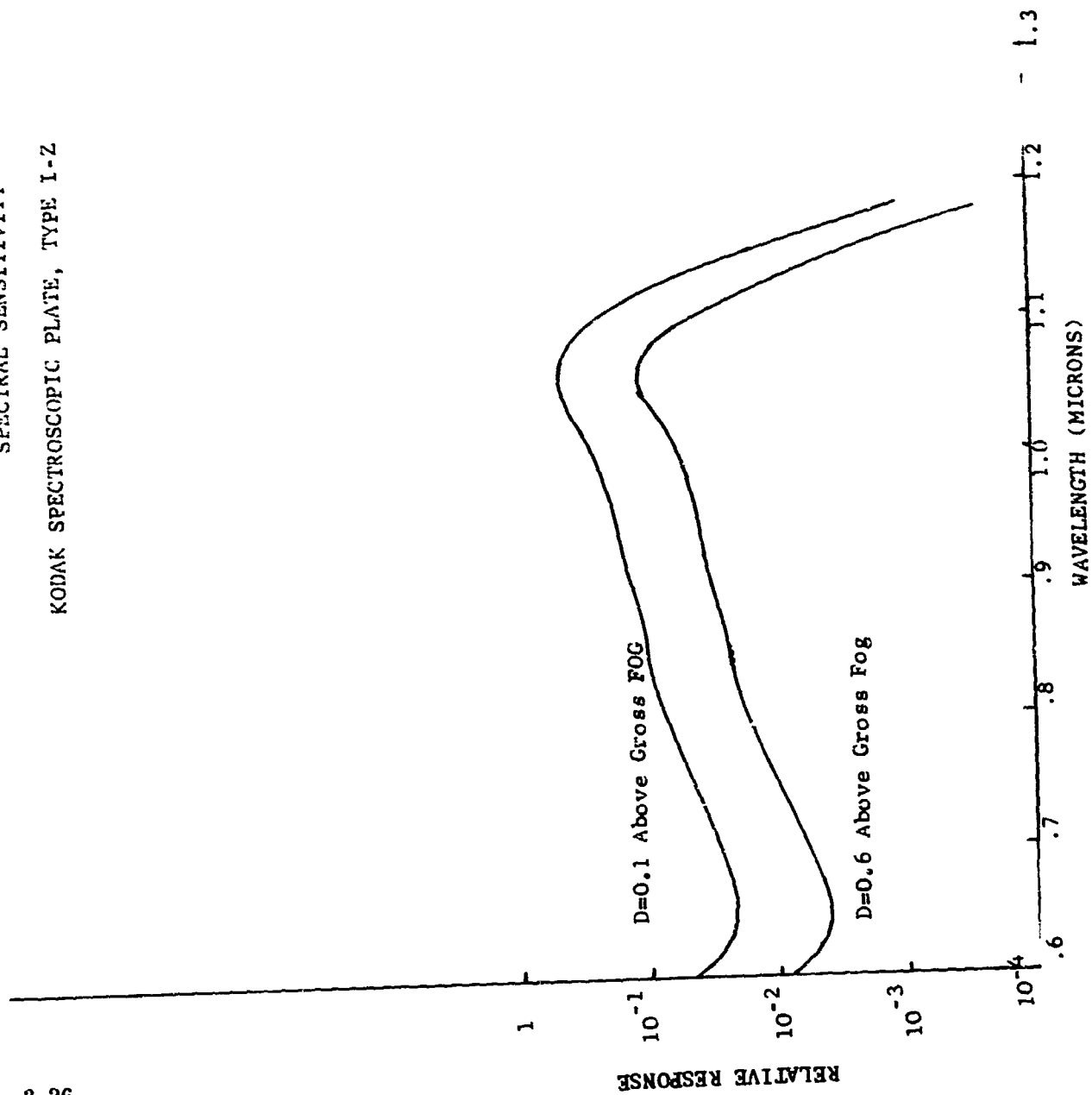
FIGURE 3-7.A

THE IRRADIANCE OF MARS (0.35 - 1.0 MICRONS)
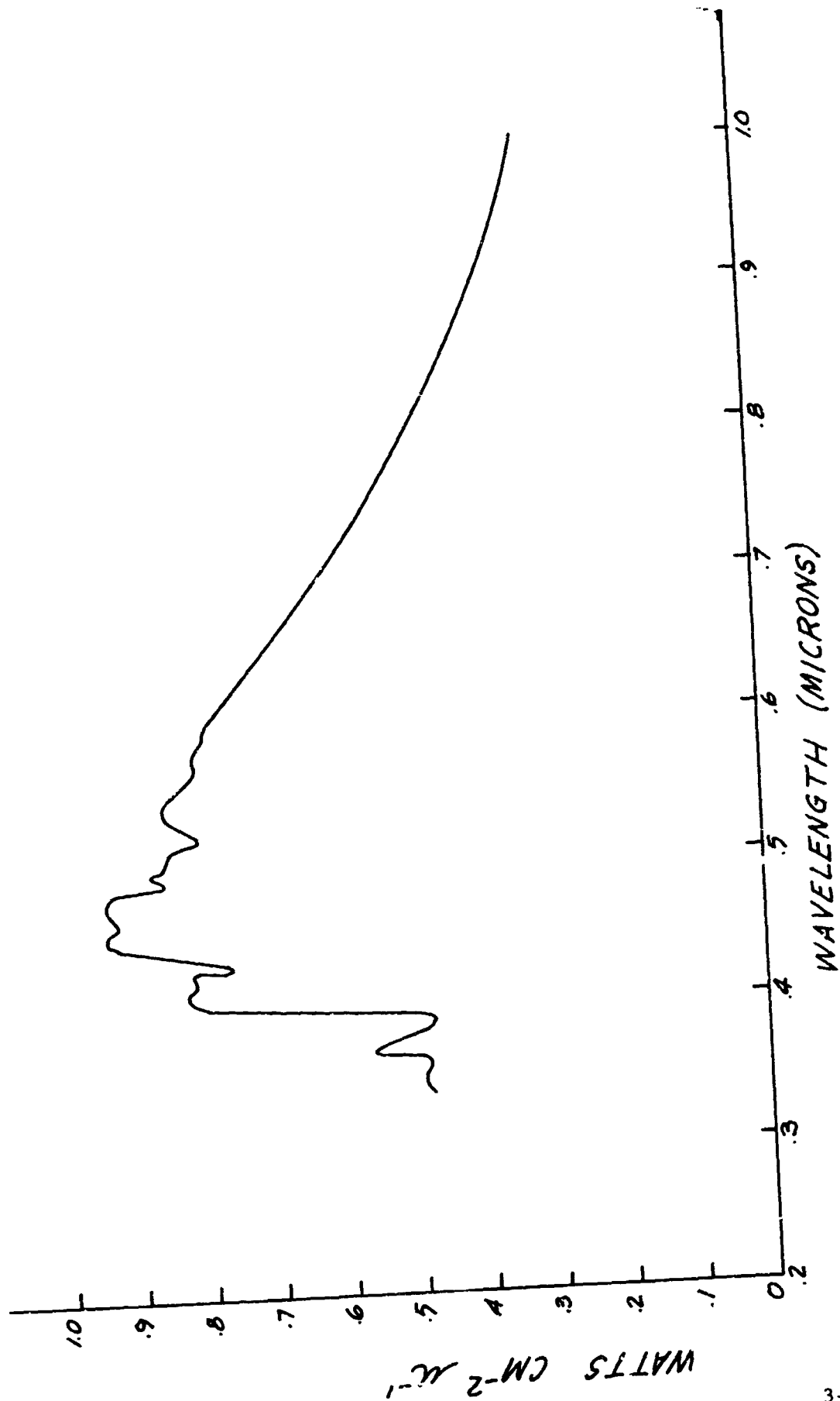
FIGURE 3-7.B

THE IRRADIANCE OF MARS (1.0 - 5.0 MICRONS)

BROAD BAND OUTPUTS   0.4μ - 0.8μ
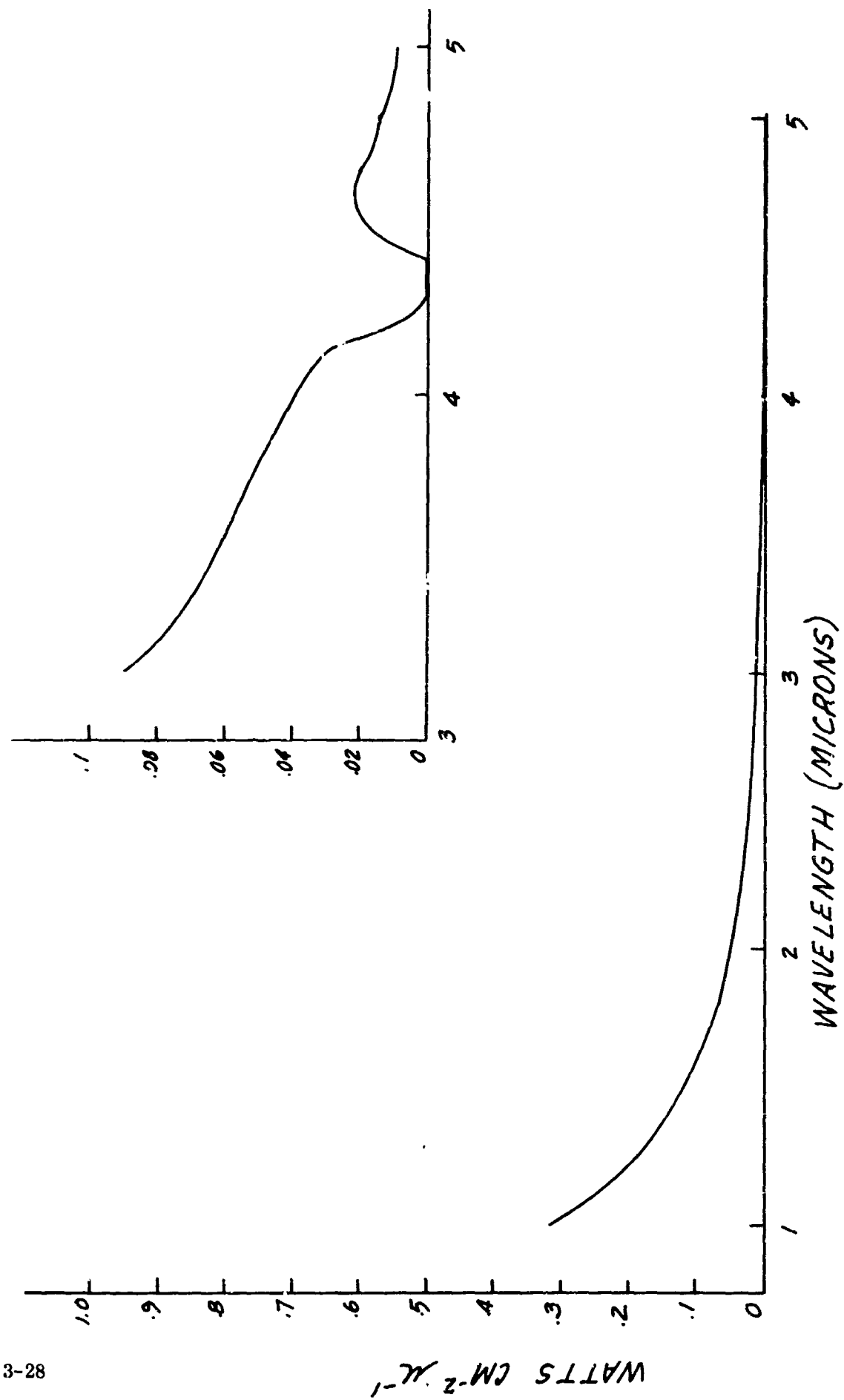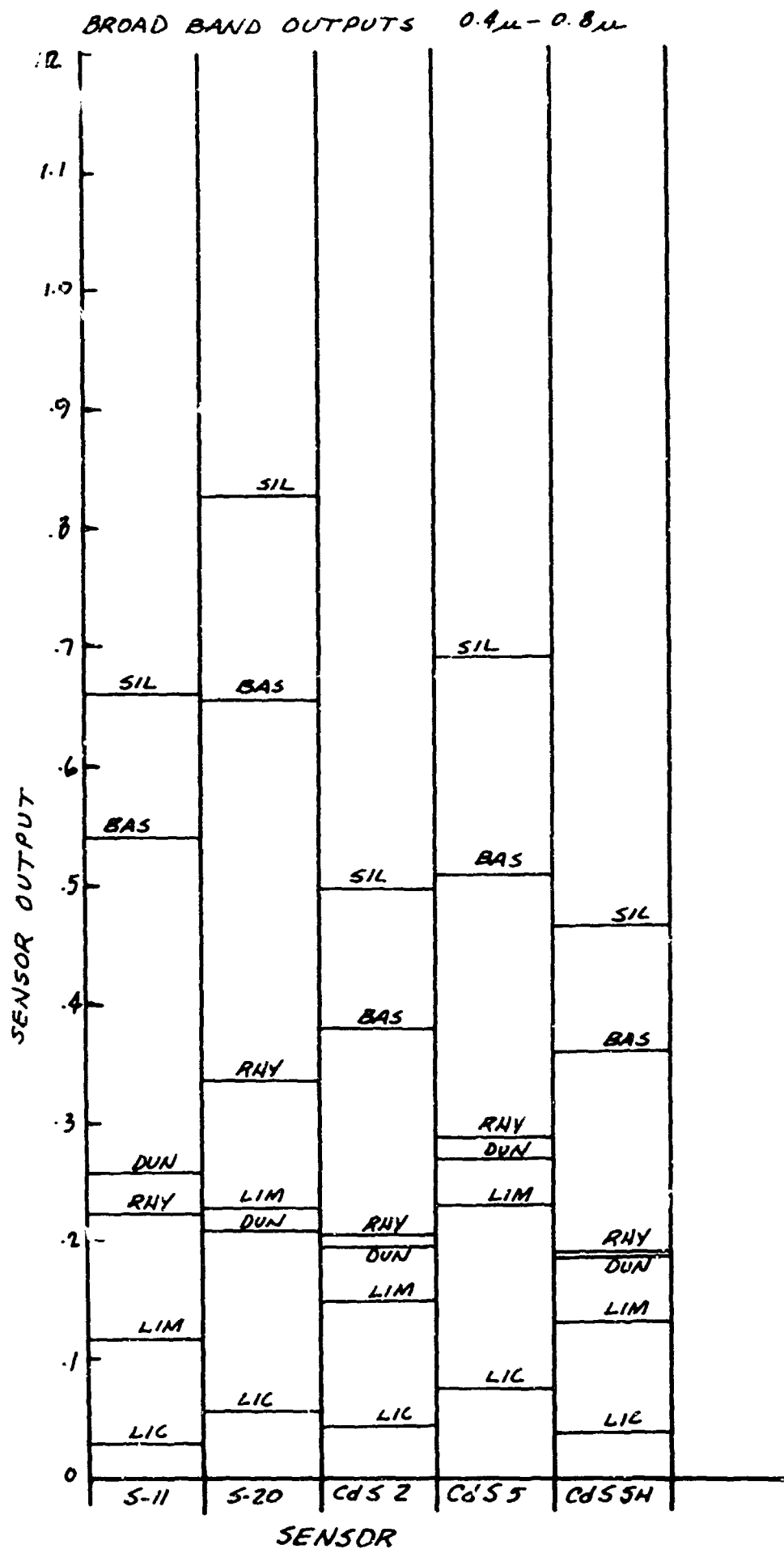
FIGURE 3-8

FIGURE 3-9
BROAD BAND OUTPUTS
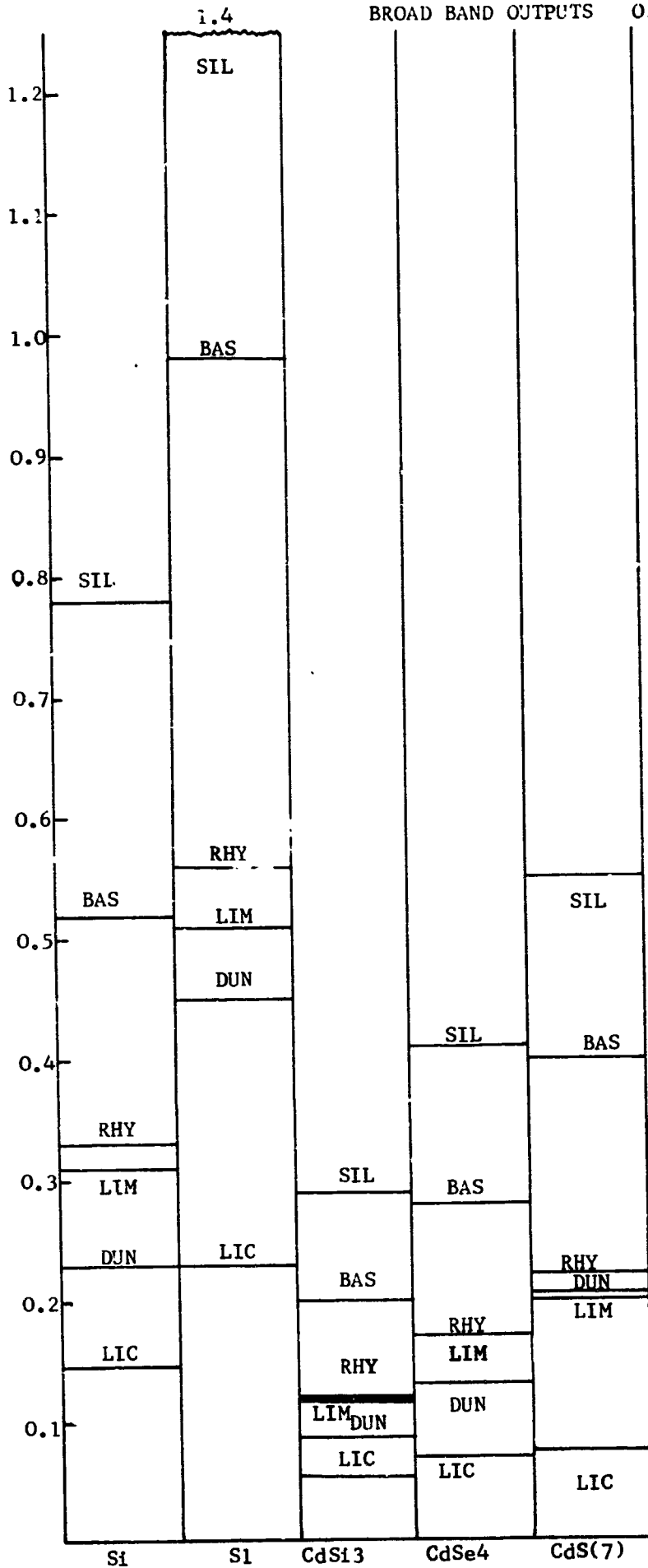
BROAD BAND OUTPUTS.

SENSOR OUTPUTS
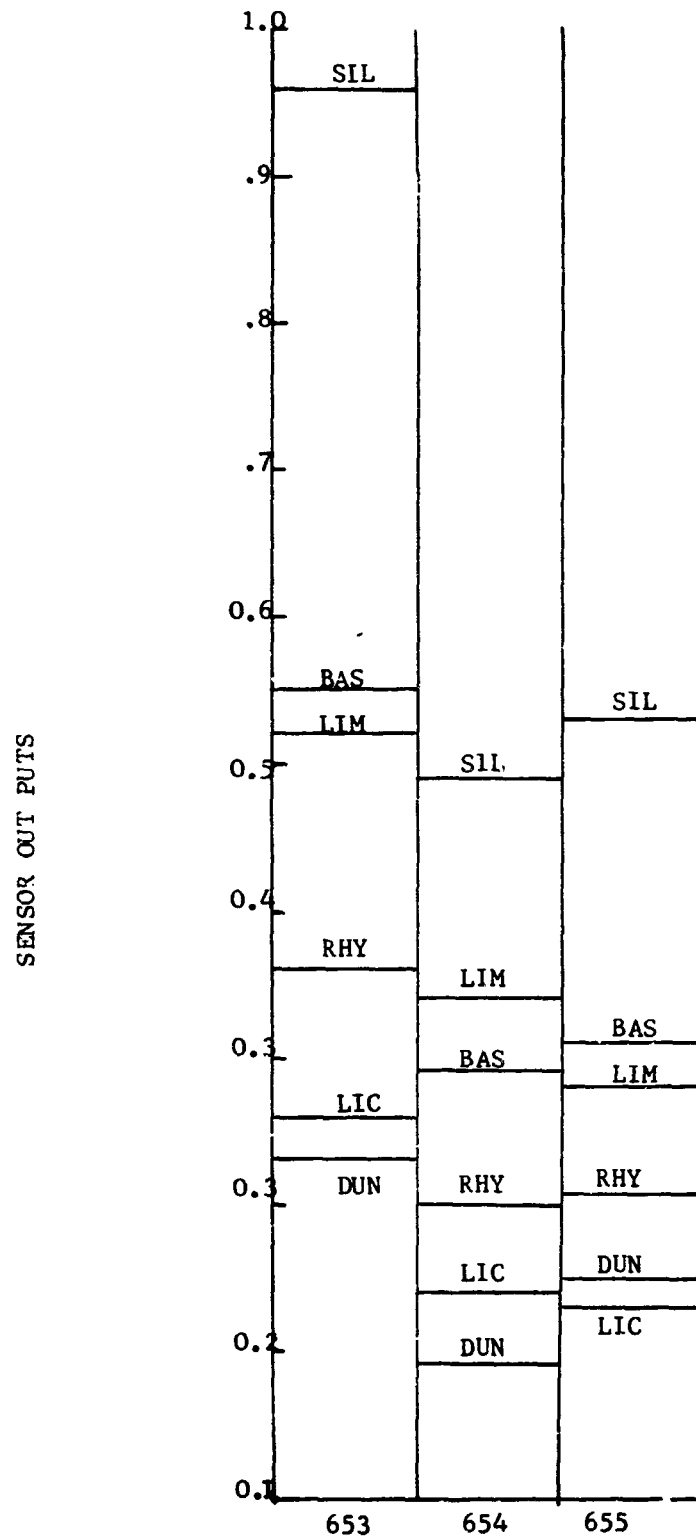
FIGURE 3-10

BROAD BAND OUTPUTS (1μ - 5μ)
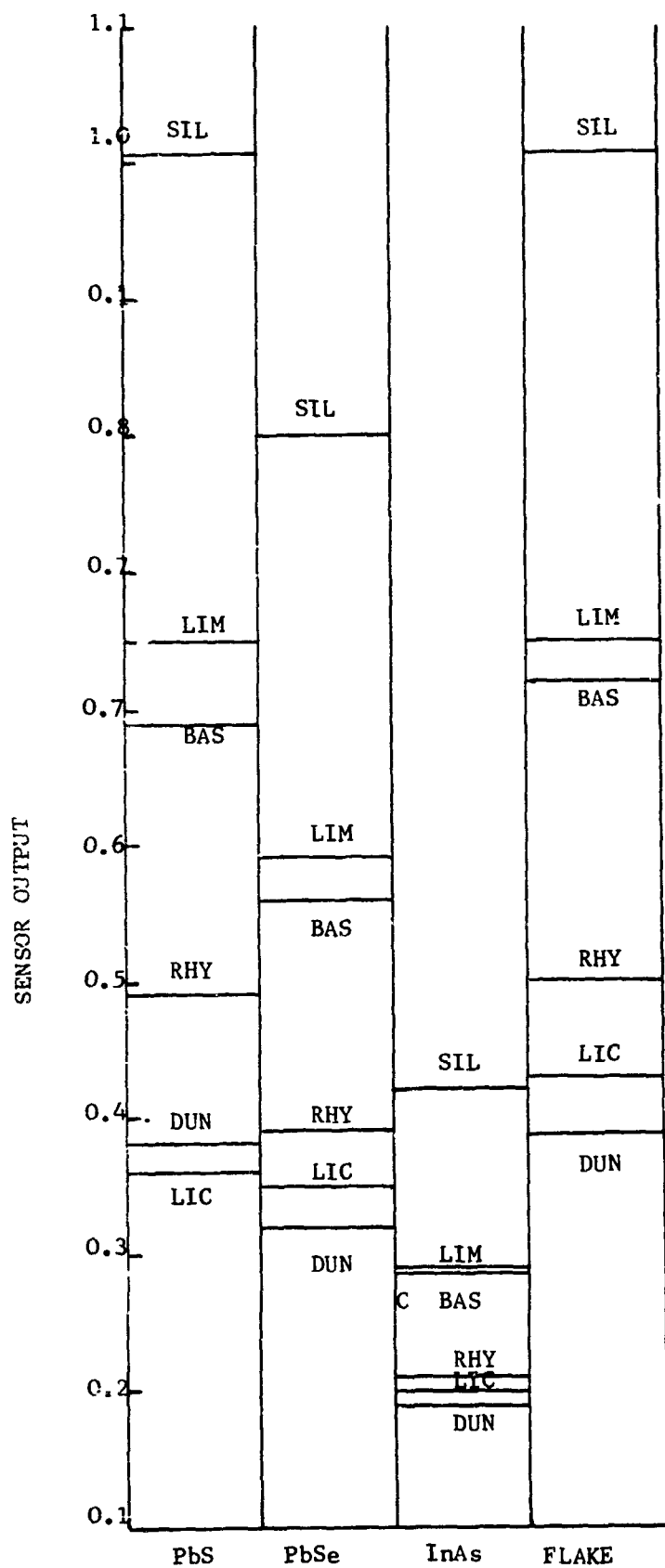
FIGURE 3-11

SCENE CONSTITUENT REFLECTIVITES

FIGURE 3-12

3-33
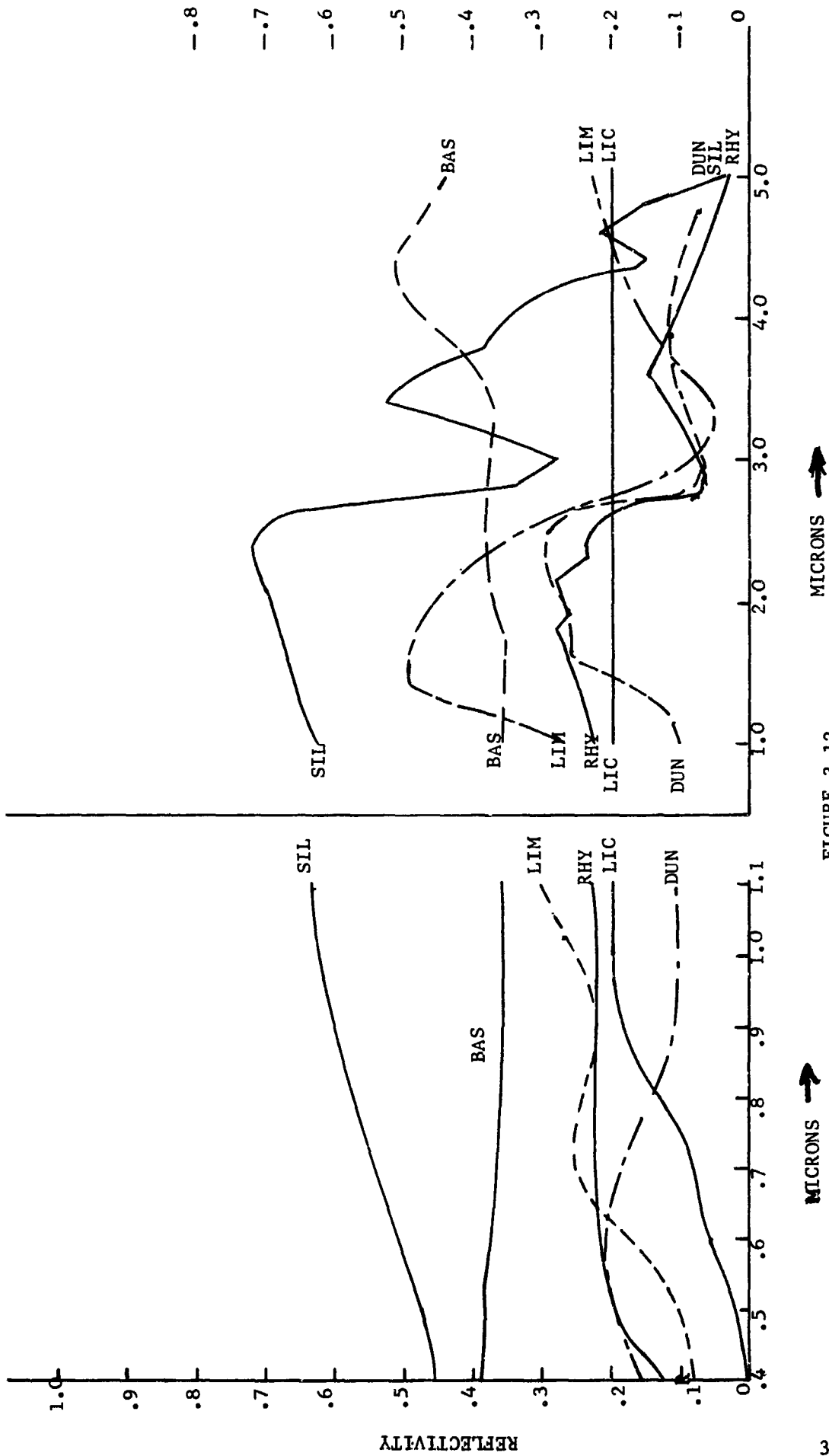
'SLIDING FILTER TECHNIQUE'
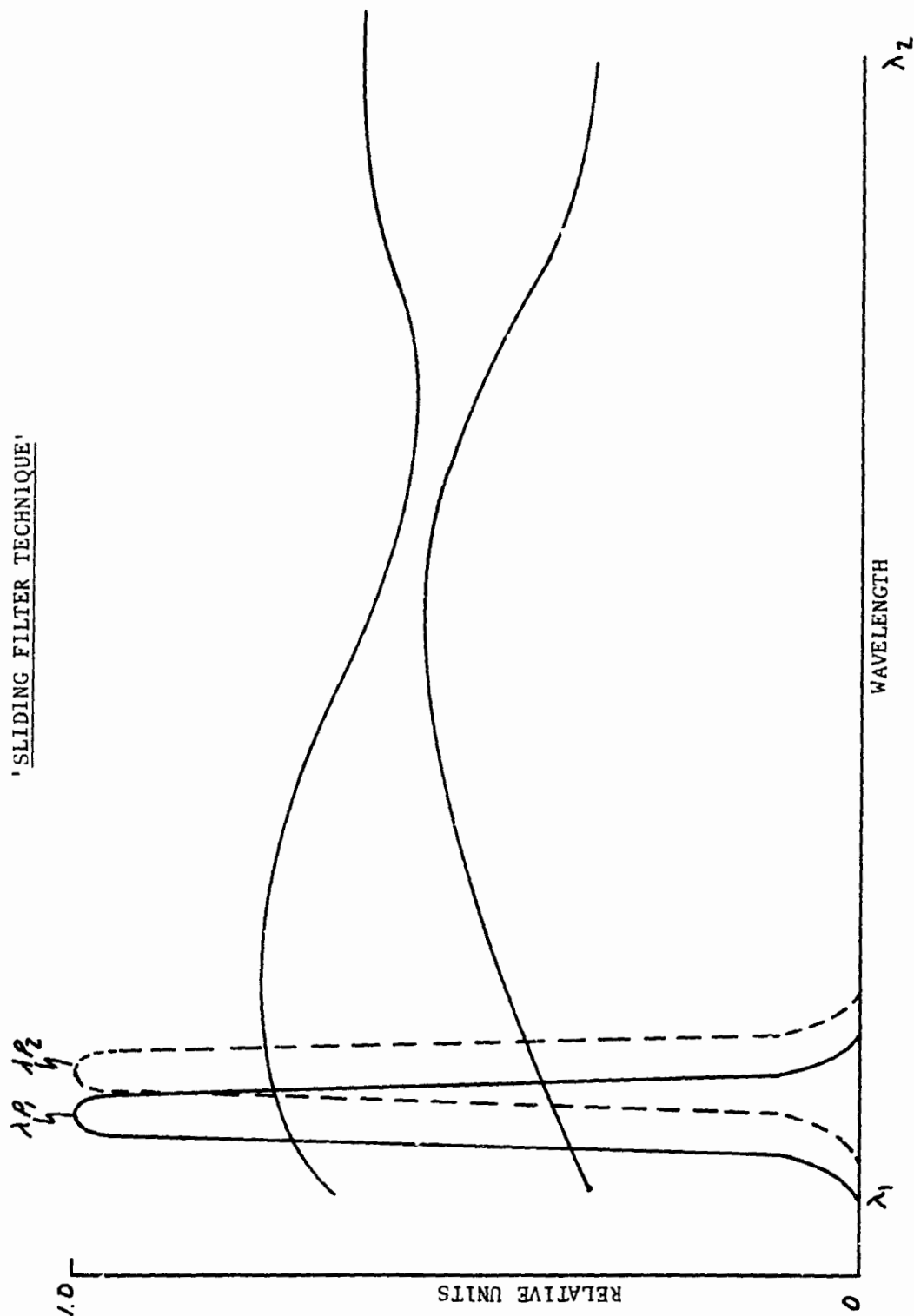
FIGURE 3-13.   The value set of the ordinates of A and B corresponding to the small subintervals $\delta\lambda$ of the filter are obtained by an interpolation routine.
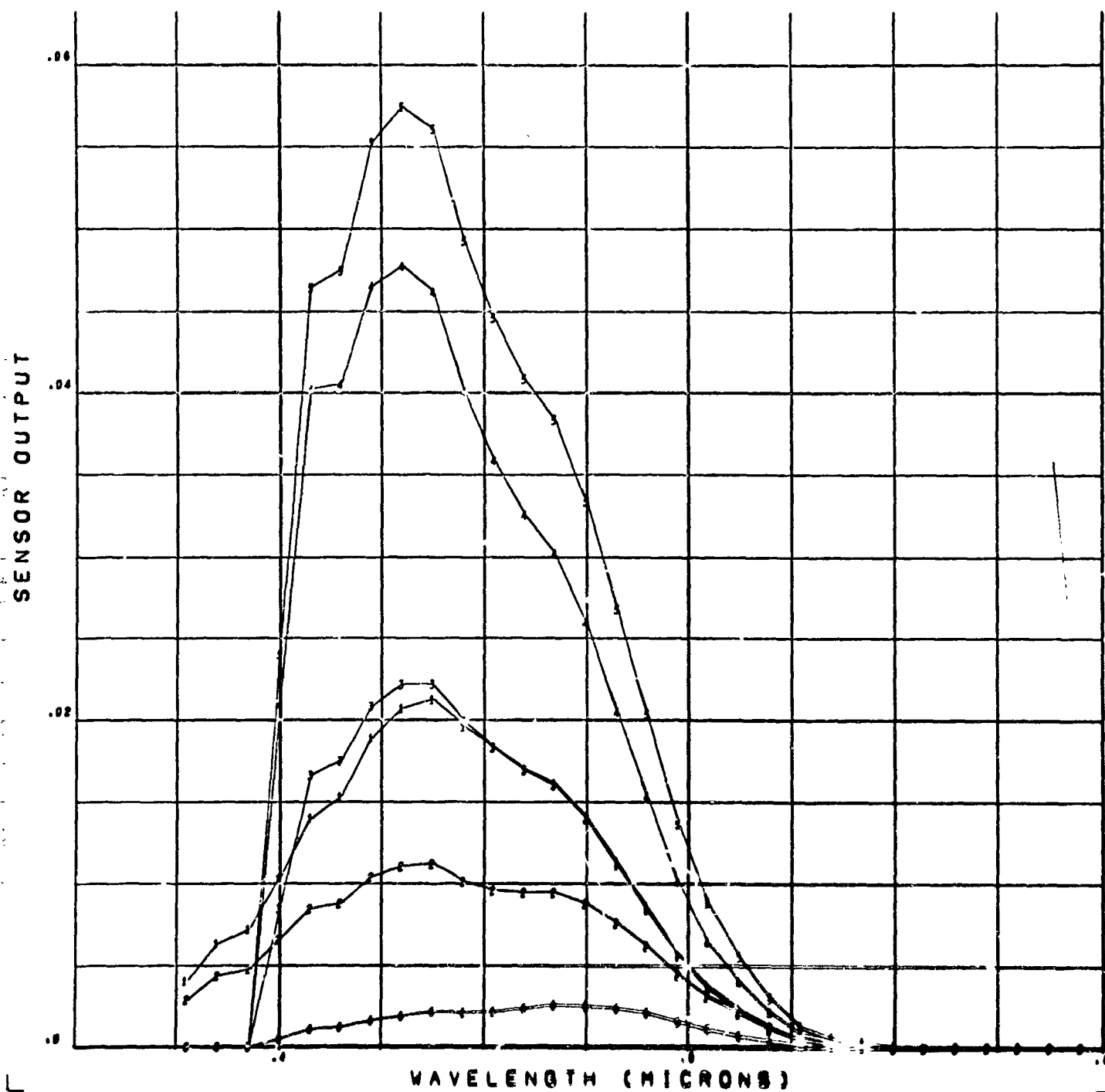
FIGURE 3-14

S 20 SENSOR OUTPUT VS. WAVELENGTH

SENSOR OUTPUT

WAVELENGTH (MICRONS)
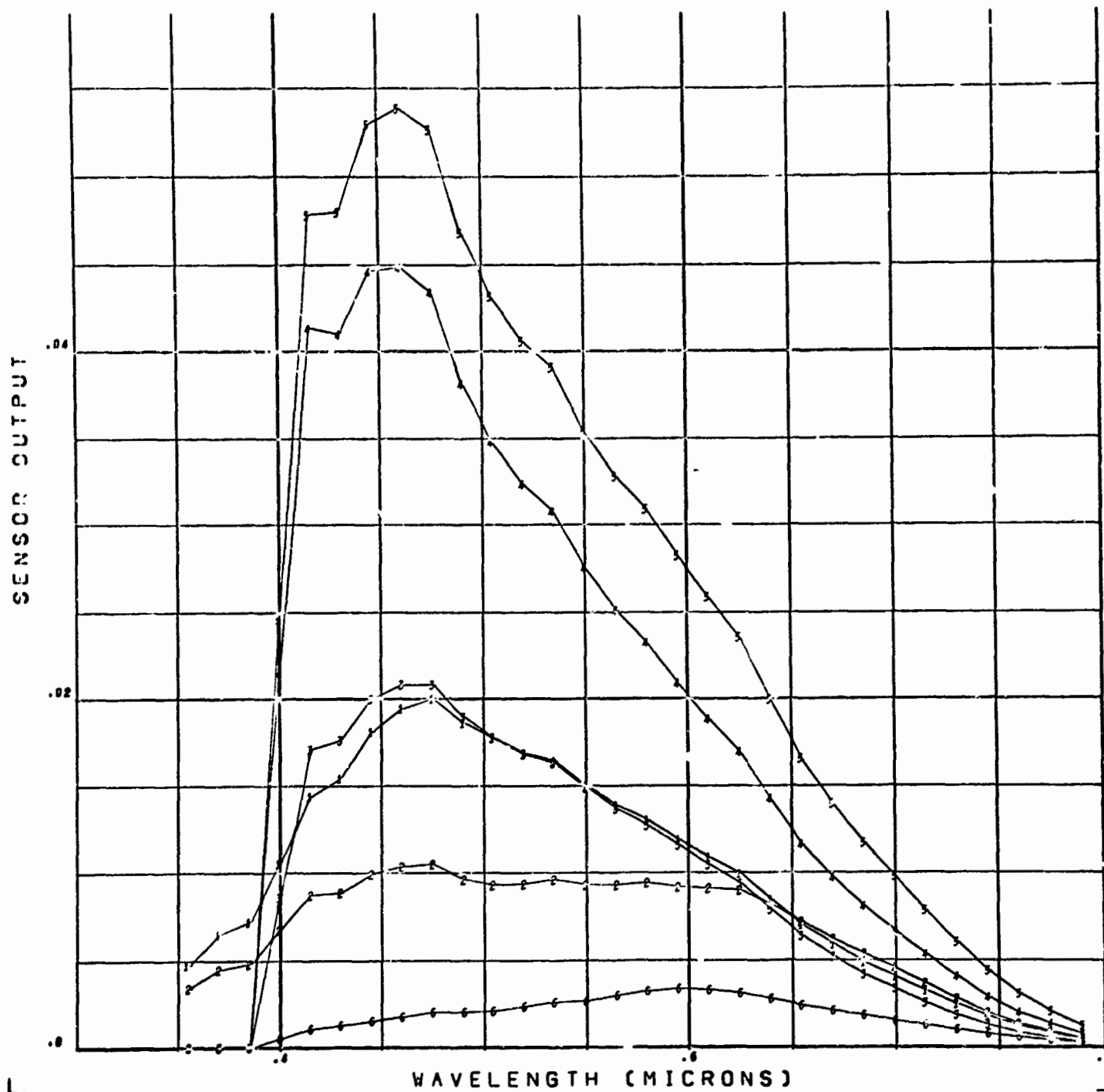
FIGURE 3-15

CdS-2 SENSOR OUTPUT VS. WAVELENGTH
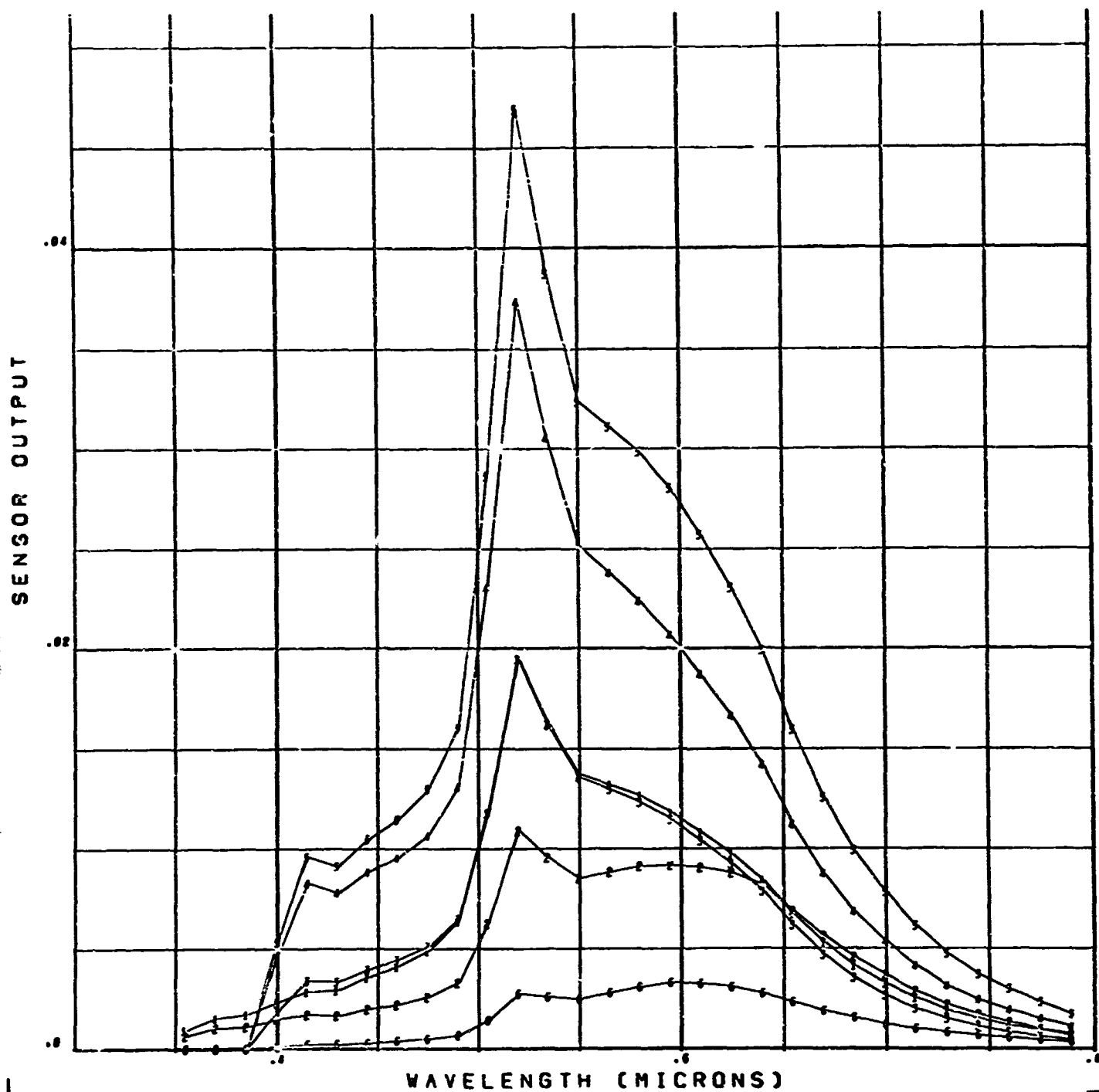
FIGURE 3-16

CdS-5 SENSOR OUTPUT VS. WAVELENGTH
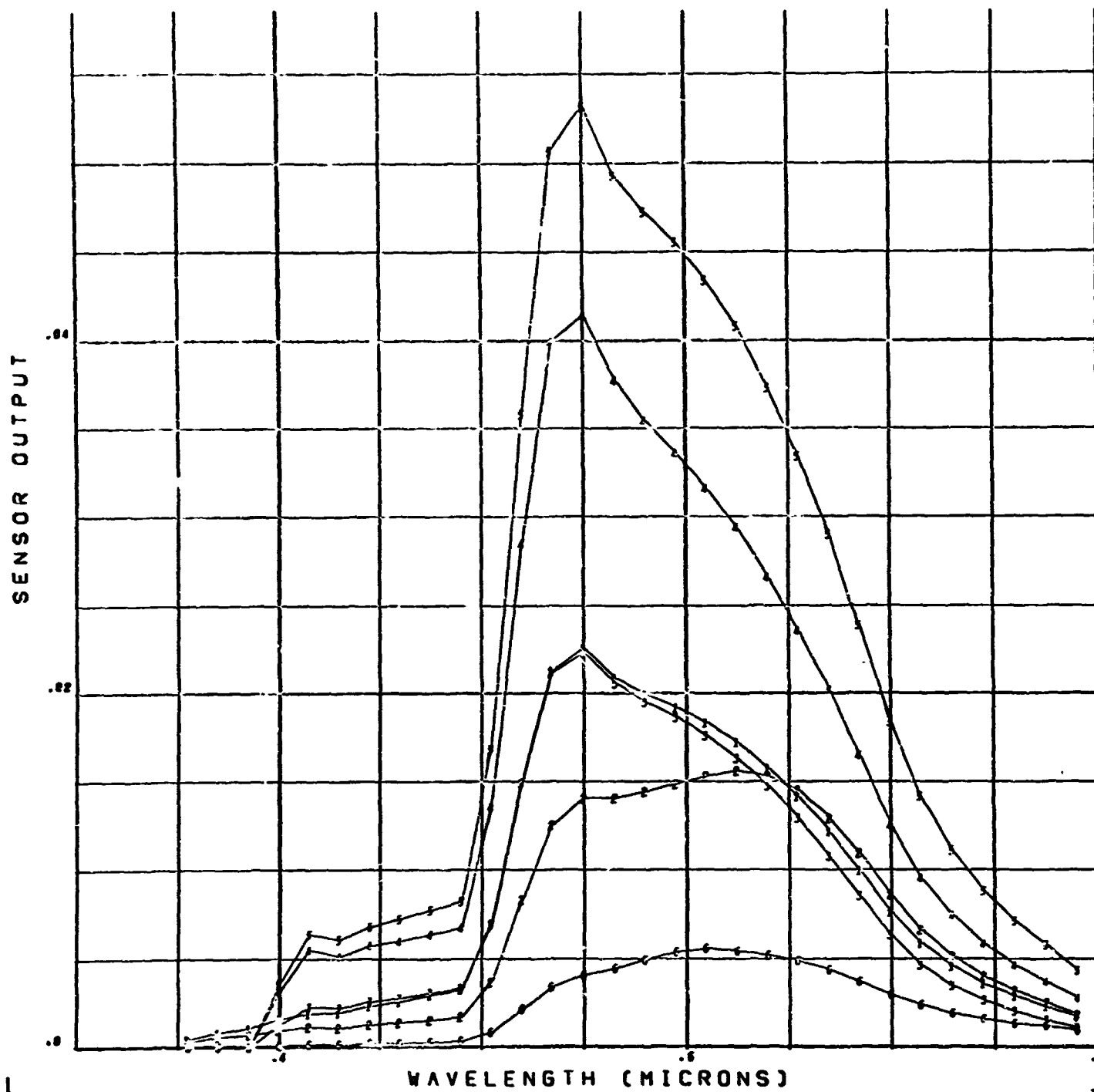
FIGURE 3-17

CdS-5H   SENSOR OUTPUT VS. WAVELENGTH   06/16/69

WAVELENGTH (MICRONS)
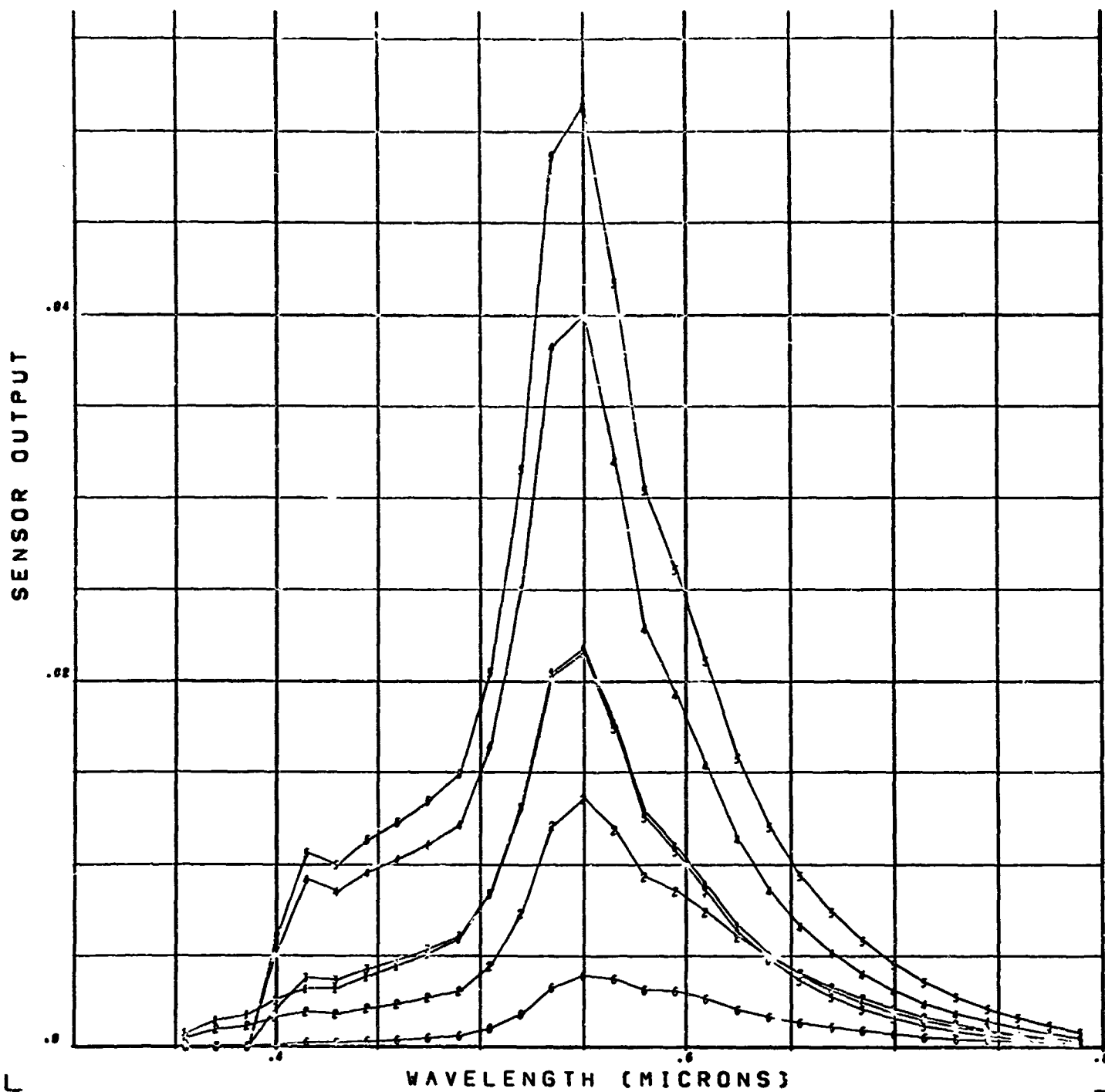
FIGURE 3-18

SILICON SENSOR OUTPUT VS. WAVELENGTH 06/16/69
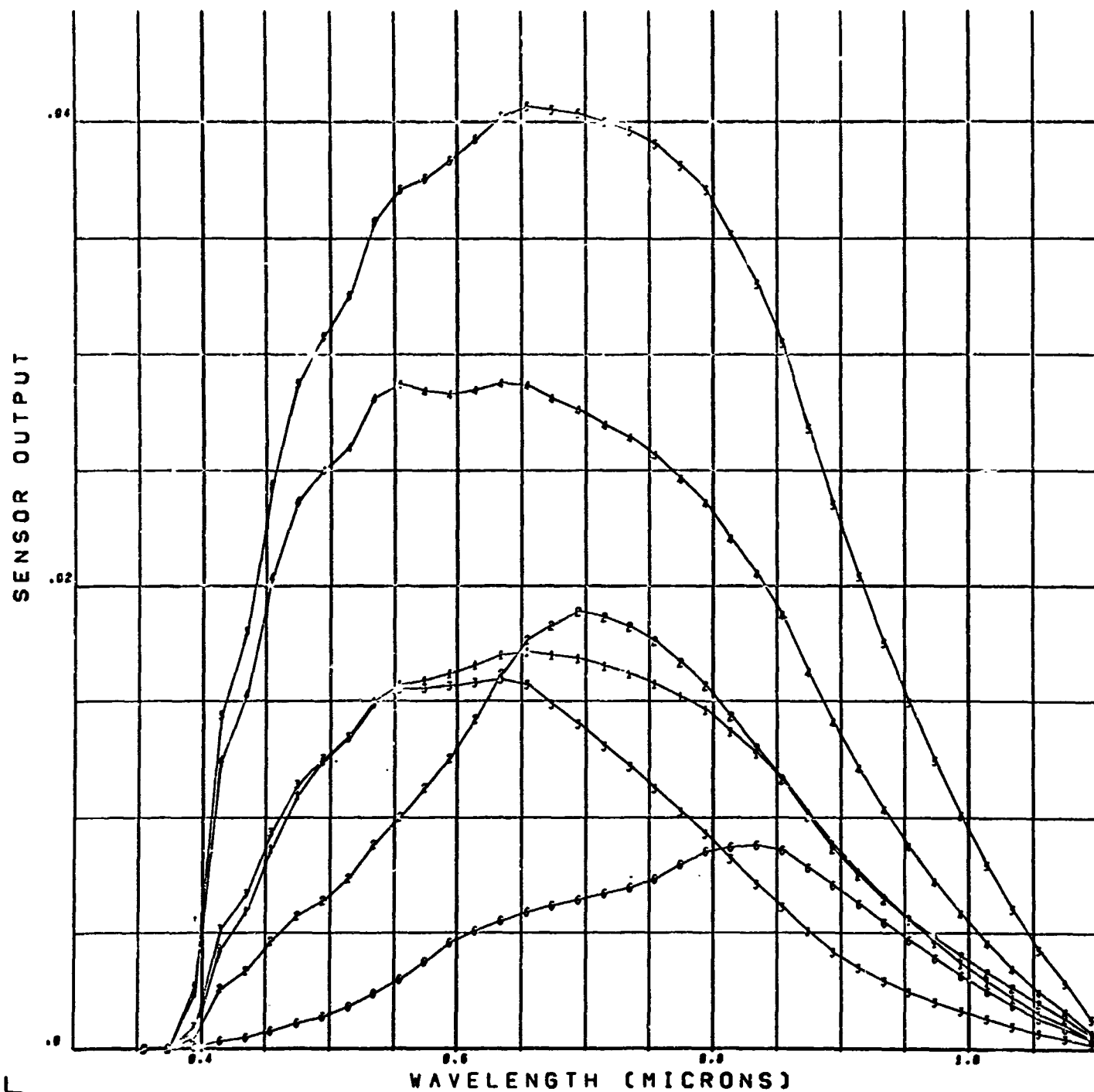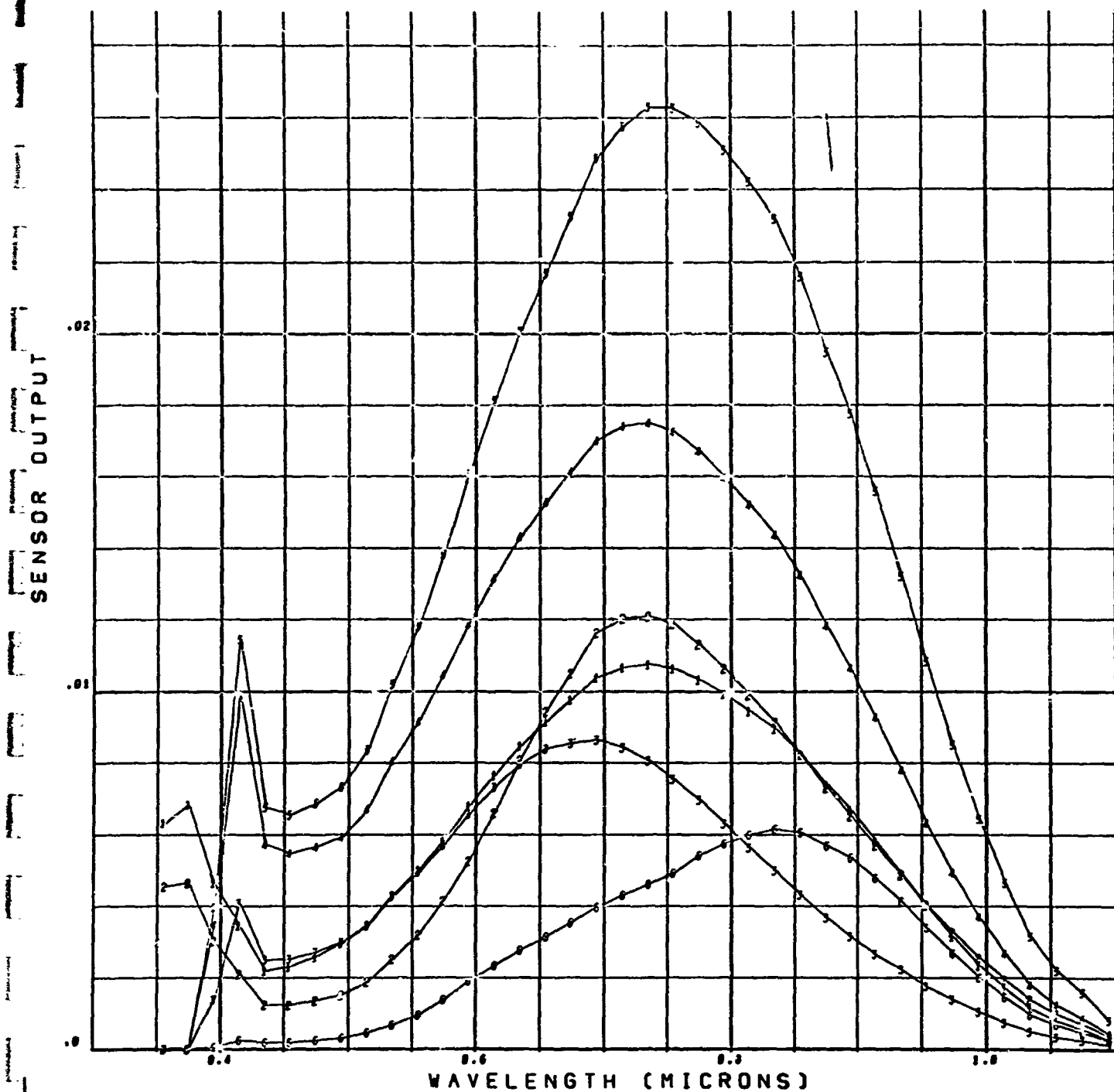
FIGURE 3-19

FIGURE 3-20

CdS-7   SENSOR OUTPUT VS. WAVELENGTH   06/16/69
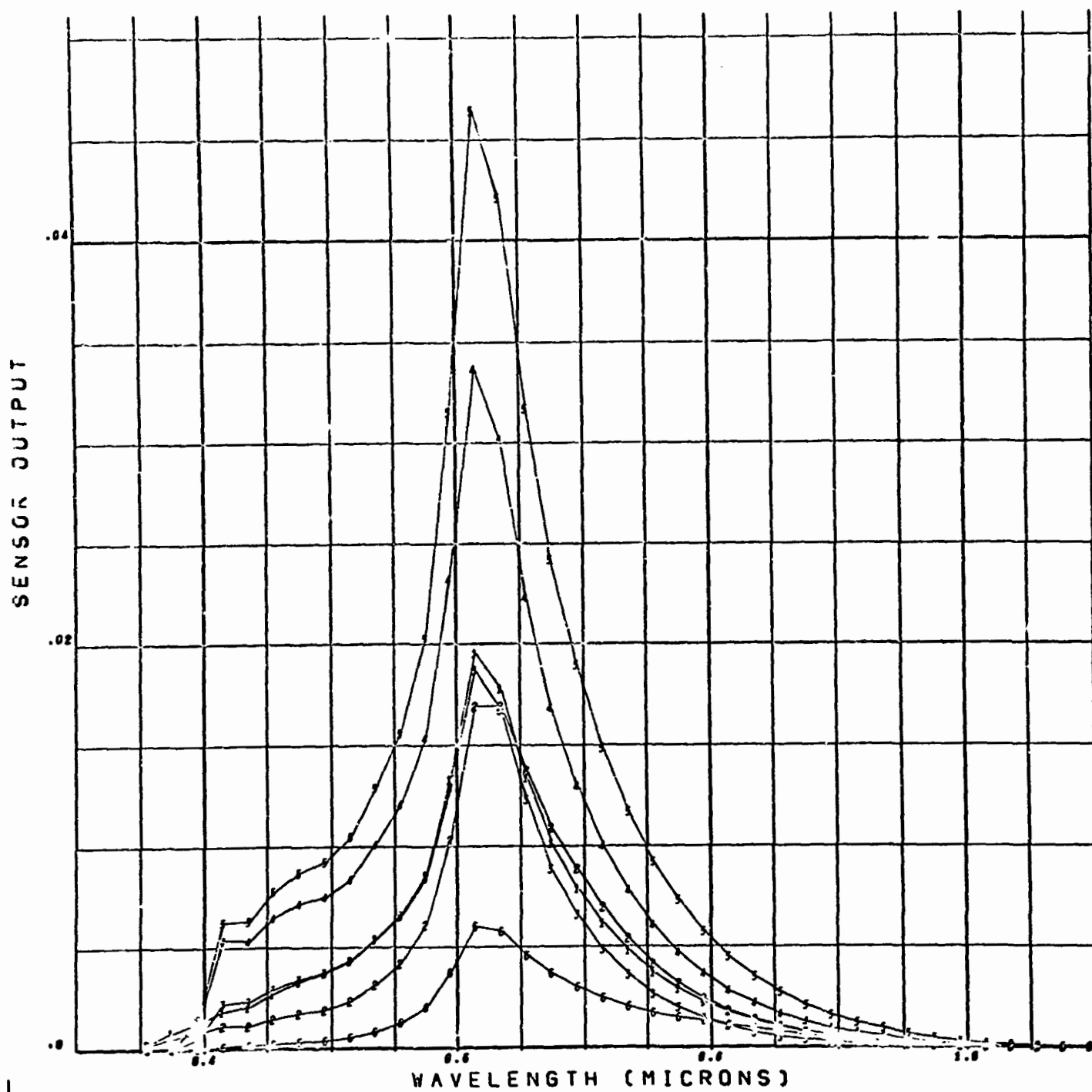
FIGURE 3-21

FIGURE 3-22

CdSe-4   SENSOR OUTPUT VS. WAVELENGTH
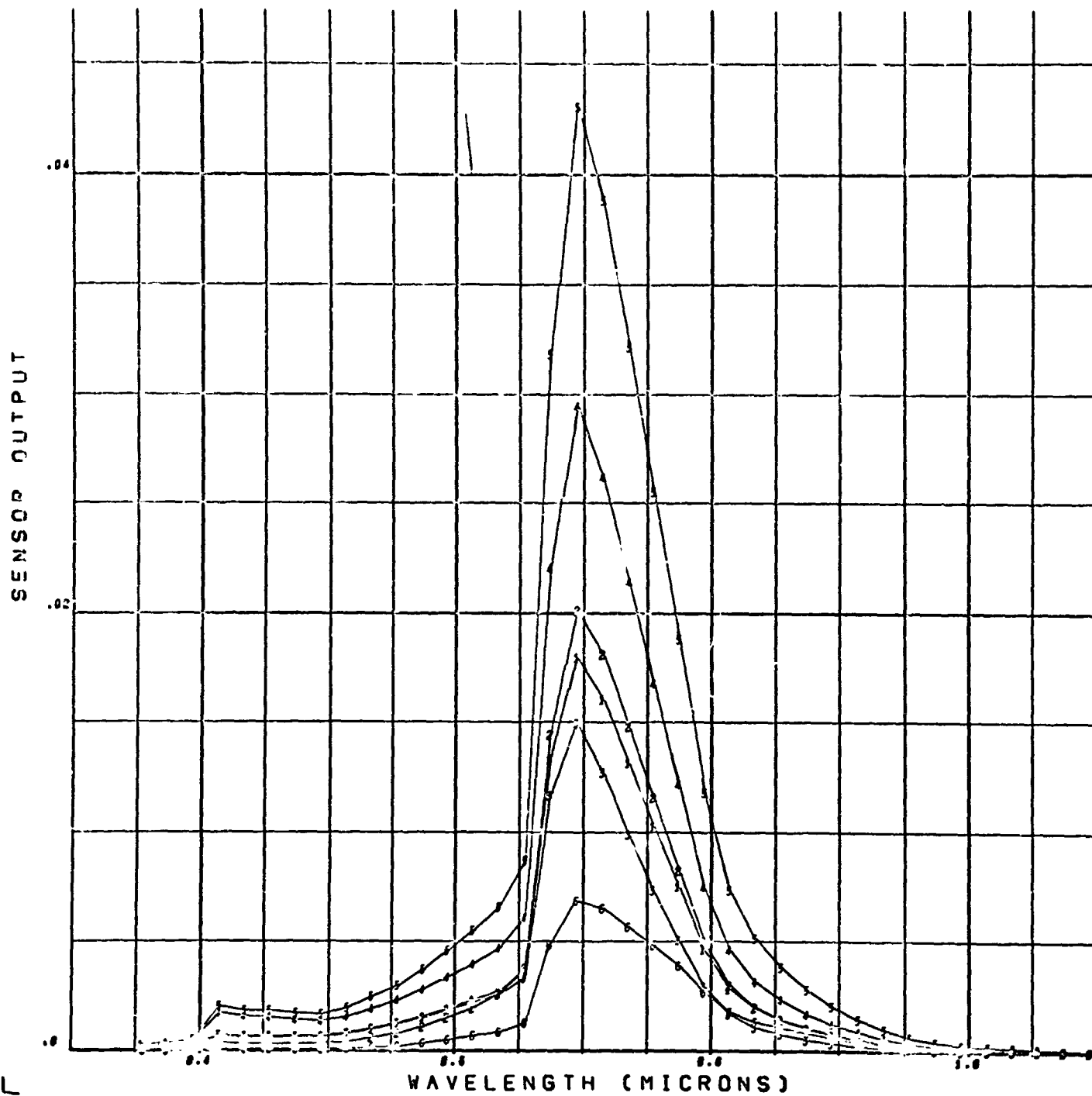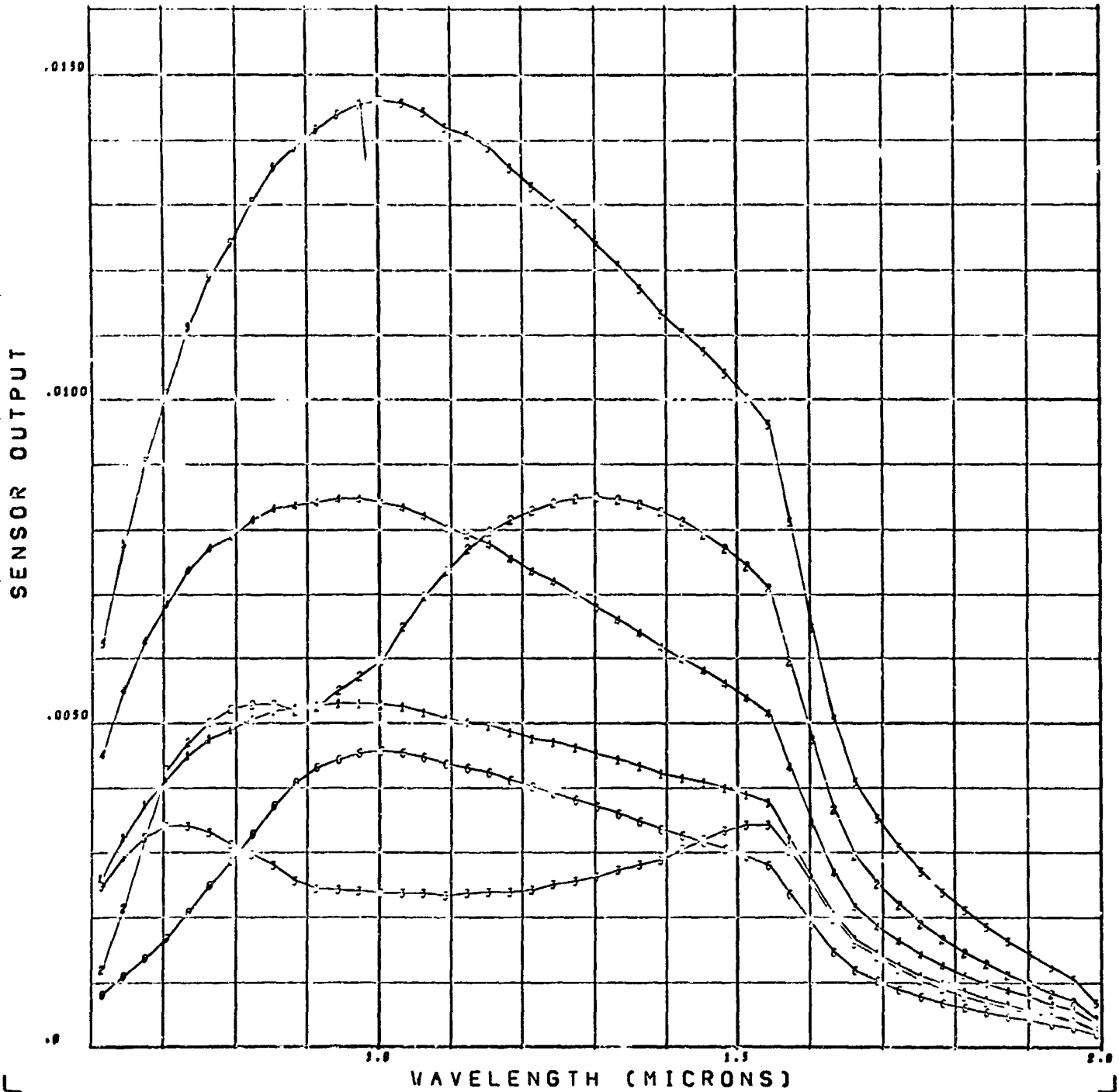
FIGURE 3-23

Ge 653
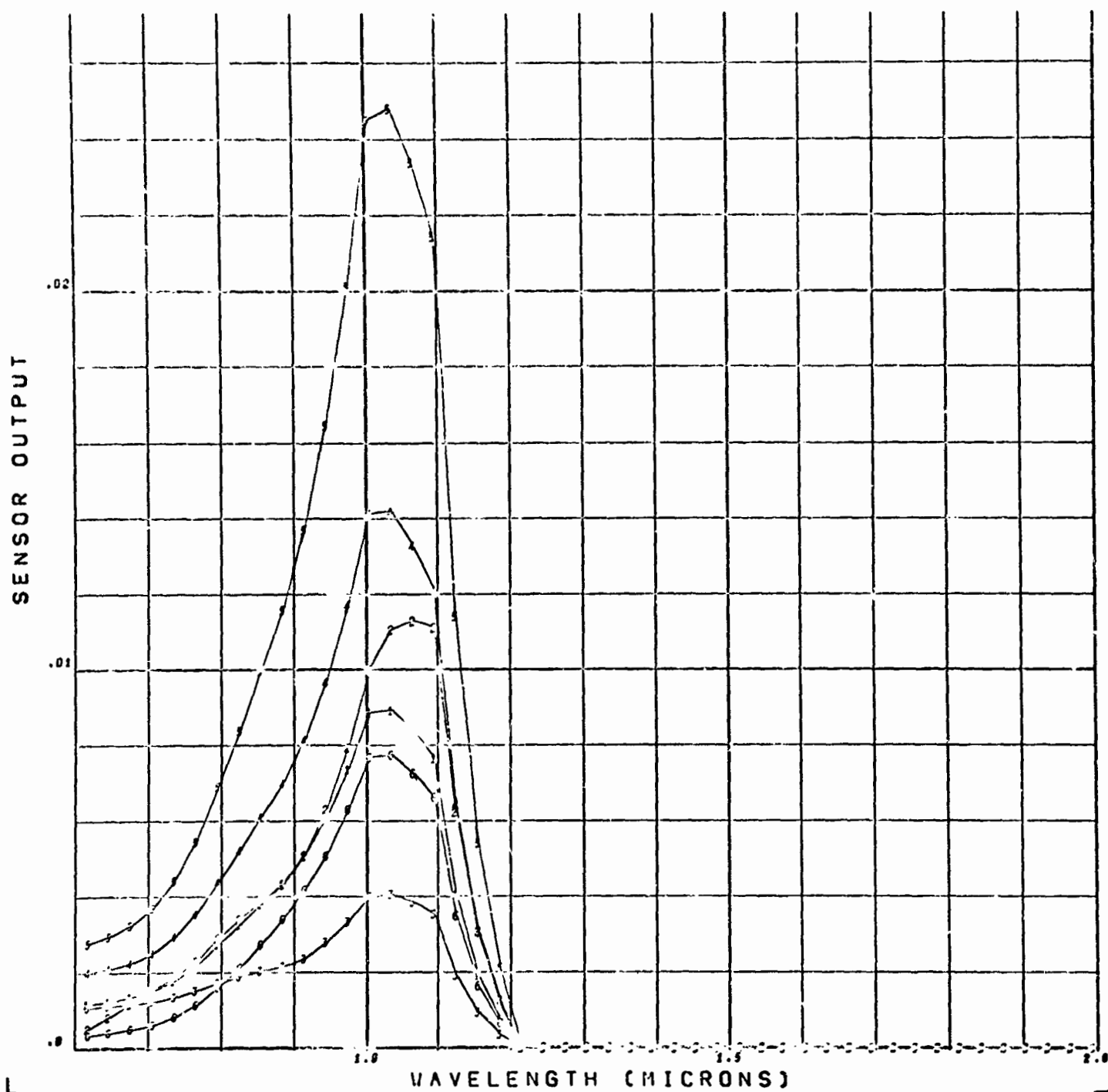
FIGURE 3-24

FIGURE 3-25

Ge 655 SENSOR OUTPUT VS. WAVELENGTH
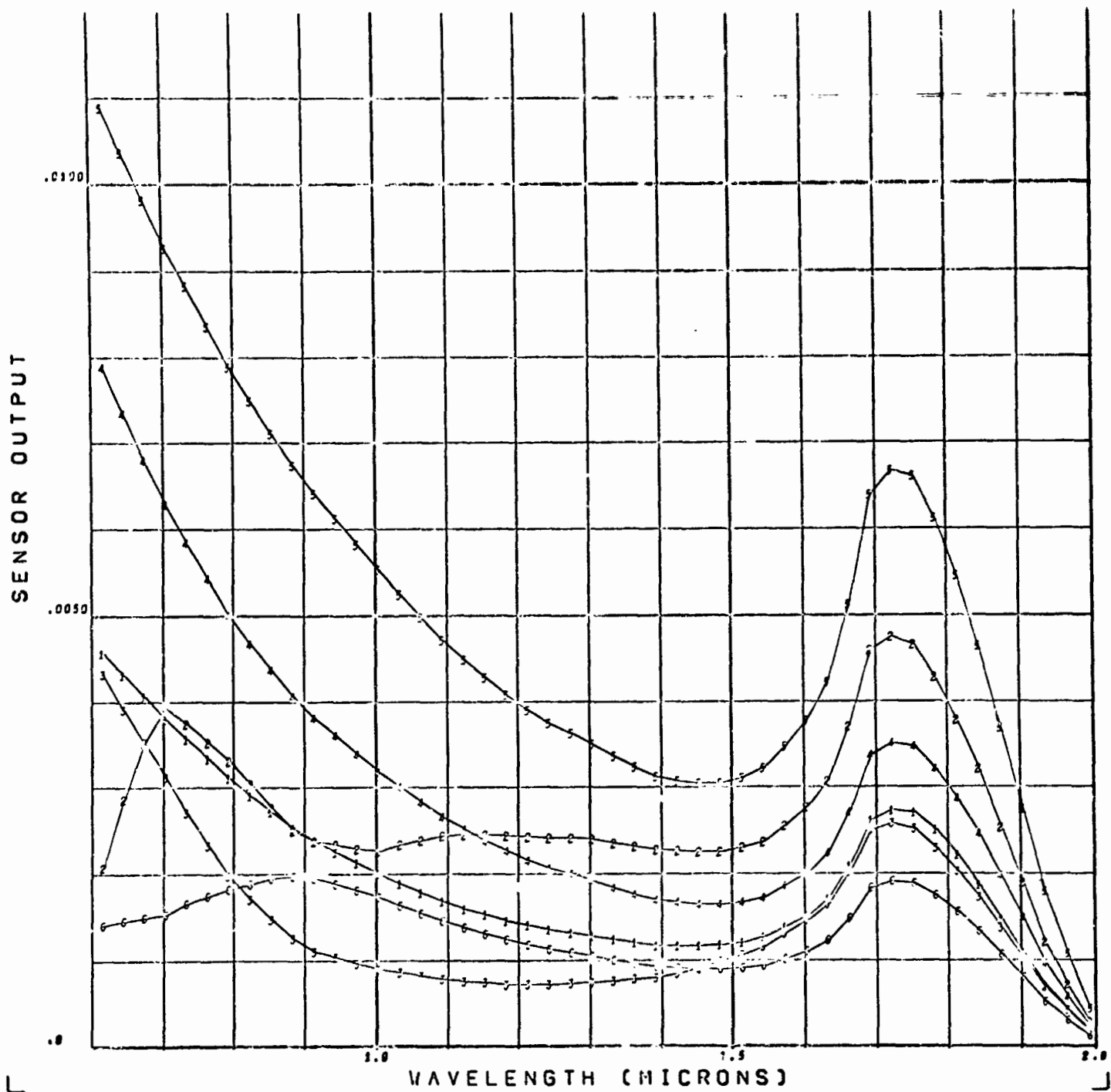
FIGURE 3-26
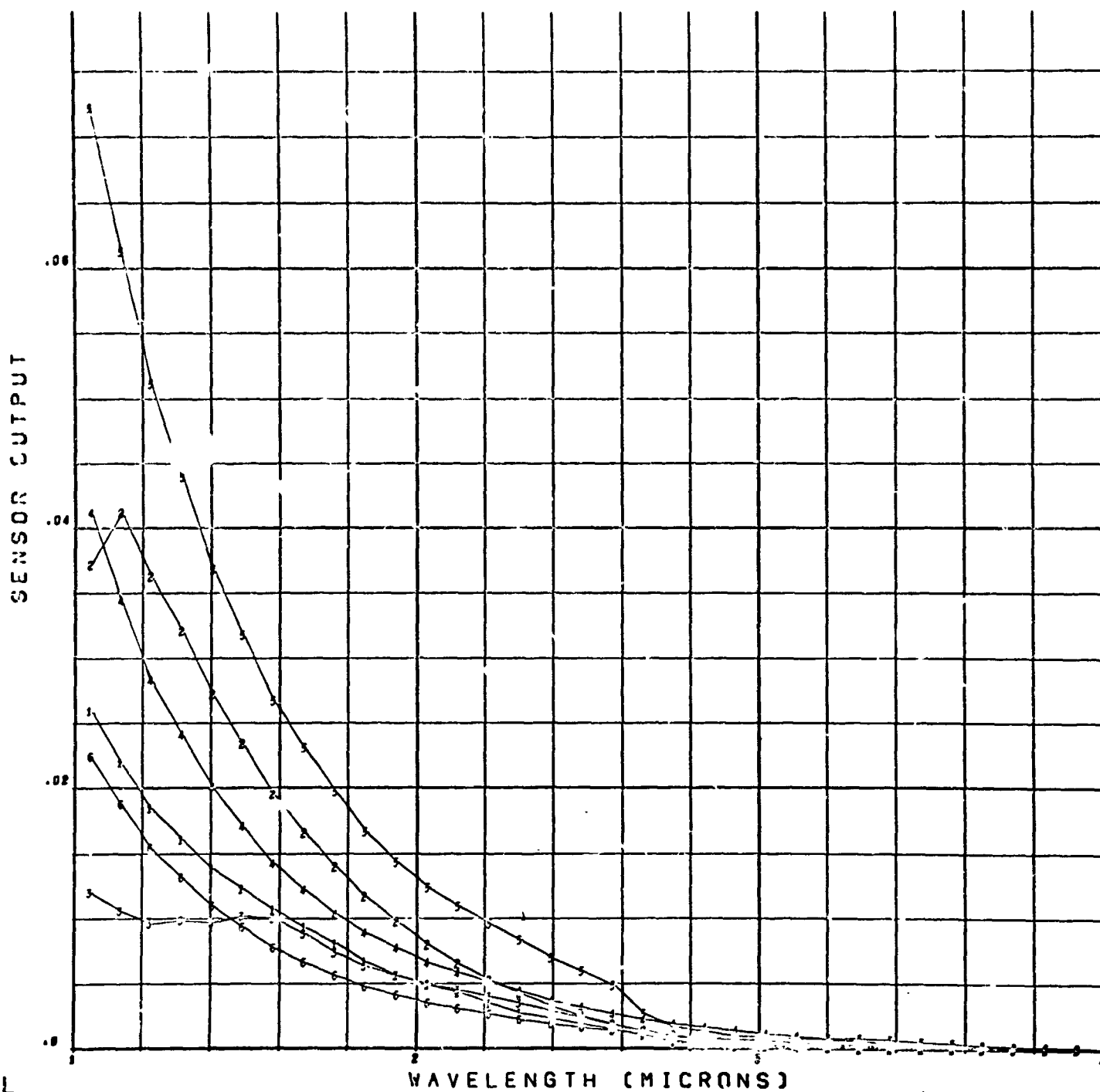
WAVELENGTH (MICRONS)
FIGURE 3-27

FIGURE 3-28

FIGURE 3-29

SENSOR OUTPUT

WAVELENGTH (MICRONS)

WAVELENGTH (MICRONS)

FIGURE 3-30

FIGURE 3-31

'SCENE' MODULATION AS A FUNCTION OF DETECTOR
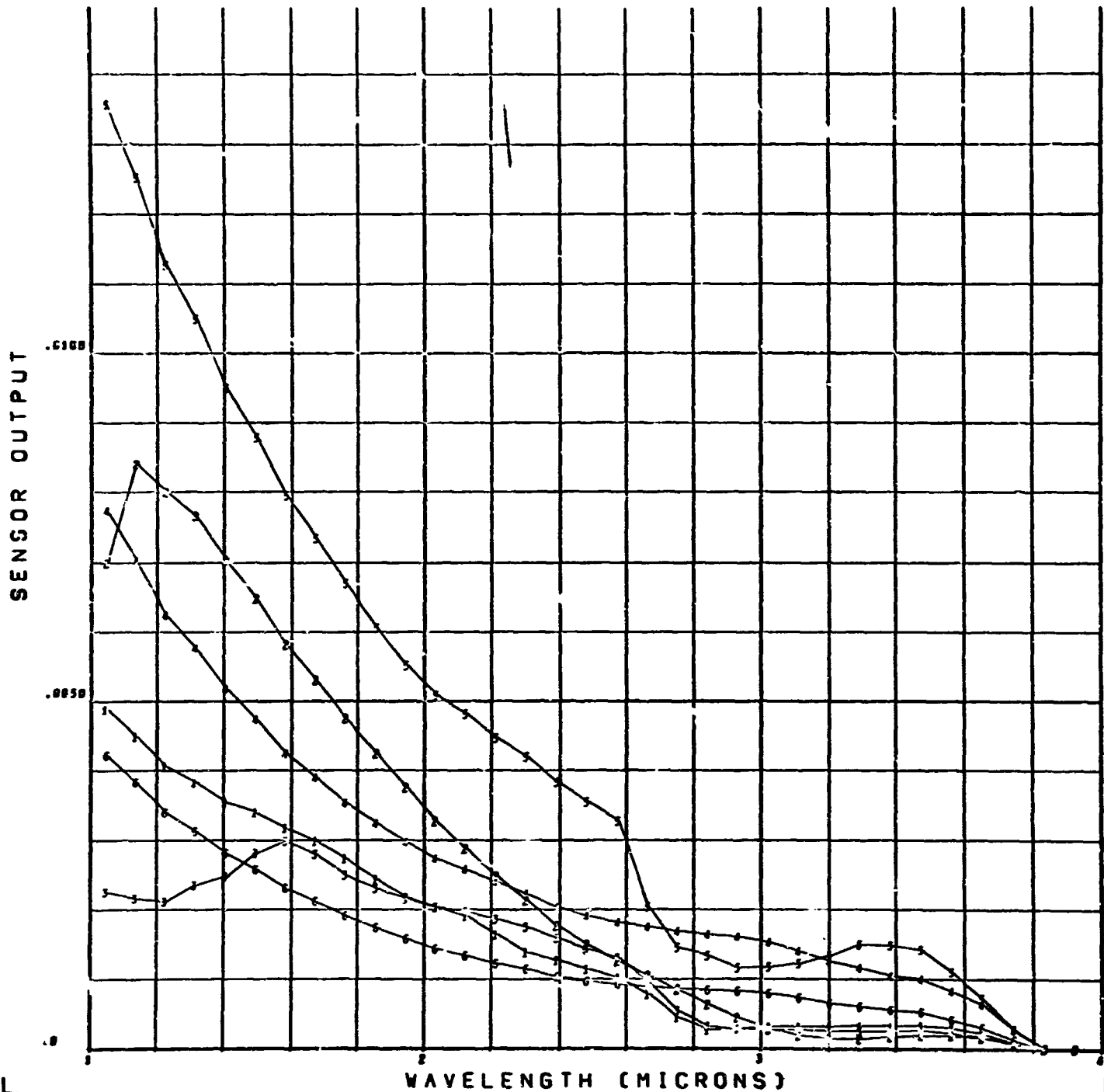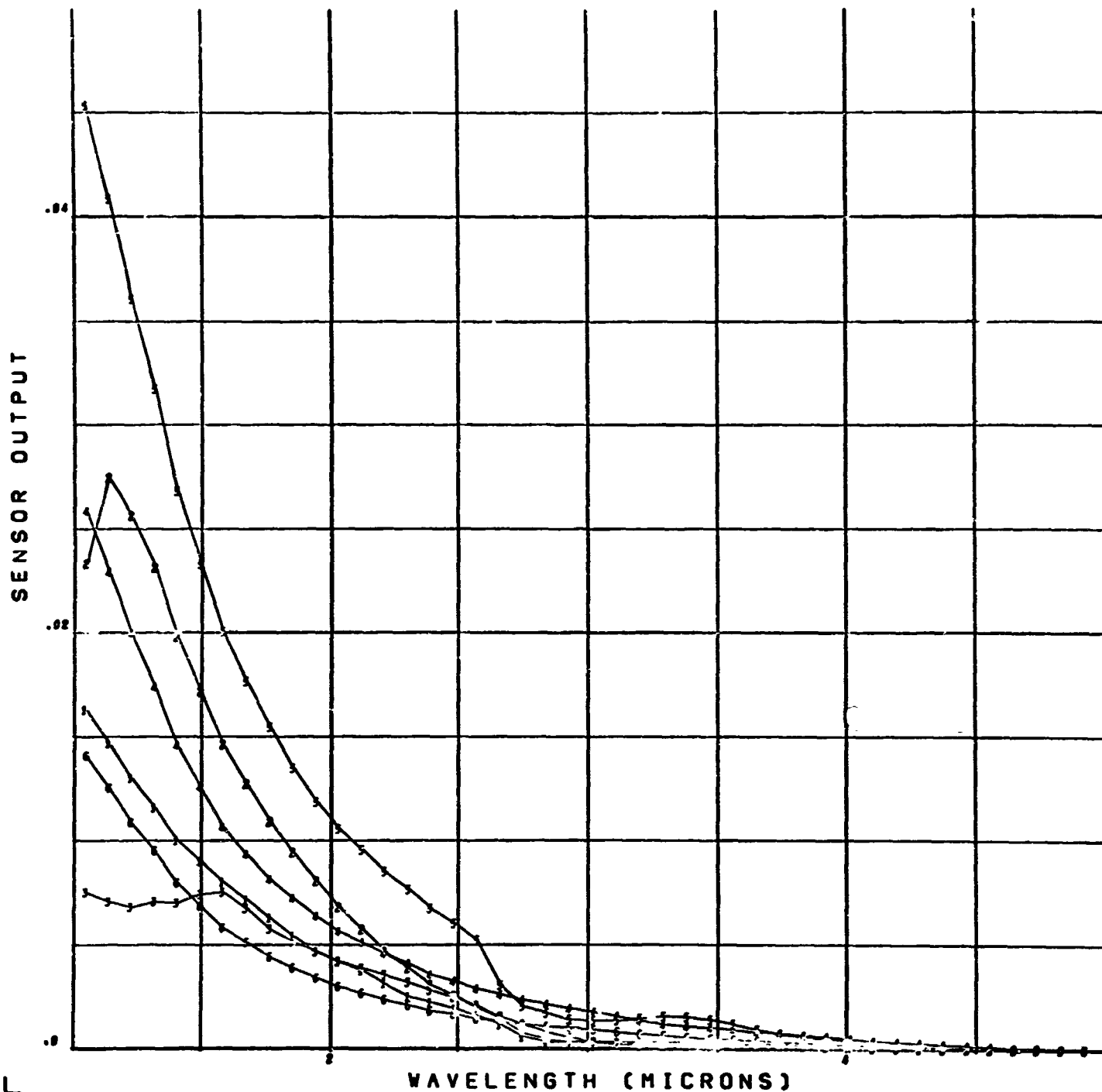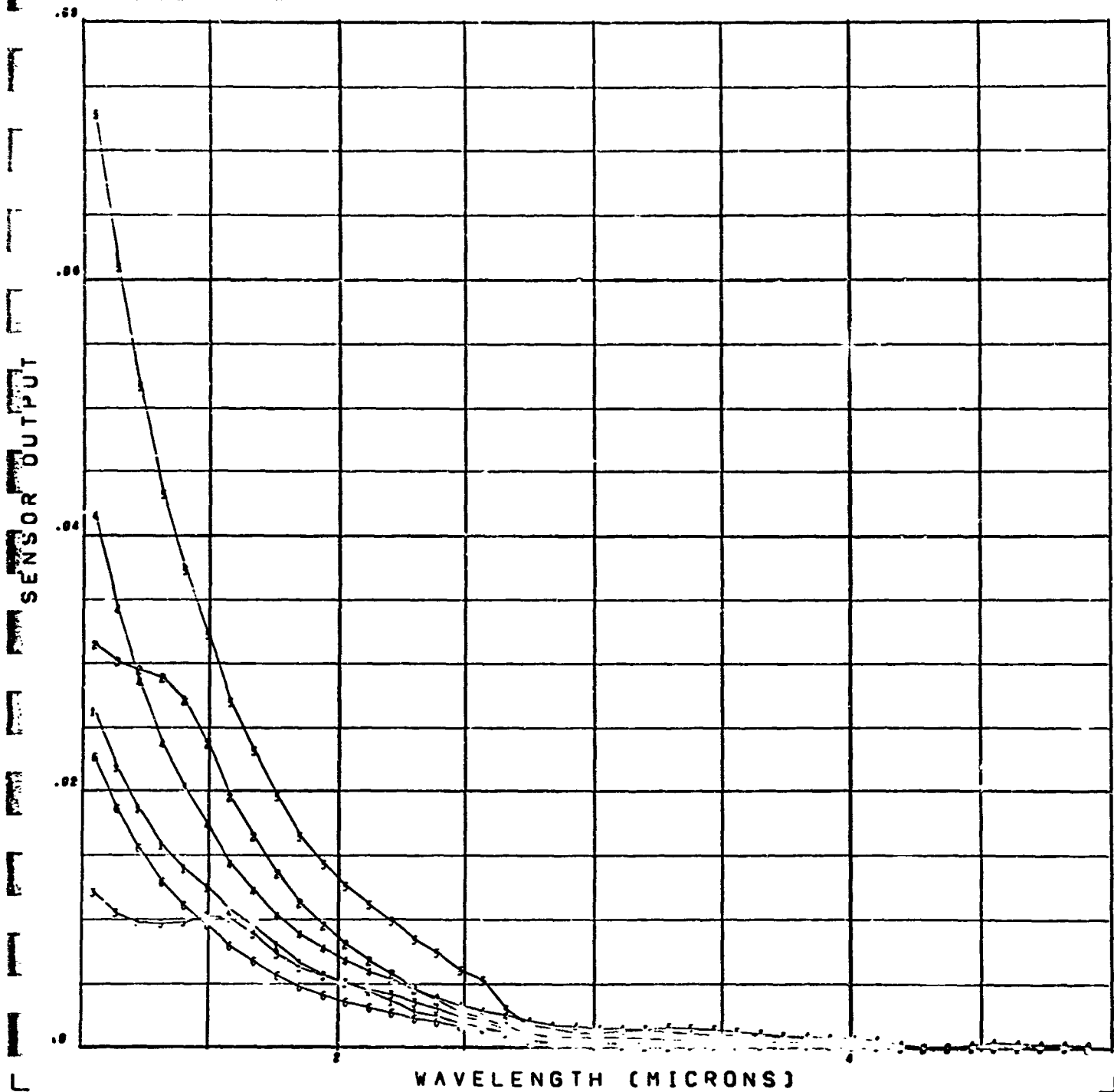
FIGURE 3-32
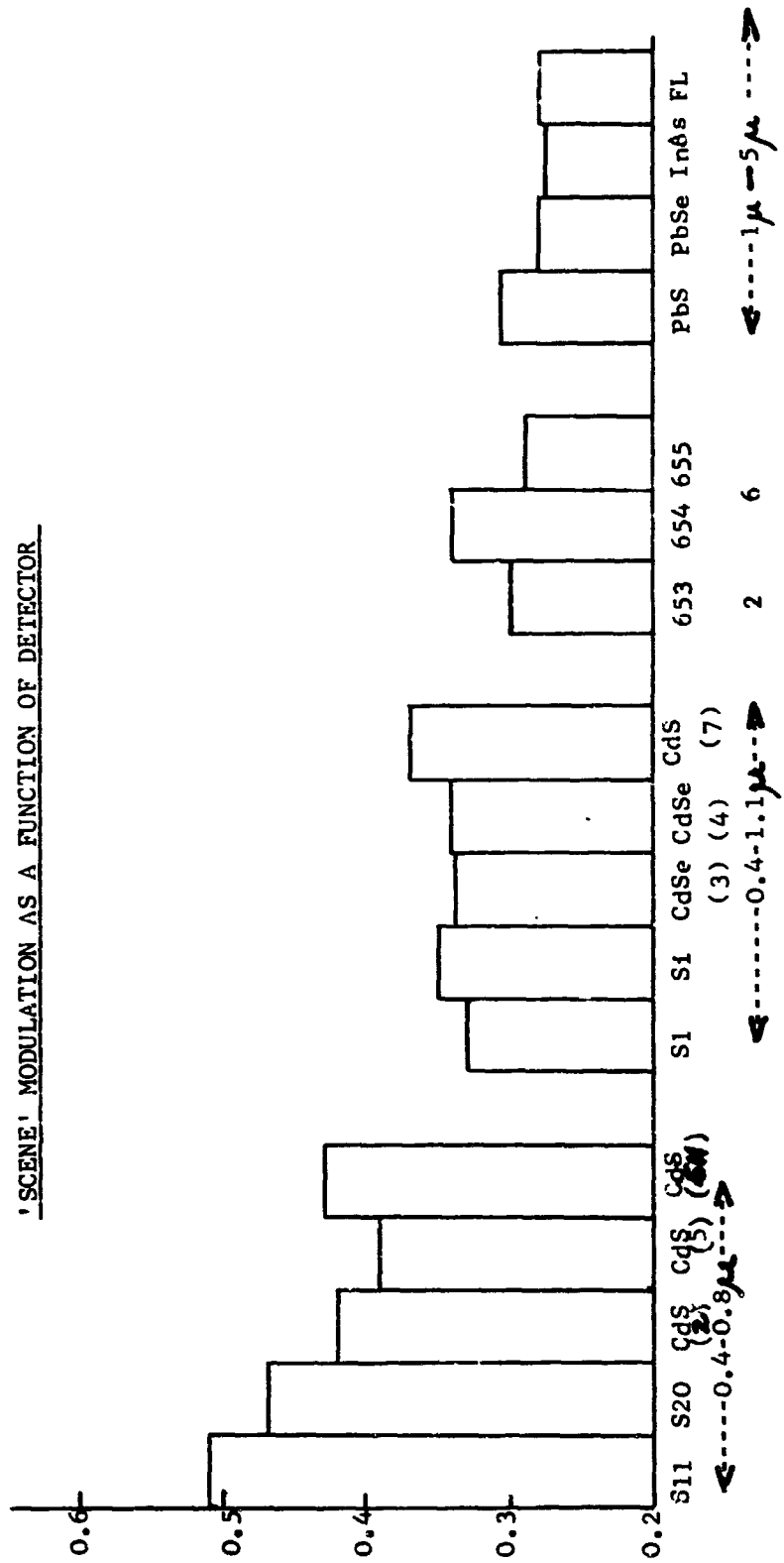
FIGURE 3-33

(0.6-2.0 μ) AVERAGE MODULATION VS. WAVELENGTH
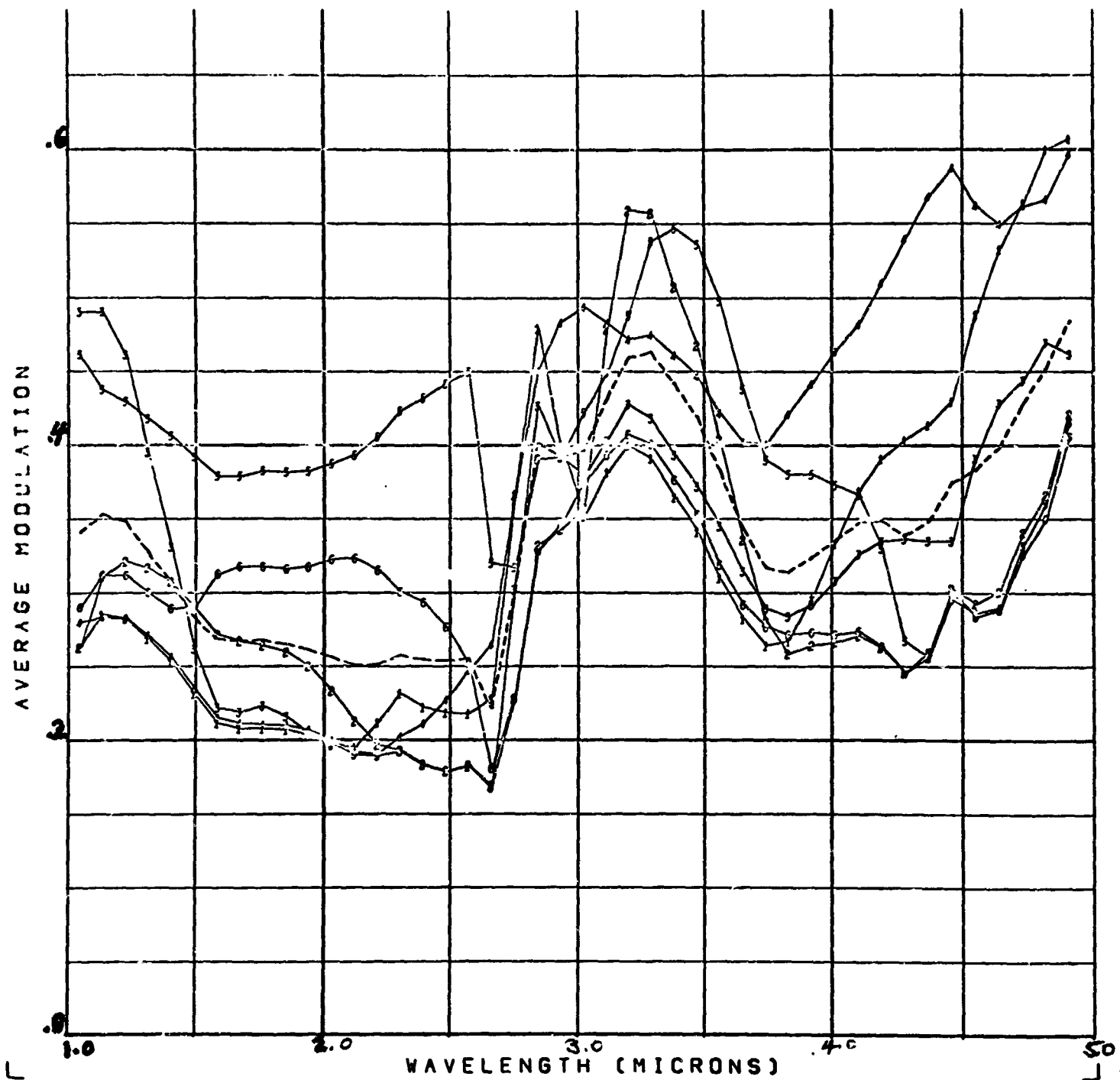
FIGURE 3-34

FIGURE 3-35

SECTION 4

PHOTOGRAPHY AND DENSITOMETRIC ANALYSIS OF A TEST SCENE

4.1   DESCRIPTION OF SPECIMEN AND TEST SCENE

Two sediments, four rocks, and one plant were selected for the photography. The photo-
graphic scene consisted of a shallow wood tray, about 30 x 40 inches, on which were arranged
five specimens against two different granular background materials (Figure 4-1). The
materials are described elsewhere in this section. The Silica Sand and Limonite were spread
on the tray so that each covered one-half of the surface, but with a six-inch interlocking
pattern along the centerline of the tray. This permitted the five specimens to be arranged so
that each of them overlapped both background materials. The advantage of this disposition
is that a single densitometer scan down the centerline of the negative image will provide
direct contrast between the specimens and each of the background materials, the latter
serving as a form of rough calibration. Control of exposures was provided by use of a
Kodak Gray Scale and a Kodak Color Control Patch, laid on the sand and parallel to the long
axis of the tray.   Some effort was made to eliminate harsh shadows around the specimens
by banking the sand to smooth the contacts.

4.1.1   SAND

A commercial building sand was obtained from coastal plain deposits at Millville, in Southern
New Jersey. The sand is very light buff, almost white, poorly sorted, with about 25 percent
passing a standard 40 mesh sieve. Since the relatively small amount of dark minerals,
consisting of biotite, hornblende, magnetite, and others, passed the 40 mesh sieve, only the
lighter fraction retained on the sieve was used. This consisted primarily of quartz grains,
many of them frosted, with small amounts of feldspar.

4.1.2   LIMONITE

Limonite was purchased from a pigment firm in Pittsburg, Pennsylvania, and is reported to
come from deposits in that vicinity. It is commercially pulverized and screened to a particle
size of less than 5 microns. As used, however, the limonite had absorbed enough moisture
to produce small balls. The limonite is a brilliant brownish yellow. It is assumed that the

bulk of the limonite is hydrated iron oxide, although it may include some goethite and hematite.

4.1.3   ROCKS

4.1.3.1   Basalt

The basalt used in this study was fine-grained blue-gray Triassic lava flow from a quarry at Chimney Rock, near New Brunswick, New Jersey. This rock is over 170 million years old, and is deeply weathered along the many fractures that cut it, but fresh surfaces are readily obtained from samples taken at the present quarry floor. No significant recrystallization of this rock has taken place, and its exact minerology will not be known until the petrographic slides are studied. It appears under examination with a hand lens that some olivine is present.

4.1.3.2   Rhyolite

This felsitic rock from Colorado was obtained from Ward's Natural Science Establishment. Unfortunately, only small pieces were available, so that several had to be used side by side in the photographic tray. The rock is dusty pink to coral, almost entirely felsitic groundmass, with a few small phenocrysts of quartz and orthoclase.

4.1.3.3   Granite

A coarse reddish granite from Barre, Vermont, was obtained from a monument firm in Philadelphia. It is almost a typical example of this rock, with fresh orthoclase,plagioclase, quartz, and biotite as the principal constituents.

4.1.3.4   Dunite

This rock from North Carolina was obtained from Ward's Natural Science Establishment. It was, unfortunately, also available only in small pieces. It is granular, like sugar, and breaks readily into its constituent olivine grains. The color ranges from light to medium green, but with a characteristic olive cast. Accessory minerals, probably magnetite or chromite, or both, occur in minute grains disseminated throughout the rock.

4-2

4.1.4 LICHEN

There are numerous species of lichen. Some of this material collected in Nova Scotia in 1968 dried out before it could be used. Another variety was substituted from Houston, Texas, this was the so-called "Spanish Moss" which grows abundantly as a parasite on trees in the Southern United States.

4.2 DESCRIPTION OF PHOTOGRAPHIC EQUIPMENT

The equipment used for photographing the samples consisted of three types of films, two cameras, and five filters. Exposures were made at several apertures and times with each camera-filter-film combination in order to obtain as wide a latitude as possible in contrast. A Series V Kodak Gray Scale and a standard Kodak Color Control Patches card were included in each scene.

4.2.1 FILMS

Table 4-1 shows the pertinent characteristics of films used. Plus X has good resolution at a fairly high speed, is readily available, and can be developed to produce various gammas. Ektachrome X is a fast film with good color reproduction and resolution. The emulsion on spectroscopic plate type I-Z has the greatest extended spectral response in the infrared is shown in Figures 3-5 and 3-6 and compared to Plus X. This film must be ordered specially because it is not kept in stock.

4.2.2 CAMERAS

A Crown Graphic camera manufactured by Graflex was used for the black and white and IR plates. It has an extendable bellows and a fixed ground glass which makes it excellent for focussing at close range. The Symmar lens by Schneider-Kreuzach is f/5.6 at 100 mm focal length. Exposures were taken usually at f/8 which is that giving maximum resolving power.

A Honeywell Pentax 35 mm single lens reflex camera was used for the color shots. The Super-Takumar lens by Asahi Optical Co. is f/1.8 at 55 mm focal length. Exposures were taken usually at small apertures (f/11 to f/22) in order to limit the exposure.

TABLE 4-1. FILM CHARACTERISTICS

Class	Type	Speed (ASA)	Developer	Size
Black & White	Plus X 120	125	Versamat (HC 110)	60 x 70 mm
Color	Ektachrome X	64	Process E-3	35 mm
Infrared	Spectroscopic Plate 1-z	–	D-19 4 min	4" x 5"

TABLE 4-2. FILTERS

Filter	λ eff	Designation
U	3600 A	9862 Corning
B	4200	5030 Corning GG13, 2 mm Schott
V	5400	3384 Corning
R	7000	BG-21 2 mm Schott BG-17 1 mm Schott
I	8600	88A gelatin Wratten

4.2.3 FILTERS

Table 4-2 shows the filters used and Figure 4-3 their spectral response. The filter nomen-
clature is that of the UBV System as known by astronomers. Their characteristics are
given by H. L. Johnson in "Basic Astronomical Data" edited by K. A. Strand.

4.2.4 EXPERIMENTAL ARRANGEMENT

The equipment was oriented to produce photographs at three nominal orientations. The
actual angles are given in Table 4-3. The sample tray was tilted towards the sun as far as
possible without exceeding the angle of repose of the rocks and sand. The camera was held
with a crane 75" above the samples with a minimum of shadow interference.

TABLE 4-3. POSITIONS

	Angle of Incidence of Solar Radiation	Camera Angle (to Sample)	Camera Angle to Sun
Nominal	0	0	0
Actual	12	6	6
Nominal	45	45	0
Actual	48	-2	6
Nominal	45	45	90
Actual	48	45	93

4.2.5 DENSITOMETRY

Transmission of the film and plates was measured on a Joyce Loebl Mark III B double beam
recording microdensitometer upgraded with a high intensity light source. The slit size was
adjusted to produce a smooth record from the individual samples which means that inhomo-
geneities were not resolved. A calibration was made with the gray scale to adjust all
records to a common base.

By dividing the density reading of the background by that of the various samples relative contrasts were obtained. These ratios were compared with the computed values.

4.3 DISCUSSION OF THE DENSITOMETRIC TEST

4.3.1 DENSITOMETER RESULTS

A Joyce Loebl dual beam densitometer was used to measure the relative densities of the test scene recorded on Plus X and I - Z plate respectively. A section of the negative containing the constituents was scanned; the densitometer outputs measured during these scans are shown in Figures 4-4 to 4-8. The filters that were used in the experiment are shown in Figure 4-3. Across each scan can be seen a reference signal obtained from a step-wedge calibrator. The latter was used to devise the equivalent linear outputs for each of the constituents. These outputs were then used to form the scene and discrimination modulation functions described in Section 3. The modulation functions obtained for both the Plus X and Z film are shown in Tables 4-4 and 4-5.

Confirmation through Figures 4-4 to 4-6 of the modulation values is difficult with the Plus X data owing to the changing density scale but the task is much easier with the I - Z results; the increased modulation resulting from the use of the 'I' as opposed to 'R' filter is clearly demonstrated in the outputs in Figures 4-7 and 4-8. The corresponding moduation values that are calculated are the averages of all possible arrangements of the scene and are better guides to the effectiveness of the filter than the figures desired for the particular constituent arrangement in the test scene.

4.3.2 COMPARISON OF COMPUTER AND EXPERIMENTAL RESULTS

The film responses can be used to calculate the relative outputs for the response - filter combinations. However such a comparison was found to be difficult because inspection of the colour photographs and the reflectivities used in the computer program (Figure 3-12) shows that the reflectivities used in the program differ somewhat from those used in the experiment.

4-6

TABLE 4-4. PLUS X FILM MODULATIONS

Constituent

Filter	Scene	RHY	LIM	DUN	BAS	SIL	LIC
None	0.27	0.23	0.19	0.19	0.22	0.45	0.34
'B'	0.26	0.22	0.35	0.19	0.19	0.38	0.23
'V'	0.29	0.20	0.25	0.20	0.28	0.43	0.35
'R'	0.30	0.20	0.20	0.21	0.25	0.53	0.39

TABLE 4-5. IZ FILM MODULATIONS

Constituent

Filter	Scene	RHY	LIM	DUN	BAS	SIL	LIC
'R'	0.16	0.11	0.12	0.11	0.14	0.35	0.17
I	0.24	0.18	0.24	0.28	0.23	0.35	0.18

Two examples demonstrate the point clearly: Figure 3-12 shows that lichen is essentially black in the visible and the reflectivity of basalt differing only 19% or so from silica. The gray scale in the photograph shows clearly that parts of the lichen have such a high reflectivity that the average reflectivity is considerably greater than the 2 - 4% used in the computer program. The reverse is true of the Basalt sample; this is a large specimen with a reflectivity of the order of 20% and has a definite greenish tinge that can be seen in the color print. For these reasons the comparison between computer output and the experiment were not made directly.

4.3.3 FILM EXPERIMENT - CONCLUSION

The results of that modulation analysis when applied to the film experiment verify semi-quantitatively the results obtained in the experiment. They show in addition the need for a more closely coupled computer - experiment comparison though the use of reflectivities in the computer program experimentally obtained from the constituents used in the film experiment.
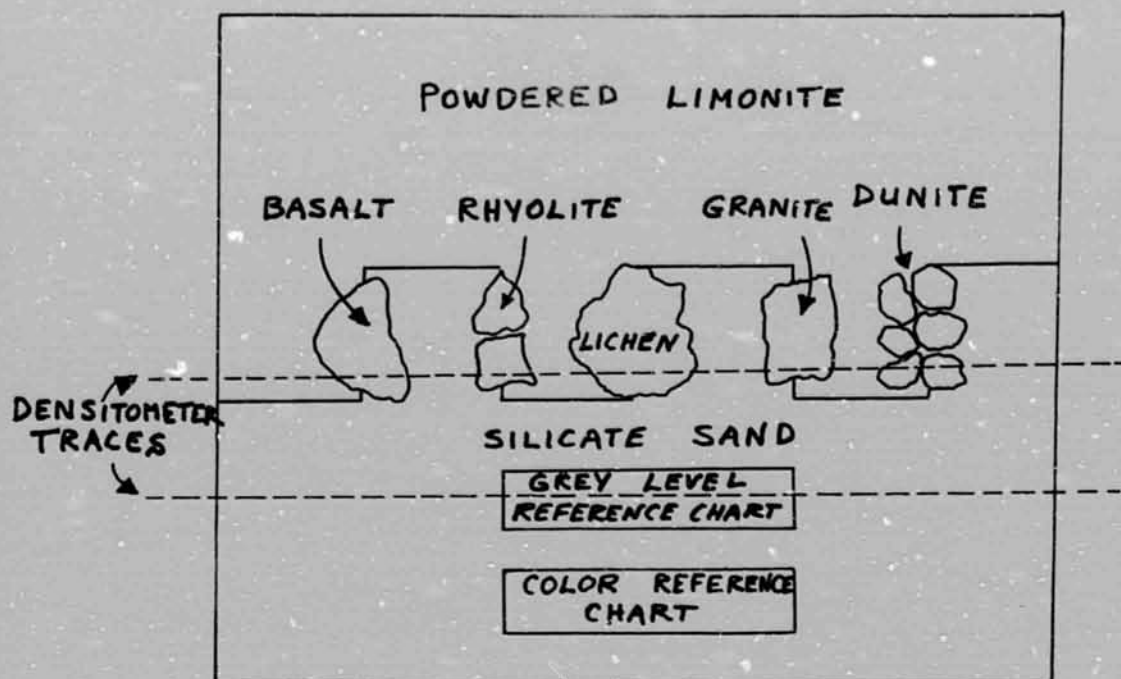
FIGURE 4-1   CONSTITUENTS IN TEST SCENE
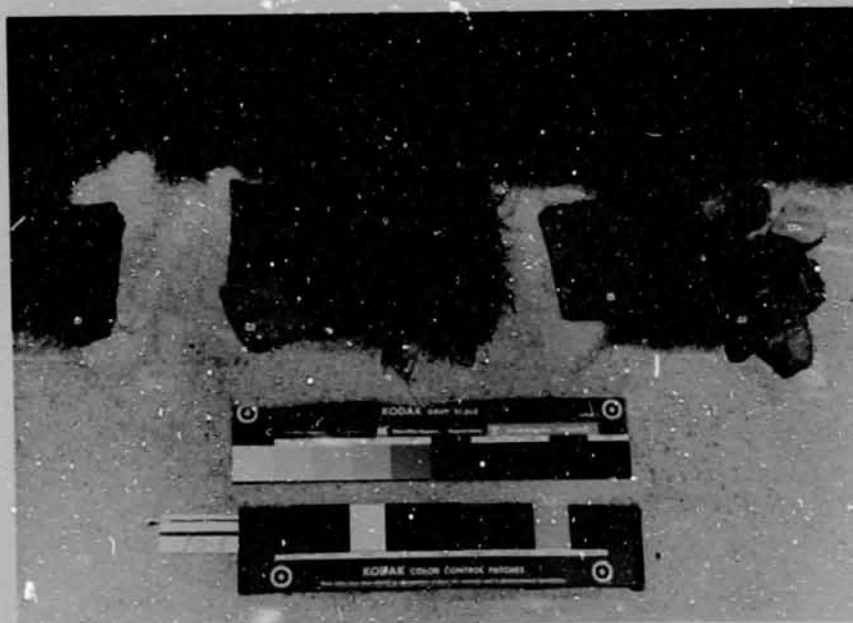
FIGURE 4-2   COLOR PHOTOGRAPH OF TEST SCENE

FIGURE 4-3.
FILTER
TRANSMISSION

FILTER TRANSMISSION IN % OF MAXIMUM

SEMI-LOGARITHMIC   359 61
2 CYCLES X 70 DIV b...

WAVELENGTH (MICRONS)

4-10
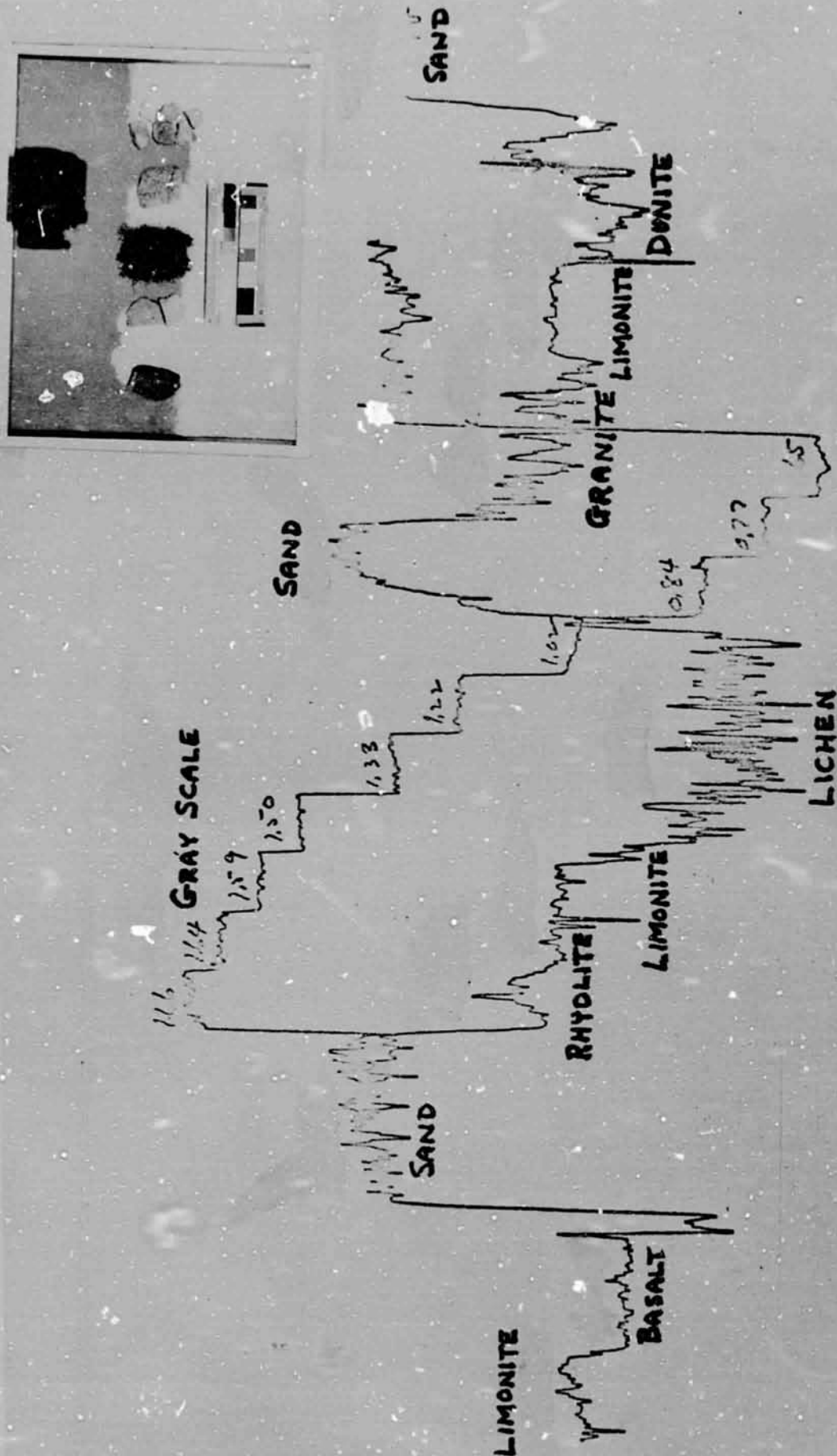
FIGURE 4-4   NO FILTER, PLUS X FILM DENSITOMETER TRACE
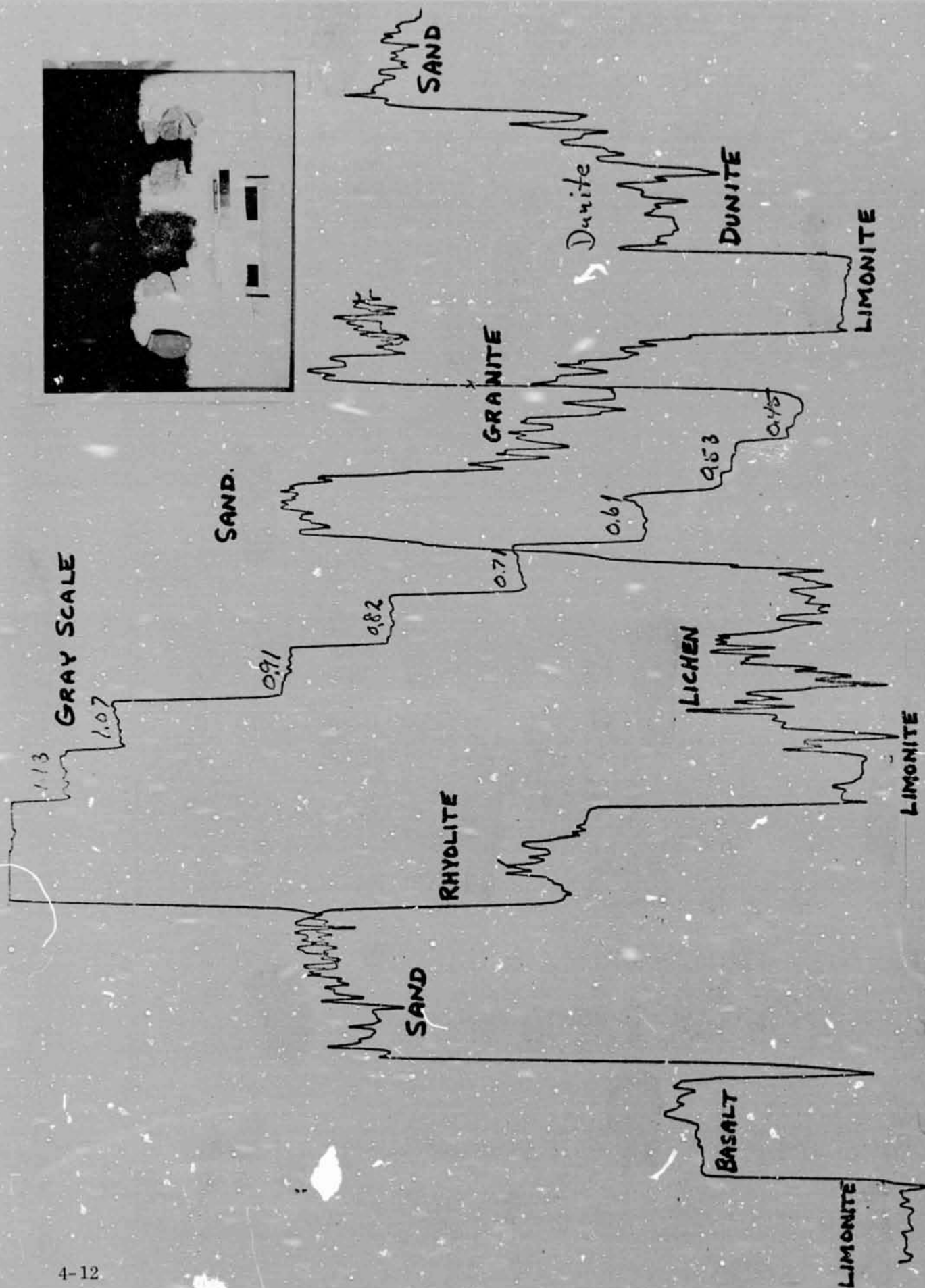
FIGURE 4-5 B FILTER, PLUS X FILM DENSITOMETER TRACE

4-12
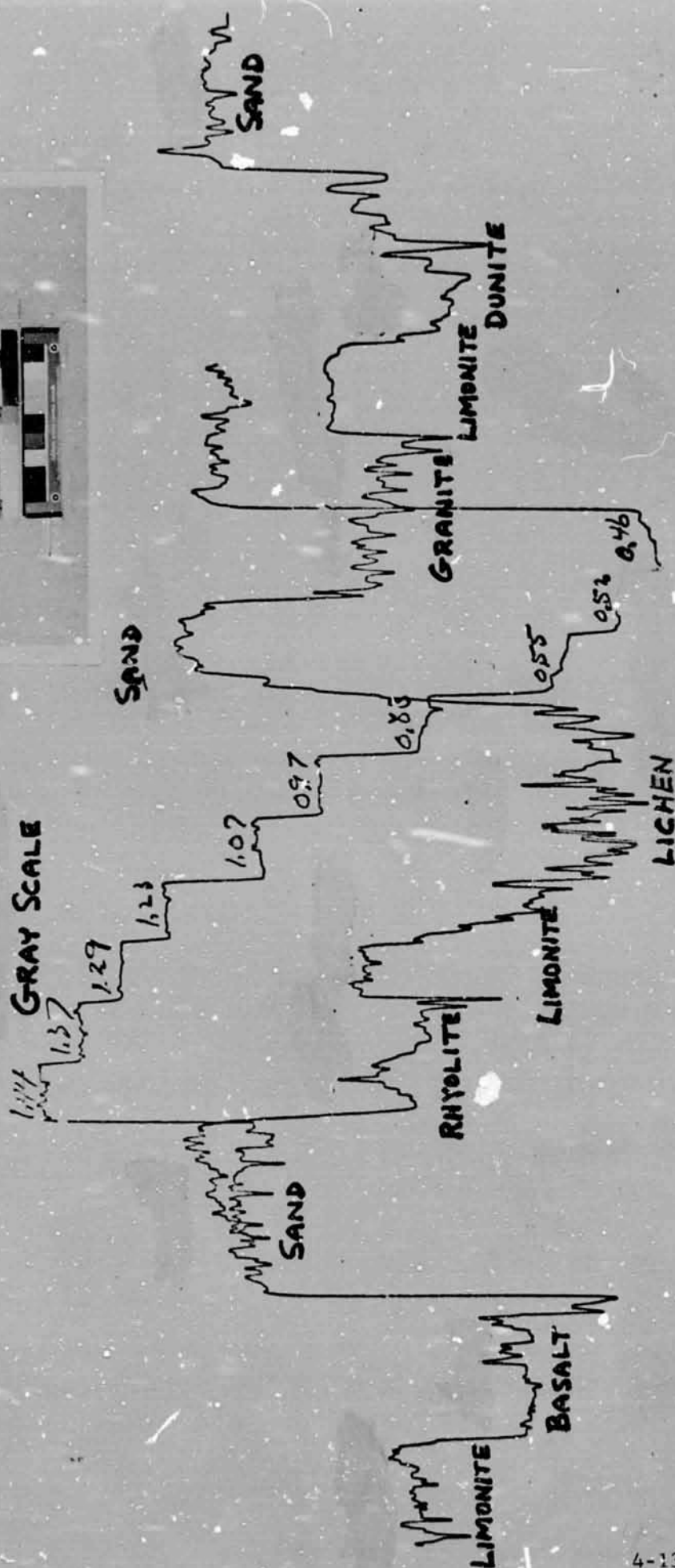
FIGURE 4-6   V FILTER, PLUS X, FILM, DENSITOMETER TRACE
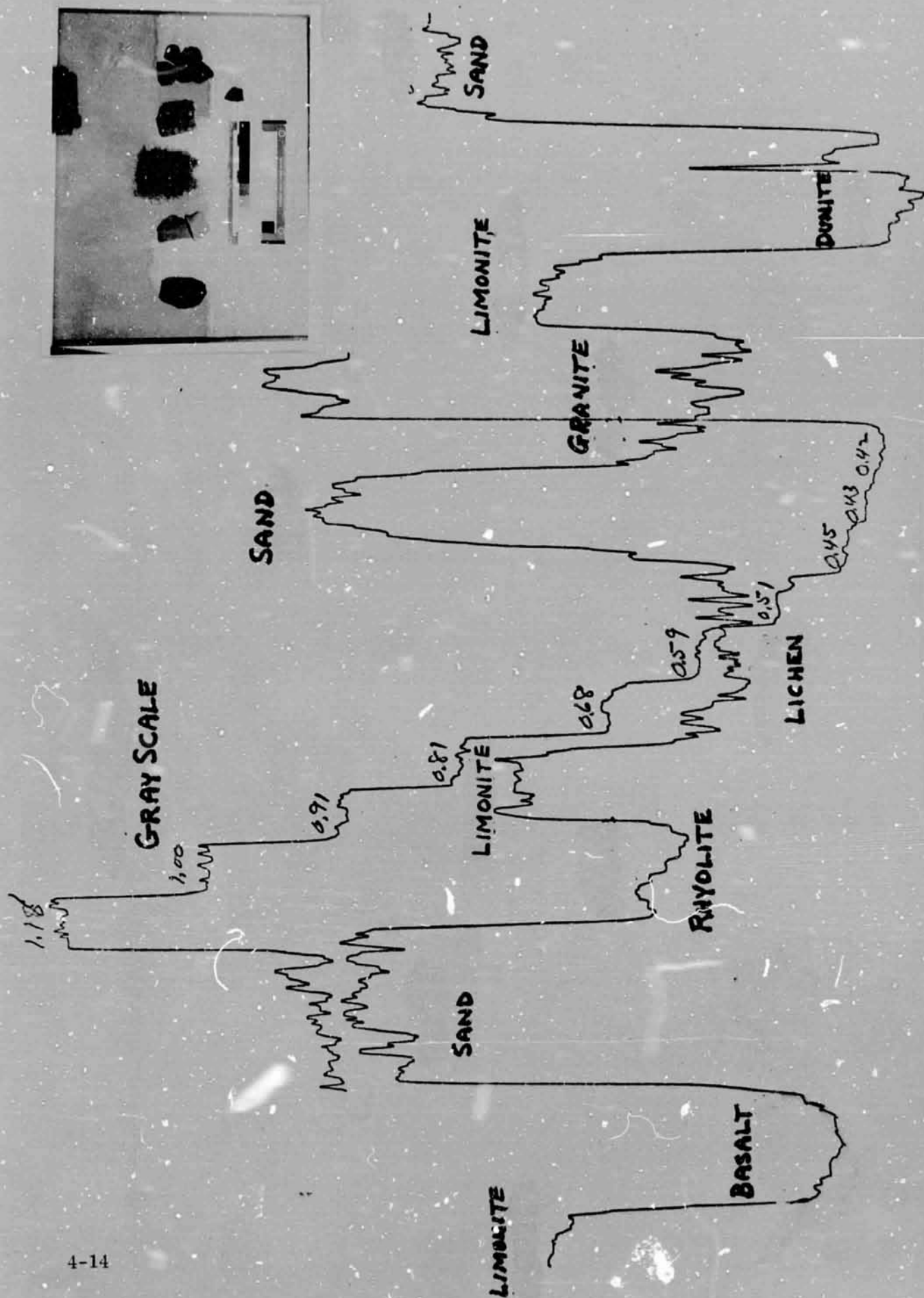
FIGURE 4-7 I FILTER, IZ SPECTROSCOPIC PLATE DENSITOMETER TRACE

4-14
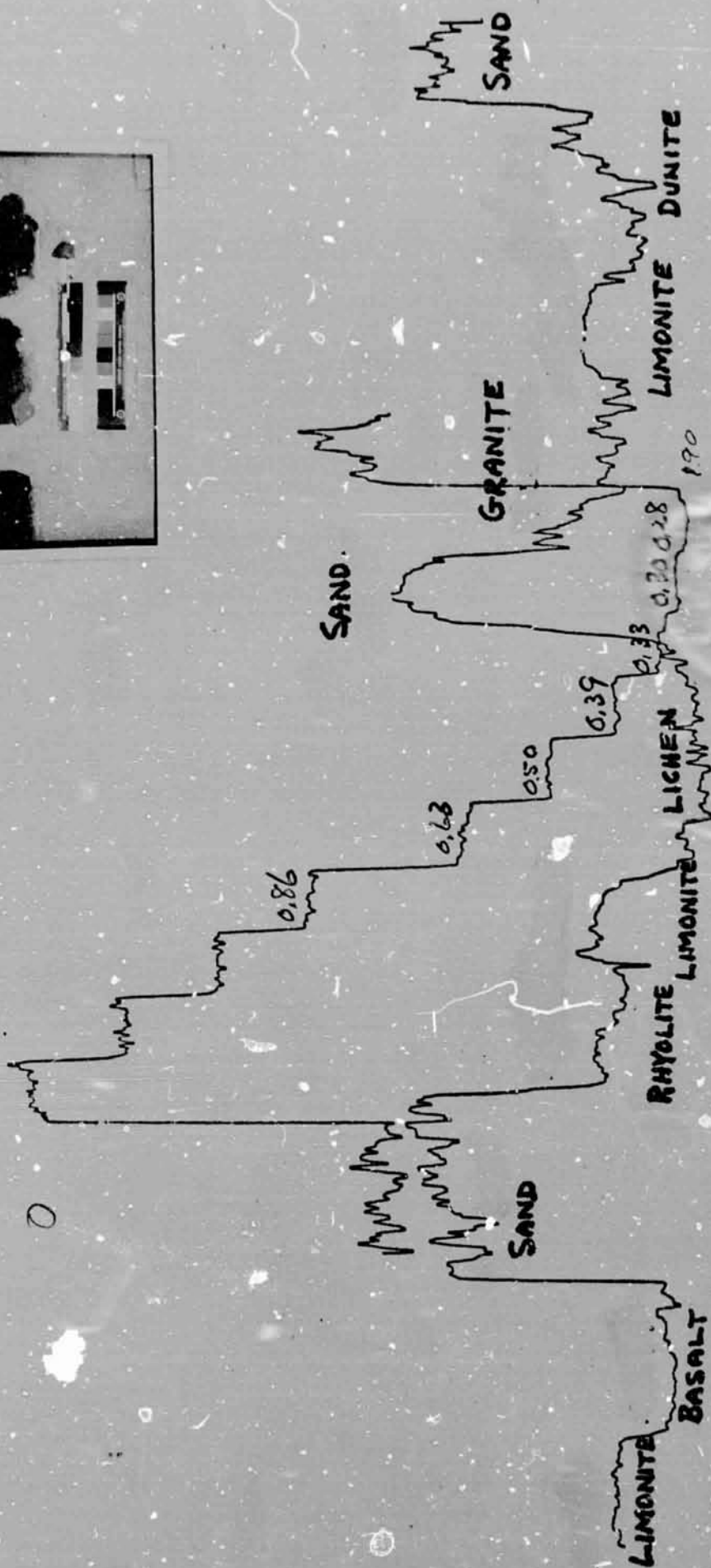
FIGURE 4-8 R. FILTER, 1Z SPECTROSCOPIC PLATE DENSITOMETER TRACE

SECTION 5

THE ASSIGNMENT OF GRAY LEVELS

The objective in using multispectral techniques is to enhance the distinguishability of items within a scene by increasing the contrast difference between them and their surrounds. This implies that fewer gray levels are needed to distinguish the desired constituents of the scene.

5.1 FACTORS INFLUENCING THE SCENE CONTRAST

Experimentally a scene consisting of the same constituents is found to display varying contrast qualities on successive imaging for several reasons.

Firstly the illumination of the scene can vary significantly; the sun angle varies throughout the day, and since most materials have directional reflectivies, the effective radiance of the surface in the direction of the sensor can alter significantly. A further complication is introduced to the relative spectral radiance of a planetary surface owing to the selective scattering properties of the surrounding gaseous atmosphere. This can cause the irradiance to be diffuse in one band and essentially plane parallel in another. This phenomenon together with the directional properties of the constituent reflecting power causes significant variations in the effective spectral surface radiance. Another variation in spectral reflectivity is caused by the differing surface forms a constituent can assume. The surface constituents are composed of mineral forms that extend from large rock structures to minute particles of less than 100 microns diameter. The spectral reflectivity of the same rock alters significantly with particle size, (Ref. 47), in magnitude and as a function of wavelength. These statements briefly give the situation as it is under real imaging conditions; the scope of this study only permits the spectral variations to be taken into account, consequently the results of this section have a limited applicability.

5.2 GRAY LEVELS FOR THE SAMPLE SCENE

The data accrued in section 3.0 will be used to define the gray level requirements in this section. The requirements themselves will vary considerably from scene to scene. Featureless desert scenes, for example, are expected to have very low contrast and hence a con-

centration of gray levels of small separation may be more appropriate than the same number of equally spaced levels about a large signal range. The terms 'minimum' and 'optimum' gray levels are likewise a function of a particular scene and cannot be associated with any fixed value that describes a general scene. For example the point radiance of a wide range of scenes has been examined by Jones and Conduit (Ref. 48 and 49), the average terrestial natural scene has a contrast ratio (integrated over the visible band) of 160 the lowest value recorded was about 25, and the highest 800-900. If a narrow band photometric device had been used instead of a broad band instrument the results would have differed from band to band.

The scene under examination in this study is composed of rock samples of various forms and according to Jones and Conduits criteria, the scene would be described as being without high contrast features. Table 5-1 below lists the bands that give the greatest contrast for the test scene. The outputs in the table listed against the constituent are proportional to the sensor outputs as before and in some cases have been multiplied by a numerical factor $(10^2$ or $10^3)$ for convenience of presentation. The data refers to narrow bands that are, for wavelength less than 1.1 microns, $150 \, A^o$ wide at half peak transmission and $300 \, A^o$ at the 1 per cent transmission points. In the infrared bands the filters are three times broader i . $450 \, A^o$ wide at 50% peak transmission and $900 \, A$ wide at 1% transmission.

5.3 GRAY LEVEL DETERMINATION

A very elementary treatment will be given here in determining the levels owing to the simple assumptions that have been made in the derivation of the constituent outputs; these are the exclusion of sensor noise and variation of constituent reflectivities.

The following procedure will be adopted; the maximum output will be divided by the smallest sensor output difference between two constituents. This will result in a non-binary number; the interval may be adjusted if it is necessary in order to separate constituents and then the full range of the gray scale will be extended up to the next complete binary number.

The first band (1) will be given as an example:

Max Output   =   14.4
Minimum Difference   =   0.7
Min. Number of Levels   = $\frac{14.4}{0.7} = 21$

Therefore complete constituent separation can be obtained with 32 gray levels of interval
0.5, 0.6 or 0.7. By having invariant outputs an unusual situation exist because it is
possible in this particular case to have only 16 gray levels which can be separated by 0.9
or 1.0 output units, still achieving each constituent in a separate gray level. The following
gray levels have been determined in the same manner.

Band II.   128 at 0.5   Band III.   32 at 1.4
             64 at 1.0

Band IV.   32 at 0.2   Band IV.   16 at 0.3

Band VI.   32 at 0.3

It is clear from the above that the separation of 6 constituents requires a considerable number
of gray levels. Even more would be required by broader bands or sensors used without filter
bands.

To reduce the number of gray levels for similar scenes that have low contrast, there are
two alternatives:

1. Reduce the number of constituents that require identification

2. Introduce logical circuiting that can simultaneously sample the outputs from
    several bands and discriminate.

The latter technique does not necessarily require the bands used for optimum contrast,
although retaining these bands will probably make logic circuitry less sophisticated.

TABLE 5-1

OPTIMUM BANDS

BAND NUMBERS →	I			II			III	
DETECTOR →	S11			Silicon			Silicon	
BAND CENTER →	0.425 μ			0.595 μ			0.715 μ	
CONSTITUENT ↓	O. P.	N.O.P.		O. P.	N.O.P.		O. P.	N.O.P.
SIL	14.4	1	SIL	38.4	1	SIL	40.1	1
BAS	12.4	0.36	BAS	28.3	0.735	BAS	27.0	0.67
DUN	5.1	0.35	RHY	16.2	0.42	LIM	18.7	0.46
RHY	4.4	0.33	DUN	15.7	0.408	RHY	16.5	0.41
LIM	2.6	0.18	LIM	12.1	0.32	DUN	13.1	0.366
LIC	0.3	0.02	LIC	4.6	0.12	LIC	6.7	0.167

BAND NUMBERS →	IV			V			VI	
DETECTOR →	Silicon			PbS/FLAKE			PbS	
BAND CENTER →	1.035 μ			1.3 μ			3.29 μ	
CONSTITUENT ↓	O.P.	N.O.P.		O.P.	N.O.P.		O. P.	N.O.P.
SIL	5.98	1	SIL	4.38	1	SIL	7.86	1
BAS	3.42	0.57	LIM	3.20	0.73	BAS	6.08	0.72
LIM	2.63	0.44	BAS	2.4	0.54	LIC	3.21	0.41
RHY	2.19	0.36	RHY	1.6	0.36	RHY	1.77	0.22
LIC	1.86	0.31	LIC	1.3	0.3	DUN	1.40	0.18
DUN	0.98	0.16	DUN	.9	0.2	LIM	0.82	0.10

O.P. - SENSOR OUTPUT

N.O.P. - NORMALIZED SENSOR OUTPUT.

TABLE 5-2(A).

RELATIVE POSITION OF THE OUTPUTS

BAND NUMBER

CONSTITUENT	I	II	III	IV	V	VI
SIL	1	1	1	1	1	1
BAS	2	2	2	2	3	2
DUN	3	4	5	6	6	5
RHY	4	3	4	4	4	4
LIM	5	5	3	3	2	6
LIC	6	6	6	5	5	3

TABLE 5-2(B).

BINARY LEVELS OF THE OUTPUTS (1 LEVEL = 0.15 UNITS)

BAND NUMBER

CONSTITUENT	I	II	III	IV	V	VI
SIL	8	8	8	8	8	8
BAS	7	6	6	5	5	6
DUN	3	4	4	4	2	2
RHY	3	4	4	3	3	2
LIM	2	3	4	4	6	1
LIC	1	1	2	2	3	4

5-5

In Table 5-2 the constituent relative outputs have been normalized so that the greatest output in each band is 1. The normalized outputs are shown in column N of Table 5-1. These normalized outputs are then assumed to be divided into eight gray levels of magnitude 0.125 each. Table 5-2B is the gray level representation of Table 5-2A which was obtained by equating a normalized value of 0.875-1.0 to be 8 etc., down to the first gray level in the range 0-0.125. Since we have six constituents we wish to identify uniquely, the minimum number of bands required is 2. Possible pairs uniquely identifying the six constituents are I&III, I&V, II&III II&V III&V V&VI. In each of these band pairs a total of only 16 gray levels are required to separate the six constituents uniquely. In practice more would be required, but the technique clearly has the potential of saving bits required for gray levels.

One of the most attractive features of the technique is that it digitizes the normalized, and not the absolute, values of the sensor outputs. This has the merit of being independant of the absolute value of the radiance of the constituents, so that those in shadow or those high-lighted are still recognized if their ratio is independant of the illumination level.

5.4 GRAY LEVEL SELECTION-SUMMARY

The requirements for gray level selection fall into one of two distinct categories:

1. Those associated with imaging a scene without identifying the constituents of the scene.

2. Those specifically aimed at identifying scene constituents.

In the first category as many levels of gray as possible are required to render observable subtle changes of irradiance that result from shadowing etc. that are independant of color content and yield particularly valuable topographical information. The selective detector-multiband approach cannot affect the number of gray levels required in this context; it can however render more noticable, by virtue of color content, the scene contrast arising from differences in the spectral qualities of the constituents. Thus if it is clear from the topographical viewpoint that two contrasting areas of the scene are similarly illuminated, then

a high probability exists that they are of a dissimilar nature. In choosing the sensor-band combination, the optical properties of the scene must be known in order to select the appropriate combination. If an incorrect combination of bands and sensors is selected some useful information may be lost but contract changes occurring as a result of illumination changes will still be retained.

In the second category, the gray levels are selected purely on the basis of discrimination, the prime objective being to selectively identify the presence of the constituents only. In this case there is no attempt to record subtle changes in contrast resulting from variation in illumination; in fact the ideal system must work independently of illumination levels.

The findings of this study are that in the latter category a very considerable saving in required gray levels can be made. In the former category the number of gray levels required in a scene are more dependent on topographical requirements; however, the use of multi-spectral bands increases the information obtained from a given number of gray levels. In both cases knowledge of the reflective properties of the scene constituents is imperative.

SECTION 6

ON-BOARD DATA PROCESSING

The multispectral sensor outputs are analog signals over a finite time interval T_s. Theoretically, they can be transmitted to the earth via an analog telemetry link in real time or recorded on an analog recorder for later analog transmission; however, it is expected that power and channel limitations will make this method infeasible. Instead, a digital (PCM or delta modulation) telemetry system will be used to transmit the sensor data. The amount of data D_t which can be returned to the earth during one transmission is given by

$$D_t = e_t R_t T_t \qquad\qquad (6-1)$$

where

e_t = fraction of telemetry bits used for data

R_t = telemetry bit rate

T_t = transmission time

Therefore, for a digital telemetry system, an on-board processor is required to extract D_t bits of information from the sensor signals during the time interval T_s. A general block diagram of the processor is shown in Figure 6-1. The source encoder transforms the N sensor signals $S_i(t)$ into M digital source signals S_i (N may or may not equal M). The channel encoder transforms the M digital source signals into one digital output signal 0 at rate $e_t R_t$. The output signal is then telemetered to the earth by the telemetry system. After detection by the earth receiver, the output bit stream is processed to recover the data about the sensor signals.

A simple processor is shown in Figure 6-2. The source encoder consists of N samplers and quantizers, one for each sensor signal. The sampling rate r_i of the i-th sampler equals the number M_i of resolution cells of the i-th sensor divided by the signal duration T_s. The i-th quantizer divides the maximum amplitude excursion A_{si} of the samples

6-1

into q_i intervals, each designated by a binary number of $L_i = [\log_2 q_i]$ digits, where $[.]$ means the next greatest interger, i.e., $[n - \epsilon] = n$, n an integer, $0 \le \epsilon < 1$. (See Figure 6-3). The channel encoder commutates and addresses the outputs from the quantizers to form a single binary data stream. If

$$R_s \cong \sum_{i=1}^{N} r_i L_i > e_t R_t \qquad (6-2)$$

then data from the source encoder enters the channel encoder at a faster rate than it leaves, so that storage is required to prevent loss of data. This is indicated by the dashed lines of the storage block in Figure 6-2. Clearly, the amount of data D_s leaving the source encoder in Figure 6-2 is given by

$$D_s = \sum_{i=1}^{N} T_s r_i L_i \qquad (6-3)$$

$$= \sum_{i=1}^{N} M_i L_i \qquad (6-4)$$

But D_s must equal D_t if no bits are to be lost in the channel encoder. Therefore, given a value for D_t determined by the telemetry system, the M_i and L_i are constrained by Equation (6-4). If it is assumed that $M_i = M_s$, all i, M_s chosen arbitrarily, then for the system in Figure C-2,

$$D_t = M_s \sum_{i=1}^{N} L_i \qquad (6-5)$$

determines the number of quantization levels $q_i = 2^{L_i}$. For identical sensor outputs, $L_i = L_s$, all i, so that

$$L_s = \frac{D_t}{M_s N} \qquad (6-6)$$

6-2

Unfortunately, the quantization rule given by Equation (6-6) is expected to be unsatisfactory for the following reason. The quality of the reconstructed sensor signal on the earth is proportional to its signal-to-noise ratio SNR_r given by

$$SNR_r = \frac{1}{\dfrac{1}{SNR_s} + \dfrac{1}{SNR_l} + \dfrac{1}{SNR_e} + \dfrac{1}{SNR_q}} \qquad (6-7)$$

where subscript s refers to sensor

$\qquad\qquad$ 1 refers to link

$\qquad\qquad$ e refers to electronics

$\qquad\qquad$ q refers to quantization

and

$$SNR_q = 12(2^{2L}) \qquad \text{(equal quantization levels)} \qquad (6-8)$$

is the peak-signal-to-mean-squared-noise power ratio for a uniform signal distribution and equal quantization levels. Thus, the quantization introduces a degradation into the overall quality of the reconstructed signal. Combining all non-quantizing error sources into a single SNR_{analog} yields

$$SNR_r = \frac{1}{\dfrac{1}{SNR_{analog}} + \dfrac{1}{12(2^{L})}} \qquad (6-9)$$

Equation (6-9) is plotted in Figure 6-4 for various values of L. To prevent the system performance from being quantization-noise-limited, a good rule, to be called Rule 1, is to make the quantization noise at least 10 dB below the remaining noise, which represents us⁴   ᵗ smallest possible L which yields an operating point on the unity-slope portion of Figure 6- Let L_s' be the value of L for the sensor outputs given by Rule 1. Let $L_s = D_t/M_s N$ be the value of L given by Equation (6-6). Assume $L_s' > L_s$. Then if L_s is used in the

design of Figure (6-2), excessive degradation of the sensor data will occur. But if L_s' is used, then

$$L_s' > \frac{D_t}{M_s N} \quad \text{where } L_s = \frac{D_t}{M_s N} \qquad (6\text{-}10)$$

or

$$NM_s L_s' \equiv D_s > D_t \qquad (6\text{-}11)$$

i.e., the telemetry system capacity will be exceeded.

Obviously, the processor in Figure 6-2 cannot be used if relation (6-11) is true. Either the source encoder must be modified until $D_s = D_t$, or the channel encoder must be modified so that it reduces the source data by the ratio D_s/D_t, or both source encoder and channel encoder must be modified so that the final output data quantity equals D_t. Clearly, the type of processor required will depend on the value of D_t, the number of sensors N, and the number of resolution cells M_s. Section 6.1 contains descriptions and analyses of several source encoding schemes to reduce D_s while obtaining satisfactory sensor data. Section 6.2 contains a description of a channel encoder scheme to remove redundancy from the source data bits and thereby compress the total data bits by the ratio D_s/D_t.

The systems in sections 6.1 and 6.2 are feasible from an implementation point of view. With the exception of a signal-to-noise-power meter for the spectral sensors mentioned in Section 6.1.1, all the equipment required exists in one form or another. Finally, for the input and output data rates expected, current logic speed of 10^7 bps and core storage access time of $1 \, \mu$s will be adequate.

It was mentioned previously that if the rate of source data accumulation R_s was greater than the channel encoder data transfer rate $e_t R_t$, then storage would be required to prevent loss of data bits. Assuming that data read-out overlaps data read-in in the channel encoder,

then the minimum storage M_{min} required is given by

$$M_{min} = T_s (R_s - e_t R_t) \quad \text{bits} \tag{6-12A}$$

It is possible that all the source data must be stored for later playback. In this case, the maximum storage M_{max} will be required, i.e.,

$$M_{max} = D_t \quad \text{bits} \tag{6-12B}$$

In order to determine the effectiveness of the schemes which follow versus their cost, further study of the expected nature of the sensor signals should be done. It is possible that more than one method of data processing can be implemented for one mission, thereby increasing the flexibility of the system and the prob ility of obtaining satisfactory data. Section 6.3 discusses this concept further.

6.1 SOURCE ENCODING SCHEMES

6.1.1 ADAPTIVE QUANTIZATION SCHEMES

6.1.1.1 Continuous Grey Level Control

Equations (6-7) through (6-9) and Figure 6-4 suggest one method to reduce the number of quantization bits required. Rearranging Equation (6-7) yields

$$SNR_r = \cfrac{1}{\cfrac{1}{SNR_f} + \cfrac{1}{SNR_s} + \cfrac{1}{12(2^{2L})}} \tag{6-13}$$

where

$$\frac{1}{SNR_f} = \frac{1}{SNR_1} + \frac{1}{SNR_e}$$

It is expected that SNR_f will vary slowly over a small range throughout the mission lifetime. However, SNR_s, due to the sensor, may vary over a relatively large range throughout each period T_s o. sensor data. If L is chosen in Equation (6-13) to satisfy Rule 1 for the maximum value of SNR_s and the given value of SNR_f, then when SNR_s is below its maximum value, L is greater than required to satisfy Rule 1, i.e., it provides greater quantization accuracy than required. An adaptive scheme to overcome this inefficiency is shown in Figure 6-5. Each sensor signal is first quantized into n bits to satisfy Rule 1 for the peak SNR_s (plus some margin) expected. The output of the quantizer is transferred to a buffer. At the same time, the signal-to-noise ratio SNR_{si} of the i-th analog sensor signal is determined and fed into the bit control logic. On the basis of Figure 6-4, the bit control logic determines the number of bits m_i required to satisfy Rule 1. The buffer discards the $(n - m_i)$ least significant bits of the quantized sample and transfers the m_i significant bits to the channel encoder buffer. The channel encoder inserts address words and commutates the variable-length data words from the N sensors into one output bit stream.

There are several problems with such a scheme. First, examining Equation (6-13), if the quality of the communication link and electronics is so poor that $SNR_f < 10\ SNR_s$ always, then fluctuations in SNR_s will not effect the number of quantization bits, which will remain constant, required to satisfy Rule 1, i.e., under the condition of low SNR_f, the scheme of Figure 6-5 will be no better than that of Figure 6-2. Second, even if $SNR_f > 10\ SNR_s$, so that the scheme of Figure 6-5 may operate adaptively as desired, it is difficult to predict the actual quantity of data D_s which the source encoder will generate because it depends on the values of SNR_s for each sensor throughout the data collection interval T_s. Third, the length of the source data words into the channel encoder varies in time; this increases the complexity of the channel encoder and could decrease the fraction e_t of the channel encoder output bit stream allocated to sensor data, depending upon the addressing scheme implemented.

6.1.1.2 Continuous Grey Level Reallocation

A scheme which overcomes these problems while maintaining some of the adaptability of scheme in Figure 6-5 is shown in Figure 6-6. Now N quantizers are provided with a fixed

number of quantization bits L_i, $i = 1, 2, \ldots N$, chosen so that $D_s = D_t$, i.e.,

$$D_t = \sum_{i=1}^{N} M_i L_i \qquad (6\text{-}14)$$

where M_i is the number of resolution cells of the i-th sensor output. Assume with no loss of generality that $L_1 \geq L_2 \geq L_3 \geq \ldots \geq L_N$. To prevent a contradiction of Rule 1, (note that Rule 1 may not necessarily be satisfied, however) the sensor with the highest SNR_{si} should be quantized into L_1 bits, the sensor with the next highest SNR_{si} quantized into L_2 bits, and so on (Rule 2). This is performed by the switching matrix which consists of $\binom{N}{2}$ comparator circuits to rank the SNR_{si} in order, and switches to connect the sampled sensor signals and the quantizers according to Rule 2. The output of each quantizer is now a fixed-length data word at the sampling rate. The switching matrix also puts out a data word consisting of $N [\log N]$ bits which tells the order of the SNR_{si}. This word is present only after some change in the existing order. The channel encoder time-multiplexes the quantized sensor data and the occasional switching matrix word to form the output bit stream.

The scheme of Figure 6-6 represents a potential data compression C over the scheme of Figure 6-2 by the ratio

$$C = NL_s \Big/ \left[\left(\sum_{i=1}^{N} L_i \right) + mN \; [\log N] \right] \qquad (6\text{-}15)$$

where m is the number of times the switching matrix puts out an SNR_{si} order word. If m gets too large, this ratio will be less than one, indicating that data expansion, rather than data compression has occurred. It is expected the individual SNR_{si} will remain relatively constant so that m will be small and C as large as described.

The possible penalty of the scheme in Figure 6-6 is that quantization may introduce more noise into the reconstructed signal than is permissible under Rule 1. For example, although Rule 2 may be satisfied, the SNR_{si} of the i-th sensor may require more quantization bits

than available from the quantizer assigned to it by Rule 2. Therefore, for uniformly high SNR_{si} in all channels the scheme of Figure 6-6 may be unsatisfactory.

6.1.1.3 SNR Meter Design

The SNR meters indicated in Figures 6-5 and 6-6 are obviously not off-the-shelf hardware. However, the nature of the signals to be measured may make their design feasible within the required time period.

To understand the problem, consider the output signal $S_i(t)$ from the i-th sensor. It can be expressed by

$$S_i(t) = d_i(t) + n_{iv}(t) + n_{ic}(t) \qquad (6-16)$$

where

$d_i(t)$ = desired signal

$n_{iv}(t)$ = variable component of undesired signal (noise)

$n_{ic}(t)$ = constant component of noise (in a statistical sense)

The variable noise will be proportional to the desired signal since it is caused by optical rather than electrical effects; i.e.,

$$n_{iv}(t) = kd_i(t) \qquad (6-17)$$

The SNR_{si} is given by

$$SNR_{si} = \frac{\overline{d_i(t)^2}}{\overline{\left(n_{iv}(t) + n_{ic}(t)\right)^2}} \qquad (6-18)$$

6-8

$$= \frac{\overline{d_i(t)^2}}{k^2 \overline{d_i(t)^2} + \overline{n_{ic}(t)^2}} \qquad (6\text{-}19)$$

since $d_i(t)$ and $n_{ic}(t)$ are independent. But k and $\overline{n_{ic}(t)^2}$ can be determined before the mission. Therefore, Figure 6-7 shows a possible implementation of the SNR meter.

6.1.1.4 Reallocation of Grey Levels by Ground Command

The scheme of Figure 6-6 can be simplified with some loss of flexibility and further possible degradation of the reconstructed sensor signals. Figure 6-8 shows the simplified system. Instead of using the SNR meter outputs to control the switching matrix, the sensor-to-quantizer connections are controlled via ground command. This obviates the need of the SNR meters and the switching matrix word (although a command verification word for the ground switching is desirable). Although Rule 2 may now be violated during one sensor signal interval T_s, if more than one interval is used to observe the same scene, then analysis of the reconstructed sensor data from the previous interval can be used to apportion the quantization bits properly for the next interval.

6.1.2 ADAPTIVE SIGNAL NORMALIZATION

The analysis in Sections 6.0 and 6.1.1 assumed that the sensor signal amplitude distribution was equally likely (uniform) over the entire range from zero to some peak value A_{si}. In that case, increasing A_{si} by amplification without increasing L_i would be equivalent to increasing the brightness of the reconstructed sensor signal without affecting its contrast, which is the important quantity. Therefore, the value of A_{si} was unimportant to conceptual design in Section 6.1.1. However, it is possible that the actual sensor signal amplitude distribution will be centered about a narrow range within 0 to A_{si}. In this case Equation (6-8) does not accurately describe the quantization effect on the reconstructed signal.

Assume, for example, that the signal is the sum of a constant (d.c. term) plus a sine wave of amplitude slightly less than $A_{si}/2^{L+1}$, which is 1/2 the quantization fineness. Further assume that the constant represents the center of some quantization aperture, i.e., has the value $A_{si}(k + 1/2)/2^L$. Then the output of a uniform level quantizer such as in Sections 6.0 and 6.1.1 is a constant word, indicating that the presence of the sinusoid will go completely undetected when the data signal is reconstructed.

This loss of resolution effect can be overcome to some degree by the scheme in Figure 6-9. The output of each sensor is fed into an amplifier of variable gain. The variation in gain is such to amplify the active or most important ranges of signal amplitude and compress the least active and uninteresting ranges. Thus, the quantization of the amplifier output achieves greater accuracy for the expanded signal regions than would be obtained without the amplifier.

The design of the amplifier is the critical consideration for this scheme. There are two main categories of possible design philosophies:

   1.   Linear gain, variable magnitude, automatically adaptive or controllable by ground command.

   2.   Non-linear gain, variable or fixed gain function, variable or fixed magnitude, automatically adaptive or controllable by ground command.

6.1.2.1 Linear Gain, Variable Magnitude

Figure 6-10 shows a general scheme to implement the first concept. The signal is monitored to determine its peak amplitude A_p. Depending upon the value of the ratio A_p/A_s where A_s is the nominal signal range, the gain G of the amplifier is controlled so that $GA_p \cong A_s$. Since G must be known on the ground to accurately reconstruct the signal, the usual method employed is to allow two or four discrete amplifier gains G_i, and use the G_i which causes $G_i A_p$ to be closest to but not exceeding A_s. A data word of $[\log_2 k]$ bits, where k is the number of amplifier gains available, is transmitted whenever the gain being used changes. The gain to be used can also be controlled via ground command as in Section 6.1.1.4.

The reduction in data for the scheme of Figure 6-10 is given by

$$\frac{D_s}{D'_s} = \frac{\sum_{i=1}^{N} M_i L_i}{\left[\sum_{i=1}^{N} M_i (L_i - \lceil \log_2 G_i \rceil)\right] + n \lceil \log_2(k) \rceil} \qquad (6-20)$$

where

D_s = data quantity without amplifiers

D'_s = data quantity with amplifiers

M_i = number of resolution cells for i-th sensor

L_i = number of quantization bits for i-th sensor

G_i = gain of amplifier for i-th sensor

n = number of amplifier change data words

k = number of allowable amplifier gains

With an equal number of resolution cells M_s and quantization bits L_s for each sensor, Equation (6-20) reduces to

$$\frac{D_s}{D'_s} = \frac{N L_s}{\left[\sum_{i=1}^{N} (L_s - \lceil \log_2 G_i \rceil)\right] + n \lceil \log_2(k) \rceil / M_s} \qquad (6-21)$$

If n/M_s is small, the second term in the denominator can be neglected and

$$\frac{D_s}{D'_s} \cong \frac{N L_s}{N L_s - \sum_{i=1}^{N} (\lceil \log_2 G_i \rceil)} \qquad (6-22)$$

6-11

Note that this scheme is very useful if there is much uncertainty about the expected sensor signal amplitudes. A_s can be made larger and/or L_s made smaller than might be chosen otherwise since the variable amplifiers will insure optimum use of the full signal ranges in the quantizing schemes.

6.1.2.2 Non-Linear Gain, Variable Gain Function

It is possible that the sensor signal amplitude may vary over the entire range from 0 to A_s, however, it may vary in a more narrow range for a large proportion of the time. In this case, the system of Section 6.1.2.1 will effect no improvement in data transfer efficiency, however, a logarithmic type of amplifier characteristic can be implemented to give improvement. Figure 6-11 shows the gain versus input amplitude of such an amplifier. The effect of this gain characteristic on a signal is shown in Figure 6-12. Clearly, for a signal which normally resides in a region near zero, such an amplifier will improve the accuracy of a uniform quantization scheme. In fact, the overall effect of non-linear amplification followed by uniform quantization is to produce a non-uniform quantization scheme tailored to the type of signal shown in Figure 6-12a.

Care must be taken to stabilize the time- and temperature- dependent drift of such an amplifier to prevent the generation of significant error in the reconstructed sensor signal. Sufficiently stable logarithmic amplifiers are now commercially available. Also, sufficient frequency bandwidth must be provided to prevent attenuation of higher-frequency components of the sensor signals.

6.1.3 VARIABLE SAMPLING RATES

The analysis of Section 6 has thusfar assumed that the number of resolution cells M_{si} for each sensor signal was a constant. The actual value chosen for M_{si} depends on the frequency content of the power spectrum of the i-th sensor signal. From the Sampling Theorem, the minimum number of resolution cells is given by $2f_s T_s$, where f_s is the highest frequency component of interest in the sensor signal. Usually M_{si} must be at least 25% greater than

6-12

theoretical due to equipment limitations. Just as in Section 6.1, if M_{si} is chosen to satisfy the sampling theorem (plus margin) for the maximum possible frequency, it will be inefficient when the actual sensor signal bandwidth is below this. Therefore, by monitoring the sensor signal frequency content (instead of the SNR), an adaptive sampling rate system can be designed to provide the least resolution cells for the required reconstructed signal quality on the earth. Figures 6-13 and 6-14 show possible schemes corresponding to different levels of adaptability (just as in Figures 6-5 and 6-6). An implementation of the "Frequency Content Monitor" is shown in Figure 6-15.

The data saving ratios in the schemes of Figures 6-13 and 6-14 are proportional to the reduction in resolution cells from the sample system of Figure 6-2.

6.1.4 DIFFERENCE TECHNIQUE

Sections 6.1.1, 6.1.2, and 6.1.3 have dealt with methods to transmit all individual sensor signals to the earth. However, it is possible (but not scientifically desirable) that images of the same scene taken in different spectral bands might have high spatial correlation, yielding high correlation between the sensor signals. This would imply redundancy of information in the individual sensor signals.

An easily implemented scheme to exploit this redundancy is shown in Figure 6-16 for three sensor signals (N = 3). Instead of sampling, quantizing, and transmitting $S_1(t)$, $S_2(t)$, and $S_3(t)$ individually, only $S_1(t)$ is treated this way. In addition, $S_{d2}(t)$ and $S_{d3}(t)$, where

$$S_{d2}(t) = S_2(t) - S_1(t) \tag{6-23}$$

$$S_{d3}(t) = S_3(t) - S_1(t) \tag{6-24}$$

are processed for transmission in the usual fashion.

Transmitting $S_1(t)$ requires the same equipment as before. However, $S_{d2}(t)$ and $S_{d3}(t)$ are expected to vary much more slowly in time than $S_2(t)$ and $S_3(t)$. Therefore, from the

sampling theorem, the rate of sampling, i.e., number of resolution cells, can be reduced for these signals without degrading the reconstructed $S_{d2}(t)$ and $S_{d3}(t)$ on the earth. Assuming that $S_1(t)$, $S_{d2}(t)$, and $S_{d3}(t)$ are satisfactorily reconstructed, then trivially,

$$S_2(t) = S_1(t) + S_{d2}(t) \qquad \qquad (6\text{-}25)$$

$$S_3(t) = S_1(t) + S_{d3}(t) \qquad \qquad (6\text{-}26)$$

The data saving available for such a scheme is proportional to the ratio of the total signal bandwidth occupancy before and after processing in the difference circuits. For example, in the commercial television system, it is possible to reduce three 4.5 MHz color channels into channels of 4.5 MHz, 1.5 MHz, and .6 MHz by a difference technique, for an equivalent data compression of $13.5/6.6 \cong 2$.

6.1.5 SIGNATURE DETECTION

It is possible that none of the schemes in Sections 6.1.1, 6.1.2, 6.1.3, and 6.1.4 will reduce D_s sufficiently. In this case a more fundamental approach to utilizing the available transmitted data capacity D_t may be considered. Suppose that all the data bits D_t are correctly received. This means that D_t questions having yes or no answers can be settled by the observation. Thus, the on-board data processing scheme is an integral part of the experiment, for it is clear the best experiment is the one that is designed to answer the D_t most significant binary questions about the specimen under observation.

This point will be elaborated further: the D_t binary questions could be used to determine (assuming perfect data) the presence or absence of 2^{D_t} specimens having different signatures. Since an unfamiliar planet is under observation, it is probably not wise to exhaust all the questions in this manner; rather, it seems to be more profitable to use the D_t bits to describe the signature observed so that a large number of types of material can be compared. This approach has the advantage in that it can be implemented to answer some questions that arise after looking at the data as well as those that can be formulated in advance.

The most straightforward way to apportion the 2^{Dt} questions is as follows. Let the N sensor outputs at a particular time instant be represented by a point in a N-dimensional vector space, in which each signal corresponds to one axis. One can construct a subset of this vector space such that the point representing the sensor outputs is always contained in the subset, shown in Figure 6-17 for N = 3. Again, A_{si} represents the peak amplitude of the i-th sensor signal. Now, this subset can be further subdivided into $Q = 2^q$ regions representing the spectral signature of a particular substance, i.e., when a region is occupied by the N-dimensional signal point, then the image being viewed contains the substance whose signature is represented by that region. Given the number of resolution cells M_s during a sample time T_s, then the number of signatures $Q = 2^q$ which can be determined without exceeding the data transmission capacity D_t can be found from

$$D_t = D_s \equiv M_s \log_2(Q) \qquad (6-27)$$

$$\equiv M_s q \qquad (6-28)$$

Solving for Q yields

$$Q = 2^{Dt/M_s} \qquad (6-29)$$

If Q is chosen to be larger than given by Equation (6-29), it is possible that further data compression can be performed in the channel encoder, to be described in Section 6.2, to prevent loss of data bits.

6.1.5.1 <u>Block Division</u>

The method of subdividing the subset containing the sensor signal points into the signature regions is now considered. One simple method can be described as block division. Each axis of the N-dimensional space is divided into line segments and the signature regions are formed by the intersection of the planes perpendicular to each axis at the subdivision points. Figure 6-18 shows an example for N = 2 and $A_{s1} = A_{s2} = 1$. In Figure 6-18 there are $Q = 2^4 = 16$ signatures (4 bits) per resolution cell, as opposed to the 6 to 8 bits which might

have been used to send each sensor signal separately (12 to 16 bits total). For equal distance between each separating plane along each axis (uniform quantization), Figure 6-19 shows a digital implementation of the signature detection.

6.1.5.2 Ratio Division

Further investigation of the nature of the sensor signals may lead to refining the system of Figure 6-19. Specifically, the analog outputs $S_i(t)$ from each sensor when viewing one particular point in a scene may be considered as follows:

$$S_i(t) = I(t)f_i \qquad (6-30)$$

where

$I(t)$ = intensity of illumination of the scene (white light) (function of time)

f_i = fraction reflected in the i-th band (function of scene)

Clearly, as $I(t)$ varies, $S_i(t)$ will vary even for the same point in the same scene. But the fractions f_i contain the important information since they can be determined on the earth for any substances whose presence on Mars is suspected. A simple way to remove the variation caused by changes in $I(t)$ is to form the N - 1 ratios $S_2(t)/S_1(t) = f_2/f_1$, $S_2(t)/S_1(t) = f_2/f_1$, ..., $S_N(t)/S_1(t) = f_N/f_1$. Block division signature detection may now by employed on the N - 1 parameters $p_1 = f_2/f_1$, $p_2 = f_3/f_1$, ..., $P_{N-1} = f_N/f_1$, as described in Section 6.1.3.1. To reduce the dynamic range for the signature subset, the largest $s_i(t)$ (and, therefore, largest f_i), should be used to normalize. This will necessitate sending a data word of $\lceil \log_2 N \rceil$ bits whenever the signal being used for normalization changes.

In terms of the discussion in Section 6.1.5, ratio division corresponds to dividing the signature subset by planes passing through the origin with slope along each axis given by f_j/f_i, $i \neq j$. Figure 6-20 shows a representation of this scheme for N = 2. Clearly, ratio division can be more efficient than block division because only an (N - 1) -dimensional space

must be divided into signature regions. However, since frequent transmission of a normalization variable change word might delete any advantage, further study must be performed on typical data to determine the actual advantage. Figure 6-21 shows a scheme for ratio division. Note that the actual normalization (division) can be done by either analog or digital components. A trade-off study would determine the proper choice between analog or digital.

6.2 CHANNEL ENCODING SCHEME

The schemes in Section 6.1 assumed that the channel encoder consisted of simply a commutator to convert the M source data outputs into one channel bit stream (plus any needed storage). Clearly for this case $D_s = D_t$, i.e., the channel encoder transferred for transmission all data generated by the source encoder. It is possible to design a channel encoder for certain types of sensor signals which accepts D_s bits, $D_s > D_t$, and removes $D_s - D_t$ bits without significantly degrading the quality of the reconstructed signals on the earth.

Figure 6-22 shows a block diagram of a typical data compression scheme for the channel encoder. The p-th order polynomial predictor uses the $k - 1$, $k - 2$, ..., $k - p$ previous data words to predict that the k-th word should be. The equality detector determines the accuracy of the prediction. All correctly predicted words are considered redundant. The address encoder transfers all non-redundant words plus an address code to the commutator. Due to the random nature of the redundant words, a buffer is required in the address encoder to insure a constant word rate into the commutator.

There are three sources of error in the reconstructed signal due solely to data compression: aperture effect, amplitude word errors due to channel noise, address word errors due to channel noise. The first error occurs when the equality detector considers as redundant not only words predicted exactly, but those predicted to within some specified degree of accuracy. The second and third errors are due to errors in the bit detection process at the earth receiver. It is useful in comparing data compression techniques to consider the rms

error e_{rms} as per cent of full scale in the reconstructed signal. In general, this can be expressed as

$$e_{rms} = (e_{aper}^2 + e_{ampl}^2 + e_{addr}^2)^{1/2} \qquad (6\text{-}31)$$

where

$\quad e_{aper} = $ rms error due to aperture effect

$\quad e_{ampl} = $ rms error due to amplitude word errors

$\quad e_{addr} = $ rms error due to address word errors

i.e., the error sources are independent and the variances add. It should be noted that e_{ampl} exists for systems with no data compression.

Equation (6-31) has been evaluated[1] for $p = 0$ and $p = 1$ with the three most common addressing schemes – run length encoding, position word encoding, and single address word encoding. An important parameter in the evaluation is the compression ratio C where $C = \dfrac{\text{total source data bits}}{\text{non-redundant bits}}$, which is a measure of the inherent redundancy in the data words coming from the source encoder. It can be determined[2] that for a fixed value of e_{rms} and a given set of telemetry system parameters, there exists a threshold for C depending on p and the addressing scheme, above which data compression gives overall system improvement and below which degradation occurs. For example, with $C = 5$, about 1 dB improvement occurs using a zero-order hold predictor and run-length addressing. The crossover point for such a scheme is approximately $C = 3$. Since the value of C for the source data is dependent not only upon the sensor signals, but also on the sampling rate and quantization bits in the source encoder, it is not easy to predict the actual saving which would occur using data compression in the channel encoder without considerable study of the data.

(1) Belver, T., and Huffman, G., Effect of Transmission Errors on Image Data Compression Techniques, TIS No. 68SD235 (GE Co., document), June 1968.

(2) Ibid.

6.3 CONCLUSIONS AND SYSTEM DESIGN CONSIDERATIONS

Sections 6.1 and 6.2 have presented individual techniques to improve the efficiency of information transfer when the data transmission capacity is not sufficient to support the basic data processor of Figure 6-2. An important aspect of all these techniques, however, is that they may cause degradation in the quality of the data received on the earth. Therefore, their use may be prohibited unless absolutely necessary. A more desirable approach may be to provide sophisticated data processing as a back-up operating mode. With the communication link operating satisfactorily, the system of Figure 6-2 might not exceed the data transmission capacity. However, should the link be degraded unexpectedly to preclude telemetry at the normal bit rate, the bit rate could be reduced, thus necessitating a reduction in sensor data transmitted and justifying use of more extensive data processing. In a sir-il. ~ fashion, continuous anticipated degradation of the communication link due to increa ɩ range, unfavorable antenna pointing, or component aging, would also indicate the usefulness of different techniques of data processing (of varying complexity) on-board the same mission, limited only by vehicle size, weight, and power constraints. Figure 6-23 shows a functional block diagram of a multi-technique data processor. Command of the switching can be automatic or by ground command.

If implementing more than one data processing scheme on the vehicle is not possible, the single scheme chosen depends upon the data compression requirements and complexity factor tolerable. In general all of the schemes presented show promise of reducing the data transmitted. However, the most feasible schemes are those for which the data saving can be determined before launch (i.e., the non-closed-loop schemes).

$S_1(t)$
$S_2(t)$
$S_N(t)$

SOURCE ENCODER

S_1
S_2
S_M

CHANNEL ENCODER

O

CHANNEL DATA

(DIGITAL)

SENSOR SIGNALS

(ANALOG)

SOURCE DATA

(DIGITAL)
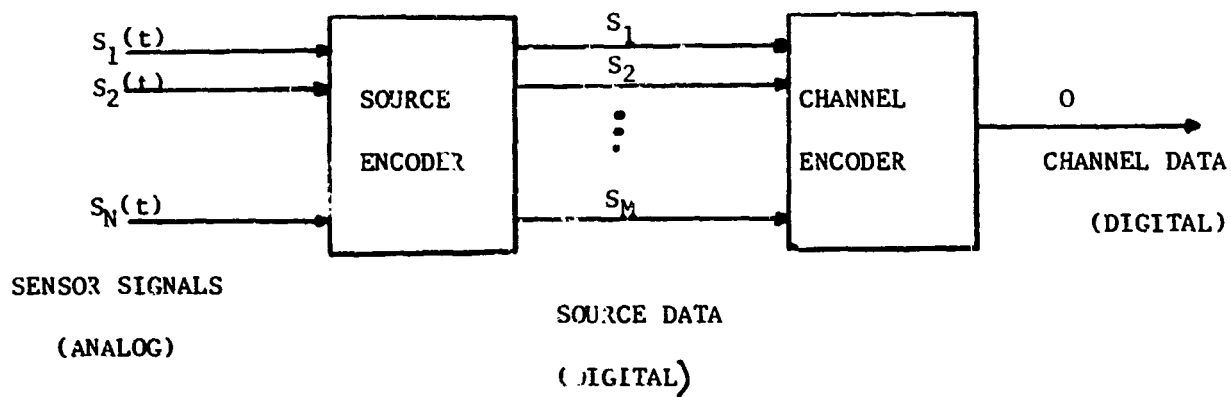
FIGURE 6-1-GENERAL ONBOARD DATA PROCESSOR

0 1   2   3 q_i-2 q_i-1 q_i A_{si}
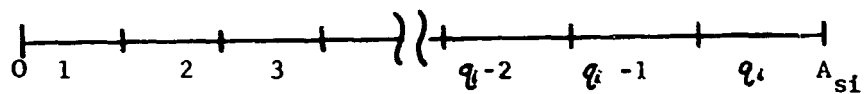
CODE TABLE

1   00 ...   01
2   00 ...   10

$(\log_2 q_i)$ digits

FIGURE 6-3 - A/D QUANTIZING (UNIFORM INTERVALS)
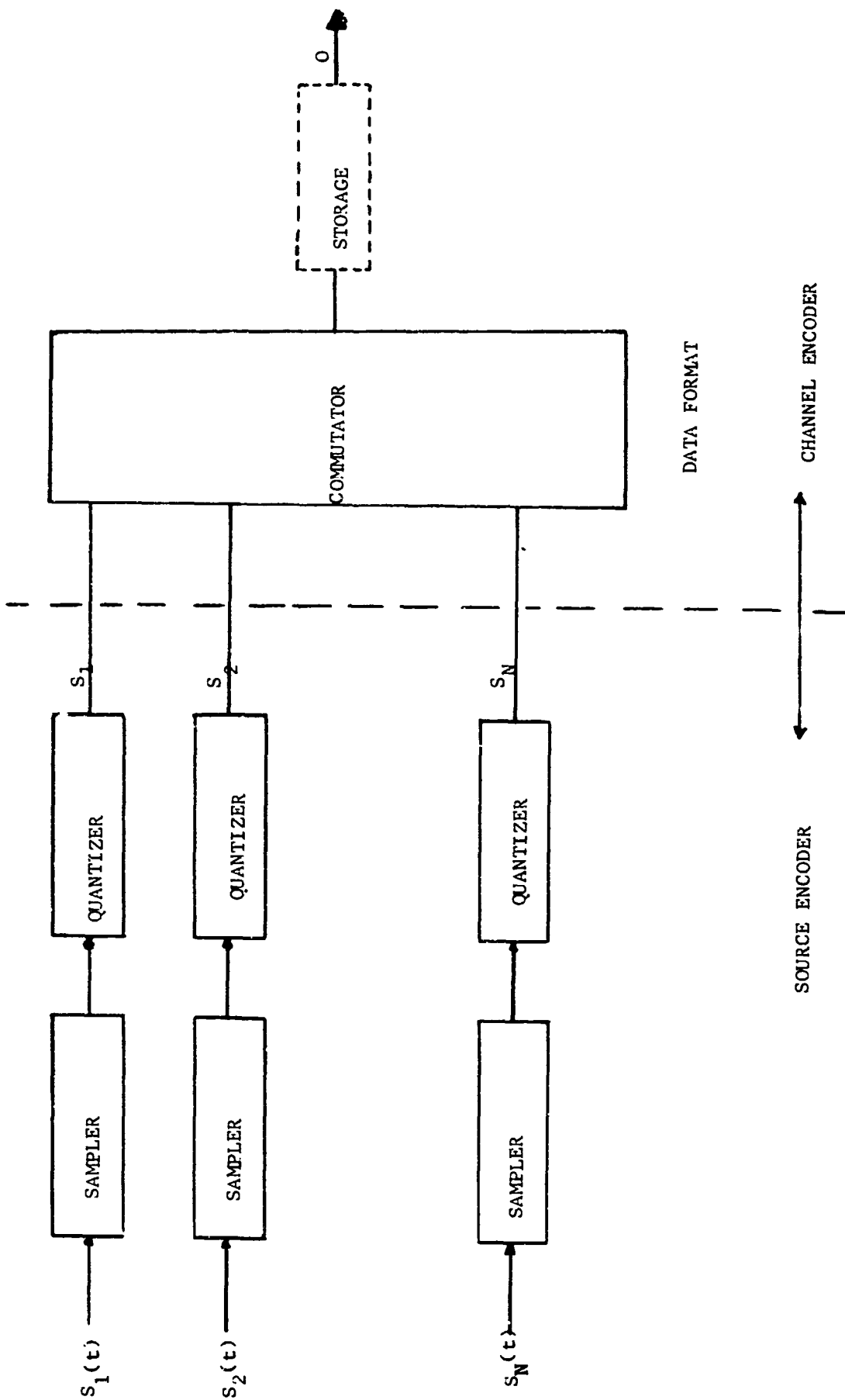
FIGURE 6-2- SIMPLE PROCESSOR
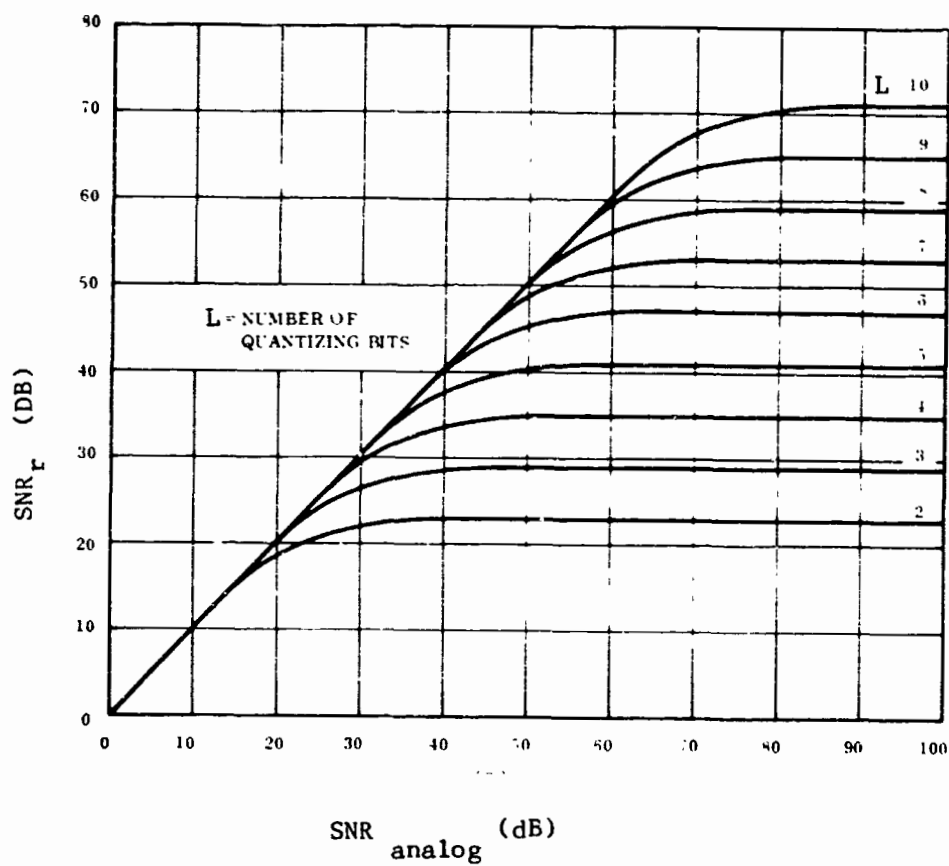
FIGURE 6-4 EFFECT OF QUANTIZATION ON RECONSTRUCTED SIGNAL
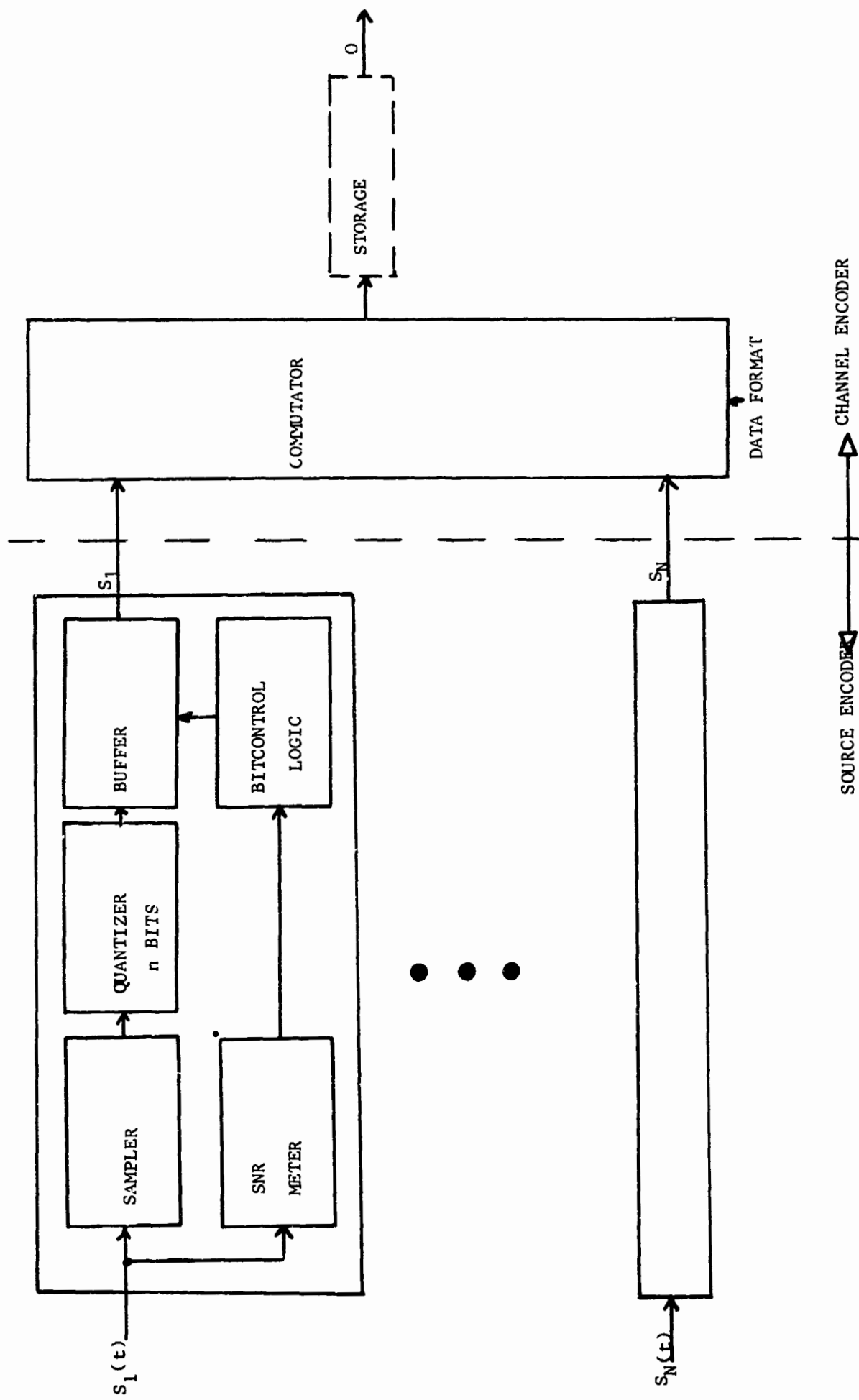
FIGURE 6-5 CONTINUOUS GREY-LEVEL CONTROL

6-23
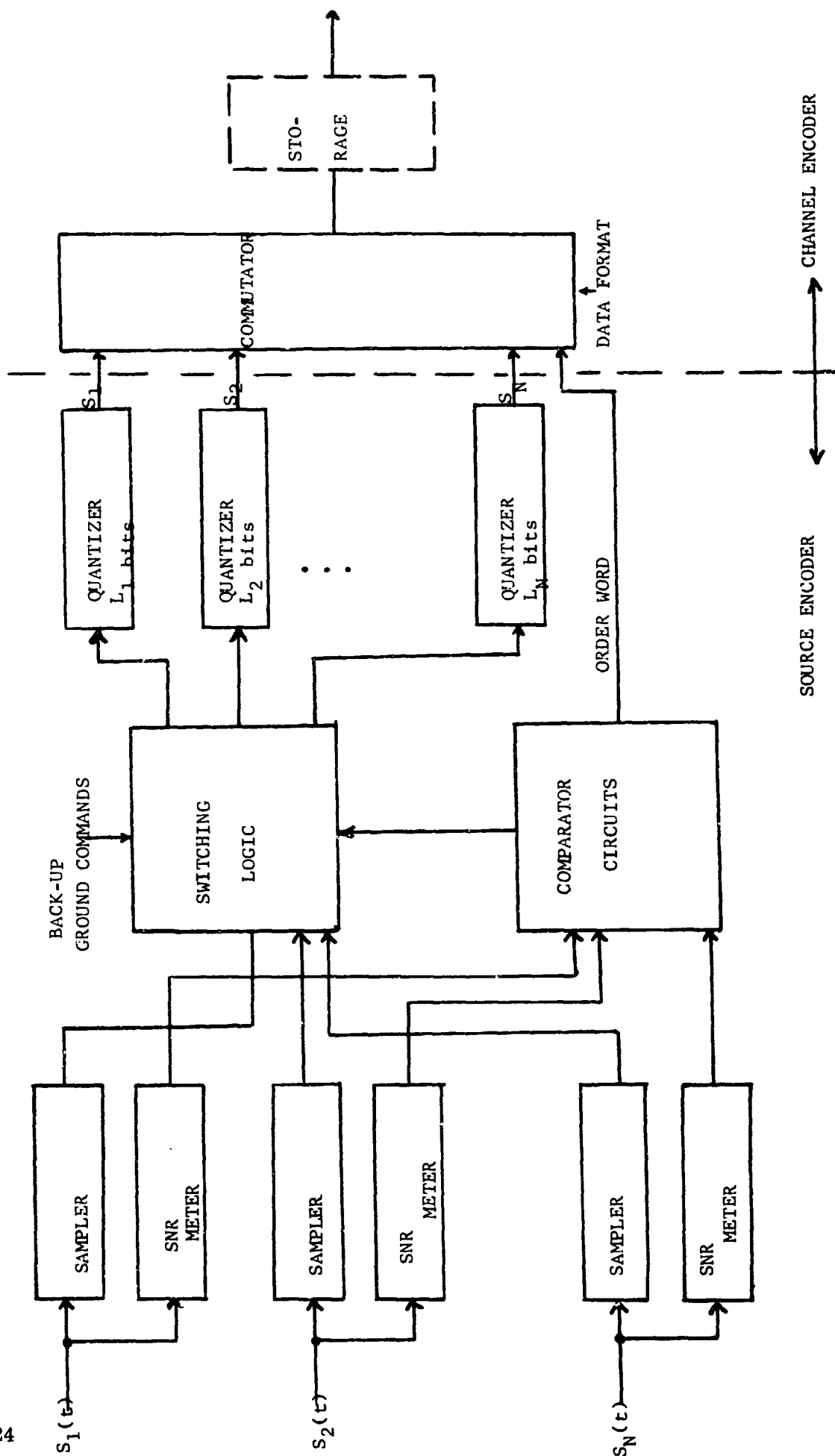
FIGURE 6-6   CONTINUOUS GREY-LEVEL REALLOCATION
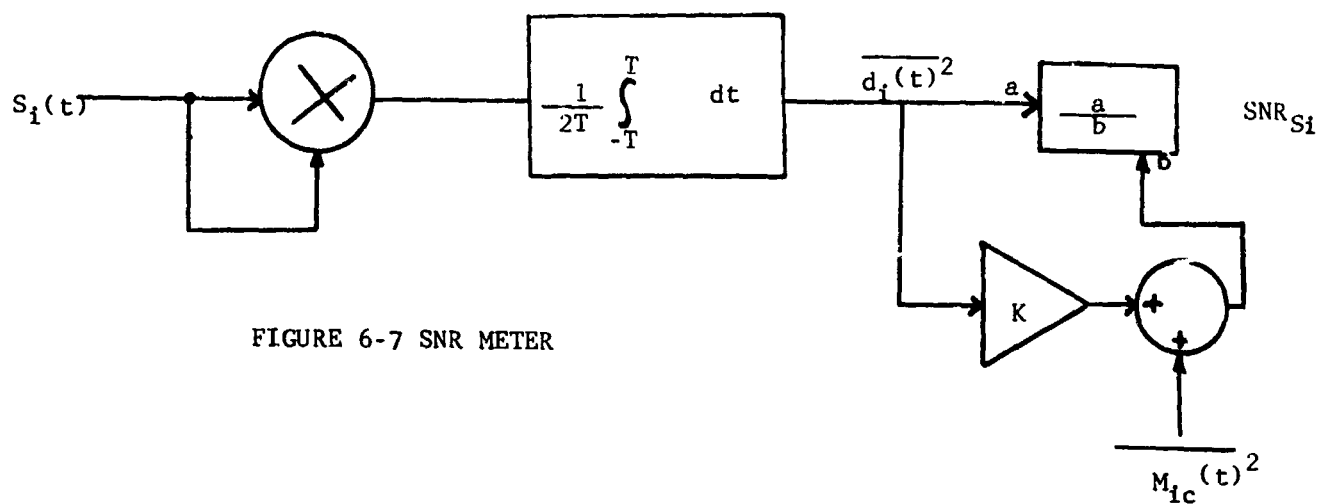
FIGURE 6-7 SNR METER
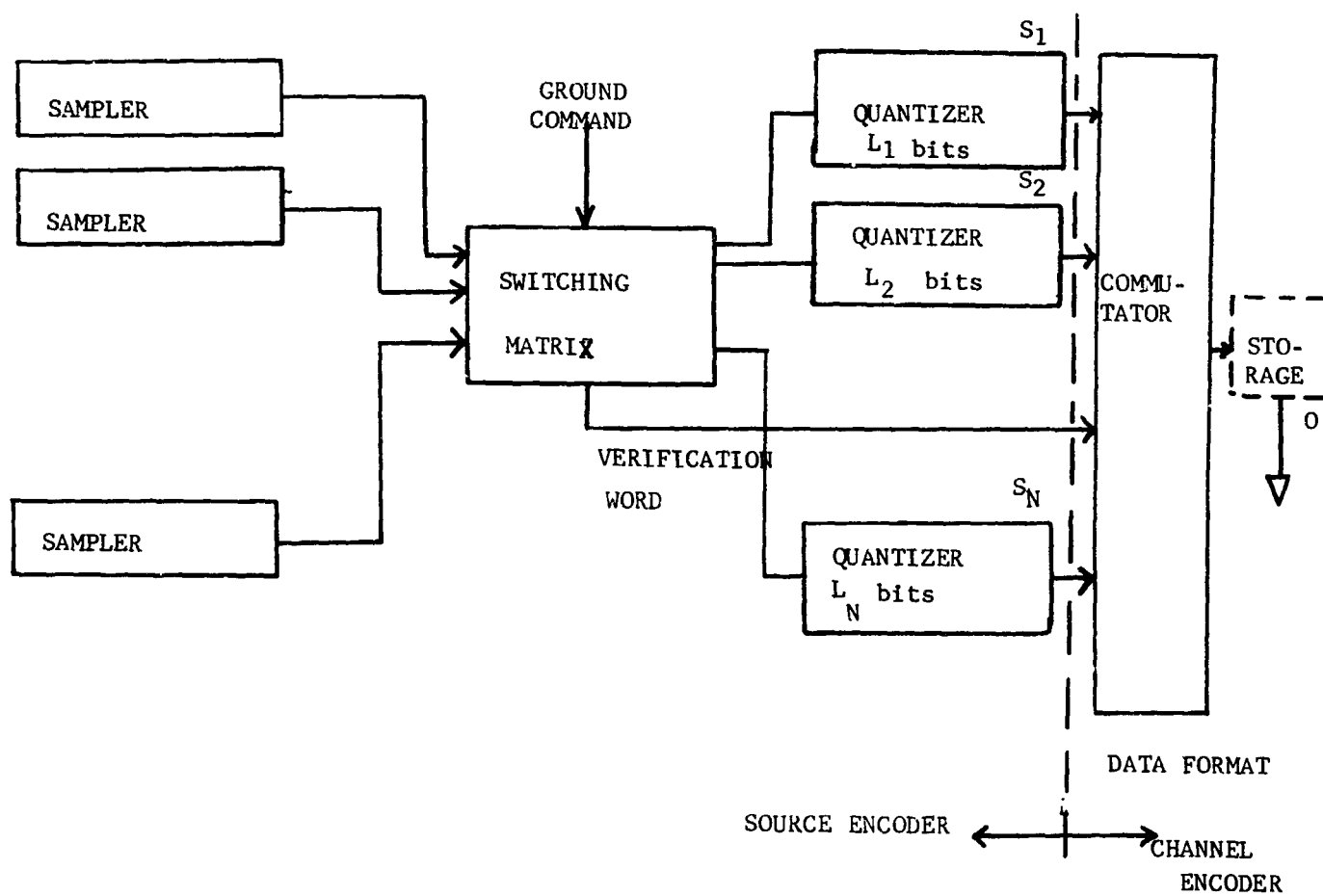
FIGURE 6-8 REALLOCATION OF GREY LEVELS BY GROUND COMMAND

6-25
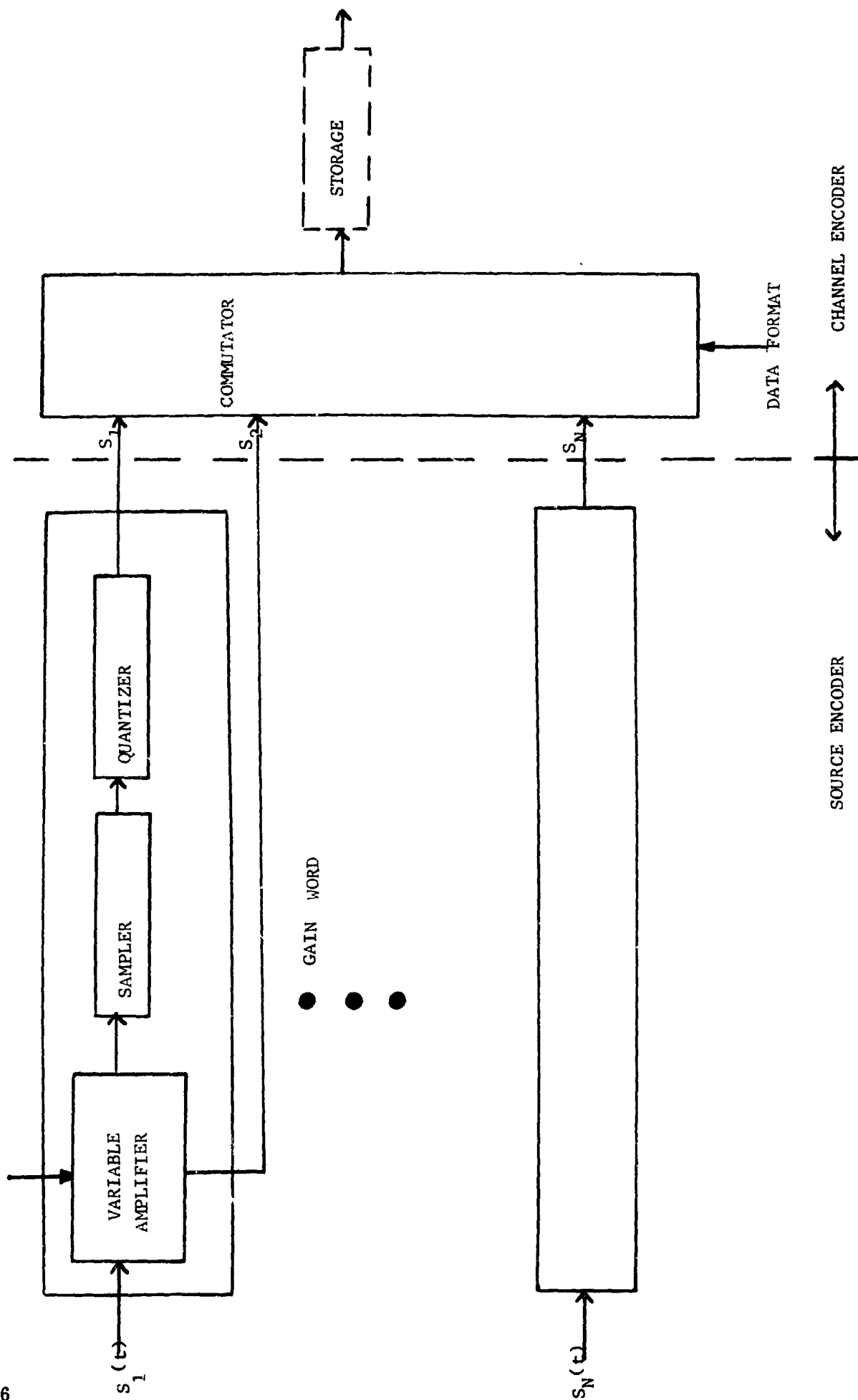
FIGURE 6-9   ADAPTIVE SIGNAL NORMALIZATION
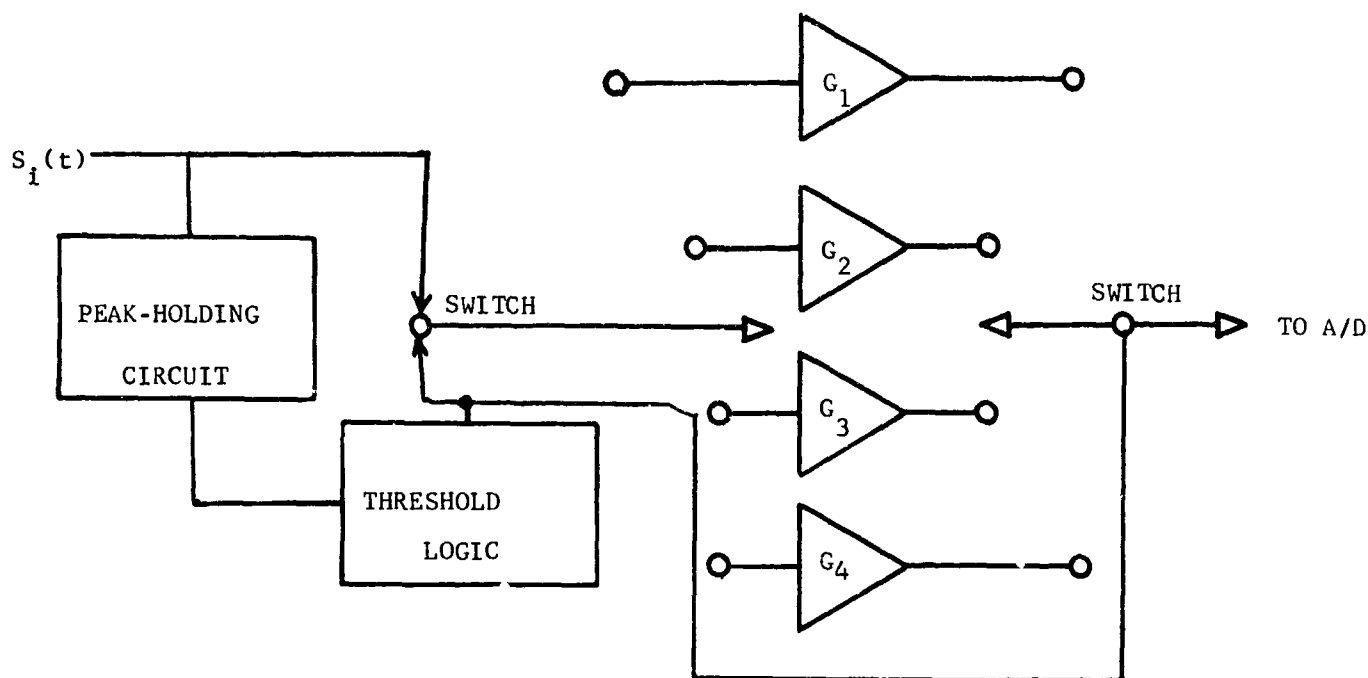
FIGURE 6-10 LINEAR GAIN, VARIABLE MAGNITUDE
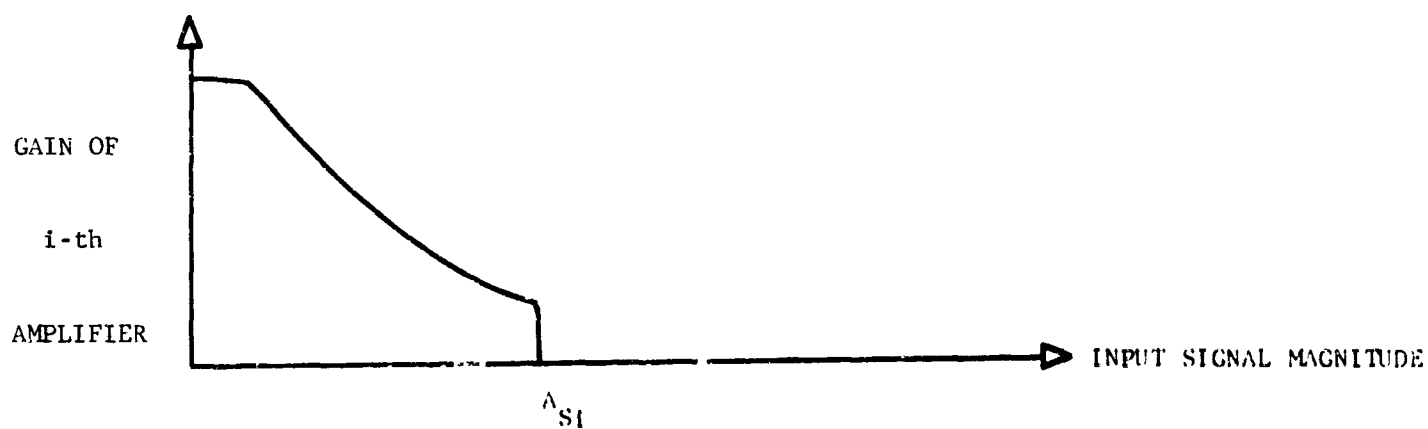
FIGURE 6-11 GAIN CHARACTERISTIC FOR LOGARITHMIC AMPLIFIER

FIGURE 6-12a-SIGNAL BEFORE AMPLIFIER
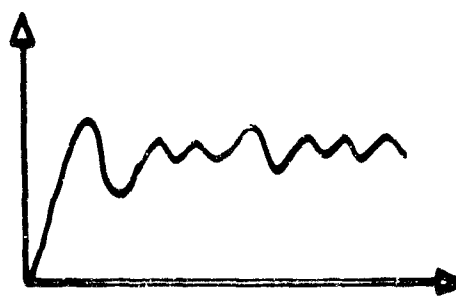
FIGURE 6-12b-SIGNAL AFTER AMPLIFIER
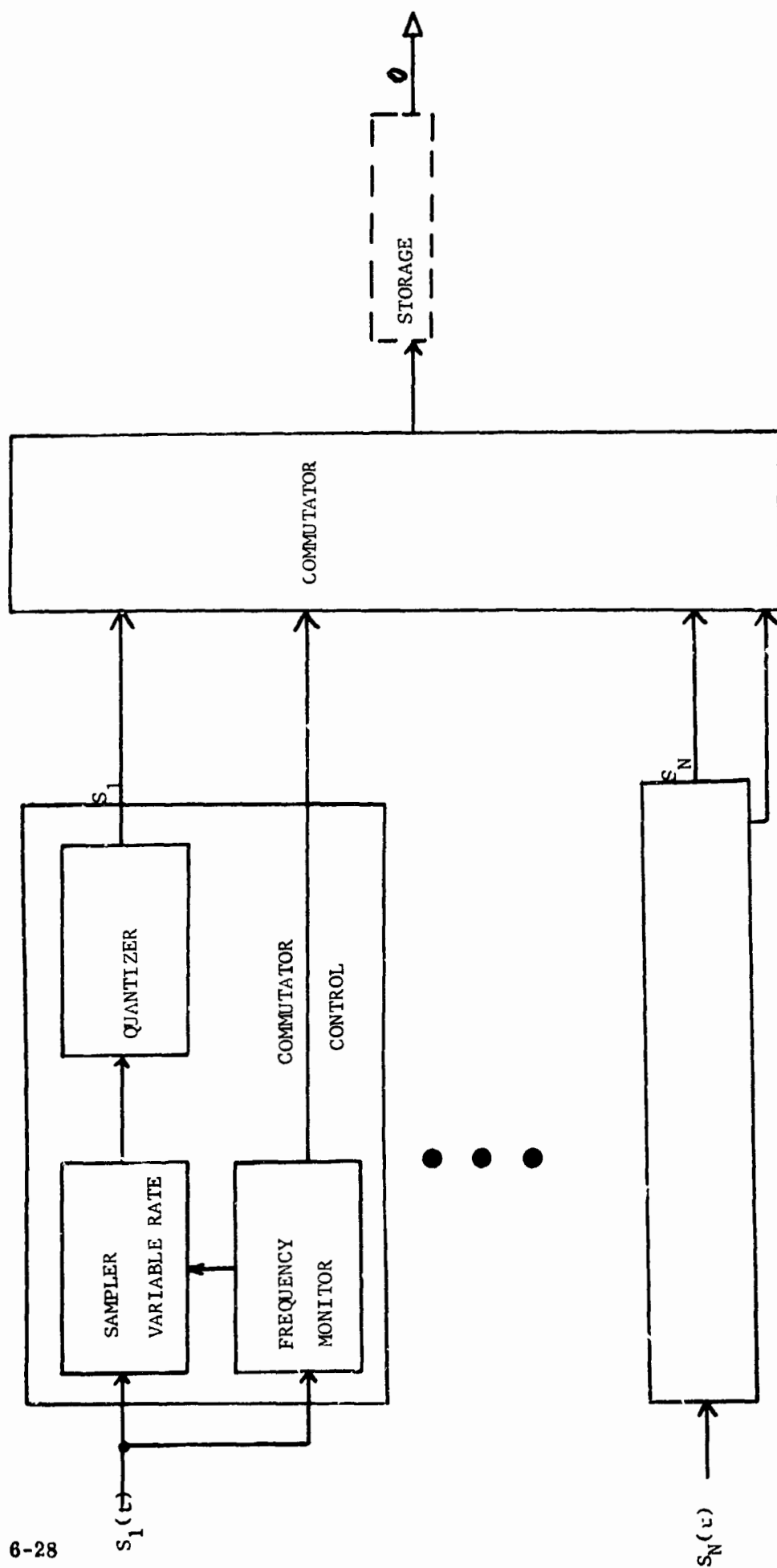
FIGURE 6-13 CONTINUOUS SAMPLING RATE CONTROL
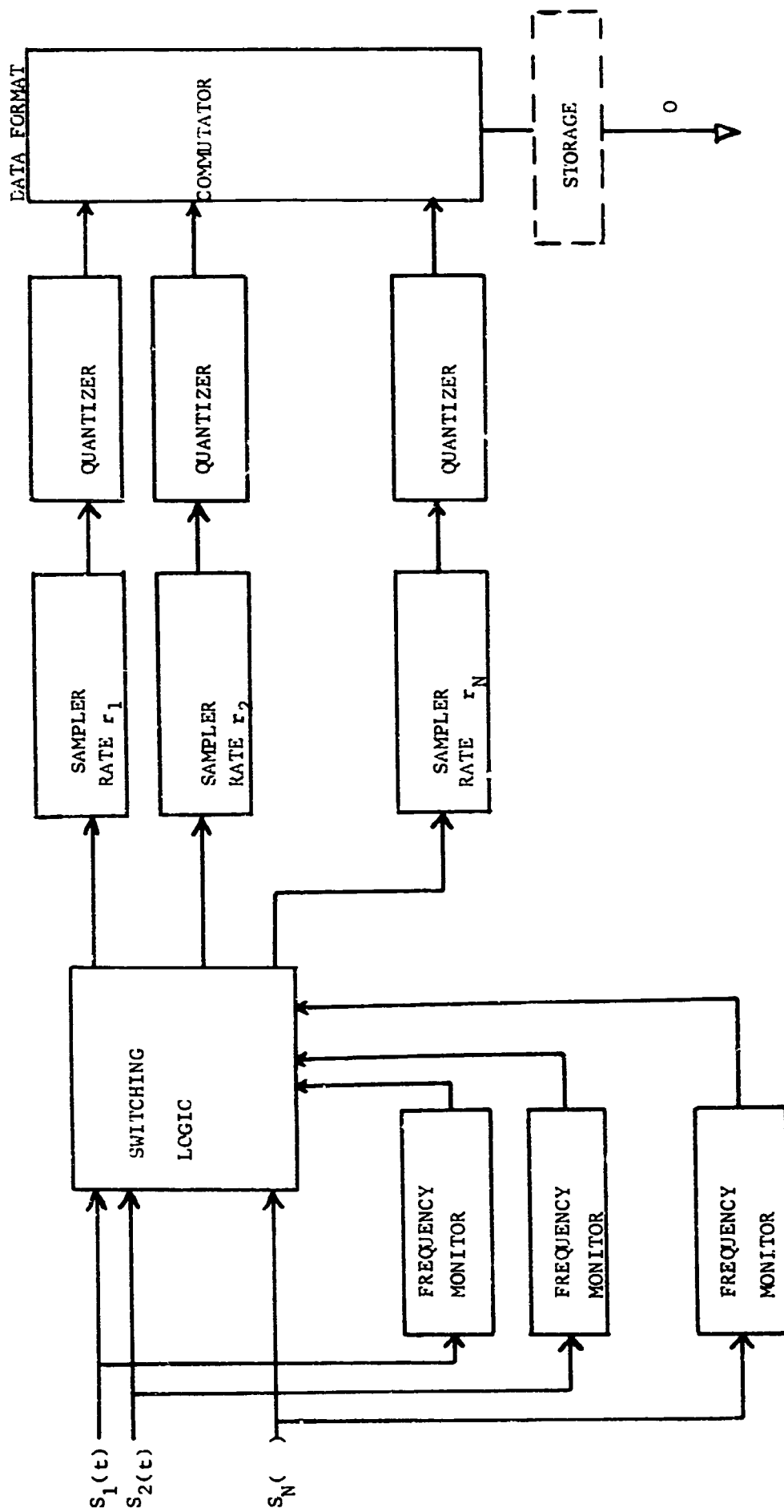
FIGURE 6-14 CONTINUOUS SAMPLING RATE REALLOCATION
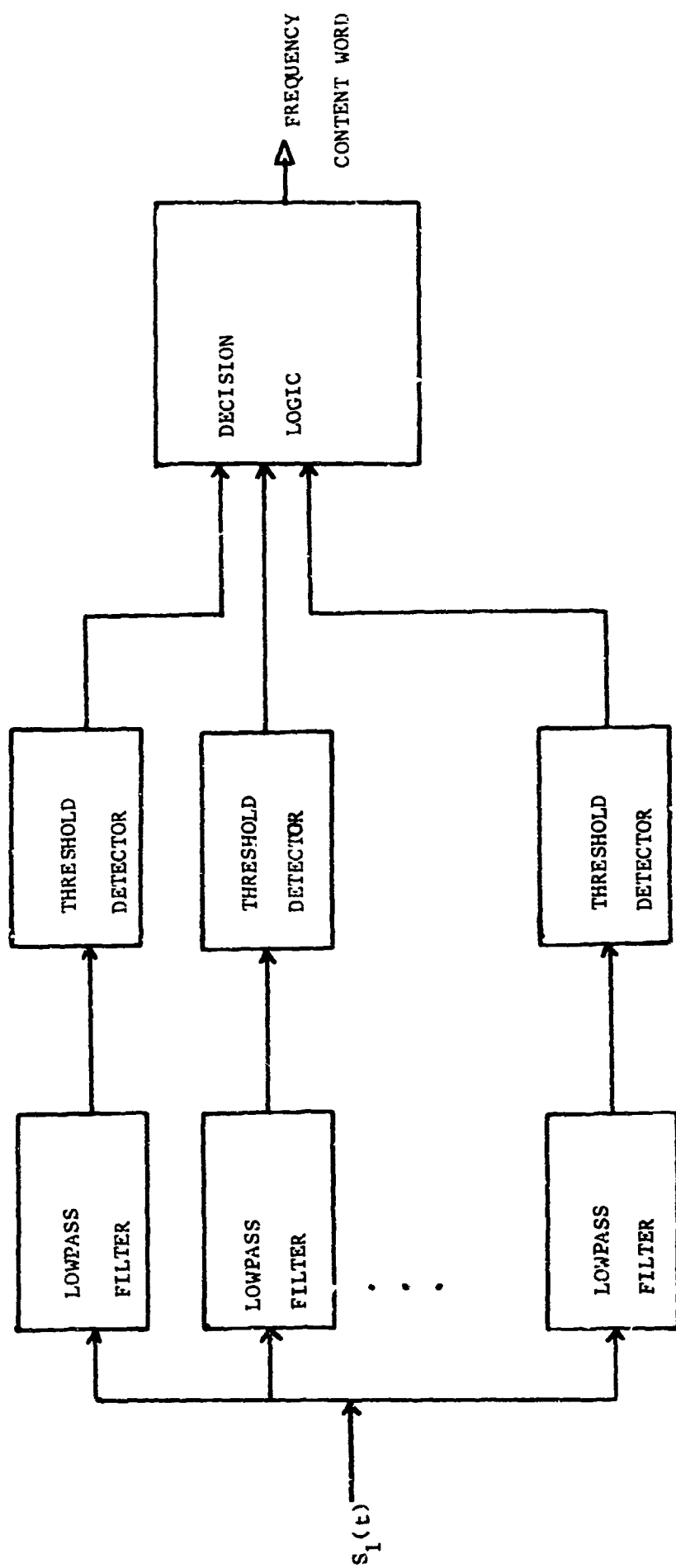
FIGURE 6-15 FREQUENCY CONTENT MONITER
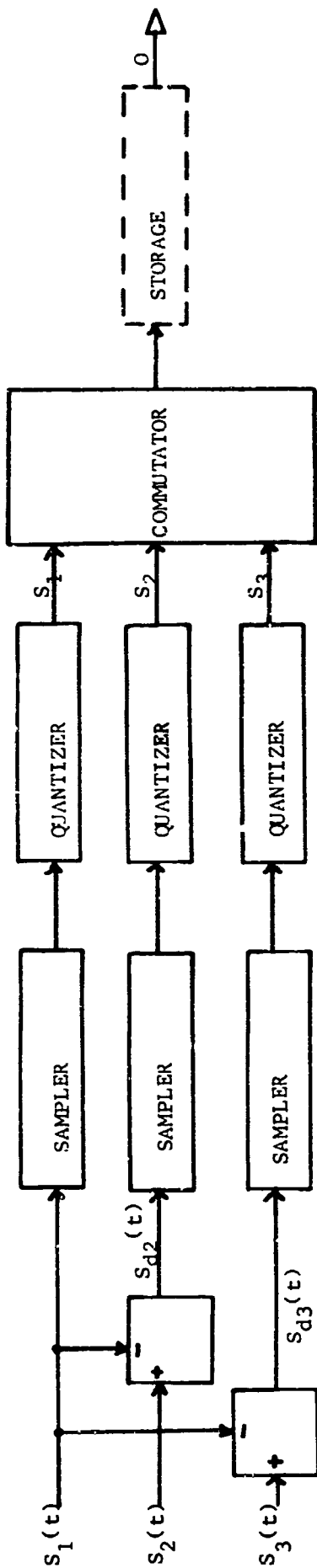
FIGURE 6-16 DIFFERENCE TECHNIQUE
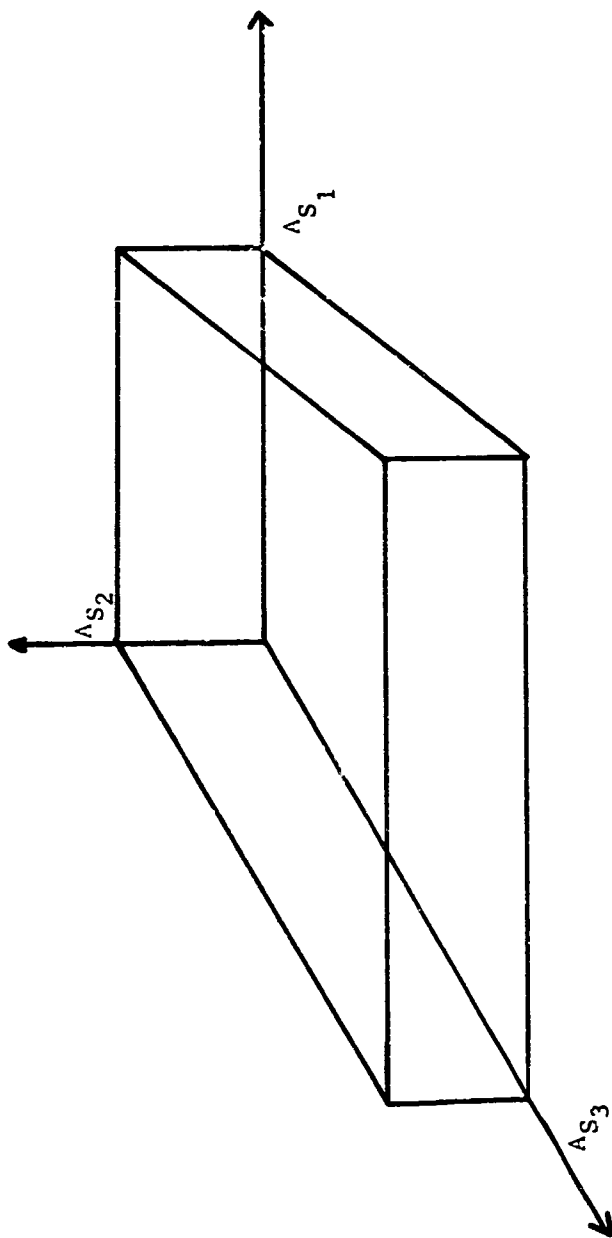
FIGURE 6-17 SENSOR SIGNALS OUTPUT SUBSET
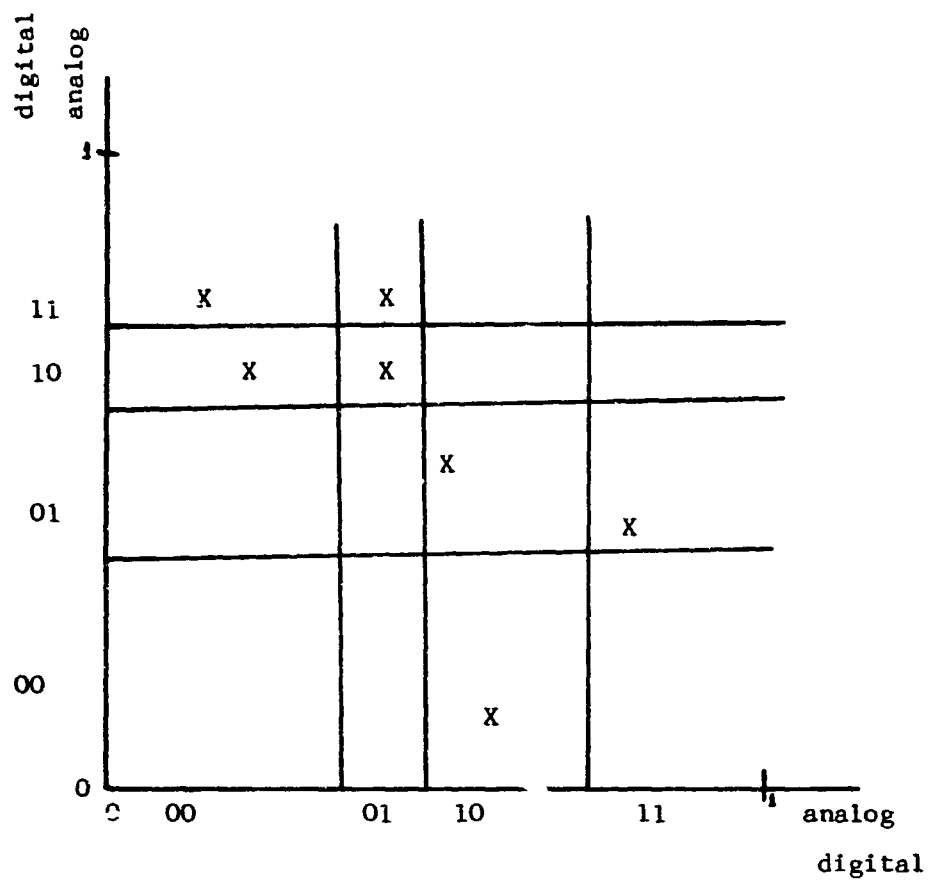
FIGURE 6-18

EXAMPLE REGIONS FOR

BLOCK DIVISION (X DENOTES TYPICAL SENSOR SIGNAL POINT)
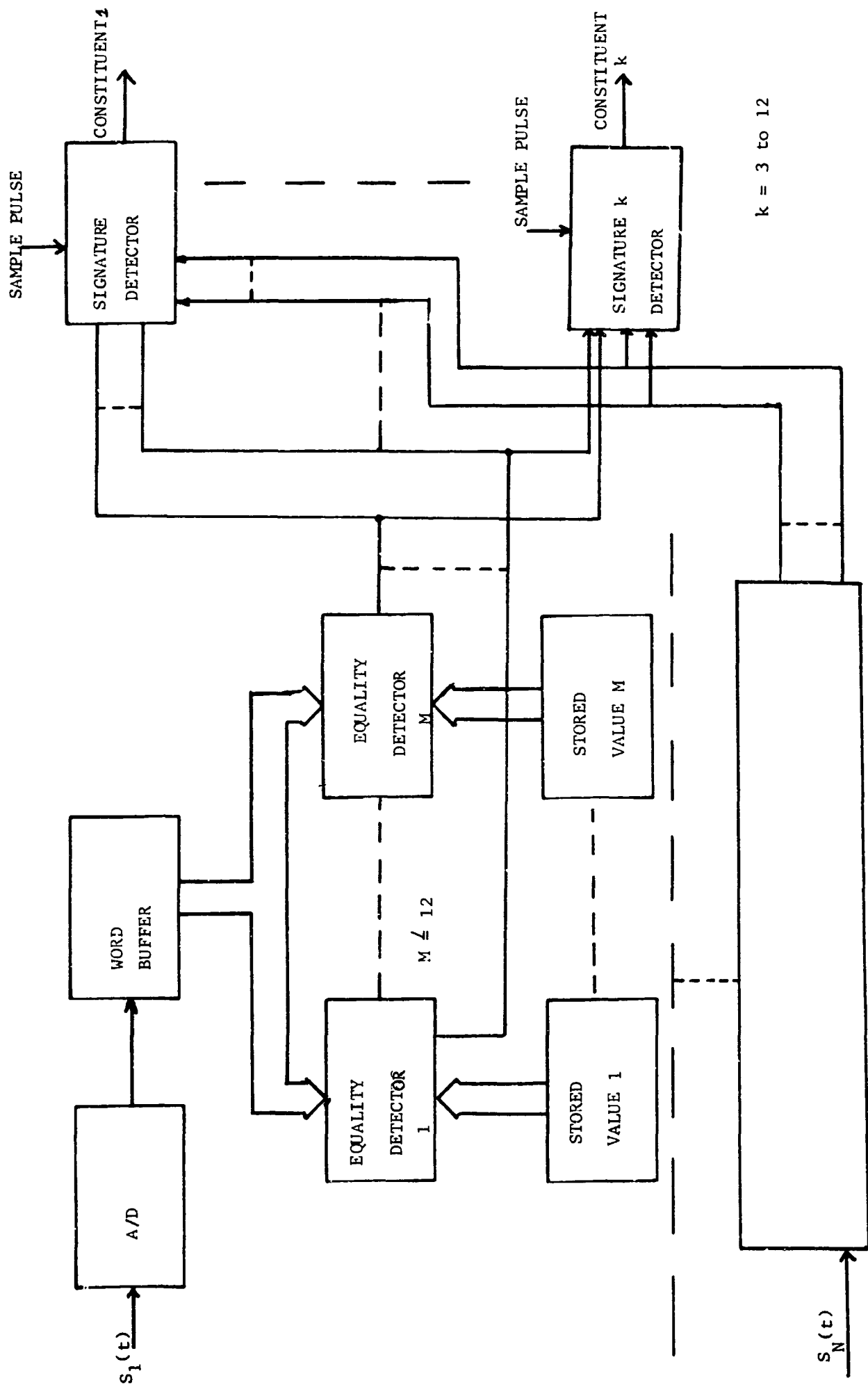
FIGURE 6-19 BLOCK DIVISION SIGNATURE DETECTION
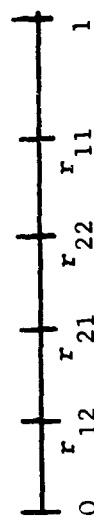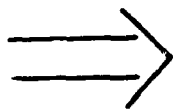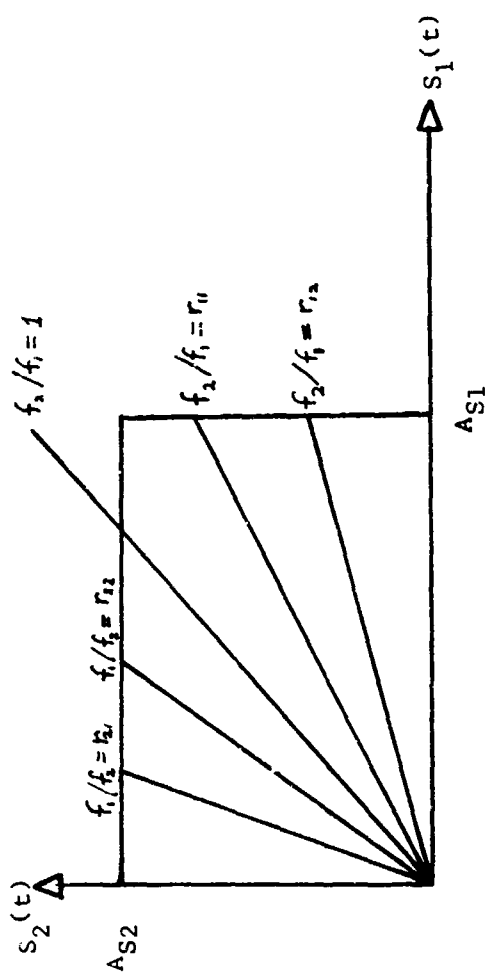
FIGURE 6-20- RATIO DIVISION
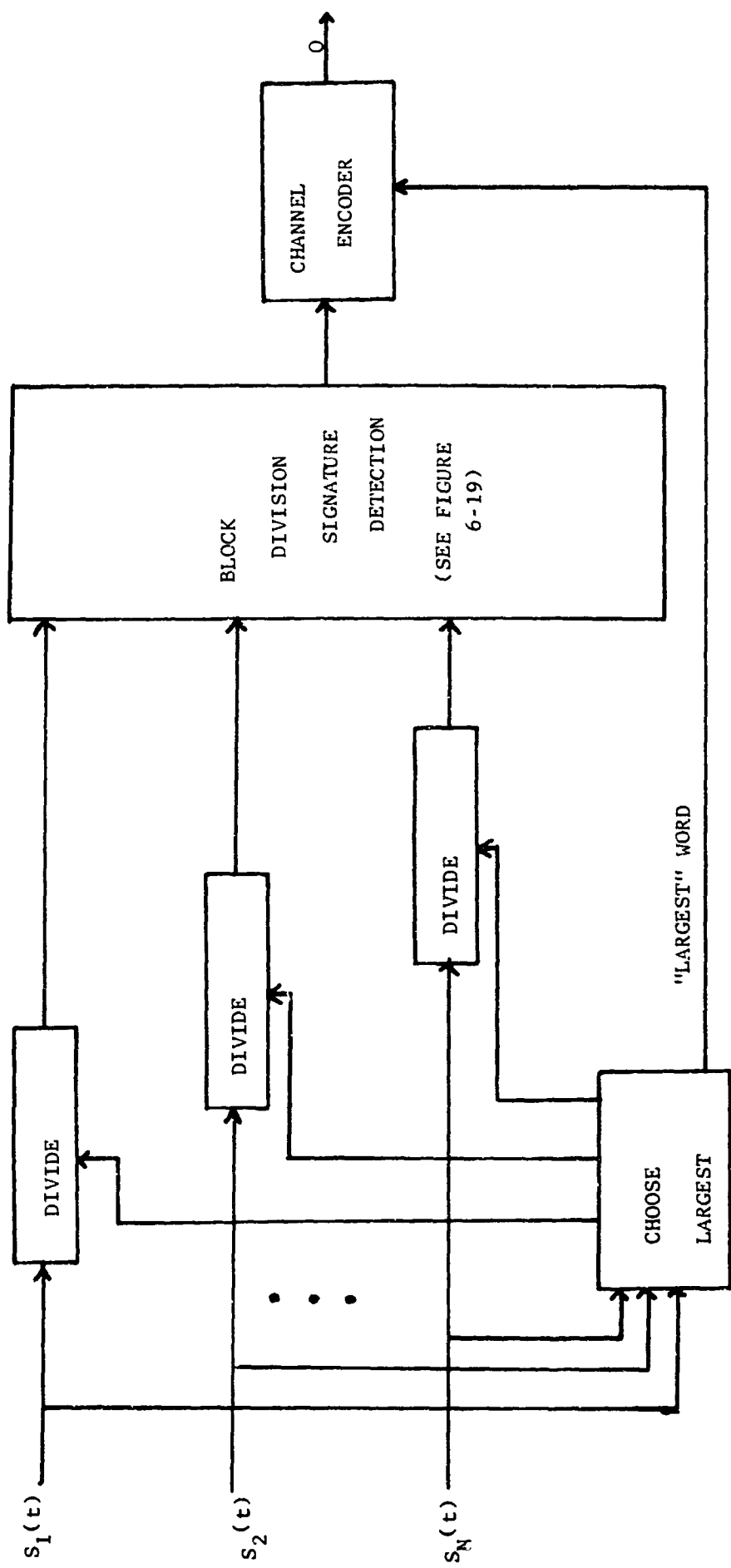
FIGURE 6-21 RATIO DIVISION SIGNATURE DETECTION
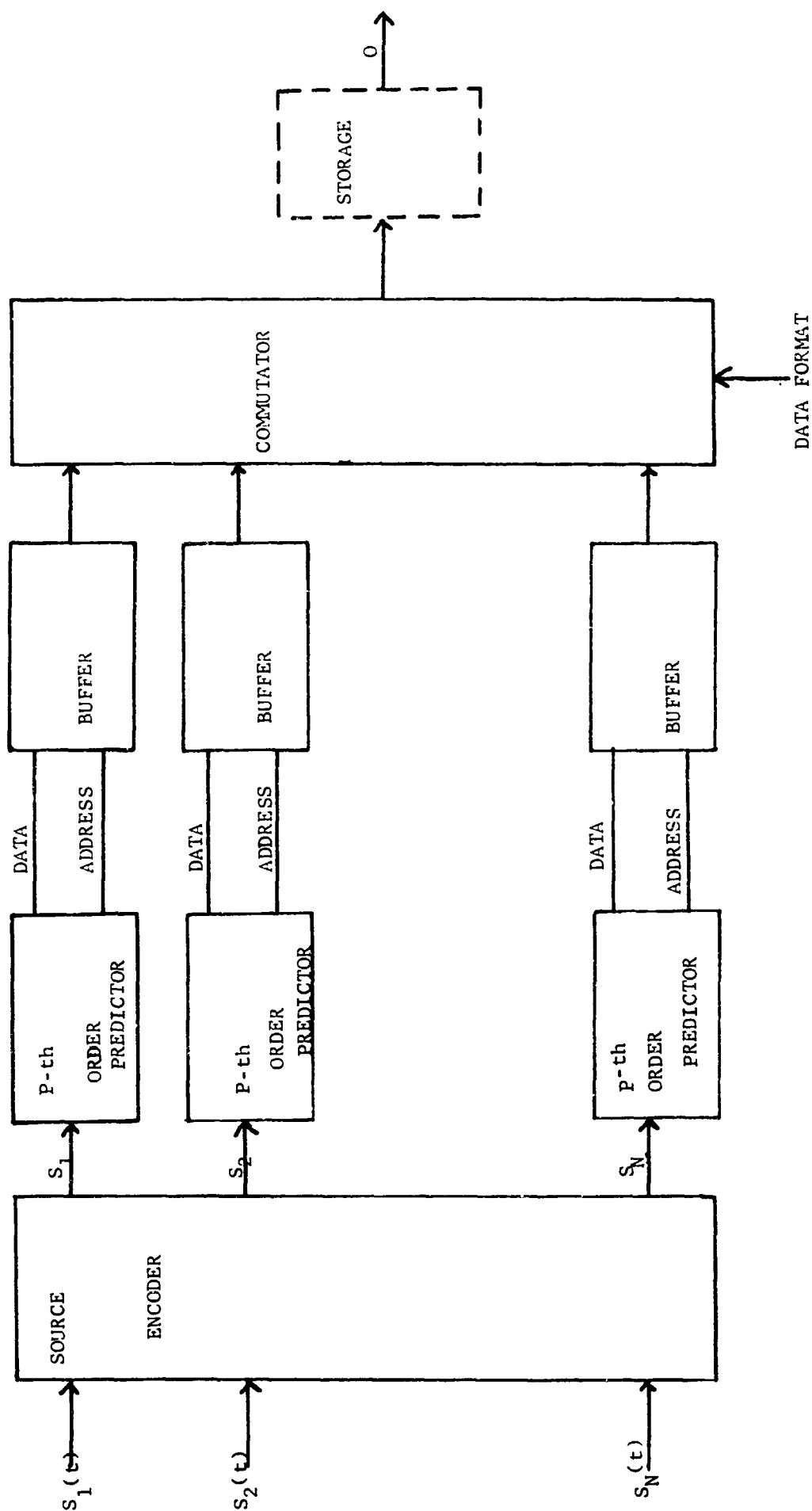
FIGURE 3-22   DATA COMPRESSION IN THE CHANNEL ENCODER
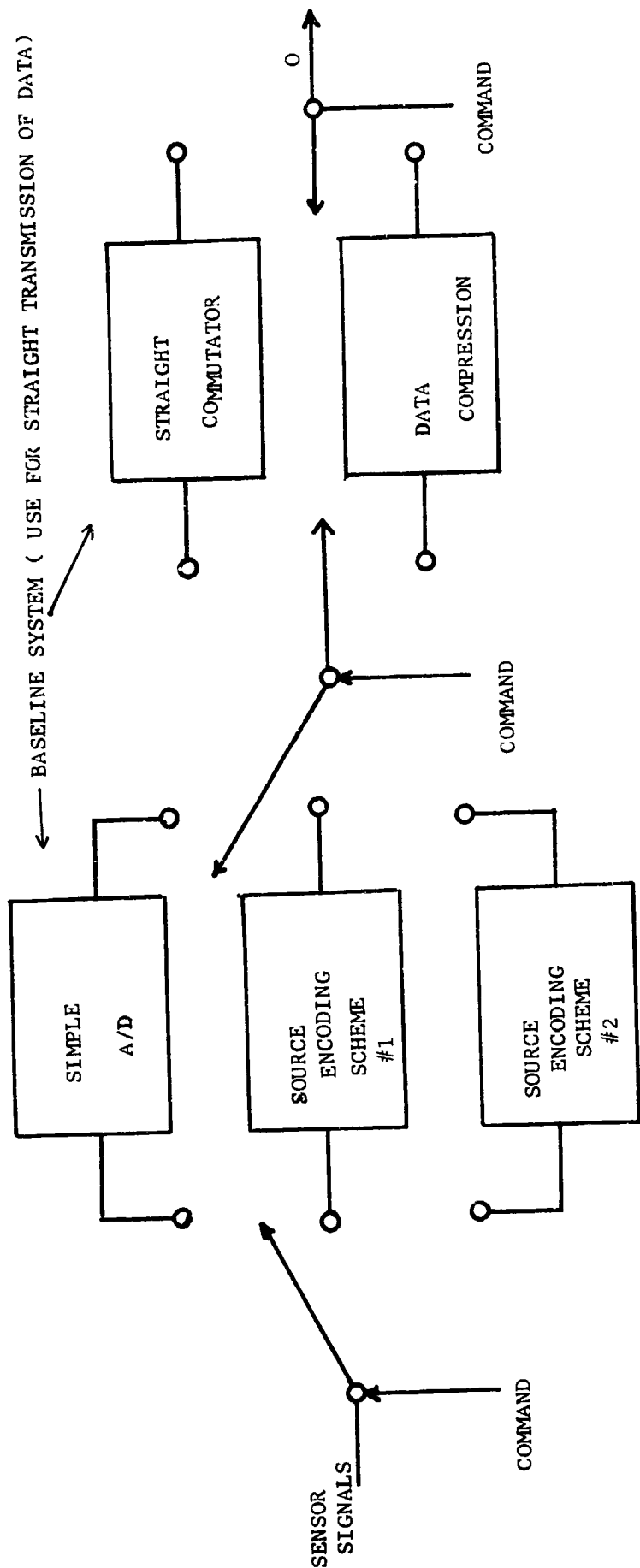
FIGURE 6-23 ONBOARD DATA PROCESSING SYSTEM

SECTION 7

MULTISPECTRAL EXPERIMENT

7.1 DESCRIPTION OF EXPERIMENT AND EQUIPMENT

The multispectral experiment was designed to verify the fact that samples of potential Martian material could be separated on the basis of their spectral reflectance character- istics, in a live scene and in real time. A test tray was constructed to contain the subject materials in an array such that a single TV scan line sampled the video signal from all the constituents. Figure 7-1 is a schematic representation of the test scene and its constituents.

The test tray was placed in the field of view of the General Electric Multispectral TV Test System. This system is shown in block diagram form in Figure 7-2, and the equipment is illustrated in the photographs of Figure 7-3. The sensor system consists of a modified General Electric PE-25A image orthicon color camera, such as those used by the com- mercial TV broadcast industry. The basic camera system includes a three channel optical system; the sensors; individual wide bandwidth sensor channel preamplifiers; channel amplifiers with provision for additive shading compensation, sync and blanking adders; a monitoring and control console with provision for image orthicon bias and registration con- trol; special power suppliers; and sync and blanking generators.

The optical system has been modified with a neutral (spectral) beam splitter and provision was added to insert spectral filters in each channel with separate facility for channel balance using neutral density filters. A remote controlled iris adusts the average illumination in the main relay optic.

The sensor focus and deflection yokes (three separate channels) are matched and will ac- comodate any standard 3 inch image orthicon camera tube (S-1, S-10, or S-20 photocathodes) facilitating the use of the entire visible spectrum (S-10) and including UV (S-1); near IR (S-20 extended red and S-1 to 1.1 microns).

For multispectral analysis the signals in each of the three channels are taken from the preamplifiers and fed into a special video preprocessor intended to linearize the otherwise non-linear outputs of the individual image orthicon camera tubes. The sequence of compensating operations is as follows:

(a) AGE (Automatic video gain control)

(b) ALC (Automatic light control)

(c) Multiplicative Shading correction

(d) Black level clamp

(e) Gamma correction (linearizes the camera tube transfer characteristic)

Following the video preprocessor is the color balance corrector which adjusts the video gain in individual channels for changes in spectral content of the illumination as detected by independent sensors filtered at the same wavelengths as the scene input.

The net result of preprocessing and color balance correction is to provide inputs to the signature analysis processor which are independent of scene illumination.

The signature analysis processor performs two types of analysis. For the first type (used principally in this program) the processor passes video signals in each channel only when the signals fall between voltage thresholds which have been established by the human analyst (operator). Thresholds are set by adjusting calibrated precision potentiometers. AND logic provides an output (single on-off) signal only when signals are passed through thresholds in all three channels simultaneously. The three pairs of thresholds thus define decsion or signature calss boundaries in a three-dimensional signature space, and an analyzer output signal at a given instant implies that the received radiation from the particular scene resolution element at that instant falls within the established signature class.

The second type of analysis uses normalization (in contrast to the linear analysis of the first type). Letting the instantaneous amplitudes of the three spectral channel video signals be represented by x, y, and z, three normalized signals are produced; i.e.

$$\frac{x}{x+y+z} \; : \qquad \frac{y}{x+y+z} \; , \qquad \frac{z}{x+y+z} \; .$$

These normalized signals are then passed through thresholds and AND logic as in the type one analysis. While normalized analysis is particularly useful in certain applications, it is not employed for signature classification in this experiment, but serves a supporting role in the production of the false color imagery presented later.

The output from the signature analysis processor consists of digital video signals corresponding to the signature class decision regions defined by the combination of thresholds. These signals become alarms for the signature classes and are displayed by adding them to the total scene video or may comprise the only video displayed. For most purposes at this point in the technological development it is useful to display these alarms superimposed on the normal video as an aid in correlation of signature classes with objects in the scene.

If a color monitor is used each alarm may be displayed in an independent arbitrary false color, and spatial information may be displayed in false color from one or more spectral channels.

Not shown in the block diagram of Figure 7-1 is the optical unit of Figure 7-2 which is designed to project independent black and white transparencies (taken in different spectral bands) onto the faceplates of three image orthicons thus allowing analysis of multispectral data recorded on film. The film recording may be done by taking pictures in selected spectral regions with a camera or by several methods of producing film analogs of data previously recorded on magnetic tape from devices such as point detector line scanners. Imagery analyzed in this mode of operation may include the entire range of spectral detectability from ultraviolet through the visible, IR, thermal IR and as far out as microwave in any combination of three.

7.2 EXPERIMENTAL DETAILS

Narrow band optical filters for this experiment were chosen on the basis of several criteria as follows:

(a) Prescribed narrow band spectral regions selected for the analytical study were matched as closely as possible with respect to remaining experimental criteria, and available filters.

(b) Maximum separation of spectral filter bands for best discrimination is desireable.

(c) Bands were selected on the basis of spectral reflectance characteristics data provided for maximum separation within the spectral regions.

(d) Maximum filter transmission in each band for optimum signal-to-noise is desired.

(e) Balanced filter transmission for calibration purposes is desired.

Figure 7.4 is a plot of filter transmission vs wavelength for the filters used in the experiment, multiplied by the normalized response of the S-10 photocathode for the type image orthicons (IO) used. Other optical transimissions withinthe system were not taken into account since each channel required the addition of neutral density filters to adjust the photocathode illumination for that portion of the IO transfer characteristic curve which provides greatest linearity and maximum signal latitude. This was accomplished experimentally by measuring signal amplitude of a standard white target over the range of amplitudes from maximum to minumum signal. Figure 7-5 is a typical characteristic curve for the IO's used. It can be seen that maximum signal latitude occurs on the steepest part of the curve.

Inputs to the spectral signature analysis processor were then set equal for the white target by adjusting the IO preamplifier gain in each channel individually using an artifical illumination source. This is necessary because natural sunlight constantly varies under most meterological conditions. Independent spectral measurements (in the bands of interest) were made of both the artifical illumination source and the sunlight to assure proper spectral (color) balance. The artifical source therefore consisted of several lamps (UV, IR

7-4

and Photo floods) in an effort to get a spectral match to the sun, resulting in illumination matched to within about 10% in spectral content and down in average level by a factor of 20 to 1. This provided a calibration which was valid for sunlight by neutral density compensation when changing from artifical to natural illumination, and verified by viewing the same standart black to white measurements performed in both situations. Calibration of this type makes it possible to repeat threshold decisions on a day to day basis for most moderate meterological conditions. This calibration does not imply, however, that precise spectral reflectivity data can be reproduced.

The subject materials were then placed in the test tray as shown in the color photo of Figure 7-6 and viewed at an angle of about 45° to a local normal on the tray. The tray was reoriented periodically in an effort to maintain a sun angle normal to the tray. This technique worked reasonably well between the hours of about 11 a.m. to 3 p.m. each day. The illumination calibration seemed to hold reasonably well within this period of time.

7.3 EXPERIMENTAL RESULTS

The results of the experimental multispectral analysis consist of a group of photos (Figure 7-7 through 7-12) and comments to aid in data correlation and interpretation. Table 7-1 is a data summary including the comments in a digested form.

Comments:

---- In general the display was generated on a studio color monitor with a red background. Actually spatial information was included in the red input to the monitor, but the red bias was turned up high enough to swamp out the picture details. There is difficulty in matching color film sensitivity to the radiant energy output of the picture tube phosphors such that the green gun looks yellow in the photographs and the blue gun looks like violet at low brightness and near white at high brightness.

7-5

---- No attempt was made to eliminate false alarms except with the subject materials. Hence some pictures show the wood of the test tray, and the concrete pavement upon which the tray was placed.

---- Adjustment of the threshold potentiometers contains a degree of subjectivity depending upon the operator, but in general the criterion was to obtain the best alarm signal with the least number of false alarms in each photo. This somewhat precludes the possibility of a purely objective set of alarm signal criteria.

---- It should be noted that reflected energy contains specular components as well as diffuse energy, and that these two phenomena will produce different video signals. Since the solid samples have various facets there are necessarily false dismissals and false alarms produced by these specular returns.

---- It should also be noted that the results are valid only for the particular constituent specimens which were used in the experiment.

---- Making use of Table 7-1, and Figures 7-6 through 7-12 one can evaluate the constituent alarms with proper notation of false alarms and false dismissals.

TABLE 7-1 DATA SUMMARY

Legend

Enhance   *
False Dismissal O
False Alarm   x

Figure -	7.7	7.8	7.9	7.10	7.11	7.12
Light-dark boundaries				x		x
Dunite						*
Very light dunite facet						O
Dark shadowed facets		x	somex			C
Granite				*		
Dark shadowed facet		x	x			
Lichen					*	
Light (sunny) edge					x	
Specular reflecting specks			x			
Rhyolite						
Very light facet	x	x				
In dark shadows of other rhyolite			x			
Semi-dark facet				x		
Basalt			*			
Semi-dark facet (limonite stained)			O		x	
Dark facet			O			
Light vein				x		
Sand	*	*				
In shadow of left side of box	O	O		x		x
In shadow of granite			x			
In shadow of rhyolite				x		
Limonite		*				
In shadow of left side of box						
In shadow of lichen		O			x	
In shadow of basalt		O			x	
Right and lower right area in box		O				
Limonite in shadow of dunite					x	
Horizontal edge of box	x	x				
Vertical edge of box				x		
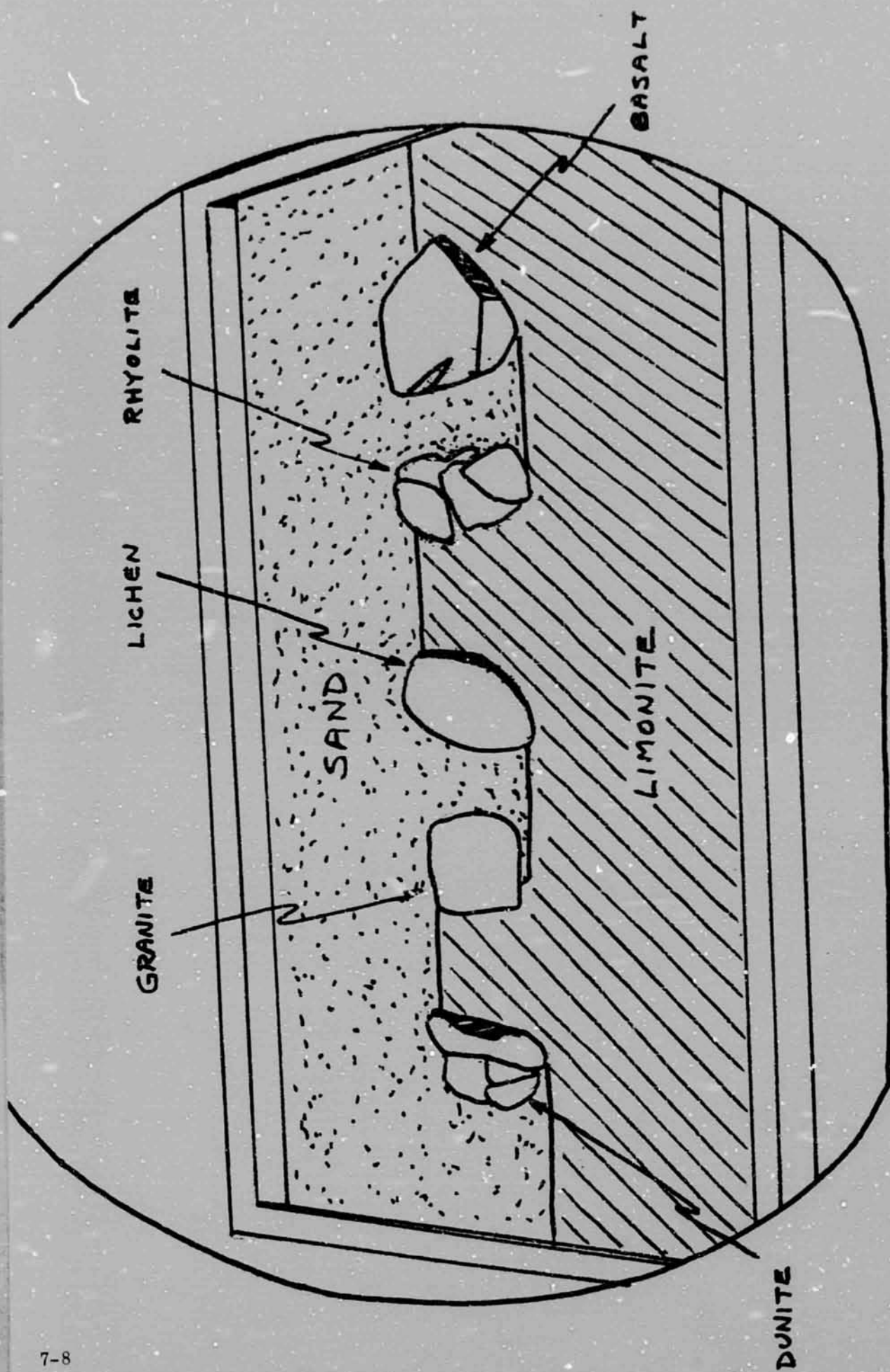
FIGURE 7-1 SCHEMATIC OF SAMPLE TRAY
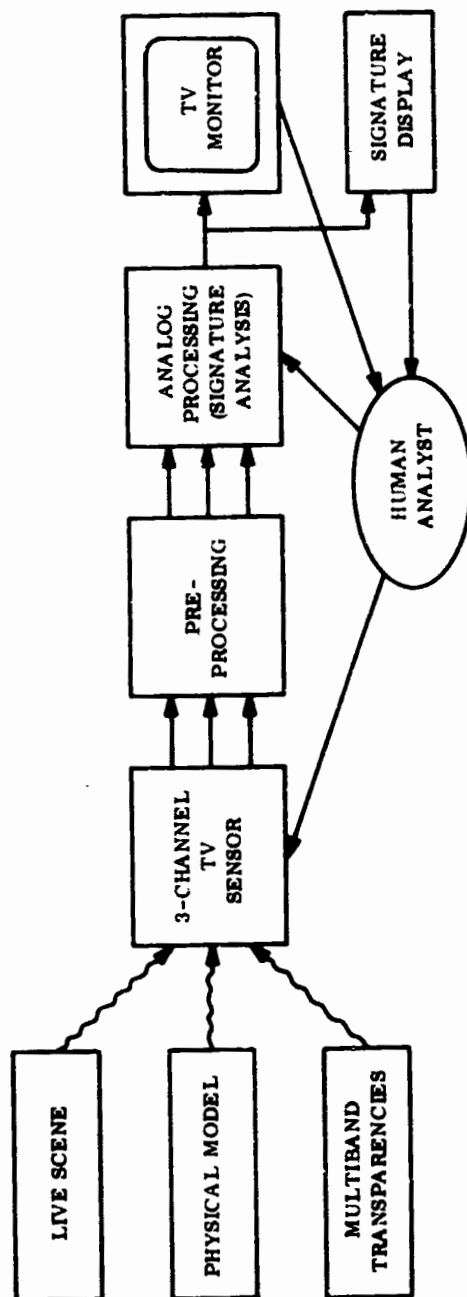
Figure 7-2. Multispectral Test System Block Diagram
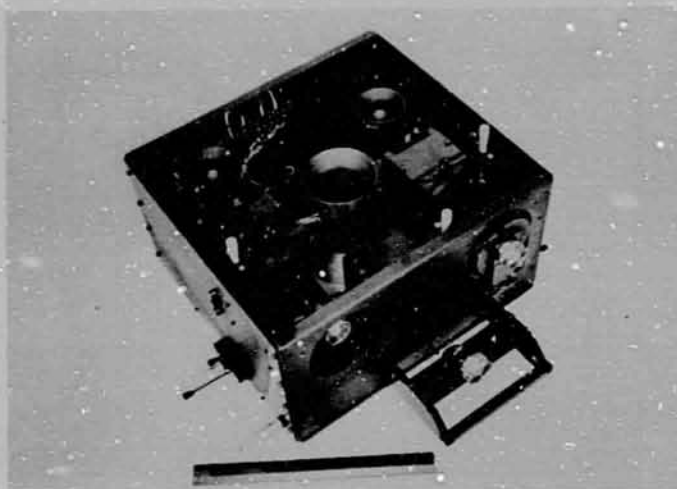
MULTISPECTRAL TV TEST SYSTEM (TOP) AND OPTICAL UNIT (BOTTOM) FOR
INPUT TO THE SYSTEM VIA MULTIBAND TRANSPARENCIES

FIGURE 7-3

FIGURE 7-4

FILTER TRANSMISSION
CHARACTERISTIC

7-10A

7-10A

FIGURE 7-5

LIGHT TRANSFER

CHARACTERISTIC

Z-7883

PHOTO CATHODE ILLUMINATION (ft-c)
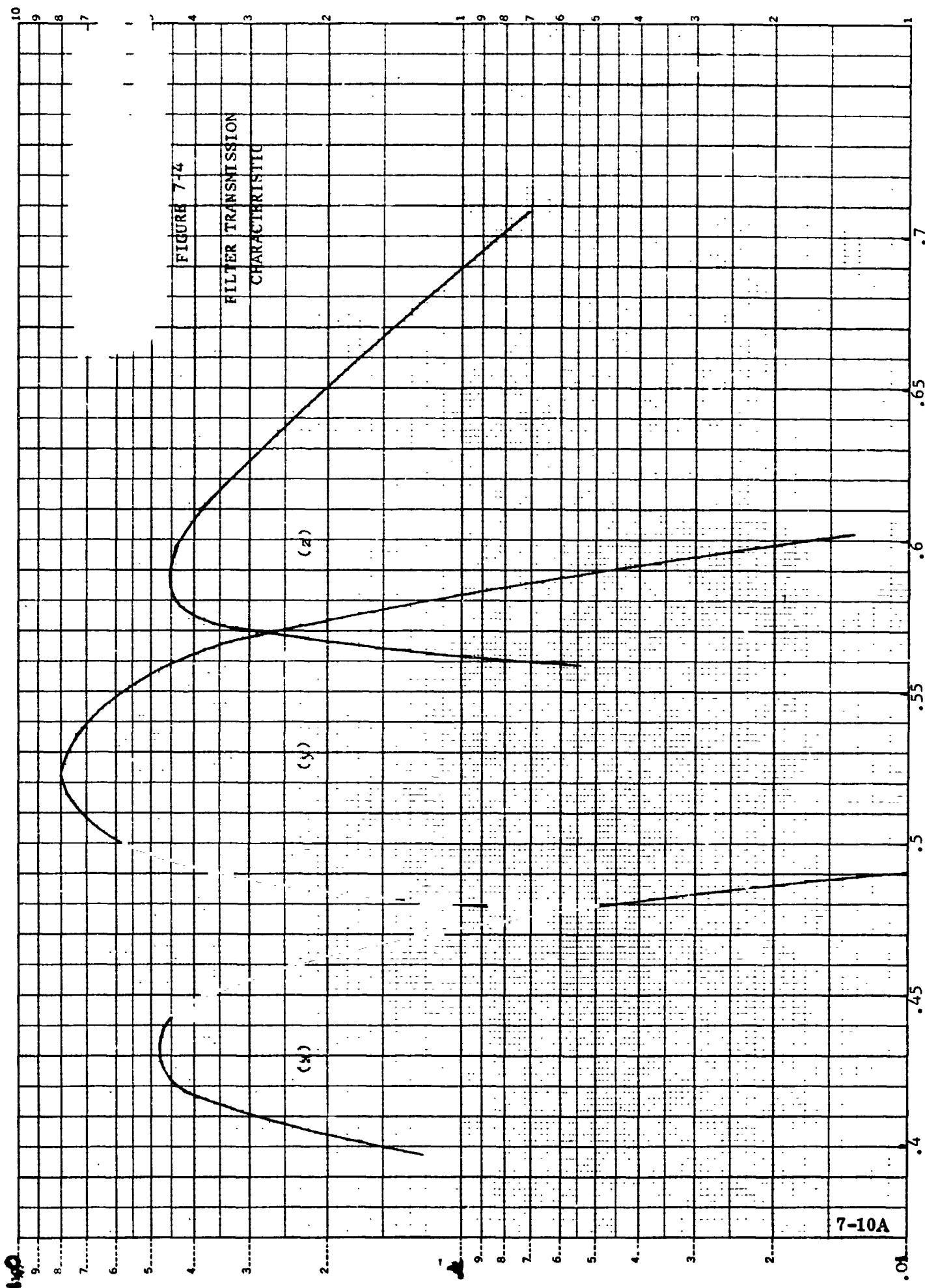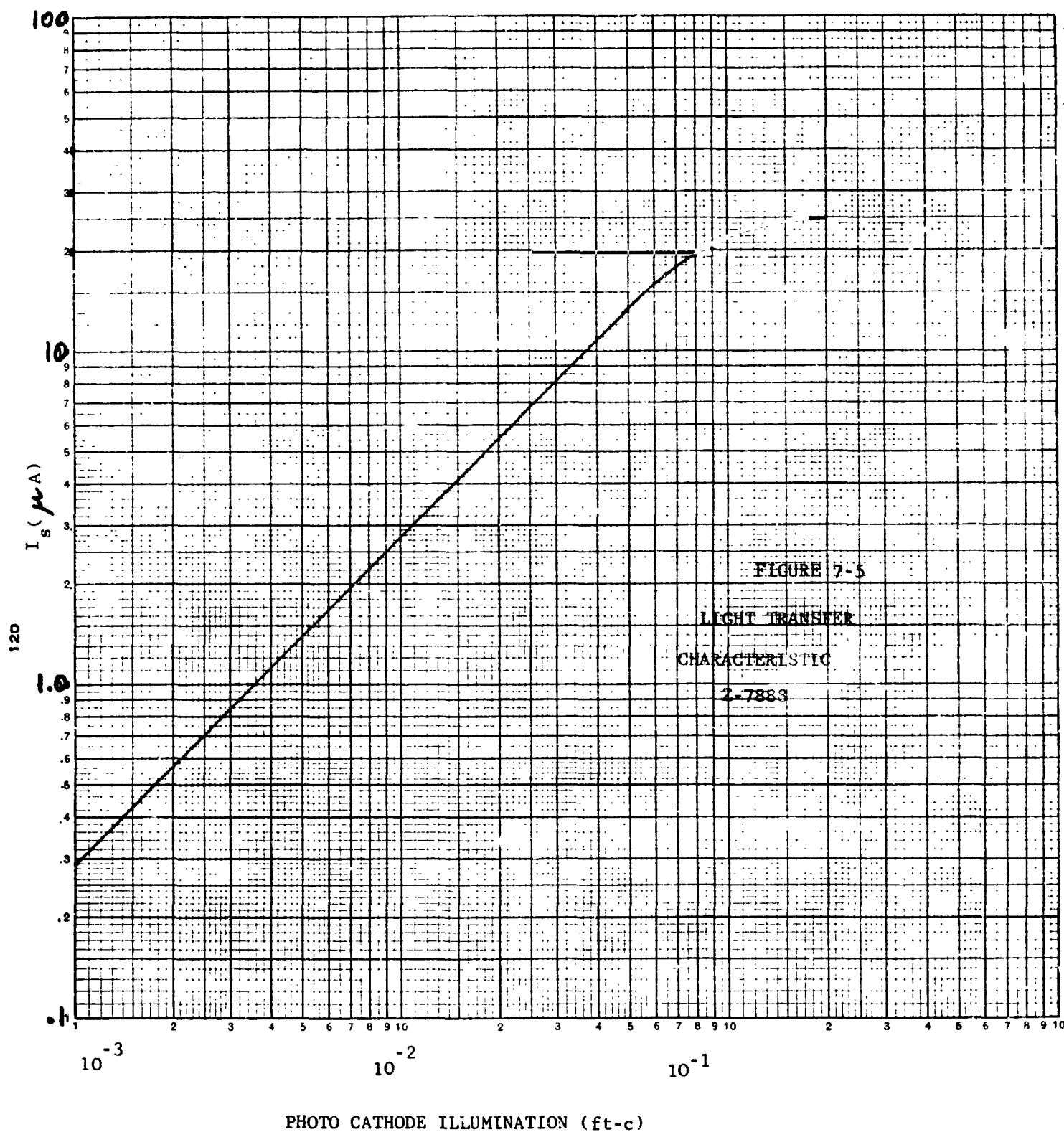
FIGURE 7-6   COLOR PHOTOGRAPH OF TEST TRAY

FIGURE 7-7   FALSE COLOR DISPLAY SAND ALARM
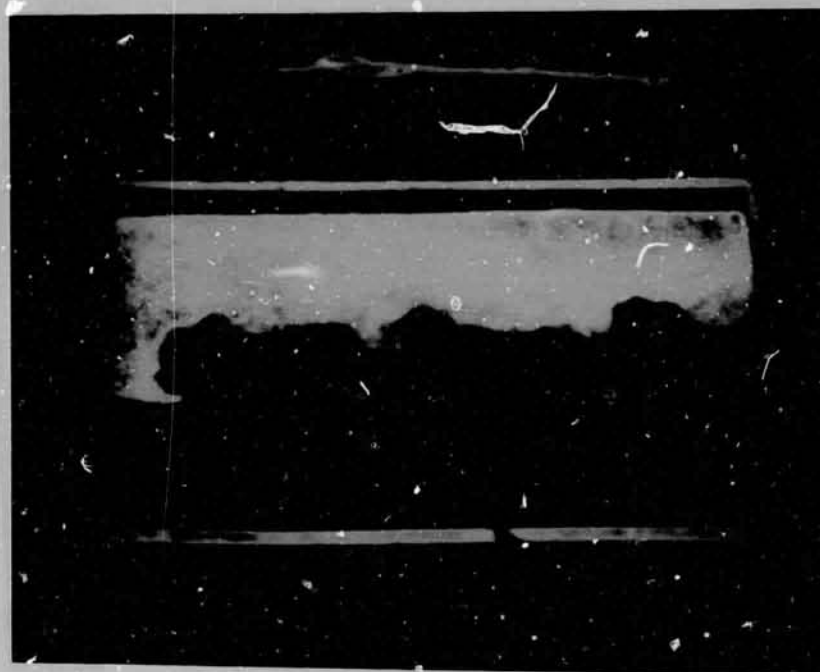
FIGURE 7-8   FALSE COLOR DISPLAY SAND ALARM (LINEAR ANALYSIS)
             LIMONITE ALARM (NORMALIZED ANALYSIS)
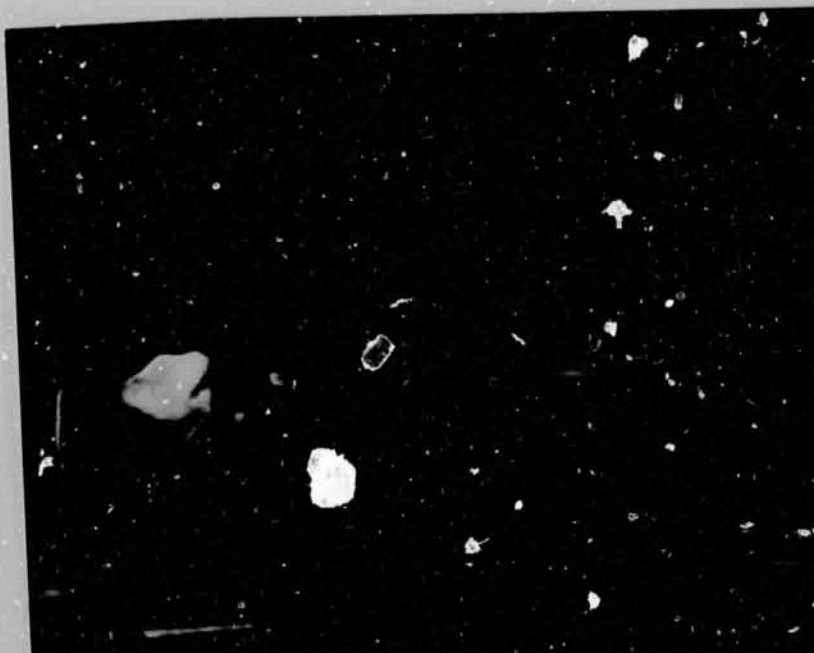
FIGURE 7-9 FALSE COLOR DISPLAY BASALT ALARM

FIGURE 7-10 FALSE COLOR DISPLAY GRANITE ALARM
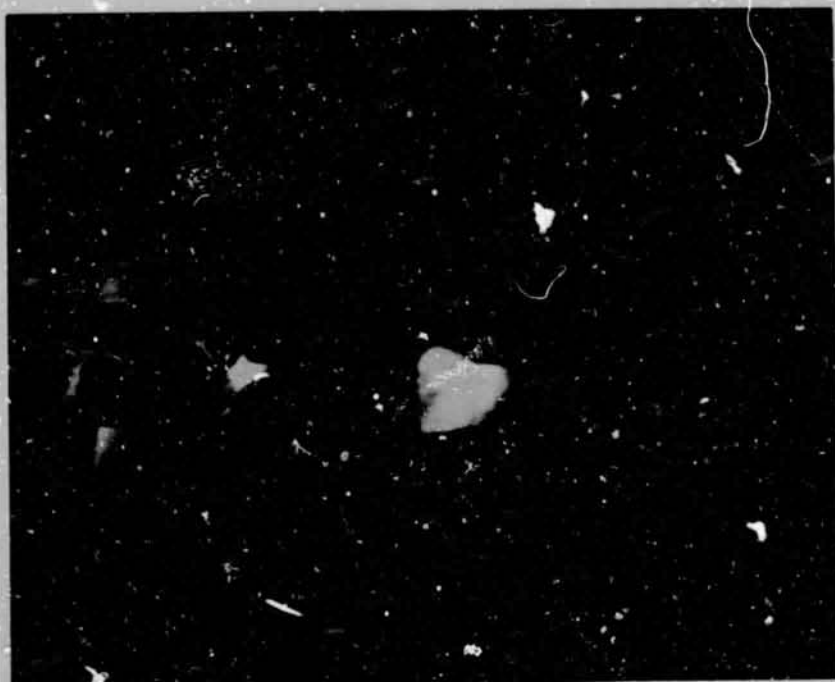
FIGURE 7-11 FALSE COLOR DISPLAY LICHEN ALARM
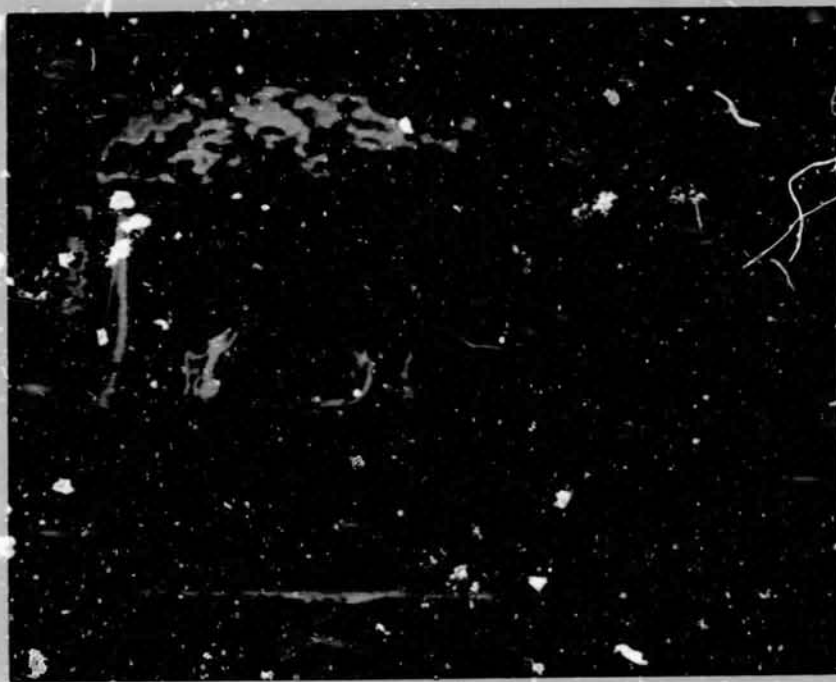
FIGURE 7-12 FALSE COLOR DISPLAY DUNITE ALARM

SECTION 8

CONCLUSIONS

8.1 BROAD BAND ANALYSIS

The study has shown that the compounded spectral properties of irradiance, reflectivity, filters and sensor can be effectively compared from sensor to sensor through the modulation concept. The modulation determined in this study was confined to varying spectral qualities only; it is felt that the method will be more effective when sensor noise, and response time are considered.

8.2 NARROW BAND ANALYSIS

The narrow band part of this study received the greatest attention. The technique devised to describe effectiveness of the filter to discriminate between the selected constituents of the test scene was the modulation criterion. The results showed that if the band is narrow enough, relative to the spectral profiles of the reflectivities, modulation performed on the reflectivities only, and not on the sensor outputs, will be sufficient to choose the best spectral location for the filters. The band-width of the filters to which these conclusions apply are of the order of 100 $\overset{o}{A}$ - 500 $\overset{o}{A}$ at half-width. This conclusion does not necessarily apply to other materials and constituents, for it has become clearly evident during this study, that detailed knowledge of the spectral characteristics of the scene is a fundamental requirement, and that any conclusion made, refers specifically to the depth of that knowledge. For band-widths that are wider than a few hundred Angstroms and narrower than the spectral range of most detectors, there is a bandwidth, beyond which the reflectivity modulation will not be the same as sensor output modulation. The band's location and width will again be a function of the constituents and their spectral characteristics. It is also possible that in this order of bandwidth some rapidly varying spectral properties of the irradiance and the scene will become important.

Within the scope of the present study the latter two parameters were not found to be significant, primarily because noise and risetime were not considered. It is felt that when these are taken into account the modulation curves for a given scene will begin to vary significantly

from detector to detector, and the technique is expected to be very powerful in this respect. The importance of the detector has not been fully shown in this study for yet another reason: a practical filter has transmission characteristics of significance at other wavelengths than those within the band for which it was designed. These often vary considerably from manufacturer to manufacturer, and a partial "break through" of radiation in a spectral region to which the detector is more sensitive is not uncommon.

The overall conclusion in the narrow band section of the study, is therefore, that the basis of a powerful technique has been laid down and that it will become a significant criterion when practically observed phenomena are included in the analysis.

8.3 THE FILM-DENSITOMETRY EXPERIMENT

The prime purpos : of this was to show the reader the nature of the scene that was being examined in natural colour and in a multispectral representation. Through not being able to empirically determine the reflectivities of the materials used in the experiment for use in the computer program, a quantitative proof of the analytical method was not possible. However the use of the modulation technique was verified under non-ideal circumstances.

8.4 THE MULTISPECTRAL T.V. EXPERIMENT

The results from this experiment were very encouraging, and clearly showed that the various constituents could be discriminated in the presence of noise. However, in this experiment, as in the analysis, more variable forms of the same constituent are needed to completely evaluate the discrimination techniques that may be used.

8.5 DATA REDUCTION

Although all of the data compression schemes presented show promise of reducing the total data load, only those for which the data saving can be determined before launch (i.e. non-adaptive, non-closed-loop schemes) are truly practical. The performance of most data reduction techniques will be aided by normalization of detector outputs; nevertheless, variations in spectral signature due to sun angle, camera angle, constituent grain size etc. may make on-board, automatic signature identification quite unreliable.

SECTION 9

FOLLOW-ON WORK RECOMMENDATIONS

Our overall strategy was to develop and test in this study a technique which would aid in the selection of combinations of detector color bands and grey levels for a set of somewhat idealized conditions e.g. we did not consider any of the known experimental variations such as changes in reflectivity with sun and camera angles. Once the approach was found to be successful under these conditions, we were planning to modify the computer programs and experimental tasks to include variations of these parameters, and repeat the study under more realistic conditions. Due to the limited funding and time, this additional work could absolutely not be included in the present contract. We therefore propose a follow-on study which would continue the examination of optimum filter-detector relationships with consideration of some or all of the following factors that are known to be important.

9.1 THE INFLUENCE OF SURFACE OPTICAL PROPERTIES

The optical behaviour of the surfaces of the constituents is a function of many parameters. In order to ascertain the variability of the spectral signature, the dominant optical parameters must be studied and experimentally examined. The ones which we think should be brought into the overall scope of the multiband study are the following:

9.1.1 VARIATION WITH GRAIN SIZE

The spectral reflectivity of most rock and mineral constituents is a strongly varying function of grain size. (Refs. 47 and 51) In some cases the reflectivity at a particular wavelength can change by factors of up to 18 or more when the grain size is reduced from the order of millimeters to tens of microns in diameter. In general the reflectivity of the material is inversely proportional to the grain size. Often a large contribution to the reflected radiation is specular, is therefore strongly directional and has the spectral properties of the illuminating source. The latter properties are particularly significant in fully describing the range of signatures a constituent can have.

9.1.2 POLARISATION

The specularly reflected light is often strongly polarised. The degree of polarisation is expected to increase with the specular component and therefore be inversely proportional to the grain size. The action of a polarised filter in imaging will clearly aid, in circumstances of high polarisation, the inherent signature of the constituent to dominate to a higher degree, and will by virtue of reducing the reflected light increase the contrast ratio.

9.1.3 NATURE OF THE ILLUMINANT

The existance of an absorbing and scattering medium lying between the source and illuminated scene, and between the latter and the imaging system, can in certain circumstances completely alter the spatial modulation of the scene. In broad terms a scattering medium will redistribute the incident light so that in extreme cases the illumination is incident in all directions instead of being concentrated in a near parallel beam. The result of destroying plane parallelism of the incident beam will be to reduce the scene contrast, and is an effect which cannot be ignored when imaging on a planet such as Mars, which has a thin atmosphere which may contain large numbers of scattering media.

The relative reflectivites of materials of different grain size will vary with sun and camera angles, as illustrated in Figures 9-1 and 9-2. This will make the contrast modulation function, described in Section 4, dependent on these angles. In a follow-on study, we would like to compose a typical scene including constituents of several different grain sizes and take narrow-band pictures of the scene at many different sun and camera angles.

9.1.4 EFFECT OF RESOLUTION

As the resolution of an imaging system is varied, not only does the intensity contrast of the scene appear to change but also the spectral reflectivity of constituents may vary. For instance, as one starts resolving individual crystallization regimes of a mineral rock, the reflectivity can vary significantly from one part to another of the same rock. We, therefore, propose to examine briefly the effect of a resolution element becoming large enough to encompass within it several surface constituents. This problem also emerges anew with the imaging of distant scenes. The instantaneous field of view of the

sensing system may cover a sufficiently large area at a distance, so that more than one constituent is contained in the observed area.

9.1.5   SURFACE OPTICS EVALUATION

It is suggested that the above surface properties are evaluated in the follow-on study in two ways:

    a.   Analytically

    b.   Experimentally

In evaluating a) existing applicable data will be used on two or three selected constituents, and run in the existing program. It is felt more practicable at this stage to evaluate a few materials in depth, and to firmly establish the technique. It is suggested that the experimental program should be done through the use of multiband MTF of the appropriate scenes using visible, near IR and infrared techniques. An example of the technique is shown below (Figure 9-3) for sections across the Death Valley in California. The two Scene Modulations are derived from a) a color slide directly and b) a positive copy of the color slide. The direct analysis of the color slide is effectively a very narrow spectral band at the wavelength of the Helium-Neon Laser that was used to determine the scene spatial modulations.

An extension to this technique is the use of an infrared camera operating between one and five microns. The display of the camera will limit the number of gray bands but the results can be analyzed like the modulation technique as before.

This approach shows the attraction of determining the effective optical frequencies in the various bands and will record through the same function, variation of the spatial frequency of the scene as a function of lighting conditions, grain size of the constituents and degree of polarisation.

9.2 OPTICAL EMISSION FROM CONSTITUENTS

Beyond several microns one expects the radiation due to thermal emission from Martian constituents to approach the intensity level due to reflection. Therefore the effect of thermal emission on the selection of spectral bands and grey levels should be investigated. The value of supplemental imaging at night to discriminate constituents on the basis of their emission signatures should also be studied.

9.3 DETECTOR NOISE

The present study was idealized to the extent that detector noise was neglected. This means we are trying to discriminate a constituent signature not against a background of noise but against a background of other constituent signatures. The next logical step is to include detector noise, typical scan rates and other parameters affecting the signal-to-noise ratio to determine how they influence our band and grey level section.

9.4 MARINER RESULTS

Provided the appropriate data is made available, the scene contrast obtained during the current Mariner flight can be compared with simulated scene compositions and the predicted output for the sensor compared with that experimentally obtained.

9.5 FOLLOW-ON EXPERIMENTS

We recommend extending the experiments into the infrared and measuring the effects of sun-camera angle, constituent grain size, polarization, and resolution upon the discriminability of constituents in a topographic scene. In addition we would like to perform a closed loop experiment to determine how the number of grey levels effects the discrimination.
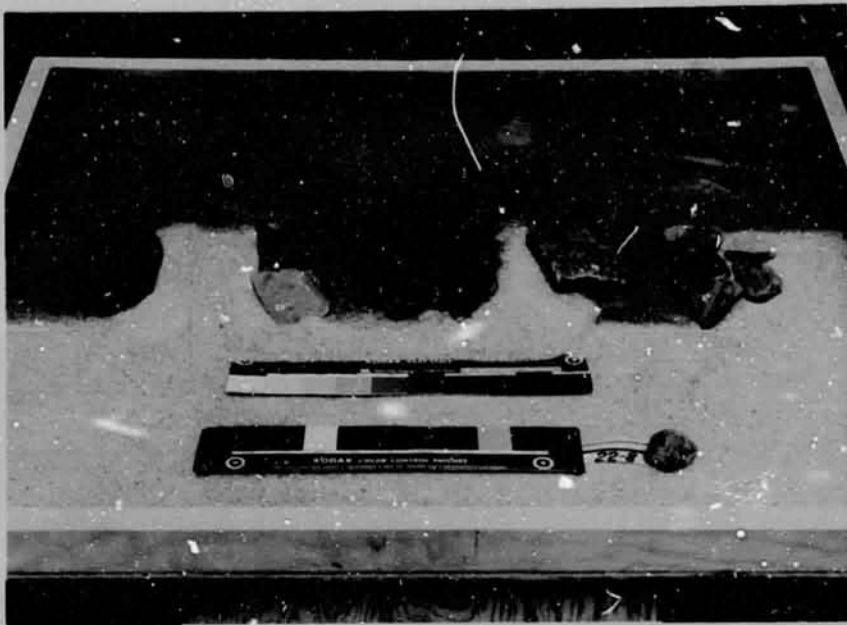
Figure 9-1. Test Scene with Sun-Zenith Angle of 45° and
Sun-Camera Angle of 0°
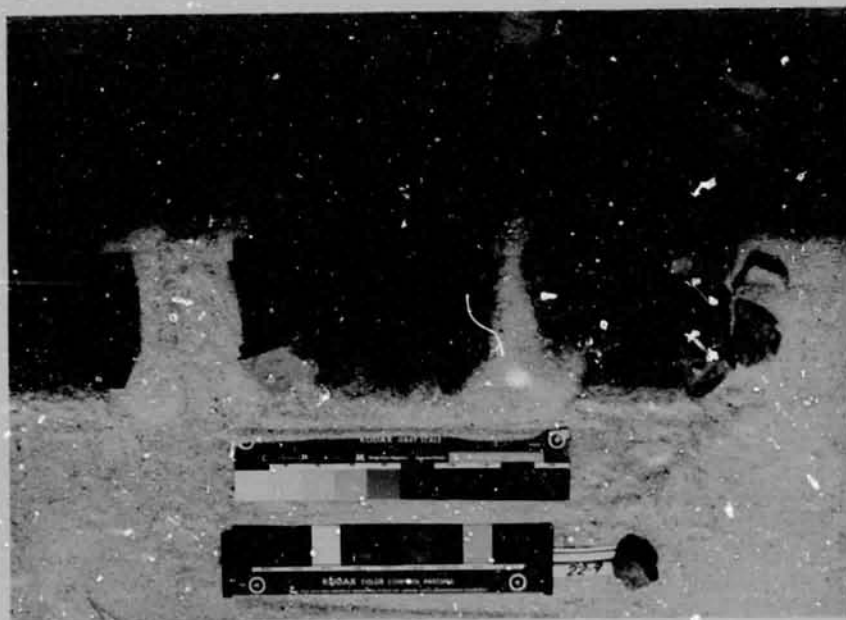
Figure 9-2. Test Scene with Sun-Zenith Angle of 45° and
Sun-Camera Angle of 90°

FIGURE 9-3. SPATIAL MODULATION OF A DEATH VALLEY SCENE

KODACHROME II

TRI-X COPY.

MODULATION

CYCLES/40M
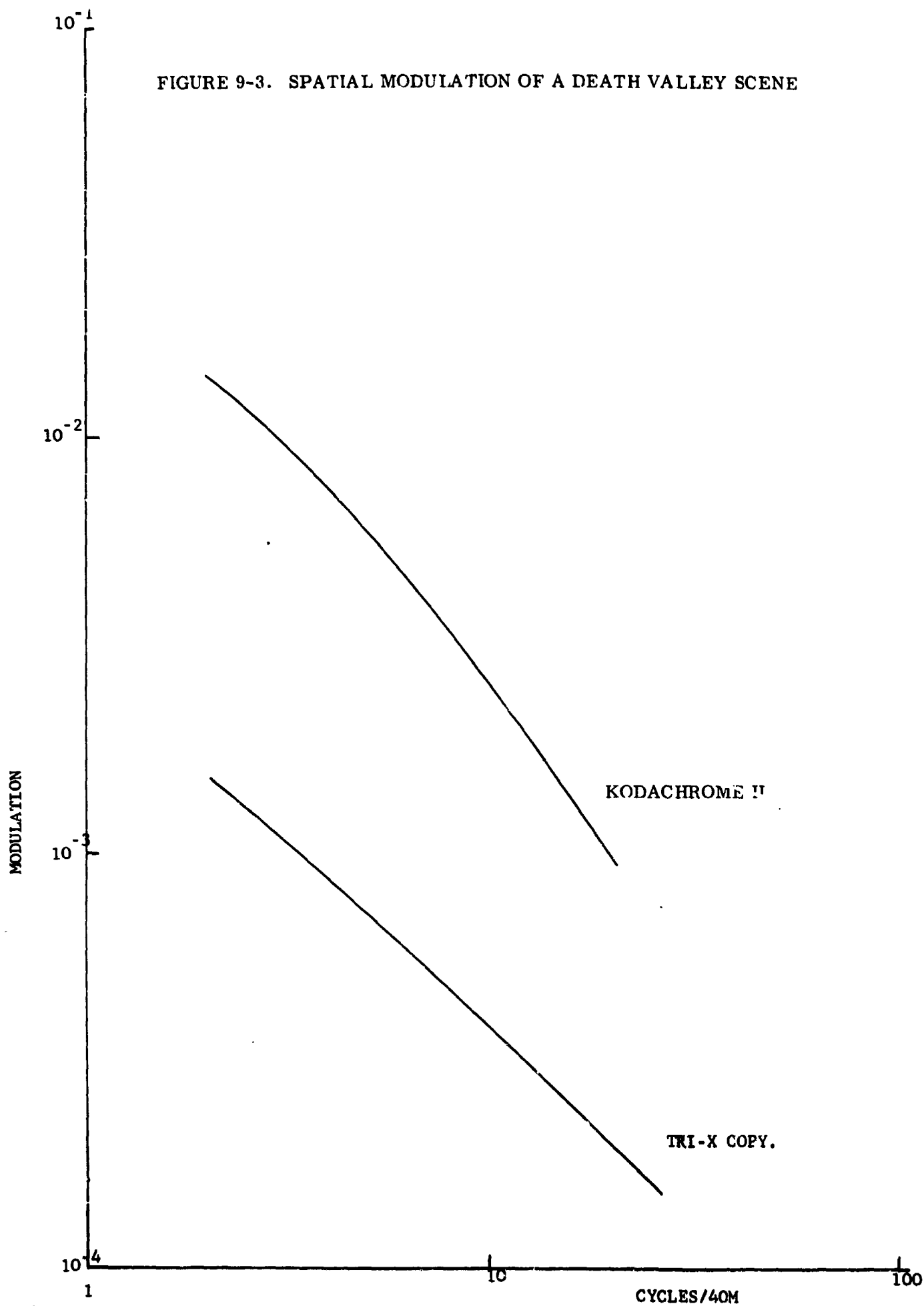
SECTION 10

REFERENCES

1. Pollack, J. S., and Sagan, C, "An Analysis of Martian Photometry and Polarimetry,"
    Space Sciences Reviews, Vol. 9:2, pp 243-299, 1969.

2. de Vaucouleurs, G., "Geometric and Photometric Parameters of the Terrestrial
    Planets," Icarus, Vol. 3, pp 187-235, 1964.

3. Mc Cord, T. B., and Adams, J. B., "Spectral Reflectivity of Mars," Science, Vol. 163,
    pp 1058-1060, 1969.

4. Moroz, V. I., Physics of Planets, Nauka Press, Moscow, 1967 (NASA Translation
    TTF-515, April 1968).

5. Tull, R. G., "The Reflectivity Spectrum of Mars in Near Infrared," Icarus, Vol. 5
    pp 505-514, 1966.

6. de Vaucouleurs, G., Physics of the Planet Mars, Faber and Faber, Ltd., London,
    1954.

7. Dollfus, A., Study of the Planets by Means of the Polarization of Their Light,
    University of Paris, May 1955, NASA Technical Translation F-188, Washington, D. C.,
    July 1964.

8. Kuiper, G. P., Ed., The Atmospheres of the Earth and Planets, University of Chicago,
    pp 362-363, 1952.

9. Schilling, G., Limiting Model Atmospheres of Mars, Report R-402-JP L, The Rand
    Corporation, Santa Monica, Calif., 1962.

10. Elder, T., and Strong, J., "The Infrared Transmission of the Atmospheric Windows,"
    Journal of the Franklin Institute, Vol. 255:3, p 189, 1953.

11. Howard, J. N., Burch, D. E., et al, A series of papers in the Journal of the Optical
    Society of America, No's. 3, 4, 5, and 6, on the Infrared Transmission Through
    Synthetic Atmospheres, 1956.

12. Leighton, R. B., "The Photographs from Mariner IV," Scientific American, Vol. 214,
    No. 4 pp 54-68, April 1966.

13. Gilluly, J., et al, "Origin of Granite," Memoir, Vol. 28, The Geological Society
    of America, Boulder, Colorado, 1948.

14. Rea, L. G., The Atmosphere and Surface of Mars, Spaces Sciences Laboratory, University of California, Berkeley, California, 1965.

15. Brooks, E. M., Comprehensive Summary of Available Knowledge of the Meteorology of Mars and Venus, NASA Contractor Report NASA CR-786, GCA Corporation, Washington, D. C., May 1967.

16. Bagnold, R. A., The Physics of Blown Sand and Desert Dunes, Methuen and Company, Ltd., London, 1941.

17. Sagan, C., Phoneuf, J. P., Ihnat, M., "Total Reflection Spectrophotometry and Thermo-gravimetric Analysis of Simulated Martian Surface Materials," Icarus, Vol. 4:1, pp 43-61, 1965.

18. Hovis, Jr., W. A., "Infrared Reflection Spectra of Some Common Minerals," Applied Optics, Vol. 5:2, pp 245-248, 1966.

19. Azmon, E., "Genetic States of Simulated Lunar Rocks," Northrop Corporate Laboratories, NASA CR-1081, Washington, D. C., June 1968.

20. Barth, T. F. W., Theoretical Petrology, John Wiley and Sons, Inc., New York, 1952.

21. Cameron, R. E., Blank, G. B., Gensel, D. R., Desert Soil Collection at the JPL Soil Science Laboratory, Technical Report No. 32-977, Jet Propulsion Laboratory, California Institute of Technology, Pasadena, California, October 1966.

22. Capen, C. F., The Mars 1964-1965 Apparition, Technical Report No. 32-990, Jet Propulsion Laboratory, California Institute of Technology, Pasadena, California, December 1966.

23. Clements, T., et al, A Study of Desert Surface Conditions, University of Southern California for Environmental Protection Research Division Technical Report EP-53, Quartermaster Research and Development Center, U. S. Army, Natick, Mass., April 1957.

24. Clements, T., et al, A Study of Windborne Sand and Dust in Desert Areas, University of Sourthern California for Earth Sciences Division Technical Report ES-8, U. S. Army Natick Laboratories, Natick, Mass., August 1963.

25. Cronin, J. F., Terrestrial Multispectral Photography, AFCRL-67-0076, Special Report No. 56, Air Force Cambridge Research Laboratories, L. G. Hanscom Field, Bedford, Mass., January 1967.

10-2

26. Evans, D.C., "Ultraviolet Reflectivity of Mars", *Science*, Vol. 149 pp 969-972, 27 August 1966.

27. French, H., "Some Notes on the Origin of the Color of the Martian Deserts," *Journal of the British Astronomical Association*, Vol. 70 No. 3, pp 136-138, March 1960.

28. Glasstone, S., *Sourcebook on the Space Sciences*, D. Van Nostrand Company Inc Princeton, New Jersey, 1965.

29. Hovis, Jr., W.A., "Infrared Reflectivity of Fe_2O_3 . H_2O: Influence on Martian Reflection Spectra," Icarus, Vol 4, pp 41-42, 1964.

30. Hovis, Jr., W.A., "Infrared Reflectivity of Iron Oxide Minerals," *Icarus*, Vol. 4, pp 425-430, 1965.

31. Hovis, Jr., W.A., and Callahan, W.P, "Infrared Reflectance Spectra of Igneous Rocks, Tuffs, and Red Sandstone from 0.5 to 22 Microns," *Journal of the Optical Society of America*, Vol 56:5, pp 39-643, 1966.

32. Levitin, I.B., *Fotografiya V Infrakrasnykh Luchakh (Infrared Photography)*, Publishing House of the Defense Department of USSR, Moscow, 1961 (Translation FTD-MT-65-187, Foreign Technology Division WP-AFB, Ohio, p 75, 1967).

33. Loney, R.A., *Structure and Composition of the Southern Coulee, Mono Craters, California-A Pumiceous Rhyolite Flow*, U.S. Geological Survey, Flagstaff, Arizona, NASA Reproduction N66-37371, 1965.

34. Loney, R.A., *The Kana-A Flow, An Alkali Basalt of the San Francisco Volcanic Field*, Arizona, Unpublished Manuscript, U.S. Geological Survey, NASA Reproduction N66-35970.

35. Lyot, B., "Research on the Polarization of Light from Planets and from Some Terrestrial Substances," *Annales de l'Observatoire de Paris*, Section de Meudon, Vol. VIII, No. 1, 1929, NASA Technical Translation F-187, Washington, D.C., July 1964.

36. Nash, D.B., *Sampling of Planetary Surface Solids for Unmanned in Situ Geological and Biological Analysis*, Technical Report 32-1225, Jet Propulsion Laboratory, California Institute of Technology, Pasadena, California, November 1967..

37. Neal, J.T., Ed., *Playa Surface Morphology: Miscellaneous Investigations*, AFCRL-68-0133, Enviromental Research Paper No. 283, Air Force Cambridge Research Laboratories, L.G. Hanscom Field, Bedford , Mass., March 1968.

38. Öpik, E.J., "The Martian Surface", <u>Science</u> Vol. 153. No. 3733, pp 255-265, 15 July 1966.

39. Pittendrigh, C.S., et al , Ed., <u>Biology and the Exploration of Mars,</u> Publication 1296, National Academy of Sciences, National Research Council, Washington, D.C., 1966.

40. Rankama, K., and Sahama, T.G., <u>Geochemistry,</u> The University of Chicago Press, Chicago, 1950.

41. Robinson, J.C., <u>Ground-Based Photography of the Mariner IV Region of Mars,</u> TN 701-66-10, New Mexico State University Observatory, Las Cruces, New Mexico, August 1965.

42. Salisbury, J.W., <u>The Light and Dark Areas of Mars,</u> AFCRL-66-722, Environmental Research Paper No. 231, Air Force Cambridge Research Laboratories, L.G. Hanscom Field, Bedford, Mass., October 1966.

43. Slipher, E.C., <u>The Photographic Story of Mars,</u> Sky Publishing Corporation, Cambridge, Mass., 1962.

44. <u>Surveyor V, A Preliminary Report,</u> NASA SP-163, Washington, D.C., December 1967.

45. Twenhofel, W.H., and Tyler, S.A., <u>Methods of Study of Sediments,</u> McGraw-Hill Book Company, Inc., New York, 1941.

46. Whipple, H.E., "Geological Problems in Lunar Research," <u>Annals of the New York Academy of Sciences,</u> Vol 123, Art. 2, pp 367-1257, New York, July 1965.

47. Adams, J.B., and Filice, A.G. "Spectral Reflectance 0.4 to 2.0 Microns of Silicate Rock Powders." Journal of Geological Research, Vol. 72, No. 22, pp. 5705-5715, 1967.

48. Jones, L.A., and Condit, H.R., Journal Optical Society of America, Vol. 38, p. 123, 1948.

49. Jones, L.A., and Condit, H.R., Journal Optical Society of America, Vol. 39, p. 94, 1949.

50. Belver, T., and Huffman, G., "Effect on Transmission Errors on Image Data Compress Techniques." TIS No. 68Sd235 (GE Co. Document), June 1968.

51. Adams, J.B., "Lunar Surface Composition and Particle Size: Implications from Spectral Reflectance Data." Journal of Geophysical Research, Vol. 72, No. 22, pp. 5717-5720, 1967.

SECTION 11

APPENDIX

11.1 SCHEMATIC OF PROGRAM "MULT-SPEC"

```
┌─────────────────────────────────────────────────────────┐
│ Insert – Irradiance Data                                 │
│          Atmospheric Transmission Data                   │
│          Optical Transmission Data                       │
│          Reflectivity Data                               │
│          Response Data                                   │
└─────────────────────────────────────────────────────────┘
                          │
                          ▼
┌─────────────────────────────────────────────────────────┐
│ Select initial wavelength, wavelength interv i and number of │
│ intervals for Integration                                │
└─────────────────────────────────────────────────────────┘
                          │
                          ▼
┌─────────────────────────────────────────────────────────┐
│ Determine value of the Irradiance dependant variable at the │
│ selected wavelengths by interpolation                    │
└─────────────────────────────────────────────────────────┘
                          │  ┌ ─ ─ ─ ─ ─ ─ ─ ─ ─ ─ ─ ─ ┐
                          ▼                              ▼
┌─────────────────────────────────────────────────────────┐
│ Determine value of the Atmospheric Transmission dependant │
│ variable at the selected wavelengths by interpolation    │
└─────────────────────────────────────────────────────────┘
                          │  ◄ ─ ─ ─ ─ ─ ─ ─ ─ ─ ─ ─ ─
                          ▼                              ▼
┌─────────────────────────────────────────────────────────┐
│ Determine value of the Optical Transmission dependant    │
│ variable at the selected wavelengths by interpolation    │
└─────────────────────────────────────────────────────────┘
                          │  ◄ ─ ─ ─ ─ ─ ─ ─ ─ ─ ─ ─ ─ ┘
                          ▼
┌─────────────────────────────────────────────────────────┐
│ Determine the value of the Constituent reflectivity at the │
│ selected wavelength by interpolation                     │
└─────────────────────────────────────────────────────────┘
                          │
                          ▼
┌─────────────────────────────────────────────────────────┐
│ Determine the value of the Sensor Response at the selected │
│ wavelengths by interpolation                             │
└─────────────────────────────────────────────────────────┘
                          │
                          ▼
┌─────────────────────────────────────────────────────────┐
│ Multiply the interpolated values of Irradiance, Atmospheric │
│ Transmission, Optical Transmission, Constituent Reflecti- │
│ vity and Sensor Response together at each selected wave-  │
│ length and integrate over the selected wavelength range  │
└─────────────────────────────────────────────────────────┘
                          │
                          ▼
┌─────────────────────────────────────────────────────────┐
│                    Sensor Output                         │
└─────────────────────────────────────────────────────────┘
```

NOTE: Dashed lines represent options for not including a
      part of the program.

11.2 AFFECT OF NOISE AND FILTER BREAKTHROUGH

Internally funded work continued after the contractual part of the study was completed and some of the activities suggested in the follow-on have been preliminarily investigated. The sections referring to these areas in the report are Sections 8.2 and 9.3.

11.2.1 THE AFFECT OF INCREASING BANDWIDTH

In Section 3.5.4 the inherent modulations of the constituents were shown to be identical to those determined for narrow bands. As the bandwidth increases the scene modulation (and discrimination modulation) are degraded. Examples of this degree of degradation are shown in Figure 11-1. These curves were derived for somewhat ideal filters; the results that may be expected from manufactured filters are discussed below.

11.2.2 THE AFFECT OF FILTER BREAKTHROUGH

Most, if not all, narrow band filters have some transmission at wavelengths outside the quoted band of their primary transmission. Typical values for the transmission of the filter in this breakthrough region is from 0.1% to 0.5%. Examples of this behavior are shown in Figure 11-2; this data was obtained from an Eastman Kodak Infrared Interference Filter catalog. The filter shape was normalized and inserted into the MULTSPEC program from which the modulation plots were derived. Note how the wavelength of peak modulation changes together with the decrease in modulation at the peak.

11.2.3 THE AFFECT OF NOISE

The uncooled detectors in the infra-red are generally detector noise limited. The introduction of this phenomenon into the modulation calculations produces the curves shown in Figure 11-3. The anticipated decline of the modulation with the decreasing response of the detector is now clearly evident. A further advance towards a more realistic experimental situation is made by considering the combined effect of breakthrough and noise. The results

are shown in Figures 11 4 and 11-5. The calculations performed on the other uncooled infra-red detectors showed that they were unsuitable, owing to the predominance of noise.

11.2.4 CONCLUSIONS

The results of this brief analysis have shown the power of the technique when noise and other optical defects of experimental equipment are included in the analysis. It was anticipated the technique would enable the optimum combination of filter and detector to be chosen; this has now been clearly demonstrated.
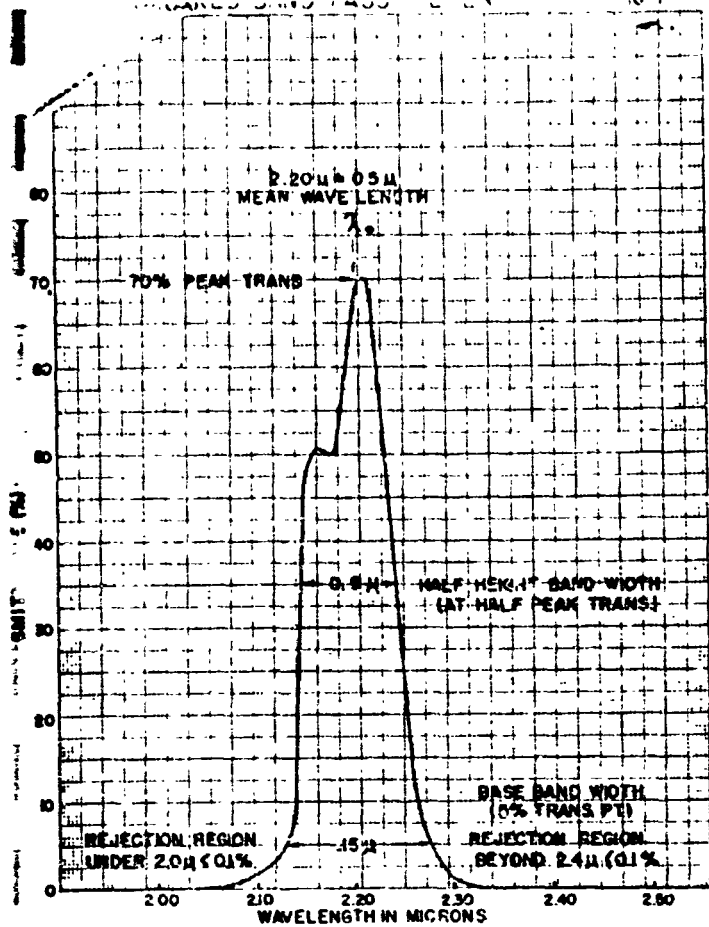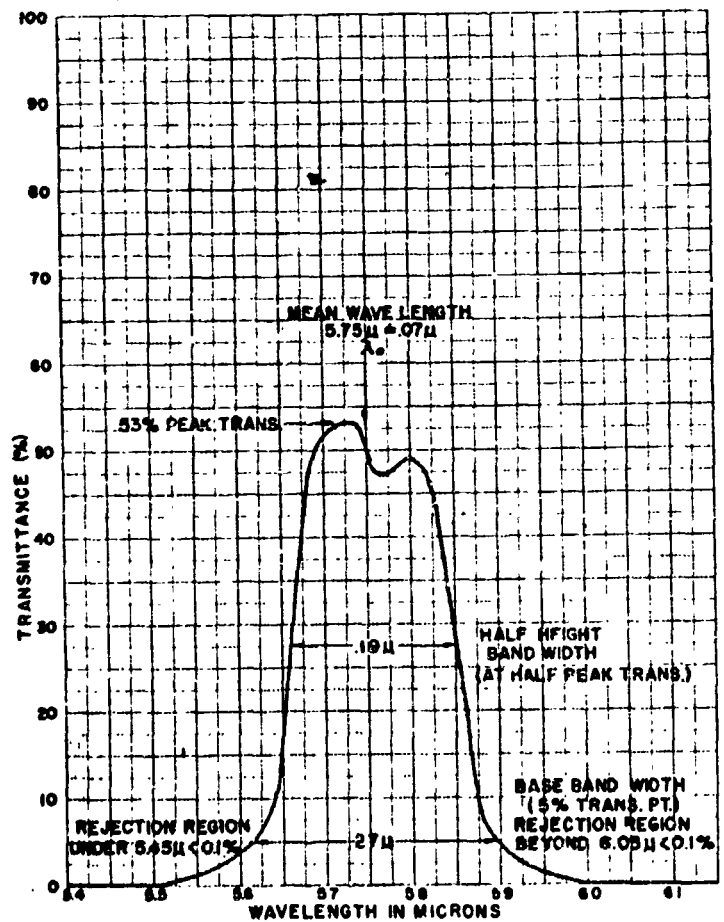
INFRARED BAND PASS FILTER 4.5 μ   FIG. 9
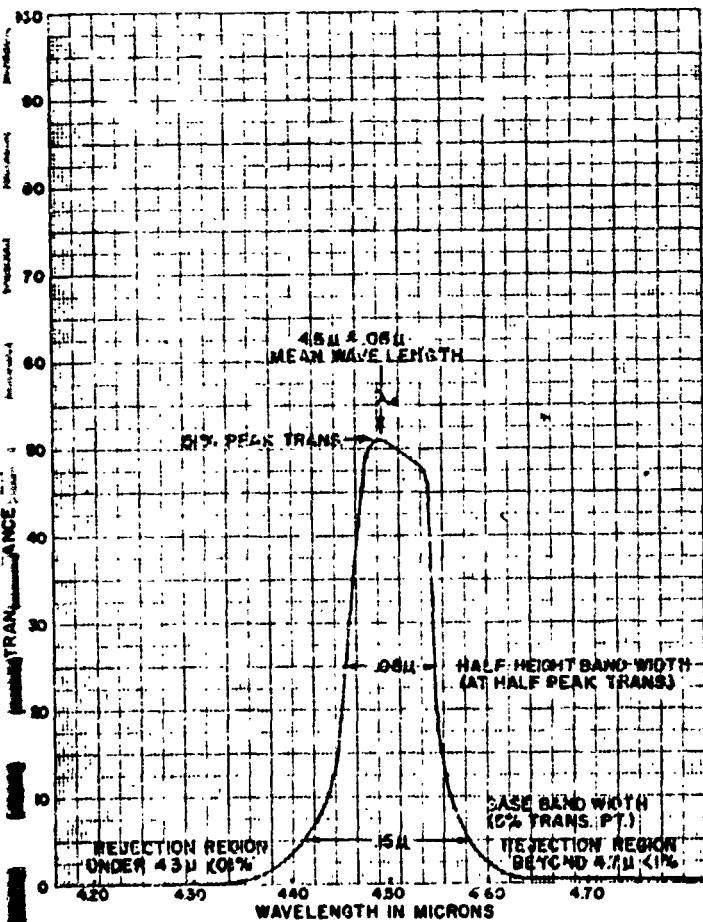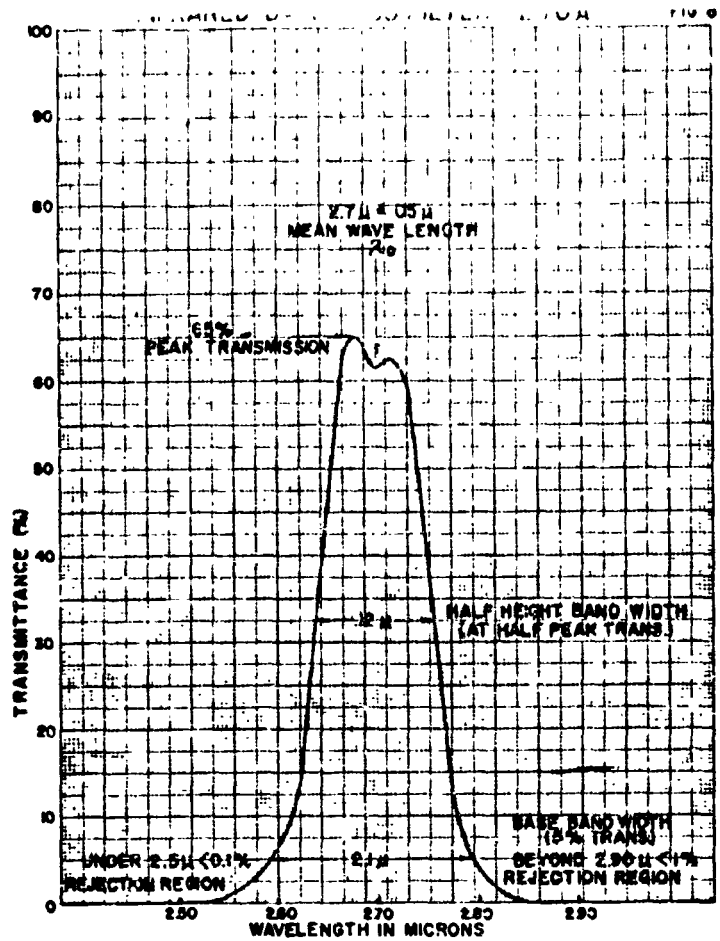
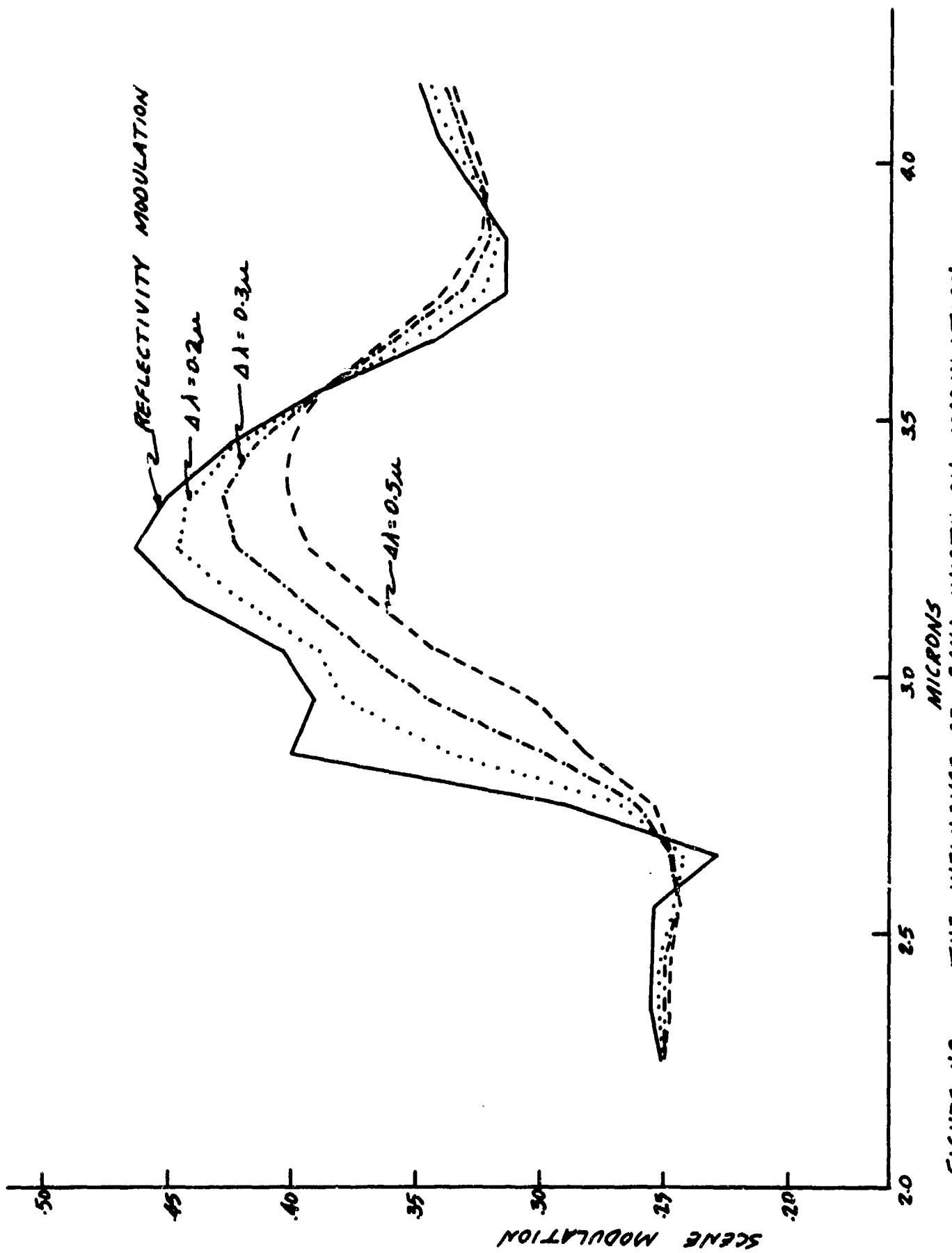INFRARED BAND PASS FILTER 5.75 μ   FIG. 11

FIGURE 11-1

FIGURE 142   THE INFLUENCE OF BAND WIDTH ON MODULATION
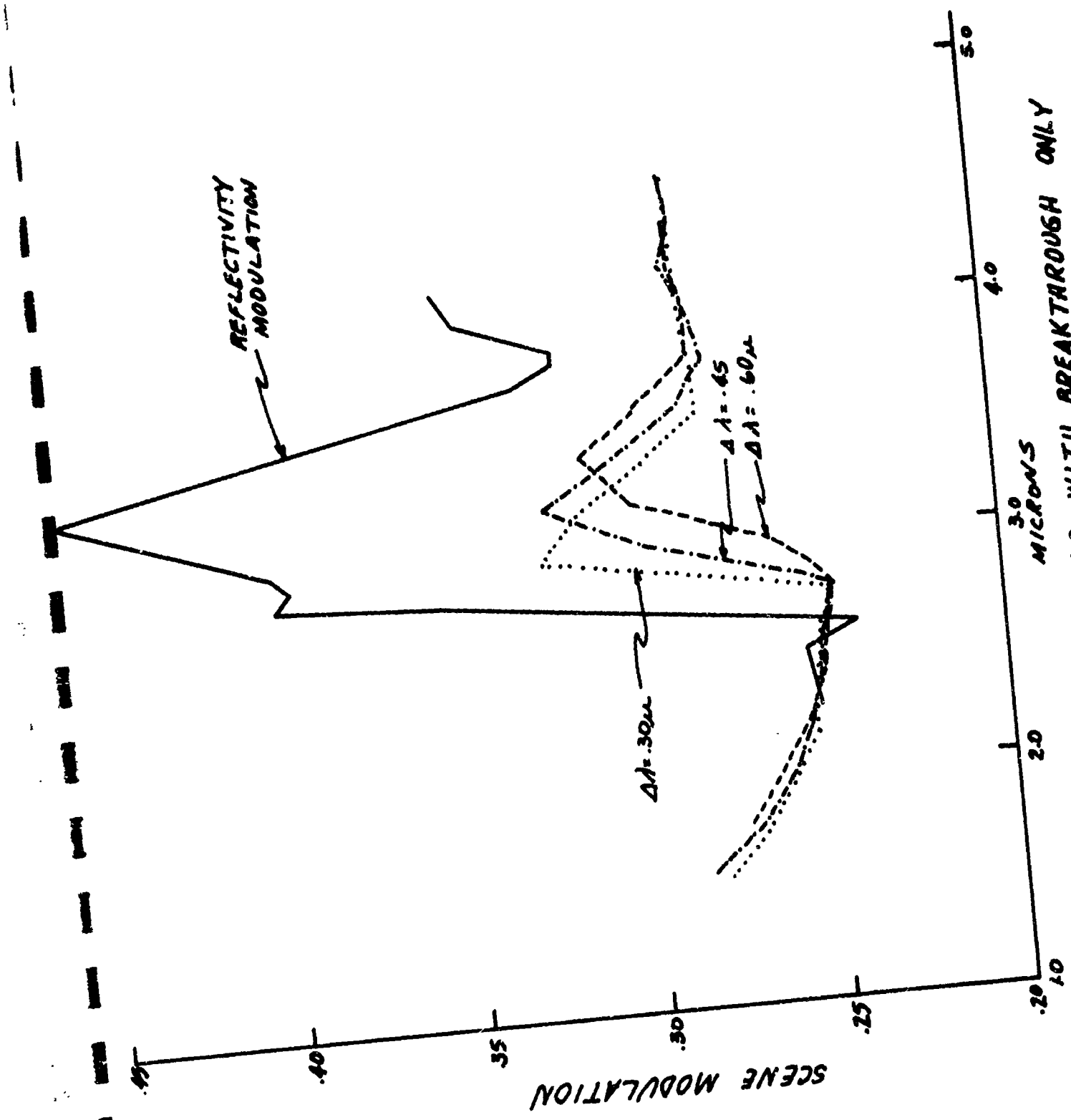
FIGURE 11-3   MODULATION FOR PbS WITH BREAKTHROUGH ONLY

REFLECTIVITY MODULATION

Δλ=0.6µ

Δλ=0.8µ

Δλ=0.4µ

SCENE MODULATION

.45

.40

.35

.30

.25

.20

.15

.10

2.0   2.5   3.0   3.5   4.0
                MICRONS

PbS WITH NOISE ONLY   (ΔF=5 Hz)
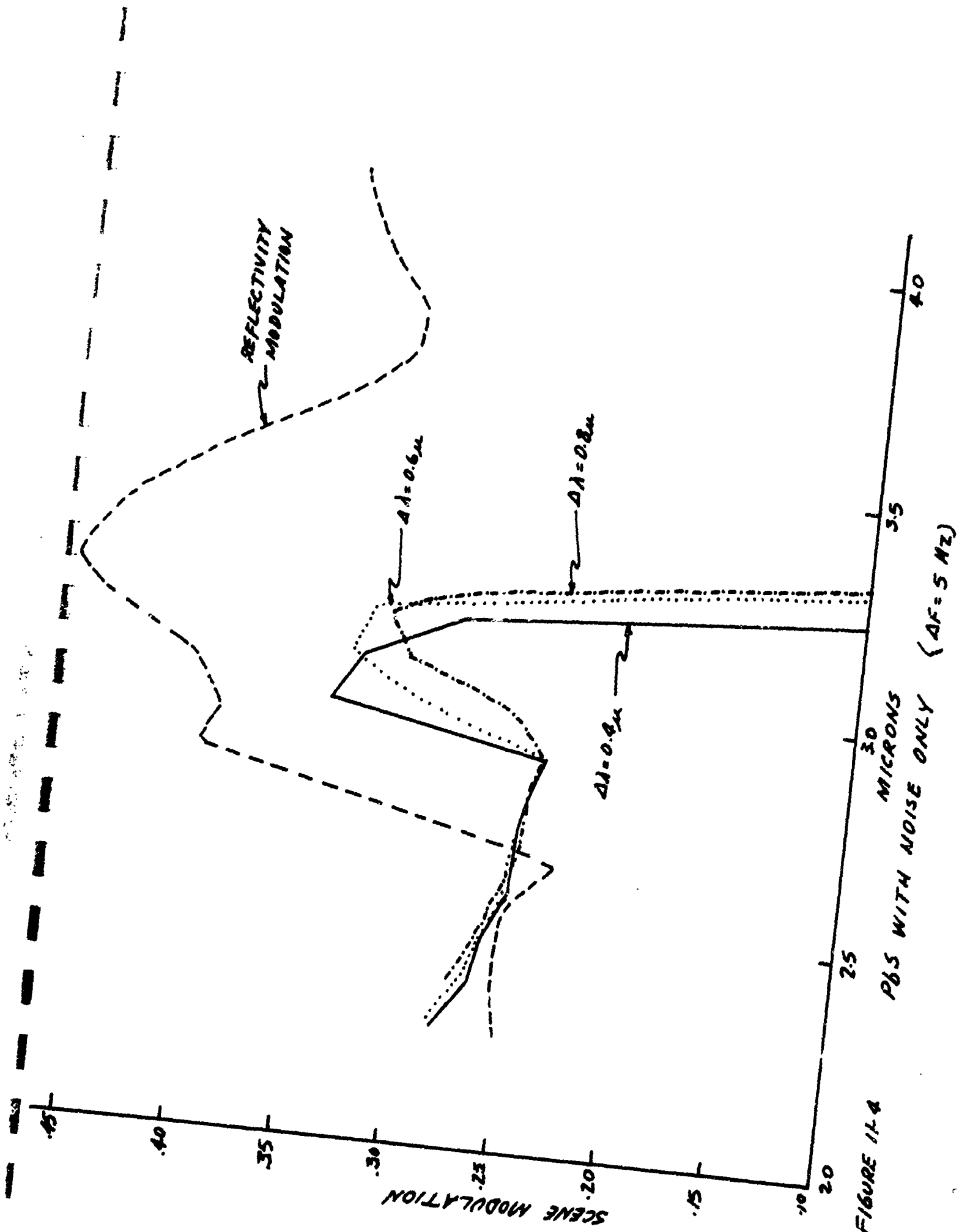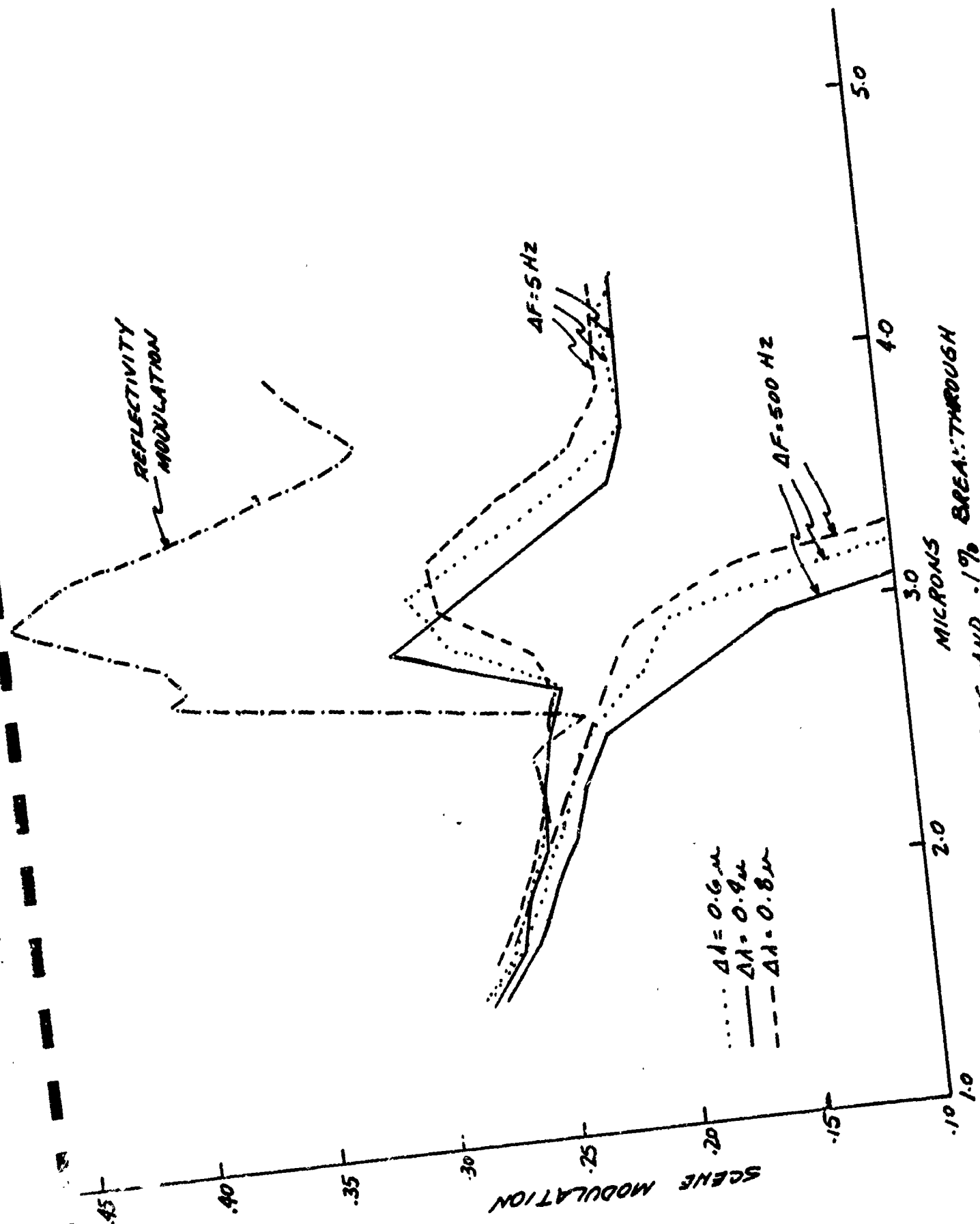
FIGURE 14-4

FIGURE 11-5 PbS WITH NOISE AND .1% BREAK-THROUGH